

THÈSE DE DOCTORAT
de l'Université de recherche Paris Science et Lettres

**Préparée au Laboratoire de Physique Statistique
de l'École normale supérieure de Paris**

**From few-body atomic physics to many-body statistical physics:
The unitary Bose gas and the three-body hard-core model**

École doctorale n° 564 Physique en Île-de-France

**Soutenue par Tommaso COMPARIN
le 6 décembre 2016**

COMPOSITION DU JURY:

M. HAMMER, Hans-Werner
TU Darmstadt, Rapporteur

M. KRAUTH, Werner
ENS Paris, Directeur de thèse

M. ROSCILDE, Tommaso
ENS Lyon, Rapporteur

M. SALOMON, Christophe
ENS Paris, Examinateur

Mme. VIGNOLO, Patrizia
Université de Nice-Sophia Antipolis,
Examinateuse

ÉCOLE DOCTORALE 564 PHYSIQUE EN ÎLE-DE-FRANCE
ÉCOLE NORMALE SUPÉRIEURE



Département
de Physique
École normale
supérieure

LABORATOIRE DE PHYSIQUE STATISTIQUE

Thèse de doctorat

**From few-body atomic physics to many-body statistical physics:
The unitary Bose gas and the three-body hard-core model**

présentée par Tommaso COMPARIN

en vue de l'obtention du diplôme de Docteur de l'Université de recherche Paris
Sciences et Lettres - PSL Research University.

Soutenue le 6 décembre 2016 devant le jury composé de:

Hans-Werner HAMMER	Rapporteur
Werner KRAUTH	Directeur de thèse
Tommaso ROSCILDE	Rapporteur
Christophe SALOMON	Examinateur
Patrizia VIGNOLO	Examinateuse

General introduction

Ultracold atoms represent a rich environment to realize and manipulate quantum mechanical systems. For atomic clouds cooled to the sub- μK temperature regime, the thermal de Broglie wavelength becomes comparable to the interparticle distance, and spectacular quantum phenomena take place. For bosonic atoms, this has lead in 1995 to the first observation of a Bose-Einstein condensate (BEC), a macroscopic quantum state with features determined by the statistics of its indistinguishable components [1, 2, 3]. In comparison with solid-state systems, the peculiarity of ultracold atoms is the large degree of control achievable in experiments, which allows to explore a wide set of physical conditions [4]. A central example is the control of the strength of interparticle interactions. The original BEC observation was obtained in the weakly-interacting regime, but the Feshbach-resonance technique currently allows to tune interactions from very weak to arbitrarily strong [5].

In the unitary limit, the interaction strength reaches its maximum. Experiments with fermionic atoms, close or at this limit, have lead to major discoveries concerning the condensation of atomic pairs [6]. The low-temperature unitary Fermi gas is a universal system, where thermodynamic properties like the equation of state are determined by the sole available length scale, the typical interparticle distance. Bosonic systems with unitary interactions require a more complex description, including the presence of Efimov trimers. These trimers constitute an infinite sequence of three-body bound states, linked by a geometric scale invariance [7]. The interest in strongly-interacting bosonic system was greatly enhanced by the first observation of Efimov trimers, obtained in 2006 with ultracold atoms [8], and the study of many-body systems of bosonic atoms with unitary interactions is an active theoretical and experimental research subject [9]. A central question is whether these systems may have a metastable gaseous phase, at low temperature.

This thesis is centered on a system of bosonic atoms, with interactions tuned to the unitary limit. In Chapter 2, we consider two- or three-body systems, interacting through

a zero-range model potential. For three particles, this corresponds to the universal Efimov theory. As compared to fermions, universality for unitary bosons includes an additional length scale, the three-body parameter [10]. We introduce it through a cutoff at short three-body distance, and show that the resulting model shares several properties with the universal theory. At finite temperature, the cutoff also assures the thermodynamic stability of the system.

The theoretical treatment of the many-body problem is made even more difficult by the presence of strong interactions. In Chapter 3, we describe the numerical scheme employed in this work, namely the path integral quantum Monte Carlo (QMC) technique. It was originally developed in the context of liquid helium [11], and it is the method of choice to treat bosonic ultracold gases. The additional difficulties caused by strong interactions are addressed through a novel algorithm, which is optimal for two particles and also allows an efficient treatment of the many-body problem.

The application to unitary bosons is described in Chapter 4. We consider a homogeneous system, which allows a precise determination of the phase diagram. This includes the three phases previously studied in the trapped case [12]. The high-temperature, normal-gas phase can be described within the virial-expansion approach [13, 12]. This cannot be extended to low temperatures, where two distinct phase transitions take place. For large values of the three-body parameter, the system enters the BEC phase. We find that the critical temperature T_c for this transition is approximately 10% smaller than its non-interacting counterpart, in contrast with the increase of T_c caused by weak repulsive interactions [14]. For small three-body parameter, the system is thermodynamically unstable towards the formation of Efimov-liquid droplets, which we identify and characterize both via an approximate analytic model and via the QMC technique. In the normal-gas and BEC phases, we also compute the momentum distribution. This is an experimentally accessible observable of key importance in the context of unitary systems, due to its universal features. The results in this chapter are the object of [Publication 2](#).

In the infinite-temperature limit, the only relevant term of our model for the unitary gas would be the cutoff on the three-body distance. In Chapter 5, we consider a classical system which is entirely defined by this three-body interaction. This is a generalization of the hard-sphere model, with a counter-intuitive behavior due to the absence of two-body interactions. We first consider the packing problem, in two and three dimensions, and propose a solution based on a variational ansatz and on the simulated-annealing technique. Extending these results to finite pressure shows that the system has a discontinuous melting transition, which we identify through the Monte Carlo technique. The results on the classical three-body hard-core model are the object of [Publication 1](#).

Other research projects in the field of ultracold atoms were completed or started in the time frame of this thesis, corresponding to the following publications:

- M. Di Liberto, **T. Comparin**, T. Kock, M. Ölschläger, A. Hemmerich, and C. Morais Smith. Controlling coherence via tuning of the population imbalance in a bipartite optical lattice, *Nature Communications* **5**, 5735 (2014).
- R. H. Chaviguri, **T. Comparin**, V. S. Bagnato, and M. A. Caracanhas. Phase transition of ultracold atoms immersed in a BEC vortex lattice, in preparation.

Contents

1 Bosons at low temperature	13
1.1 Bose-Einstein condensation	13
1.2 Ultracold atomic gases	19
1.3 Density matrix and path integrals	21
1.4 Recursion method for non-interacting bosons	24
2 Few-body physics with strong interactions	27
2.1 Two-body physics	28
2.1.1 Scattering theory	28
2.1.2 Two-body density matrix	33
2.1.3 Correlation functions	36
2.2 Three-body physics and Efimov effect	41
2.2.1 Efimov trimers	42
2.2.2 Three-body-cutoff model	45
2.3 Ultracold atoms with strong interactions	50
2.3.1 Feshbach resonances	51
2.3.2 Signatures of the Efimov effect	52
3 Path-Integral quantum Monte Carlo	59
3.1 Monte Carlo sampling	59
3.1.1 Direct sampling	60
3.1.2 Markov-chain Monte Carlo	63
3.1.3 Variable-dimensionality sampling	66
3.2 Sampling quantum paths	68
3.2.1 Path integrals and Monte Carlo	69
3.2.2 Closed-sector moves	73

3.2.3	Open-sector moves	79
3.2.4	Sector-changing moves	84
3.3	Observables	89
3.3.1	Spatial correlation functions	89
3.3.2	Permutation cycles and superfluid density	91
3.3.3	One-body-reduced density matrix	94
3.3.4	Momentum distribution and condensate fraction	95
3.4	Additional aspects related to PIMC	97
3.4.1	Superfluid transition and finite-size scaling	97
3.4.2	Large-momentum tail of $n(\mathbf{k})$	100
4	Many-body unitary bosons	107
4.1	Imaginary-time discretization revisited	108
4.2	Efimov liquid	110
4.2.1	Liquid/gas phase coexistence	111
4.2.2	QMC observation of the Efimov liquid	114
4.3	Normal-gas phase	119
4.3.1	Momentum distribution	119
4.3.2	Contact density	121
4.4	BEC phase	122
4.4.1	Critical temperature	122
4.4.2	Momentum distribution	125
4.4.3	Contact density	127
	Appendix 4.A Contact density at high temperature	128
5	Classical three-body hard-core model	131
5.1	Sampling configurations at fixed pressure	133
5.1.1	Box rescaling	134
5.1.2	Insertion/removal move	136
5.2	Packing problem	138
5.2.1	Variational ansätze	140
5.2.2	Simulated annealing	149
5.3	Finite-pressure phase diagrams	152
5.3.1	Two dimensions	153
5.3.2	Three dimensions	161
	General conclusion	165
	Acknowledgements	167
	Bibliography	169

CONTENTS

11

Publications	187
Publication 1	187
Publication 2	195

CHAPTER 1

Bosons at low temperature

1.1 Bose-Einstein condensation

The phenomenon of Bose-Einstein condensation (BEC) for a system of indistinguishable particles corresponds to the macroscopic occupation of a single-particle quantum state [15]. For low-temperature bosonic systems a novel phase of matter emerges (the Bose-Einstein condensate), which is a direct consequence of the quantum statistics of its constituents. Predicted in the 1920s, this phenomenon was first clearly identified through ultracold-atomic experiments, in the 1990s.

In this chapter, we define the BEC phase, in connection with the phenomenon of superfluidity, and describe the experimental set-ups where it was first observed (*cf.* Section 1.2). The path-integral formalism provides a useful alternative view on the BEC phase, which turns into a powerful calculation scheme for non-interacting bosons (*cf.* Section 1.4). Its generalization to include interactions is obtained through the quantum Monte Carlo (QMC) technique, as described in Chapter 3.

Indistinguishable quantum particles

Bose-Einstein condensation emerges as a direct consequence of quantum statistics, as is easily shown for the non-interacting gas [16]. In the absence of interactions, the Hamiltonian of N particles is the sum of N commuting single-particle terms. A configuration is defined by assigning each particle to one of the single-particle available states $|i\rangle$. This leads to an occupation number N_i for each state $|i\rangle$, with $\sum N_i = N$. Assuming here that the number M of single-particle states is finite, we compute the number of states which

realize a certain $\{N_i\}$. For distinguishable particles, this reads

$$W_{\text{dist}}(\{N_1, \dots, N_M\}) = \frac{N!}{\prod_{i=1}^M N_i!}, \quad (1.1)$$

which is the number of ways of assigning N different objects to M groups. W_{dist} has a maximum for configurations where all occupation numbers are close to N/M . In contrast, it is suppressed when a large fraction of particles occupies a small number of states, as for $\{N_i\} = \{N, 0, \dots, 0\}$. This property changes drastically in the case of indistinguishable bosonic particles. As the particles bear no difference, exchanging two of them does not lead to a different state. Thus the number of ways to obtain a certain occupation-number sequence $\{N_i\}$ is simply

$$W_{\text{bos}}(\{N_1, \dots, N_M\}) = 1. \quad (1.2)$$

In this case, unlike W_{dist} , the homogeneous distribution $N_i = N/M$ has the same weight as an extreme configuration like $\{N_i\} = \{N, 0, \dots, 0\}$. The different statistical weight assigned to configurations with a large occupation number for a single state is at the basis of the BEC phenomenon. Single-particle states have different energies, so that a larger population of the ground state $|0\rangle$ is favored, at any finite temperature. For bosons, the average occupation number of $|0\rangle$ is larger than any other average N_i , and this effect is more pronounced at low temperatures. For distinguishable particles, however, a large occupation of $|0\rangle$ is prevented by the strong suppression of W_{dist} for configurations with one occupation number much larger than the others. The difference between distinguishable particles and bosons becomes stronger when the average occupation number per state increases. $W_{\text{dist}}(\{N, 0, \dots, 0\})$, for instance, decays exponentially at large N , for a given M . For bosons in a periodic box, a rigorous condition for the regime where indistinguishability has a drastic effect is found below (*cf.* Eq. 1.10), leading to a threshold for the temperature at which the occupation of $|0\rangle$ becomes macroscopic.

Bose-Einstein condensation in a periodic box

We consider three-dimensional non-interacting particles in a periodic cubic box. The eigenstates of the single-particle Hamiltonian are plane waves, labeled by an index $\mathbf{n} \in \mathbb{Z}^3$. The \mathbf{n} -th state has wave number \mathbf{k}_n and energy E_n equal to

$$\mathbf{k}_n = \frac{2\pi}{L}\mathbf{n}, \quad E_n = \frac{\hbar^2 \mathbf{k}_n^2}{2m} = \frac{1}{2m} \left(\frac{2\pi\hbar}{L} \right)^2 \mathbf{n}^2, \quad (1.3)$$

where L is the edge length of the box, and m is the particle mass. A distribution of N bosons in the single-particle energy states is defined through the set of occupation numbers $\{N_n\}$. The statistical weight of one such configuration is given by the Boltzmann

factor

$$\exp \left(-\beta \sum_{\mathbf{n} \in \mathbb{Z}^3} N_{\mathbf{n}} E_{\mathbf{n}} \right), \quad (1.4)$$

where $\sum_{\mathbf{n}} N_{\mathbf{n}} E_{\mathbf{n}}$ is the total energy and $\beta = 1/(k_B T)$ is the inverse temperature. We compute the threshold condition for Bose-Einstein condensation within the grand canonical ensemble, where the total number of particles $N = \sum_{\mathbf{n}} N_{\mathbf{n}}$ can fluctuate. In this case, the statistical weight for a given set of occupation numbers $N_{\mathbf{n}}$ is

$$\exp \left(-\beta \sum_{\mathbf{n} \in \mathbb{Z}^3} N_{\mathbf{n}} (E_{\mathbf{n}} - \mu) \right) = \prod_{\mathbf{n} \in \mathbb{Z}^3} \left[e^{-\beta(E_{\mathbf{n}} - \mu)} \right]^{N_{\mathbf{n}}}, \quad (1.5)$$

where the chemical potential μ can be fixed by setting the average number of particles, $\langle N \rangle$. The thermal average for $N_{\mathbf{n}}$ reads

$$\langle N_{\mathbf{n}} \rangle = \frac{\sum_{N_{\mathbf{n}}=0}^{\infty} N_{\mathbf{n}} e^{-\beta N_{\mathbf{n}} (E_{\mathbf{n}} - \mu)}}{\sum_{N_{\mathbf{n}}=0}^{\infty} e^{-\beta N_{\mathbf{n}} (E_{\mathbf{n}} - \mu)}} = \frac{1}{e^{\beta(E_{\mathbf{n}} - \mu)} - 1}, \quad (1.6)$$

which only depends on \mathbf{n} through the energy $E_{\mathbf{n}}$. The total number of particles is the sum of $\langle N_{\mathbf{n}} \rangle$ for $\mathbf{n} \in \mathbb{Z}^3$, which we split into two parts: $\langle N_0 \rangle$ is the average number of condensed particles, occupying the single-particle ground state, while $\langle N_{\text{th}} \rangle = \langle N \rangle - \langle N_0 \rangle$ is the average number of thermal particles. For a given temperature and volume, an upper bound N_{\max} exists for the number of thermal atoms. If $N > N_{\max}$, then at least $N - N_{\max}$ atoms necessarily occupy the single-particle ground state. We compute N_{\max} through the continuous-spectrum approximation, which consists in replacing the sum over excited single-particle states (that is, excluding the ground state) with an integral over their wave vectors. This is valid for large systems at finite temperature, where the spacing between energy levels (proportional to $\hbar^2/(mL^2)$, cf. Eq. 1.3), is much smaller than the thermal energy $k_B T$. The upper bound for N_{th} reads

$$\begin{aligned} N_{\max} &= \sum_{\mathbf{n} \in \mathbb{Z}^3 \setminus \{0\}} \frac{1}{\exp(\beta E_{\mathbf{n}}) - 1} \simeq \left(\frac{2\pi}{L} \right)^3 \int d\mathbf{k} \frac{1}{\exp\left(\beta \frac{\hbar^2 k^2}{2m}\right) - 1} = \\ &= g_{3/2}(1) \times \frac{V}{\lambda_{\text{th}}^3}, \end{aligned} \quad (1.7)$$

where

$$\lambda_{\text{th}} \equiv \sqrt{\frac{2\pi\hbar^2\beta}{m}} \quad (1.8)$$

is the thermal de Broglie wavelength, and

$$g_{3/2}(1) = \sum_{l=1}^{\infty} \frac{1}{l^{3/2}} \simeq 2.612. \quad (1.9)$$

The critical temperature T_c^0 for Bose-Einstein condensation is obtained by setting $N_{\max} = \langle N \rangle$, so that at temperatures below T_c^0 any additional boson would be placed in the ground state. From Eq. 1.7, we find

$$k_B T_c^0 = \frac{2\pi\hbar^2}{m} \left(\frac{\rho}{g_{3/2}(1)} \right)^{2/3} \simeq 3.3125 \times \frac{\hbar^2 \rho^{2/3}}{m}, \quad (1.10)$$

where $\rho = N/V$ is the number density of the system. This can be recast in a threshold for the phase-space density $\rho \lambda_{\text{th}}^3$,

$$\rho \lambda_{\text{th}}^3 = g_{3/2}(1) \simeq 2.612, \quad (1.11)$$

meaning that Bose-Einstein condensation takes place when the thermal wavelength λ_{th} becomes comparable with the typical interparticle spacing $\rho^{-1/3}$.

BEC for interacting systems

In the presence of interactions, the Hamiltonian is not a sum of commuting single-particle terms, and a many-body eigenstate is not simply defined by the assignment of each boson to a single-particle eigenstate. Thus the definition of BEC as the macroscopic occupation of the single-particle ground state breaks down. This has lead to the generalized definition of Bose-Einstein condensation introduced by Penrose and Onsager in 1956 [17], linked to the concept of off-diagonal long-range order (ODLRO) [18].

We consider the eigenstates $\Psi_n(\mathbf{x}_1, \dots, \mathbf{x}_N)$ and eigenvalues E_n which solve the N -body Schrödinger equation, and we introduce the one-body reduced density matrix,

$$g^{(1)}(\mathbf{x}, \mathbf{x}') = \frac{N}{Z} \sum_n e^{-\beta E_n} \int d\mathbf{x}_2 \dots d\mathbf{x}_N \Psi_n^*(\mathbf{x}, \mathbf{x}_2, \dots, \mathbf{x}_N) \Psi_n(\mathbf{x}', \mathbf{x}_2, \dots, \mathbf{x}_N), \quad (1.12)$$

where the normalizing constant in Eq. 1.12 is the partition function $Z = \sum_n \exp(-\beta E_n)$. An equivalent definition of $g^{(1)}(\mathbf{x}, \mathbf{x}')$ in the path-integral formalism is given in Section 3.3.3. Due to its hermiticity, $g^{(1)}$ can be decomposed as

$$g^{(1)}(\mathbf{x}, \mathbf{x}') = \sum_j N_j \chi_j^*(\mathbf{x}) \chi_j(\mathbf{x}'), \quad (1.13)$$

on a complete orthogonal set of single-particle states χ_j , with

$$\begin{aligned} \int d\mathbf{x}' g^{(1)}(\mathbf{x}, \mathbf{x}') \chi_j(\mathbf{x}') &= N_j \chi_j(\mathbf{x}), \\ \int d\mathbf{x} \chi_j^*(\mathbf{x}) \chi_j(\mathbf{x}) &= \delta_{ij}, \\ \sum_j N_j &= N. \end{aligned} \quad (1.14)$$

Apart from specific cases as a non-interacting system, the states χ_j are different from the eigenstates of the single-particle Hamiltonian. The Penrose-Onsager condition is that Bose-Einstein condensation takes place when one of the eigenvalues N_j is macroscopic, that is, it scales linearly with N for large N . By rewriting Eq. 1.14 as

$$g^{(1)}(\mathbf{x}, \mathbf{x}') = N_0 \chi_0^*(\mathbf{x}) \chi_0(\mathbf{x}') + \sum_{j \neq 0} N_j \chi_j^*(\mathbf{x}) \chi_j(\mathbf{x}'), \quad (1.15)$$

an equivalent version of the Penrose-Onsager criterion is that Bose-Einstein takes place if the limit

$$\lim_{|\mathbf{x}-\mathbf{x}'| \rightarrow \infty} g^{(1)}(\mathbf{x}, \mathbf{x}') = \frac{N_0}{N} \quad (1.16)$$

is finite, which corresponds to a finite condensate fraction N_0/N . This is known as off-diagonal long-range order (ODLRO, *cf.* Section 3.3.3). The fact that the term

$$\sum_{j \neq 0} N_j \chi_j(\mathbf{x}) \chi_j^*(\mathbf{x}') \quad (1.17)$$

vanishes in the limit of large distance is due to destructive interference between the different states. For the case of a homogeneous Bose gas, this can be directly verified by using the explicit expression for the eigenfunctions of $g^{(1)}$, that is, plane-wave states with momenta \mathbf{k}_n (*cf.* Eq. 1.3).

Superfluidity

Closely-related to the Bose-Einstein condensation is the phenomenon of superfluidity. Its first signatures have been observed in the 1930s in liquid ${}^4\text{He}$: At the so called λ transition (for temperature $T \simeq 2.17$ K), several physical properties have a sudden change: The liquid flows without apparent viscosity in a narrow channel, and its response to a rotation of the container shows a non-classical rotational inertia. The connection between the λ transition and Bose-Einstein condensation was proposed soon after the first experimental discoveries [19], although these remain two distinct phenomena (a striking example is the absence of a finite-temperature BEC phase for a two-dimensional homogeneous system, for which superfluidity can take place). Due to the strong inter-particle interactions, the theoretical description of superfluidity in ${}^4\text{He}$ has mostly been phenomenological, and the main ab initio approach (based on path integral quantum Monte Carlo, *cf.* Chapter 3) only became available in the 1980s. The main phenomenological approach consists in describing liquid helium below the λ transition as a mixture of normal and superfluid components, with densities ρ_n and ρ_s . Within this description, the main properties of the superfluid state (for instance the decrease in the rotational inertia, when the liquid is subject to rotation) directly follow from the presence of a finite superfluid density ρ_s . It is convenient to introduce a superfluid order parameter, $\Psi(\mathbf{x})$. This is a complex-valued function, with squared absolute value equal to the condensate

density. The phase $\phi(\mathbf{x})$ of the order parameter, in contrast, encodes information about the superfluid velocity, $\mathbf{v}_s(\mathbf{x})$:

$$\mathbf{v}_s(\mathbf{x}) = \frac{\hbar}{m} \nabla \phi(\mathbf{x}), \quad \text{where } \Psi(\mathbf{x}) = |\Psi(\mathbf{x})| e^{i\phi(\mathbf{x})}. \quad (1.18)$$

This fact is directly related to the presence of topological defects (that is, vortices) in $\Psi(\mathbf{x})$, another peculiar feature of the superfluid state [16].

Helicity modulus and superfluid fraction

While the original description of superfluidity in liquid helium is based on its dynamical features, it is useful to characterize this phenomenon through equilibrium properties, accessible through thermodynamic theoretical tools. The main ingredient of this characterization is the formal definition of the superfluid density, formulated in a general way which also includes spin systems [20]. We concentrate on phase transitions described by an order-parameter field $\mathbf{M}(\mathbf{x})$ with at least two dimensions. For a spin model, this is the local magnetization, which is a two- or three-dimensional vector in the XY and Heisenberg models (the Ising-model, in contrast, has a one-dimensional order parameter). For the superfluid phase of a Bose gas, the local order-parameter $\mathbf{M}(\mathbf{x})$ is the aforementioned complex field $\Psi(\mathbf{x})$, corresponding to a two-dimensional real field. If the energy of the system does not include terms favoring a specific orientation of \mathbf{M} , the ensemble average $\langle \mathbf{M} \rangle$ is equal to zero, both above and below the critical temperature. In the ordered phase, the average $\langle \mathbf{M} \rangle$ can be made finite by including an external field which breaks the rotational symmetry. This can be for instance an external magnetic field which favors a certain spin orientation. Another way to make $\langle \mathbf{M}(\mathbf{x}) \rangle$ non-zero is by setting a specific boundary condition, that is, by pinning $\mathbf{M}(\mathbf{x})$ to a specific value for \mathbf{x} on the boundaries of the system. As a concrete example, we consider a three-dimensional system (in a cubic box of volume L^3) with a two-dimensional order parameter $\mathbf{M}(\mathbf{x})$, and we denote by $\phi(\mathbf{x})$ the phase angle of \mathbf{M} with respect to a reference axis. To make $\langle \mathbf{M}(\mathbf{x}) \rangle$ finite, we use twisted boundary conditions, that is, we set the values of the phase $\phi(\mathbf{x})$ to θ_1 and θ_2 on two opposite faces of the cubic box. For a small

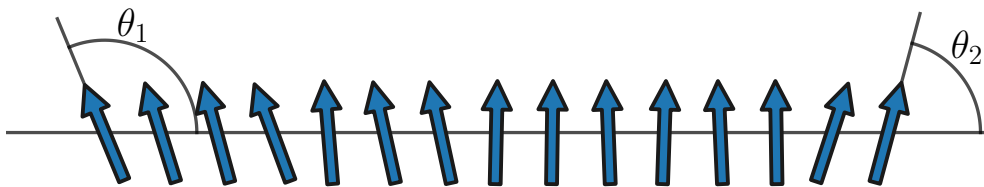


Figure 1.1: Schematic view of the order-parameter field $\mathbf{M}(\mathbf{x})$ for a one-dimensional XY model, with the twisted boundary conditions pinning its phase to θ_1 and θ_2 on the two ends of the system.

difference $\theta_1 - \theta_2$, the order-parameter field changes smoothly across the system, with

the phase angle rotating from θ_1 on one wall to θ_2 on the other (*cf.* Fig. 1.1). This would not be possible for systems with a scalar order parameter (as the Ising model), which would rather be separated into two domains. By imposing these boundary conditions, the free energy F of a certain system (for given temperature and system size) acquires a dependence on the pinning angles: $F = F(\theta_1, \theta_2)$. We consider the free-energy difference $\Delta F(\theta) = F(-\theta, \theta) - F(\theta, \theta)$, for a small twisting angle 2θ . This difference is an extensive quantity, proportional to the system volume L^3 . Moreover, it is proportional to the square of $\langle\langle \nabla\phi \rangle\rangle$, the average gradient¹ of the order-parameter phase [20]. $\langle\langle \nabla\phi \rangle\rangle$ is equal to $2\theta/L$: The total angle difference (2θ) divided by the length over which the change takes place (L). The expansion of ΔF for small θ leads to the definition of the helicity modulus, Y , through

$$\Delta F(\theta) \approx \frac{Y}{2} \langle\langle \nabla\phi \rangle\rangle^2 L^3 = (2YL) \times \theta^2. \quad (1.19)$$

Y encodes the response of the system to an imposed phase twist: A large value of Y corresponds to a rigid systems, where the phase twist has a large free-energy cost. This definition of Y through the small- θ expansion of $\Delta F(\theta)$ is general, and it holds for instance for the XY and Heisenberg spin models. In the specific case of the Bose gas, the helicity modulus corresponds to the superfluid density ρ_s , via

$$\rho_s = \left(\frac{m}{\hbar}\right)^2 Y, \quad (1.20)$$

which follows from the connection between $(\hbar/m)\nabla\phi(\mathbf{x})$ and the superfluid velocity \mathbf{v}_s (*cf.* Eq. 1.18). This definition of ρ_s through Eqs. 1.19 and 1.20 (or analogous expressions related to twisted boundary conditions), is only based on equilibrium properties, and it is of fundamental importance for several applications: It has been applied to the ideal Bose gas, leading to the exact expression [20, 21]

$$\frac{\rho_s}{\rho} = \begin{cases} 1 - \left(\frac{T}{T_c^0}\right)^{3/2} & \text{for } T < T_c^0, \\ 0 & \text{for } T > T_c^0, \end{cases} \quad (1.21)$$

for a three-dimensional system in the thermodynamic limit, it is a key ingredient in the formulation of the finite-size scaling theory (*cf.* Section 3.4.1 and Ref. [22]), and it is at the basis of the measure of the superfluid density in quantum Monte Carlo (*cf.* Section 3.3.2 and Ref. [23]).

1.2 Ultracold atomic gases

The first atomic system used to probe low-temperature physics and the effects of quantum mechanics has been liquid helium [24], for which the λ transition (*cf.* Section 1.1)

¹The double bracket $\langle\langle \dots \rangle\rangle$ denotes a double average, over the statistical ensemble and over space.

takes place at $T_c \simeq 2.17$ K. The critical temperature for Bose-Einstein condensation of non-interacting bosons with the mass and density of ${}^4\text{He}$ ($\rho \simeq 2 \times 10^{28} \text{ m}^{-3}$) is $T_c^0 \simeq 3.13$ K. While being quantitatively different from T_c , the non-interacting theory captures the correct order of magnitude for Bose-Einstein condensation, which motivated the first connection between the phenomena of BEC and superfluidity [19]. Nevertheless, liquid helium is a strongly interacting system: The main features of the interaction potential (the repulsive core for distances below 2.5 Å and the minimum at 2.8 Å) take place at distances comparable to the typical interparticle separation (of the order of 3–4 Å). This modifies the zero-temperature condensate fraction, which is reduced to below 10% (as compared to the non-interacting case, where $N_0/N = 1$ at zero temperature).

Liquid helium has to be compared with the currently available ultracold atomic gases, a different class of systems where Bose-Einstein condensation takes place [25]. The progress in cooling techniques allowed to reach temperatures as low as tens of nK. The transition to the solid phase, which would exist at such low temperature, is avoided by using extremely dilute systems (with typical densities of the order of 10^{19} – 10^{20} m^{-3} , leading to interparticle distances of approximately 100 nm). These systems are therefore metastable. The major instability mechanism is given by inelastic three-body losses, which are scattering processes resulting into a bound dimer and a third atom carrying away the binding energy. The rate of these collisions sets a finite life-time, typically larger than the other time scales of the system². Considering the example of ${}^{87}\text{Rb}$, the temperature at which the phase-space density $\rho \lambda_{\text{th}}^3$ becomes of order one is $\approx 10^2$ nK. It is in this temperature regime that the first direct observation of Bose-Einstein condensation has been realized, with clouds of Rb, Li and Na atoms [1, 2, 3]. Alkali atomic species are the most commonly used for ultracold experiments. Other species are chosen for some specific features, as the long-range interactions caused by the large magnetic dipole moment of Er atoms [26].

Differently from liquid helium, ultracold atomic systems offer an unprecedented degree of control, and their application spectrum largely exceeds the sole observation of Bose-Einstein condensation. Some of the main tunability directions include the interaction strength tuning through Feshbach resonances, the confinement of the atomic clouds on the sites of an optical lattice, the mimicking of artificial magnetic fields for neutral atoms, and the use of anisotropic confinement to obtain low-dimensional systems (see Ref. [4] for a review). In this work, we concentrate on the low-temperature properties of spinless bosonic atoms, in the regime of strong interactions.

The main observable to detect the onset of Bose-Einstein condensation is the momentum distribution, $n(\mathbf{k})$, which develops a narrow peak at zero momentum in the condensed phase (*cf.* Section 3.3.4). In the majority of experiments, an atomic cloud of less than 10^7 atoms is confined by an external trap, well approximated by an harmonic potential. In this case the BEC transition is also visible in the non-uniform density profile of the gas. More recently, the same transition has been realized for a gas confined in

²This does not hold for strongly-interacting systems, *cf.* Section 2.3.2.1.

a uniform-box trap [27, 28]. This novel set-up has an advantage in the study of critical behavior with diverging correlation lengths, since there is no inhomogeneity caused by the external trapping potential.

A useful criterion to classify experimental and theoretical studies of ultracold atomic systems is the strength of interactions. The theory for non-interacting bosons is only qualitatively valid (apart from cases where interactions are artificially tuned to zero strength), despite the correct order-of-magnitude estimate of the critical temperature in the strongly-interacting case of liquid helium. The ideal-gas model fails in capturing several properties of interacting systems, including the shape of the condensate wave function in a harmonic trap. Moreover, the BEC transition is qualitatively modified by the presence of any finite interaction strength, and the critical behavior of the interacting system belongs to a distinct universality class (*cf.* Section 3.4.1). This motivates why several contradictory predictions have been proposed for the lowest-order effect of weak interactions on the Bose-gas critical temperature, taking more than 40 years before consensus was reached (*cf.* Ref. [14] for a detailed review).

The next level of approximation is a mean-field approximation, as Gross-Pitaevskii theory [29]. This approach is valid in the regime of low temperature and weak interactions, where it correctly reproduces several observables, including for instance the condensate wave function for a trapped gas. However, it cannot describe systems with strong thermal or quantum fluctuations. A recent example of this limitation is the observation of stable quantum droplets of dipolar quantum gases in regimes where mean-field theory predicts a mechanical collapse [30, 31]. Beyond-mean-field corrections have been predicted [32], and later identified in the equation of state of an interacting BEC [33].

This classification in terms of the interaction strength naturally continues towards the regime of strong interactions and the unitary limit. This is the main subject of this work, and the status of experiments in this direction is reviewed in Section 2.3.

1.3 Density matrix and path integrals

The density matrix is the basic tool to treat a statistical mixture of quantum states. In particular, it is at the basis of the path-integral formulation for equilibrium thermodynamics, extensively used in this work.

The partition function Z of a quantum system at inverse temperature β is the trace of the density-matrix operator $\exp(-\beta H)$. The simplest way to represent this trace is through a basis where the Hamiltonian H operator is diagonal, so that

$$Z = \text{Tr} e^{-\beta H} = \sum_n \exp(-\beta E_n), \quad (1.22)$$

where E_n are the eigenvalues of the Hamiltonian H . The formulation at the basis of the work described here is, however, is in the position representation. For the simple case

of one quantum particle in three dimensions, the trace in Eq. 1.22 becomes

$$Z = \int d\mathbf{x} \rho_1(\mathbf{x}, \mathbf{x}; \beta), \quad (1.23)$$

where $\rho_1(\mathbf{x}, \mathbf{x}; \beta)$ is the diagonal component of

$$\rho_1(\mathbf{x}, \mathbf{x}'; \beta) = \sum_n \Psi_n^*(\mathbf{x}') e^{-\beta E_n} \Psi_n(\mathbf{x}). \quad (1.24)$$

This expression includes the full set of single-particle eigenfunctions Ψ_n and eigenvalues E_n of H , and the summation has to be replaced by an integration in case of a continuous spectrum. An analogous definition holds for the density matrix of an N -body system,

$$\rho_N(\mathbf{X}, \mathbf{X}'; \beta) = \sum_n \Psi_n^*(\mathbf{X}') e^{-\beta E_n} \Psi_n(\mathbf{X}), \quad (1.25)$$

where Ψ_n and E_n are the eigenfunctions and eigenvalues of the N -body Schrödinger equation, and where we use the shorthands $\mathbf{X} = \{\mathbf{x}_1, \dots, \mathbf{x}_N\}$ and $\mathbf{X}' = \{\mathbf{x}'_1, \dots, \mathbf{x}'_N\}$. Despite encoding the full thermodynamics of a many-body system, the expression in Eq. 1.25 is rarely of practical use for realistic many-body problem (that is, for a large number of interacting quantum particles), since it requires the full knowledge of the spectrum and eigenfunctions of H . Nevertheless, it constitutes the basis for powerful approximation schemes, leading to unbiased solutions for some challenging problems in many-body physics.

The density matrix is conveniently treated within the path-integral formalism. In its original formulation, this formalism consists in a rewriting of the real-time propagator of a quantum system [34]. The central quantity is the amplitude for the system being in state $|A\rangle$ at time t_0 and in state $|B\rangle$ at time t_1 , given by

$$\left\langle B \left| \exp \left(-i \frac{H(t_1 - t_0)}{\hbar} \right) \right| A \right\rangle. \quad (1.26)$$

This propagator, generally unknown, can be rewritten as a weighted sum over all the space-time paths connecting $|A, t = t_0\rangle$ with $|B, t = t_1\rangle$. Through the formal replacement of the time interval $t_1 - t_0$ with an imaginary-time variable, the real-time propagator in Eq. 1.26 is related to the density matrix in Eq. 1.25, for which the same idea of summing over paths is applicable [35, 36]. The analogy goes even further, since the main approximation scheme used for imaginary-time path integrals (that is, the discretization into small imaginary-time intervals) was already used to treat the original time-evolution problem. This is discussed more in detail in Section 3.2.1. Furthermore, the path-integral formulation provides a mapping between the thermodynamics of a quantum system in d dimensions with a classical system in $d + 1$ dimensions, which can be treated by Monte Carlo algorithms.

For bosons, the eigenstates Ψ_n in Eq. 1.25 are symmetric under the exchange of any pair of coordinates, $x_i \leftrightarrow x_j$. In this case, the bosonic density matrix $\rho_N^{\text{bos}}(\mathbf{X}, \mathbf{X}'; \beta)$ remains unchanged when \mathbf{X}' is replaced by $P\mathbf{X}' \equiv x'_{P_1}, \dots, x'_{P_N}$, where $P = P_1, \dots, P_N$ is a permutation of the indices $1, \dots, N$. Starting from the N -body density matrix for distinguishable particles, $\rho_N(\mathbf{X}, \mathbf{X}'; \beta)$, its bosonic counterpart is obtained as an average over all permutations P ,

$$\rho_N^{\text{bos}}(\mathbf{X}, \mathbf{X}'; \beta) = \frac{1}{N!} \sum_P \rho_N(\mathbf{X}, P\mathbf{X}'; \beta). \quad (1.27)$$

For a given permutation P , a cycle is a subset of $\{1, \dots, N\}$ such that its elements only exchange place with one another, upon repeated application of P (see Fig. 1.2). The cycle length is the number of elements in one such subset. From the bosonic density matrix, it is simple to state a rough condition for the appearance of long cycles at thermal equilibrium. The typical interparticle distance is $\rho^{-1/3}$, and the distinguishable-particle density matrix ρ_N is exponentially suppressed if any pair x_j, x'_{P_j} is at distance larger than λ_{th} (cf. Section 2.1.2). A permutation P different from the identity has a relevant weight in Eq. 1.27 only if the distance between any pair x_j, x'_{P_j} is comparable to λ_{th} . If this is not the case, the contribution of P is strongly suppressed. Therefore, the regime where cycles longer than one become important is when $\rho\lambda_{\text{th}}^3$ is of the order of unity, corresponding to the BEC criterion in Section 1.1. High temperature or low density decrease the statistical weight of permutations which include long cycles, while low temperature or high density have the opposite effect. In the next section, the concept of permutation

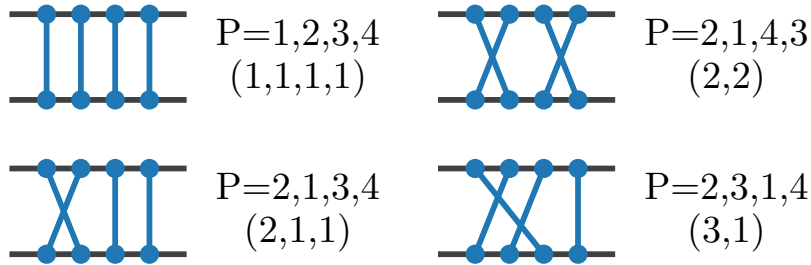


Figure 1.2: Schematic view of some of the $4! = 24$ permutations for $N = 4$, together with their decomposition into cycles (in parentheses).

cycles is quantitatively related to the appearance of a BEC phase, for non-interacting bosons. The general connection of permutation cycles with BEC and superfluidity is given in Sections 3.3.2 and 3.3.3, within the path-integral framework.

1.4 Recursion method for non-interacting bosons

For the non-interacting Bose gas, the study of permutation cycles leads to a powerful method to exactly compute observables as the energy and the condensate fraction. This method provides insight into the connection between permutation cycles and Bose-Einstein condensation. Moreover, it is valuable to benchmark our QMC algorithm (*cf.* Fig. 3.15 and Table 3.1).

For a single quantum particle in a three-dimensional periodic box, the partition function at inverse temperature β reads

$$z(\beta) = \left[\sum_{n \in \mathbb{Z}} \exp \left(-\frac{\beta}{2m} \left(\frac{2\pi\hbar}{L} \right)^2 n^2 \right) \right]^3. \quad (1.28)$$

In the density-matrix formalism, this is equal to the integral of $\rho_1(\mathbf{x}, \mathbf{x}; \beta)$ (*cf.* Eq. 1.23). The partition function for N non-interacting bosons can be expressed through the following recursion relation [37, 38],

$$Z_N(\beta) = \frac{1}{N} \sum_{k=1}^N z(k\beta) Z_{N-k}(\beta), \quad (1.29)$$

with $Z_0(\beta) = 1$. For $N = 2$, Eq. 1.29 gives

$$Z_2(\beta) = \frac{(z(\beta))^2}{2} + \frac{z(2\beta)}{2}. \quad (1.30)$$

The same quantity can be computed through the bosonic two-body density matrix (*cf.* Eq. 1.27), and it reads

$$\begin{aligned} Z_2(\beta) &= \int d\mathbf{x}_1 \int d\mathbf{x}_2 \rho_2^{\text{bos}} (\{\mathbf{x}_1, \mathbf{x}_2\}, \{\mathbf{x}_1, \mathbf{x}_2\}; \beta) = \\ &= \int d\mathbf{x}_1 \int d\mathbf{x}_2 \left[\frac{\rho_2 (\{\mathbf{x}_1, \mathbf{x}_2\}, \{\mathbf{x}_1, \mathbf{x}_2\}; \beta)}{2} + \frac{\rho_2 (\{\mathbf{x}_1, \mathbf{x}_2\}, \{\mathbf{x}_2, \mathbf{x}_1\}; \beta)}{2} \right] = \quad (1.31) \\ &= \frac{(\int d\mathbf{x} \rho_1(\mathbf{x}, \mathbf{x}; \beta))^2}{2} + \frac{\int d\mathbf{x}_1 \int d\mathbf{x}_2 \rho_2 (\{\mathbf{x}_1, \mathbf{x}_2\}, \{\mathbf{x}_2, \mathbf{x}_1\}; \beta)}{2}. \end{aligned}$$

This shows that the two terms in Eq. 1.30 correspond to the two available permutations for two particles, $P = 1, 2$ and $P = 2, 1$ (with the notation of Fig. 1.2). The recursion relation in Eq. 1.29 provides a compact way to obtain $Z_N(\beta)$, which would naively require a sum over all $N!$ permutations. $Z_N(\beta)$ gives access to several thermodynamic observables. The average energy, for instance, is obtained through its definition,

$$\langle E_N \rangle = \frac{1}{Z_N(\beta)} \frac{\partial Z_N(\beta)}{\partial \beta}, \quad (1.32)$$

and a recursion relation for $\partial Z_N(\beta) / \partial \beta$ which is derived from Eq. 1.29.

The recursive expression for $Z_N(\beta)$ is connected with the statistics of permutation cycles. The k -th term in Eq. 1.29 is the product of $z(k\beta)$ and $Z_{N-k}(\beta)$, which corresponds to assigning a given particle to a cycle of length k and weighting this choice with the partition function of the other $N - k$ particles, $Z_{N-k}(\beta)$. Therefore, the normalized probability for a given particle to be on a cycle of length k reads

$$\pi_k = \frac{1}{N} \frac{z(k\beta) Z_{N-k}(\beta)}{Z_N(\beta)}. \quad (1.33)$$

As particles are identical, the average number of particles on cycles of length k is $k \times \pi_k$. In Chapter 3, this expression is used to benchmark our QMC technique (*cf.* Fig. 3.15).

The recursion scheme for Z_N also determines the probability of having N_0 particles in the single-particle ground state, which is [39]

$$p(N_0) = \frac{1}{Z_N(\beta)} \begin{cases} Z_{N-N_0}(\beta) - Z_{N-(N_0+1)}(\beta) & \text{if } N_0 < N, \\ 1 & \text{if } N_0 = N, \end{cases} \quad (1.34)$$

for cases in which the ground state energy is equal to zero (*cf.* Eq. 1.3). The condensate fraction $\langle N_0 \rangle$ is $\sum_{N_0} N_0 \times p(N_0)$. Moreover, the integer derivative of the average permutation-cycle occupation is proportional to $p(N_0)$ [40, 39, 41], that is

$$\frac{p(N_0 = k)}{N} = k\pi_k - (k + 1)\pi_{k+1}, \quad (1.35)$$

for $k \gg 1$. This establishes a connection between the condensate fraction and the appearance of long permutation cycles. At large N and $T < T_c^0$, for instance, $k\pi_k$ drops to zero for $k \simeq \langle N_0 \rangle$, which allows to identify the condensate fraction with the length of the longest cycle with a finite occupation number.

The recursion scheme for $Z_N(\beta)$ also gives access to other observables, like the one-body reduced off-diagonal density matrix [40, 42] and the superfluid fraction (*cf.* Section 3.3.2), but it is restricted to ideal particles. The generalization to interacting systems can only be obtained approximately, for instance through corrections to Eq. 1.29 based on the high-temperature virial coefficients (see for instance Ref. [43], where this is used to study the unitary Bose gas).

CHAPTER 2

Few-body physics with strong interactions

In this chapter, we consider systems of two or three strongly-interacting quantum particles. Two limits are of particular interest, the scaling and the unitary limit. In the scaling limit, the range of the interparticle potential vanishes. This is the relevant regime for experiments with dilute ultracold atomic gases, where the interaction range is typically much smaller than the average interparticle distance between atoms. The unitary limit corresponds to interactions which realize a diverging scattering length. This is the extreme strongly-interacting limit, since the corresponding cross section for two-body collisions saturates a theoretical upper bound. Unitary interactions can be induced in ultracold atomic samples, through the Feshbach-resonance technique (see Section 2.3).

We first review the general basics of scattering theory for two quantum particles (see Section 2.1). Analytical results for the case of zero-range unitary interactions allow us to compute thermal correlation functions, including the momentum distribution and the pair-correlation function. These are of particular interest, since they share some relevant features with the case of a unitary-interacting many-body system, described in Chapter 4. For the case of three strongly-interacting particles, the Efimov effect appears, consisting in a scale-invariant sequence of three-body bound states. This phenomenon is connected to universal properties, which do not depend on microscopic details of the interparticle interactions. In Section 2.2, we review the description of the Efimov effect and verify that our theoretical model (based on a three-body cutoff) is consistent with the universal theory. The verification is based on numerical results for the ground-state trimer, obtained through the quantum Monte Carlo technique (*cf.* Chapter 3).

Throughout Sections 2.1 and 2.2, we combine two different approaches to the few-body problem. The study of two-body scattering and of the Efimov effect is based on wave functions for single quantum states, while the density-matrix approach is used to obtain finite-temperature results. For $N = 2$, the latter provides analytical, approx-

imate expressions for the relevant correlation functions. More generally, numerically exact results can be obtained at any temperature, by combining the density-matrix approach with the quantum Monte Carlo technique. This powerful method is also used to describe the many-body case (*cf.* Chapter 4).

2.1 Two-body physics

In the present section, we describe the two-body quantum problem for strong, short-ranged interactions. We first review the basics of scattering theory for two particles, providing the specific examples of the square-well and zero-range model potentials (see Section 2.1.1). From the study of wave functions, we then move to the finite-temperature density-matrix formalism, and report the exact solution for the density matrix of two particles with zero-range, unitary interactions (see Section 2.1.2.1). This is useful for two applications. On one hand, it gives direct access to thermal correlation functions for two particles, like the one-particle-reduced density matrix $g^{(1)}(\mathbf{r})$ and the pair-correlation function $g^{(2)}(\mathbf{r})$ (see Section 2.1.3). These show the small-distance features typical of systems with strong, short-ranged interactions, like the cusp singularity of $g^{(1)}(\mathbf{r})$ and the divergence of the pair-correlation function. On the other hand, the exact knowledge of the two-body density matrix constitutes the essential ingredient for our quantum Monte Carlo scheme (see Section 3.2.1). This technique is used to benchmark other calculations for $N = 2$ (e.g. for correlation functions), and to obtain new results for $N \geq 3$, concerning Efimov trimers (*cf.* Section 2.2.2) and the unitary Bose gas (*cf.* Chapter 4).

2.1.1 Scattering theory

We consider two distinguishable particles of mass m , interacting through a potential $V_2(|\mathbf{x}_1 - \mathbf{x}_2|)$ which only depends on their distance. The Hamiltonian is the sum of the center-of-mass and relative-motion terms, $H^{\text{c.m.}}$ and H^{rel} , as in

$$H = \frac{\mathbf{p}_1^2}{2m} + \frac{\mathbf{p}_2^2}{2m} + V_2(|\mathbf{x}_1 - \mathbf{x}_2|) = \underbrace{\frac{\mathbf{P}^2}{4m}}_{H^{\text{c.m.}}} + \underbrace{\left[\frac{\mathbf{p}^2}{m} + V_2(r) \right]}_{H^{\text{rel}}}, \quad (2.1)$$

where $\mathbf{P} = (\mathbf{p}_1 + \mathbf{p}_2)$, $\mathbf{p} = (\mathbf{p}_1 - \mathbf{p}_2)/2$, $\mathbf{r} = \mathbf{x}_1 - \mathbf{x}_2$, and $r = |\mathbf{r}|$. $H^{\text{c.m.}}$ corresponds to the Hamiltonian of a free particle with mass $2m$, while the presence of two-body interactions only affects H^{rel} . We consider the relative-motion problem, and assume that the $V_2(r)$ decays to zero at large r . We look for scattering eigenstates $\Psi_{\mathbf{k}}^{\text{rel}}(\mathbf{r})$ of H^{rel} , that solve the time-independent Schrödinger equation,

$$\left(\frac{\mathbf{p}^2}{m} + V_2(r) \right) \Psi_{\mathbf{k}}^{\text{rel}}(\mathbf{r}) = E_k \Psi_{\mathbf{k}}^{\text{rel}}(\mathbf{r}), \quad (2.2)$$

with a positive energy $E_k = \hbar^2 k^2 / m$. For large distance r , a scattering eigenstate is the superposition of the incoming plane wave (with wave number \mathbf{k}) and a scattered spherical wave:

$$\Psi_{\mathbf{k}}^{\text{rel}}(\mathbf{r}) \sim e^{ikr \cos \theta} + f(k, \theta) \frac{e^{ikr}}{r}, \quad (2.3)$$

where θ is the angle between \mathbf{k} and \mathbf{r} . The scattering amplitude $f(k, \theta)$ encodes the effects of interactions on a two-body collision process. The total scattering cross section $\sigma(k)$, for instance, is the solid-angle integral of $|f(k, \theta)|^2$. As the system is characterized by axial symmetry (for rotations with axis \mathbf{k}), a scattering state can be written as a partial-wave expansion

$$\Psi^{\text{rel}}(\mathbf{r}) = \sum_{l=0}^{\infty} A_l P_l(\cos \theta) R_{k,l}(r), \quad (2.4)$$

where A_l are constant coefficients and P_l are the Legendre polynomials. The radial wave function $R_{k,l}(r)$ solves the one-dimensional Schrödinger equation

$$\left(-\frac{1}{r^2} \frac{d}{dr} r^2 \frac{d}{dr} + \frac{l(l+1)}{r^2} + \frac{mV_2(r)}{\hbar^2} \right) R_{k,l}(r) = k^2 R_{k,l}(r), \quad (2.5)$$

which depends on l through a centrifugal barrier proportional to $l(l+1)/r^2$. At large distance, the solution of Eq. 2.5 satisfies

$$R_{k,l}(r) \propto \frac{2 \sin(kr - \frac{\pi}{2}l + \delta_l(k))}{r} = \frac{1}{ir} \left[(-i)^l e^{i(kr + \delta_l(k))} - i^l e^{-i(kr + \delta_l(k))} \right], \quad (2.6)$$

where $\delta_l(k)$ is a constant phase shift. By using this expression and comparing Eqs. 2.3 and 2.4, the coefficients A_l are found to be [44]

$$A_l = \frac{1}{2k} (2l+1) i^l e^{i\delta_l(k)}. \quad (2.7)$$

The phase shifts $\delta_l(k)$ encode the effect of the interaction potential $V_2(r)$ on the scattering wave functions $R_{k,l}(r)$, for distances much larger than the potential range. By comparing Eqs. 2.3 and 2.4 at large r , the scattering amplitude reads

$$f(k, \theta) = \frac{1}{2ik} \sum_{l=0}^{\infty} (2l+1) P_l(\cos \theta) \left[e^{2i\delta_l(k)} - 1 \right]. \quad (2.8)$$

This leads to the total cross section

$$\sigma(k) = 2\pi \int_{-1}^1 d \cos \theta |f(k, \theta)|^2 = \frac{4\pi}{k^2} \sum_{l=0}^{\infty} \sin^2 \delta_l(k), \quad (2.9)$$

for two distinguishable particles. For $l > 0$, the centrifugal barrier in Eq. 2.5 suppresses $R_{k,l}(r)$ at short r , that is, in the region where $V_2(r)$ is strongest. Thus the contribution of

$l > 0$ partial waves should vanish in the zero-energy limit, $k \rightarrow 0$. More precisely, the $k \rightarrow 0$ limit of the phase shifts reads¹

$$\delta_l(k) \propto k^{2l+1} \quad \text{modulo } \pi. \quad (2.10)$$

Therefore all contributions in Eqs. 2.8 and 2.9 vanish in the $k \rightarrow 0$ limit, except for the $l = 0$ term.

The low-energy regime for two-body scattering is realized in ultracold atomic gases, due to the extremely low temperature. This leads to the s-wave approximation, which consists in truncating the partial-wave expansion at $l = 0$. Within this scheme, the effect of interactions on scattering properties is encoded in the phase shift $\delta_0(k)$. This quantity is conveniently expressed through the s-wave scattering length a , defined as

$$a = -\lim_{k \rightarrow 0} \frac{\tan \delta_0(k)}{k}. \quad (2.11)$$

For k going to zero, the total cross section $\sigma(k)$ tends to $4\pi a^2$ (cf. Eq. 2.9), which is the area of a sphere of radius a . Thus the scattering length can be interpreted as the length scale over which the incoming plane wave is substantially modified by interactions. In the case of a hard-sphere potential (where $V_2(r)$ is infinite for distances smaller than the particle diameter, and zero otherwise), this interpretation becomes exact, as the scattering length a is equal to the particle diameter [45].

For ultracold atomic gases, the typical interaction potential $V_2(r)$ is strongly repulsive at small r , has a minimum at intermediate distance, and falls off as a power law. The attractive large- r tail is

$$V_2^{\text{tail}}(r) = -\frac{C_6}{r^6}, \quad (2.12)$$

which allows to define the van der Waals length l_{vdW} as

$$l_{\text{vdW}} = \frac{1}{2} \left(\frac{m C_6}{\hbar^2} \right)^{1/4}. \quad (2.13)$$

For ${}^{87}\text{Rb}$, for instance, $l_{\text{vdW}} \approx 4 \text{ nm}$ [5]. This potential supports several molecular bound states with large binding energy. This indicates that ultracold gases are only metastable, while the equilibrium state would correspond to a solid phase. Therefore, this realistic potential cannot be used directly within thermal-equilibrium theories (including the path-integral QMC technique) [46]. However, ultracold atomic systems are experimentally realized in the dilute regime, where the range of the two-body potential is significantly smaller than the typical interparticle distance. Theoretical predictions in this regime only depend on the scattering properties of the potential, rather than on the specific form of $V_2(r)$. At low temperature, in particular, they depend only on the

¹If $V_2(r)$ decays at large r as r^{-n} , with $n > 3$, Eq. 2.10 is only valid for the partial waves such that $l < (n - 3)/2$. For larger n , the small- k limit of $\delta_l(k)$ is k^{n-2} modulo π [45].

s-wave scattering length a . Thus an arbitrary model can be chosen, provided it reproduces the required value of a . The choice is dictated by simplicity in the calculations, and by the fact the model potential should be amenable to a thermal-equilibrium treatment (that is, it should not have deeply-bound molecular states, which may lead to a instability towards a solid phase). An example of this choice is the use of the hard-sphere potential to study bosonic gases with small scattering length (see for instance [47]). In Sections 2.1.1.1 and 2.1.1.2, we describe two possible models: The attractive square-well potential, and its zero-range limit. The latter is then used throughout the rest of this chapter and in Chapter 4.

2.1.1.1 Square-well potential

The attractive square-well potential is defined as

$$V_2^{\text{sw}}(r) = \begin{cases} -U_0 & \text{for } r < r_0, \\ 0 & \text{for } r > r_0, \end{cases} \quad (2.14)$$

with $U_0 \geq 0$ (see Fig. 2.1a). For the s-wave channel (that is, for $l = 0$), the solution of the

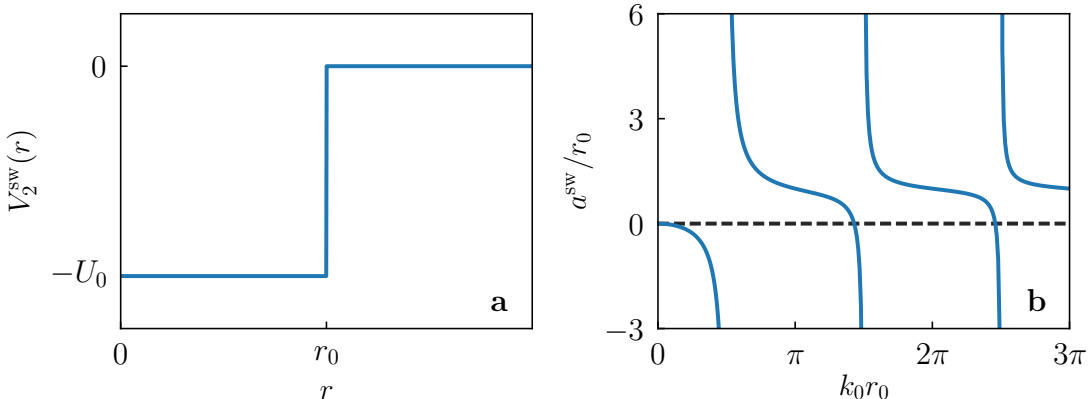


Figure 2.1: Panel a: Attractive square-well potential $V_2^{\text{sw}}(r)$, with range r_0 and depth U_0 . Panel b: s-wave scattering length a^{sw} for the attractive square-well potential (blue solid line, cf. Eq. 2.17).

radial Schrödinger equation in Eq. 2.5 reads

$$R_{k,0}(r) = \begin{cases} \frac{A \sin(r\sqrt{k^2 + k_0^2})}{r} & \text{for } r < r_0, \\ \frac{A' \sin(kr + \delta_0^{\text{sw}}(k))}{r} & \text{for } r > r_0, \end{cases} \quad (2.15)$$

where $k_0 = \sqrt{mU_0/\hbar^2}$, and A and A' are constant coefficients. $\delta_0^{\text{sw}}(k)$ corresponds to the $l = 0$ phase shift introduced in Eq. 2.6, as can be seen by a direct comparison of the two

wave functions at large r . By imposing the continuity of $R_{k,0}(r)$ and of its logarithmic derivative $R'_{k,0}(r)/R_{k,0}(r)$ at $r = r_0$, we find the $l = 0$ phase shift

$$\delta_0^{\text{sw}}(k) = -kr_0 + \arctan \frac{k \tan \left(r_0 \sqrt{k_0^2 + k^2} \right)}{\sqrt{k_0^2 + k^2}}. \quad (2.16)$$

As a consequence, the s-wave scattering length for the square-well potential reads

$$a^{\text{sw}} \equiv \lim_{k \rightarrow 0} \frac{-\delta_0^{\text{sw}}(k)}{k} = r_0 \left(1 - \frac{\tan(k_0 r_0)}{k_0 r_0} \right). \quad (2.17)$$

This quantity (*cf.* Fig. 2.1b) vanishes when $U_0 = 0$, and it is negative for a weak potential, that is, for $k_0 r_0 \leq \pi/2$. Upon increasing $k_0 r_0$, the scattering length diverges every time that $k_0 r_0$ is an odd multiple of $\pi/2$, which corresponds to the point where new bound states for $V_2^{\text{sw}}(r)$ appear. Thus the attractive square-well interaction can realize all values of the scattering length: Positive or negative, and of arbitrary magnitude. A repulsive-barrier potential (the same as in Eq. 2.14, but with $U_0 < 0$), in contrast, only leads to non-negative scattering lengths [45].

2.1.1.2 Zero-range potential

The square-well potential depends on two parameters, from which the scattering length is computed as in Eq. 2.17. A more convenient choice consists in the zero-range potential [46], which is fully determined by the value of the scattering length. Moreover, the s-wave approximation becomes exact for this potential, as all phase shifts δ_l with $l > 0$ are identically zero [45].

One possible realization of the zero-range potential consists in taking the $r_0 \rightarrow 0$ and $U_0 \rightarrow \infty$ limits for the square-well potential (see Eq. 2.14), while keeping the scattering length in Eq. 2.17 fixed. In this limit, the s-wave scattering wave function reads

$$R_{k,0}(r) = \sqrt{\frac{2}{\pi}} \frac{\sin(kr - \arctan(ka))}{r}, \quad (2.18)$$

where only the $r \geq r_0$ part of Eq. 2.15 is relevant, since $r_0 \rightarrow 0$. This form of $R_{k,0}(r)$ highlights the fact that the zero-range interaction is fully defined by the choice of the scattering length a . For positive a , the contact potential also supports a dimer bound state, with energy

$$E_D = -\frac{\hbar^2}{ma^2}. \quad (2.19)$$

The corresponding wave function reads

$$R_{\text{b.s.}}(r) = \sqrt{\frac{2}{a}} \frac{e^{-r/a}}{r}, \quad (2.20)$$

as can be verified by inserting $R_{\text{b.s.}}$ in the Schrödinger equation, Eq. 2.5.

An alternative way to describe the contact potential is to directly consider the zero-range limit, rather than passing through the square-well potential. In this case, $V_2(r)$ is identically zero in the $l = 0$ Schrödinger equation (*cf.* Eq. 2.5), but a specific boundary condition is imposed for small distance:

$$R_{k,0}(r) \xrightarrow{r \rightarrow 0} C \left(\frac{1}{r} - \frac{1}{a} \right), \quad (2.21)$$

known as Bethe-Peierls boundary condition [48, 49]. Both the diffusive and bound states of the contact potential (*cf.* Eqs. 2.18 and 2.20) satisfy the boundary condition in Eq. 2.21, with prefactors

$$C = \begin{cases} -\sqrt{\frac{2}{\pi}} \frac{ka}{\sqrt{1+k^2a^2}} & \text{for } R_{k,0}(r), \\ \sqrt{\frac{2}{a}} & \text{for } R_{\text{b.s.}}(r). \end{cases} \quad (2.22)$$

The small-distance divergence of the wave function has peculiar consequences on the correlation functions of a system with zero-range interactions (see Section 2.1.3).

The phase shift $\delta_0(k)$ for the zero-range model is equal to $-\arctan(ka)$ (*cf.* Eq. 2.18). By using the partial-wave expansion for the total scattering cross section (Eq. 2.9, truncated to $l = 0$), we find

$$\sigma(k) = \frac{4\pi a^2}{1 + (ka)^2}. \quad (2.23)$$

For vanishing a , this expression tends to $4\pi a^2$, which is the standard result for low-energy scattering [45]. When $|a| \rightarrow \infty$, in contrast, $\sigma(k)$ tends to $4\pi/k^2$. This saturates the upper bound on the cross section which follows from the unitarity of the quantum evolution operator [46]. For this reason, the $|a| \rightarrow \infty$ limit is known as the unitary limit, independently of the setting in which this is realized (either a theoretical zero-range potential or a realistic finite-range potential).

A specific feature of the zero-range interaction model is that the properties of a two-body system are fully determined by a single length scale (the scattering length a). This leads to a continuous scaling symmetry: When a is multiplied by a real factor λ , other physical properties should be rescaled by a certain power of λ , as dictated by dimensional analysis. As an example, the dimer energy E_D has to scale as λ^{-2} , when $a \rightarrow \lambda a$. This constraint is satisfied by the expression in Eq. 2.19. Another example is the total cross section $\sigma(k)$, which scales as λ^2 , since it has the units of an area. Continuous scale invariance has to be confronted with the discrete scale invariance associated to the Efimov effect (see Section 2.2.1).

2.1.2 Two-body density matrix

In Section 1.3 we have introduced the general expression for the density matrix of N distinguishable particles (see Eq. 1.25). This quantity allows to pass from considering

individual quantum states to a finite-temperature treatment, where each state has a statistical weight proportional to the Boltzmann factor of its energy. In this section we consider the case of two quantum particles interacting via a zero-range potential, and we construct an exact expression for the two-body density matrix ρ_2 by making use of the solutions in Section 2.1.1.2. The exact knowledge of ρ_2 constitutes the building block for an approximate expression of the N -body density matrix, which is at the basis of our QMC approach (*cf.* Section 3.2.1) Focusing on the unitary limit, where the scattering length diverges, we also use the expression of ρ_2 to compute several non-trivial correlation functions of a two-body system (*cf.* Section 2.1.3). These observables share several relevant features with their many-body counterparts, in the unitary Bose gas (see Chapter 4).

The full solution of a quantum-mechanical problem, in terms of the wave functions and spectrum of its Hamiltonian, gives access to the corresponding density-matrix. As an example, we consider a quantum particle in free space, with Hamiltonian $H = \mathbf{p}^2/(2m)$. As in Eq. 1.25, the density matrix is

$$\rho_1(\mathbf{x}, \mathbf{x}'; \beta) = \int_{\mathbb{R}^3} d\mathbf{k} \psi_{\mathbf{k}}^*(\mathbf{r}') e^{-\beta E_k} \psi_{\mathbf{k}}(\mathbf{r}), \quad (2.24)$$

where $\psi_{\mathbf{k}}(\mathbf{r}) = \exp(-i\mathbf{k} \cdot \mathbf{r})/(2\pi)^{3/2}$ are plane-wave eigenstates with energy $E_k = \hbar^2 k^2/(2m)$. The free-space single-particle density matrix reads

$$\rho_1(\mathbf{x}, \mathbf{x}'; \beta) = \left(\frac{m}{2\pi\hbar^2\beta} \right)^{3/2} \exp \left(-\frac{m(\mathbf{x} - \mathbf{x}')^2}{2\hbar^2\beta} \right). \quad (2.25)$$

This expression is a necessary ingredient to construct the density matrix for $N > 1$.

For a two-body problem, the Hamiltonian is the sum of two commuting terms ($H^{\text{c.m.}}$ and H^{rel} , *cf.* Eq. 2.1), corresponding to the center-of-mass and relative-motion problems. The two-body density matrix, ρ_2 , can be factorized as

$$\rho_2(\{\mathbf{x}_1, \mathbf{x}_2\}, \{\mathbf{x}'_1, \mathbf{x}'_2\}; \beta) = \rho_2^{\text{c.m.}}(\mathbf{X}, \mathbf{X}'; \beta) \rho_2^{\text{rel}}(\mathbf{r}, \mathbf{r}'; \beta), \quad (2.26)$$

with $\mathbf{X} = (\mathbf{x}_1 + \mathbf{x}_2)/2$, $\mathbf{X}' = (\mathbf{x}'_1 + \mathbf{x}'_2)/2$, $\mathbf{r} = \mathbf{x}_1 - \mathbf{x}_2$, and $\mathbf{r}' = \mathbf{x}'_1 - \mathbf{x}'_2$. Since $H^{\text{c.m.}}$ is the Hamiltonian of a free particle with mass $2m$, the corresponding density matrix directly reads

$$\rho_2^{\text{c.m.}}(\mathbf{X}, \mathbf{X}'; \beta) = \rho_1(\mathbf{X}, \mathbf{X}'; \beta/2), \quad (2.27)$$

where the $1/2$ factor in front of β corresponds to the fact that the reduced mass of the center-of-mass problem is twice as large as m (*cf.* Eq. 2.25). In the absence of interactions, also H^{rel} is a free-particle Hamiltonian (with reduced mass $m/2$), so that the non-interacting relative-motion density matrix reads

$$\rho_2^{\text{rel},0}(\mathbf{r}, \mathbf{r}'; \beta) = \rho_1(\mathbf{r}, \mathbf{r}'; 2\beta). \quad (2.28)$$

The dependence of ρ_2^{rel} on interactions can be absorbed in a correction factor g^{rel} , as in

$$\rho_2^{\text{rel}}(\mathbf{r}, \mathbf{r}'; \beta) = \rho_2^{\text{rel},0}(\mathbf{r}, \mathbf{r}'; \beta) + \Delta\rho_2^{\text{rel}}(\mathbf{r}, \mathbf{r}'; \beta) = \rho_2^{\text{rel},0}(\mathbf{r}, \mathbf{r}'; \beta) g^{\text{rel}}(\mathbf{r}, \mathbf{r}'; \beta), \quad (2.29)$$

where g^{rel} is defined by

$$g^{\text{rel}}(\mathbf{r}, \mathbf{r}'; \beta) \equiv 1 + \frac{\Delta\rho_2^{\text{rel}}(\mathbf{r}, \mathbf{r}'; \beta)}{\rho_2^{\text{rel},0}(\mathbf{r}, \mathbf{r}'; \beta)}. \quad (2.30)$$

This correction factor is equal to one in the absence of interactions, and otherwise quantifies the deviation from the non-interacting relative-motion density matrix. The knowledge of g^{rel} represents the full solution of the two-body problem at finite temperature, and it is useful for the many-body treatment described in Section 3.2.1.

2.1.2.1 Two-body correction factor for zero-range potential

We consider the zero-range two-body potential $V_2(r)$ introduced in Section 2.1.1.2. In Eq. 2.24, the single-particle density matrix ρ_1 is obtained through an integral over the eigenstates of the Hamiltonian. In an analogous way, the eigenstates found in Section 2.1.1.2 for the zero-range potential give access to the exact form of the two-body density matrix ρ_2^{rel} , as we show in this section.

The partial-wave expansion which we used for the two-body scattering states (see Eq. 2.4) also applies to the relative density matrix $\rho_2^{\text{rel}}(\mathbf{r}, \mathbf{r}'; \beta)$. For the zero-range potential, the difference $\Delta\rho_2^{\text{rel}}(\mathbf{r}, \mathbf{r}'; \beta)$ only includes the $l = 0$ terms, while corrections for higher partial waves vanish. The s-wave term in the expansion of ρ_2^{rel} reads [50]

$$\frac{1}{4\pi} \int_0^\infty dk R_{k,0}^*(r') R_{k,0}(r) \exp\left(-\frac{\beta\hbar^2 k^2}{m}\right), \quad (2.31)$$

with the eigenfunctions $R_{k,0}(r)$ in Eq. 2.18. If a bound state exists (that is, for $a > 0$), $\rho_2^{\text{rel}}(\mathbf{r}, \mathbf{r}'; \beta)$ also includes the corresponding term

$$R_{b.s.}^*(r') R_{b.s.}(r) \exp\left(\frac{\hbar^2}{ma^2}\right), \quad (2.32)$$

with $R_{b.s.}$ defined as in Eq. 2.20. The $l = 0$ contribution to $\rho_2^{\text{rel}}(\mathbf{r}, \mathbf{r}'; \beta)$ consists in the sum of Eqs. 2.31 and 2.32, and can be computed analytically (cf. Appendix 3.B in Ref. [51]). This results in a unique expression, not depending on whether the bound state exists. $\Delta\rho_2^{\text{rel}}(\mathbf{r}, \mathbf{r}'; \beta)$ is then obtained as the difference between the $l = 0$ parts of $\rho_2^{\text{rel}}(\mathbf{r}, \mathbf{r}'; \beta)$ and $\rho_2^{\text{rel},0}(\mathbf{r}, \mathbf{r}'; \beta)$. The correction factor g^{rel} for a three-dimensional contact potential with scattering length a thus reads

$$g^{\text{rel}}(\mathbf{r}, \mathbf{r}'; \beta) = 1 + \frac{2\beta\hbar^2}{mr'r'} \exp\left(-\frac{rr' + \mathbf{r} \cdot \mathbf{r}'}{2\beta\hbar^2/m}\right) F_a(r, r'; \beta), \quad (2.33)$$

where

$$F_a(r, r'; \beta) = 1 + \frac{\hbar}{a} \sqrt{\frac{\pi\beta}{m}} e^{\left(\sqrt{\frac{m}{\beta}} \frac{r+r'}{2\hbar} - \sqrt{\frac{\beta}{m}} \frac{\hbar}{a}\right)^2} \operatorname{erfc}\left(\sqrt{\frac{m}{\beta}} \frac{r+r'}{2\hbar} - \sqrt{\frac{\beta}{m}} \frac{\hbar}{a}\right). \quad (2.34)$$

The function $F_a(r, r'; \beta)$ tends to 0 for $a \rightarrow 0^-$, giving back the non-interacting limit (that is, $g^{\text{rel}} = 1$). For $|a| \rightarrow \infty$, in contrast, $F_a(r, r'; \beta)$ tends to 1, so that the correction factor at unitarity reads

$$g^{\text{rel}}(\mathbf{r}, \mathbf{r}'; \beta) = 1 + \frac{2\beta\hbar^2}{mr'r'} \exp\left(-\frac{rr' + \mathbf{r} \cdot \mathbf{r}'}{2\beta\hbar^2/m}\right). \quad (2.35)$$

The correction factor diverges as $(rr')^{-1}$ for small r and r' , which corresponds to imposing the Bethe-Peierls boundary conditions on the pair wave functions (see Eq. 2.21). This implies that the zero-range potential at unitarity has an effective short-range attraction, since the weight of configurations with small r and r' is greatly enhanced when $r, r' \rightarrow 0$. Nevertheless, the two particles do not form a bound state, since the binding energy E_D vanishes in the unitary limit (*cf.* Eq. 2.19). The short-range divergence of g^{rel} has peculiar consequences on the correlation functions for two or more unitary particles (e.g., the non-smoothness of the single-particle correlation function $g^{(1)}$), which we describe in the next section (see Section 2.1.3).

The correction factor in Eq. 2.35 is also the building block to construct an approximate expression of the N -body density matrix (see Eq. 3.32). For this reason, it has been used in several QMC studies of both bosonic and fermionic systems with zero-range unitary interactions [52, 12, 53, 54, 55]. ρ_2^{rel} has also been computed in the presence of a trapping potential [53].

2.1.3 Correlation functions

In this section, we compute the main correlation functions for two unitary bosons, and compare them to the exact numerical curves obtained through the QMC method (*cf.* Chapter 3). We consider two particles in a periodic cubic box of edge length L . The bosonic two-body density matrix is obtained as an average over the two possible permutation structures (*cf.* Eq. 1.27), namely

$$\rho_2^{\text{bos}}(\{\mathbf{x}_1, \mathbf{x}_2\}, \{\mathbf{x}'_1, \mathbf{x}'_2\}; \beta) = \frac{\rho_2(\{\mathbf{x}_1, \mathbf{x}_2\}, \{\mathbf{x}'_1, \mathbf{x}'_2\}; \beta) + \rho_2(\{\mathbf{x}_1, \mathbf{x}_2\}, \{\mathbf{x}'_2, \mathbf{x}'_1\}; \beta)}{2}. \quad (2.36)$$

The one-body reduced density matrix $g^{(1)}$ and the pair-correlation function $g^{(2)}$ are defined as

$$g^{(1)}(\mathbf{x}, \mathbf{x}') = 2 \frac{\int d\mathbf{x}_2 \rho_2^{\text{bos}}(\{\mathbf{x}, \mathbf{x}_2\}, \{\mathbf{x}', \mathbf{x}_2\}; \beta)}{\int d\mathbf{x}_1 d\mathbf{x}_2 \rho_2^{\text{bos}}(\{\mathbf{x}_1, \mathbf{x}_2\}, \{\mathbf{x}_1, \mathbf{x}_2\}; \beta)}, \quad (2.37)$$

and

$$g^{(2)}(\mathbf{x}, \mathbf{x}') = \frac{\rho_2^{\text{bos}}(\{\mathbf{x}, \mathbf{x}'\}, \{\mathbf{x}, \mathbf{x}'\}; \beta)}{\int d\mathbf{x}_1 d\mathbf{x}_2 \rho_2^{\text{bos}}(\{\mathbf{x}_1, \mathbf{x}_2\}, \{\mathbf{x}_1, \mathbf{x}_2\}; \beta)}. \quad (2.38)$$

For a translation-invariant system, both $g^{(1)}(\mathbf{x}, \mathbf{x}')$ and $g^{(2)}(\mathbf{x}, \mathbf{x}')$ only depend on $\mathbf{r} = \mathbf{x} - \mathbf{x}'$. In the path-integral description, $g^{(1)}$ is the distribution for the endpoints of an open path, while $g^{(2)}$ is the distance distribution for closed-path configurations. This is developed further in Sections 3.3.1 and 3.3.3, where these observables are defined for a general many-body system.

The effects of unitary zero-range interactions on these correlation functions are represented in Fig. 2.2. The one-body reduced density matrix has a cusp singularity at $\mathbf{r} = 0$ (cf. Fig. 2.2a), so that the momentum distribution $n(\mathbf{k})$ decays as a power law for large momenta (cf. Fig. 2.2b). Moreover, the pair-correlation function $g^{(2)}(\mathbf{r})$ diverges as $1/r^2$ for small r (cf. Fig. 2.2c). These features have been extensively studied for bosonic or fermionic systems in the regime of large scattering length and small range of potential [56, 57, 58, 49, 59]. For $N = 2$, they can be obtained directly from the knowledge of the two-body density matrix, see Sections 2.1.3.1 and 2.1.3.2.

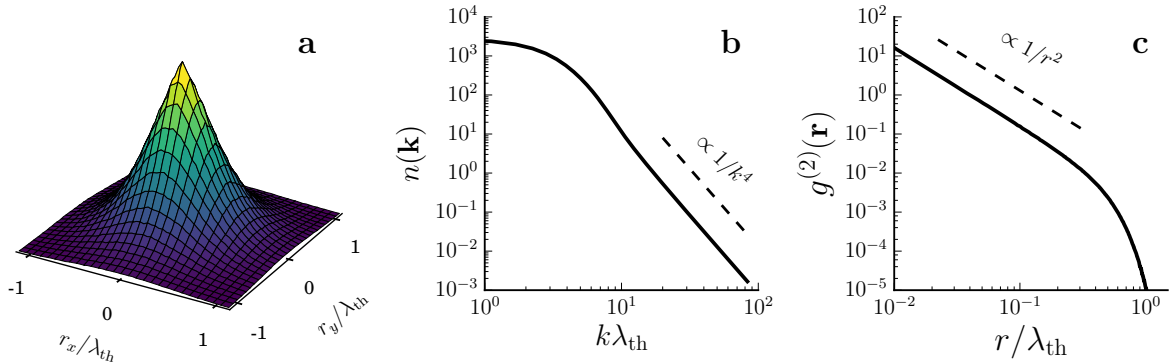


Figure 2.2: Schematic view of correlation functions at unitarity (data obtained through the QMC simulation of two co-cyclical bosons at low temperature, see Section 3.2). The one-body reduced density matrix $g^{(1)}(\mathbf{r})$ has a cusp at $r_x = r_y = r_z = 0$ (panel a, shown for $r_z/\lambda_{\text{th}} \approx 0$), leading to a power-law decay of its Fourier transform $n(\mathbf{k})$ (panel b). Panel c: Pair-correlation function $g^{(2)}(\mathbf{r})$, diverging at short distance.

2.1.3.1 One-body reduced density matrix and momentum distribution

Following its definition in Eq. 2.37, $g^{(1)}(\mathbf{r})$ tends to $\rho = N/V$ for r going to zero. This implies that the momentum distribution,

$$n(\mathbf{k}) = V \int d\mathbf{r} g^{(1)}(\mathbf{r}) e^{-i\mathbf{k}\cdot\mathbf{r}}, \quad (2.39)$$

satisfies the normalization condition $\int d\mathbf{k} n(\mathbf{k}) = 2 \times (2\pi)^3$. We compute $g^{(1)}(\mathbf{r})$ in the high-temperature limit, i.e. for a thermal wavelength λ_{th} much smaller than L . In this regime, the following approximation is justified

$$\int_{[0,L]^3} d\mathbf{x} \int_{[0,L]^3} d\mathbf{x}' \exp\left(-\pi \frac{(\mathbf{x}-\mathbf{x}')^2}{\lambda_{\text{th}}^2}\right) \simeq L^3 \int_{\mathbb{R}^3} d\mathbf{r} \exp\left(-\pi \frac{\mathbf{r}^2}{\lambda_{\text{th}}^2}\right) = (L\lambda_{\text{th}})^3, \quad (2.40)$$

which simplifies the analytical calculation. The integral in Eq. 2.37 then gives

$$g^{(1)}(\mathbf{r}) = \frac{\rho}{\gamma} \left[e^{-\frac{\pi r^2}{\lambda_{\text{th}}^2}} + \underbrace{\left(\frac{\lambda_{\text{th}}}{L\sqrt{2}}\right)^3 e^{-\frac{\pi r^2}{2\lambda_{\text{th}}^2}}}_{\text{2nd term}} + \underbrace{\left(\frac{\lambda_{\text{th}}\sqrt{2}}{L}\right)^3 e^{-\frac{\pi r^2}{2\lambda_{\text{th}}^2}} \text{erfc}\left(\frac{r\sqrt{\pi/2}}{\lambda_{\text{th}}}\right)}_{\text{3rd term}} \right], \quad (2.41)$$

where the normalization factor γ reads

$$\gamma = 1 + \left(\frac{\lambda_{\text{th}}}{L\sqrt{2}}\right)^3 + \left(\frac{\lambda_{\text{th}}\sqrt{2}}{L}\right)^3. \quad (2.42)$$

The expression in Eq. 2.41 is the sum of three terms: The result for non-interacting distinguishable particles, followed by the two corrections due to bosonic statistics and to unitary interactions. Both corrections vanish in the infinite-temperature limit, $\lambda_{\text{th}}\rho^{1/3} \rightarrow 0$. The second term in $g^{(1)}(\mathbf{r})$ (due to bosonic statistics) has a slower large- r decay than the first term. This is a signature of off-diagonal long-range order, which would take place at low temperature (see Sections 1.1 and 3.3.3). The third term in Eq. 2.41 is the effect of zero-range, unitary interactions, for the one-body reduced density matrix of two bosons. Due to the erfc function, the derivative of $g^{(1)}(\mathbf{r})$ with respect to r remains finite in the $r \rightarrow 0$ limit, generating a cusp singularity (see Fig. 2.2a). The non-smoothness of $g^{(1)}$ in real space corresponds to a power-law decay of $n(\mathbf{k})$ at large momentum, namely $n(\mathbf{k}) \simeq C_2/k^4$. This asymptotic scaling of the momentum distribution is a general feature due to strong short-ranged interaction potentials, and it is also present in the many-body case (see Sections 4.3.1 and 4.4.2). The prefactor C_2 , known as Tan's contact [57] regulates the short-distance behavior of $g^{(1)}(\mathbf{r})$ and $g^{(2)}(\mathbf{r})$ (see also Section 2.1.3.2). Moreover, it is related to global observables, as the derivative of the total energy with respect to the scattering length [57, 49].

A direct connection exists between the cusp singularity in $g^{(1)}(\mathbf{r})$ and the power-law decay of its Fourier transform at large k [60]. The one-body reduced density matrix is

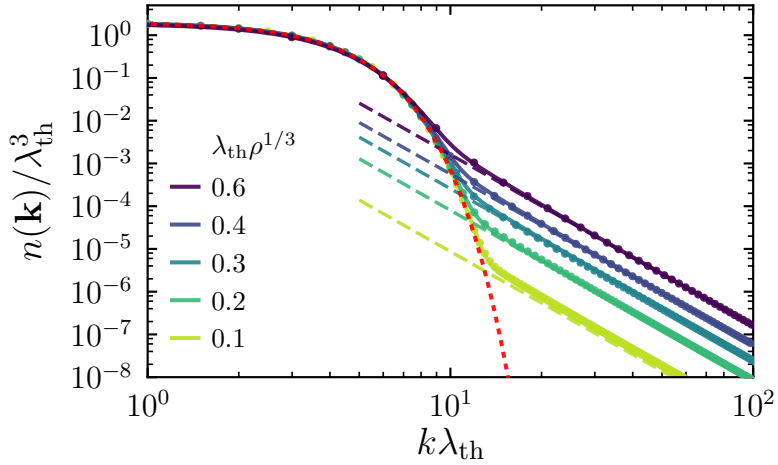


Figure 2.3: Momentum distribution for two unitary bosons in a cubic box, at different temperatures (see legend). For each temperature, the numerical Fourier transform of Eq. 2.41 (solid lines) is indistinguishable from the exact numerical result (dots, obtained with the QMC method described in Chapter 3). The large- k part of $n(\mathbf{k})$ is well captured by C_2/k^4 , with the value of C_2 extracted from the pair-correlation function (dashed lines, cf. Eq. 2.48). We also show $n(\mathbf{k})$ for two non-interacting distinguishable particles (red dotted line, cf. Eq. 3.102).

conveniently rewritten as

$$\begin{aligned} g^{(1)}(\mathbf{r}) &= \frac{1}{V(2\pi)^3} \int d\mathbf{k} n(\mathbf{k}) e^{-i\mathbf{k}\cdot\mathbf{r}} = \frac{N}{V} + \frac{1}{V(2\pi)^3} \int d\mathbf{k} n(\mathbf{k}) (e^{-i\mathbf{k}\cdot\mathbf{r}} - 1) = \\ &= \underbrace{\frac{N}{V} + \frac{1}{V(2\pi)^3} \int d\mathbf{k} \frac{C_2}{k^4} (e^{-i\mathbf{k}\cdot\mathbf{r}} - 1)}_{\mathcal{I}_A} + \underbrace{\int d\mathbf{k} \left(n(\mathbf{k}) - \frac{C_2}{k^4}\right) (e^{-i\mathbf{k}\cdot\mathbf{r}} - 1)}_{\mathcal{I}_B}, \end{aligned} \quad (2.43)$$

where the second term, \mathcal{I}_A , can be computed exactly. Assuming that $n(\mathbf{k}) \simeq C_2/k^4$ at large k , \mathcal{I}_B is $O(r^2)$ [58]. Thus the small- r expansion of $g^{(1)}(\mathbf{r})$ reads

$$g^{(1)}(\mathbf{r}) \xrightarrow{r \rightarrow 0} \frac{N}{V} - \frac{C_2}{8\pi V} r + O(r^2). \quad (2.44)$$

Thus the contact density $c_2 \equiv C_2/V$ corresponds to the r -derivative of $g^{(1)}(\mathbf{r})$ for $r \rightarrow 0$, up to numerical prefactors, and it can be computed from Eq. 2.41. This leads to

$$c_2 \rho^{-4/3} = \frac{128\pi}{8 + 9\sqrt{2}(\lambda_{\text{th}}^3 \rho)} \left(\lambda_{\text{th}} \rho^{1/3}\right)^2, \quad (2.45)$$

which holds for two particles in the high-temperature regime ($\lambda_{\text{th}} \rho^{1/3} \ll 1$). At smaller temperatures, the shape of the box becomes relevant and Eq. 2.41 is not valid, since it is based on the approximation in Eq. 2.40.

The full momentum distribution can be computed from the expression in Eq. 2.41, by performing the Fourier transform in Eq. 2.39 numerically. For $\lambda_{\text{th}}\rho^{1/3}$ up to 0.6, the resulting $n(\mathbf{k})$ curves agree with the exact results obtained through the QMC method (see Fig. 2.3). The small- k part is well described by the momentum distribution of non-interacting distinguishable particles, which crosses over into the asymptotic power-law tail at $k \approx k^*$. The length scale over which the derivative of $g^{(1)}(\mathbf{r})$ is finite is set by the thermal wavelength λ_{th} (cf. Eq. 2.41). Therefore the crossover momentum k^* should be proportional to $1/\lambda_{\text{th}}$. This is confirmed by the results shown in Fig. 2.3, where we find that $k^* \approx 10/\lambda_{\text{th}}$.

2.1.3.2 Pair-correlation function

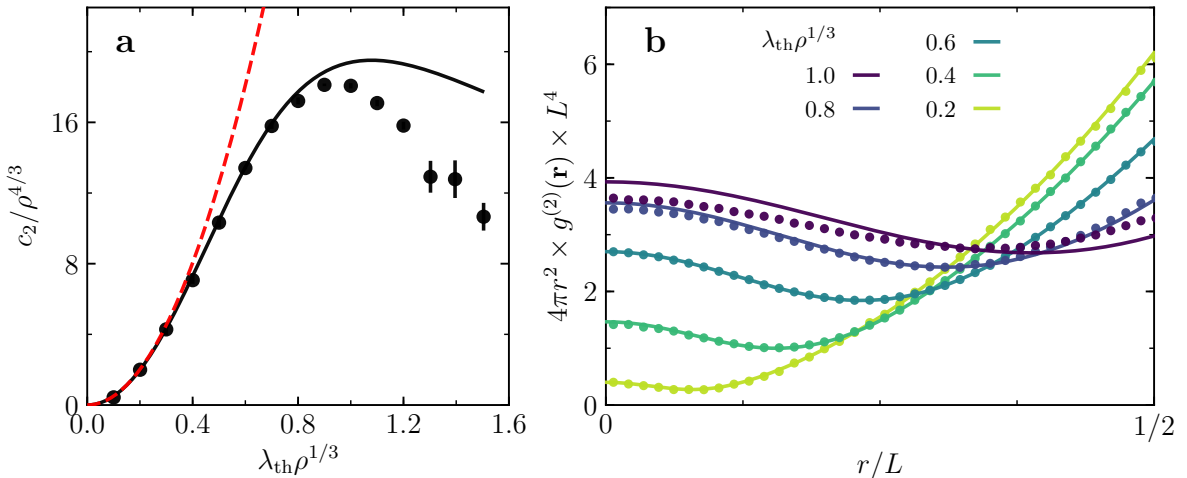


Figure 2.4: Panel **a**: Rescaled contact density for two bosons in a periodic cubic box. Approximate expressions are computed starting from $g^{(1)}(\mathbf{r})$ (black solid line, cf. Eq. 2.45) and $g^{(2)}(\mathbf{r})$ (dashed red line, cf. Eq. 2.48), and compared with the exact results (black dots, obtained through QMC). Panel **b**: Pair-correlation function for two bosons in a periodic cubic box, at different temperatures (see legend). At each temperature, the approximate high-temperature expression (solid line, cf. Eq. 2.46) is compared with the exact QMC curve (dots, cf. Chapter 3). The expression in Eq. 2.46 is multiplied by the distribution of periodic distances for two non-interacting particles (different from unity only for $r > L/2$), and then rescaled to obtain the correct normalization (cf. Section 4.4.3).

We also compute the pair-correlation function $g^{(2)}(\mathbf{r})$ analytically, in the limit of high

temperature. Starting from the definition in Eq. 2.38, we find

$$g^{(2)}(\mathbf{r}) = \frac{2}{V^2} \left[1 + \underbrace{\exp\left(-\frac{2\pi r^2}{\lambda_{\text{th}}^2}\right)}_{\text{2nd term}} + \underbrace{\frac{2\lambda_{\text{th}}^2}{\pi r^2} \exp\left(-\frac{2\pi r^2}{\lambda_{\text{th}}^2}\right)}_{\text{3rd term}} \right]. \quad (2.46)$$

As for $g^{(1)}(\mathbf{r})$, the pair-correlation function is the sum of three terms. The first is the result for two distinguishable non-interacting particles, where $g^{(2)}(\mathbf{r})$ is a constant. The second term corresponds to the boson-bunching effect [61]: Bosonic statistics leads to the doubling of the statistical weight of configurations with the two particles at zero distance. The third term is the correction due to unitary, zero-range interactions for two bosons, and it diverges as $1/r^2$ at short distance. This leads to an alternative expression for the contact density c_2 , which can be obtained through [49, 59]

$$c_2 = \lim_{r \rightarrow 0} [(4\pi r)^2 g^{(2)}(\mathbf{r})], \quad (2.47)$$

for any N -body system. By applying Eq. 2.48 to the high-temperature pair-correlation function for two bosons (*cf.* Eq. 2.46), we find

$$c_2 \rho^{-4/3} = 16\pi (\lambda_{\text{th}} \rho^{1/3})^2. \quad (2.48)$$

This corresponds to the second-order virial-expansion result [62, 63, 64], up to a factor of two (which is a finite- N correction, see Appendix 4.A).

The contact densities in Eqs. 2.45 and 2.48 (obtained through $g^{(1)}(\mathbf{r})$ and $g^{(2)}(\mathbf{r})$, respectively) are equal at high temperature. Both expressions are only approximately valid, and cannot be used at low temperature. By a comparison with the exact QMC data, however, we observe that Eq. 2.45 better captures the temperature dependence of c_2 , for two bosons in a periodic box (see Fig. 2.4a). At high temperature, the rescaled contact density $c_2 \rho^{-4/3}$ is proportional to $(\lambda_{\text{th}} \rho^{1/3})^2$. c_2 reaches its maximum value for $\lambda_{\text{th}} \rho^{1/3} \approx 0.9$, and then decreases for larger $\lambda_{\text{th}} \rho^{1/3}$. A similar behavior is observed for the many-body case, *cf.* Sections 4.3.2 and 4.4.3. Eq. 2.46 for the pair-correlation function is only valid in the high-temperature regime, for small $\lambda_{\text{th}} \rho^{1/3}$, as is clear when comparing it with the exact curves obtained through QMC simulations (see Fig. 2.4b). The temperature at which deviations first appear corresponds to $\lambda_{\text{th}} \rho^{1/3} \approx 0.8$.

2.2 Three-body physics and Efimov effect

In the Section 2.1, we described two bosons interacting through a zero-range potential with infinite scattering length. In the $|a| \rightarrow \infty$ limit, the shallow dimer state (which

exists for $a > 0$) becomes unbound, as its size diverges and its binding energy vanishes. If a third identical boson is added, however, an infinite sequence of three-body bound states appears. This was first described by V. Efimov in 1970 [7, 65], in the context of nuclear physics. These states are characterized by a discrete scale invariance, where the $(n + 1)$ -th trimer has an energy which is ≈ 515 times smaller than the n -th state, and a linear size which is ≈ 22.7 times larger. Moreover, they have universal properties, which can be obtained starting from different two-body potentials having a short range and a large scattering lengths. For $a \leq 0$, Efimov trimers are Borromean states, since three particles form a bound state even in the absence of any two-body binding.

Forty years after the prediction of Efimov trimers, signatures of these states have been observed in experiments with strongly-interacting ultracold atomic gases (see Section 2.3). This has lead to an renewed experimental and theoretical interest towards Efimov physics, which has reached diverse fields as quantum magnets [66] and three-stranded DNA (see [67] and references therein).

In this section, we describe the basic derivation of the Efimov effect, for the case of a model two-body potential with zero range and infinite scattering length [10]. This mainly consists in obtaining a certain class of solutions of the $N = 3$ Schrödinger equation, in the low-energy regime. This theory allows to obtain the infinite tower of scale-invariant, universal Efimov trimers. However, using a zero-range two-body potential leads to the Thomas collapse, where a trimer state exists with infinite binding energy and vanishing size. To regularize the problem, we introduce a three-body regulator (*cf.* Section 2.2.2), in the form of a cutoff on the three-body distance. This model only weakly deviates from the universal Efimov theory (*cf.* Section 2.2.2), and it will be the basis for our study of the many-body case (the unitary Bose gas, see Chapter 4).

Furthermore, we explain in Section 2.2.2.1 how some specific properties of Efimov trimers also provide a method to calibrate the quantum Monte Carlo scheme described in Chapter 3. This method is used here to study the ground-state Efimov trimer (see Section 2.2.2), and in Chapter 4 for the unitary Bose gas.

2.2.1 Efimov trimers

Here we sketch the derivation of the universal theory for the Efimov effect, for the case of three identical bosons with infinite scattering length and zero-range interactions². The three-body Hamiltonian reads

$$H = \sum_{i=1}^3 \frac{\mathbf{p}_i^2}{2} + V_2(r_{12}) + V_2(r_{23}) + V_2(r_{31}), \quad (2.49)$$

and we are only interested in the relative-motion problem, in the frame of the center of mass of the three particles. In this case, a configuration is defined through six degrees

²Section 2.2.1 is mainly based on Ref. [10].

of freedom. It is convenient to express the three-body problem by using different sets of variables, namely the Jacobi and hyperspherical coordinates. Given three positions $\mathbf{x}_1, \mathbf{x}_2$ and \mathbf{x}_3 , Jacobi coordinates read

$$\mathbf{r}_{ij} = \mathbf{x}_i - \mathbf{x}_j, \quad \mathbf{r}_{k,ij} = \mathbf{x}_k - \frac{\mathbf{x}_i + \mathbf{x}_j}{2}, \quad (2.50)$$

for any permutation $\{i, j, k\}$ of $\{1, 2, 3\}$. In the center-of-mass frame, a configuration is specified by any pair of vectors \mathbf{r}_{ij} and $\mathbf{r}_{k,ij}$. The hyperradial coordinates consist in the hyperradius R , the Delves hyperangle α_k , and the two unit vectors $\hat{\mathbf{r}}_{ij} \equiv \mathbf{r}_{ij}/|\mathbf{r}_{ij}|$ and $\hat{\mathbf{r}}_{k,ij} \equiv \mathbf{r}_{k,ij}/|\mathbf{r}_{k,ij}|$. The hyperradius is defined through

$$R \equiv \sqrt{\frac{r_{12}^2 + r_{23}^2 + r_{31}^2}{3}} = \sqrt{\frac{1}{2}r_{ij}^2 + \frac{2}{3}r_{k,ij}^2} \quad (2.51)$$

while the Delves hyperangle reads

$$\alpha_k = \arctan \left(\frac{\sqrt{3}r_{ij}}{2r_{k,ij}} \right), \quad (2.52)$$

with $\alpha_k \in [0, \pi/2]$. We collectively denote the angular variables by $\Omega = (\alpha_k, \hat{\mathbf{r}}_{ij}, \hat{\mathbf{r}}_{k,ij})$.

The three-body wave function $\Psi(R, \Omega)$, which satisfies the Schrödinger equation for the Hamiltonian in Eq. 2.49, can be decomposed on a complete set of hyperangular functions $\Phi_n(\Omega, R)$:

$$\Psi(R, \Omega) = \frac{1}{R^{5/2}} \sum_n f_n(R) \Phi_n(\Omega; R), \quad (2.53)$$

and the Faddeev decomposition of Φ_n reads

$$\Phi_n(\Omega; R) = \sum_{k=1}^3 \frac{\phi(\Omega; R)}{\sin 2\alpha_k}, \quad (2.54)$$

for three identical bosons. In the low-energy regime, the dependence of ϕ on $\hat{\mathbf{r}}_{ij}$ and $\hat{\mathbf{r}}_{k,ij}$ can be neglected, which is equivalent to only considering the first term in the corresponding partial-wave expansions. The solution for Φ_n introduces an additional effective potential $V_n(R)$ in the Schrödinger equation for the n -th hyperradial wave function, $f_n(R)$. The different channels are in principle not independent, but their coupling can be neglected in the low-energy limit. We consider the $n = 0$ channel, which is the only one with an attractive effective potential supporting a bound state [65]. The effective potential $V_0(R)$ is proportional to R^{-2} , and it depends on $s_0 = 1.0062378..$, the solution of

$$s_0 \cosh \frac{\pi s_0}{2} = \frac{8}{\sqrt{3}} \sinh \frac{\pi s_0}{6}. \quad (2.55)$$

The Schrödinger equation for $f_0(R)$ reads

$$-\frac{\hbar^2}{2m} \left(\frac{\partial^2}{\partial R^2} + \frac{s_0^2 + 1/4}{R^2} \right) f_0(R) = Ef_0(R), \quad (2.56)$$

and the binding momentum κ reads

$$\kappa = \sqrt{\frac{-mE}{\hbar^2}}. \quad (2.57)$$

The solution of Eq. 2.56 which decays exponentially at large hyperradius is

$$f_0(R) = \frac{2\kappa\sqrt{R} K_{is_0}(\sqrt{2}\kappa R)}{\sqrt{\pi s_0 \operatorname{csch}(\pi s_0)}}, \quad (2.58)$$

where csch is the hyperbolic cosecant and K_{is_0} is the Bessel function with imaginary index is_0 .

The wave function $f_0(R)$ depends on a single parameter, namely its binding momentum κ . Fixing a small- R boundary conditions for its logarithmic derivative sets a constraint on κ , which is restricted to take a discrete set of values κ_n . These values form an infinite geometric sequence, defined by [65]

$$\frac{\kappa_n}{\kappa_{n+1}} = e^{\pi/s_0} \approx 22.694 \quad \text{for } n \in \mathbb{Z}. \quad (2.59)$$

Therefore there exists an infinite sequence of states, known as Efimov trimers, with energies E_n which satisfy

$$\frac{E_n}{E_{n+1}} = e^{2\pi/s_0} \approx 515. \quad (2.60)$$

The peculiarity of these states is their scale invariance: The n -th and $(n+1)$ -th are simply a rescaled version of one another, with a length scale set by $1/\kappa_n$. The knowledge of the binding momentum κ_n for a specific $n = n^*$ determines the whole sequence $\{\kappa_n\}$. This corresponds to the fact that the universality of a system of three strongly-interacting unitary bosons is not fully determined by the scattering length, but it also depends on a three-body parameter. In Section 2.2.2 we show how this parameter is fixed in our model, while in Section 2.3.2 we describe its experimental characterization.

The size of a trimer can be measured through its average squared hyperradius,

$$\langle R^2 \rangle = \frac{\int_0^\infty dR |f_0(R)|^2 R^2}{\int_0^\infty dR |f_0(R)|^2}. \quad (2.61)$$

which is connected to the trimer binding momentum κ through

$$\kappa^2 = \frac{1+s_0^2}{3} \frac{1}{\langle R^2 \rangle}, \quad (2.62)$$

as obtained directly through Eqs. 2.58 and 2.61³. For $n \rightarrow \infty$, the binding energy of the n -th trimer tends to zero (*cf.* Eq. 2.60) and its characteristic size diverges, while for $n \rightarrow \infty$ the binding energy $|E_n|$ diverges and the trimer collapses to a single point in space at any temperature. The latter is known as the Thomas collapse [68], which we discuss further in Section 2.2.2.

2.2.2 Three-body-cutoff model

As the Efimov spectrum is not bounded from below, three unitary bosons with zero-range interactions would collapse to a single point, at any temperature. This is also visible in the small- R behavior of the hyperradial wave function $f_0(R)$, which reads

$$f_0(R) \simeq -\frac{2\kappa\sqrt{R}}{\sqrt{s_0}} \sin(s_0 \log(\kappa R) + \alpha_0), \quad (2.63)$$

where $\alpha_0 \simeq -0.0477$ is a constant depending on s_0 [10]. The signature of Thomas collapse is that the oscillatory function in Eq. 2.63 has infinitely many nodes, for a given value of κ (see Fig. 2.5). Starting from the outermost node, the values of κR for these nodes differ by integer multiples of $\exp(-\pi/s_0)$. Therefore, for any trimer state (characterized by κ) there exist infinitely many other trimers with larger energy and smaller size [69].

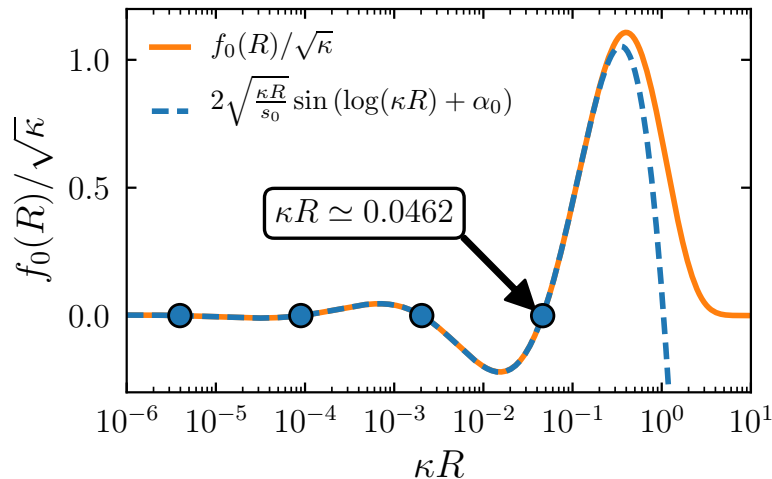


Figure 2.5: Hyperradial wave function of an Efimov trimer (*orange solid line*, *cf.* Eq. 2.58) and its small- R expansion (*blue dashed line*, *cf.* Eq. 2.63). The four outermost nodes of $f_0(R)$ are marked by blue circles.

³Eq. 2.62 is incorrectly reported in §5.5 of Ref. [10], where an additional factor of two is included in the right hand side. The same error is present in Ref. [51].

The pathological Thomas collapse is a consequence of using the zero-range two-body potential. This potential does not include any information about the short-range part of realistic interactions, which would otherwise lead to a small- R repulsive term in the Schrödinger equation for $f_0(R)$ [70]. Using a realistic two-body potential with range r_0 would set a large energy scale $\propto 1/r_0^2$. This would provide a lower bound on the Efimov spectrum, leading to the appearance of one specific ground-state trimer.

Within the model based on zero-range two-body interactions, Thomas collapse can be avoided introducing a small- R cutoff on $f_0(R)$ [69, 10, 71, 12]. This corresponds to setting $f_0(R) = 0$ for any $R \leq R_0$, where R_0 is chosen as the outermost node of $f_0(R)$ – see Fig. 2.5. This introduces a lower bound on the Efimov spectrum, so that there exists a well-defined ground-state trimer, with binding momentum⁴

$$\kappa_0 = \frac{e^{-(\pi+\alpha_0)/s_0}}{R_0} \simeq \frac{0.046203}{R_0}, \quad (2.64)$$

and energy

$$E_T = -\frac{\hbar^2 \kappa_0^2}{m} \simeq -\frac{\hbar^2}{m} \frac{0.0021347}{R_0^2}. \quad (2.65)$$

Setting a cutoff for $R \leq R_0$ corresponds to considering the Hamiltonian

$$H = \sum_{i=1}^3 \frac{\mathbf{p}_i^2}{2m} + \sum_{i < j} V_2(r_{ij}) + V_3(R), \quad (2.66)$$

where V_3 is a three-body hard-core repulsion:

$$V_3(R) = \begin{cases} \infty & \text{if } R < R_0 \\ 0 & \text{if } R > R_0 \end{cases}. \quad (2.67)$$

Eq. 2.66 can be generalized to the N -body case, as in

$$H = \sum_{i=1}^N \frac{\mathbf{p}_i^2}{2m} + \sum_{i < j} V_2(r_{ij}) + \sum_{i < j < k} V_3(R_{ijk}), \quad (2.68)$$

which constitutes the model for our study of the unitary Bose gas (see Chapter 4).

An alternative regularization scheme consists in replacing the three-body cutoff with a soft repulsive potential $V_3(R)$ [72]. This choice is easier to treat through the QMC method (*cf.* Chapter 3), at the price of an additional dependence on the functional form for V_3 .

⁴Among the roots of the small- R asymptotic expression (*cf.* Eq. 2.63), we choose the one closest to the outermost root of $f_0(R)$. The root of $f_0(R)$ is at $\kappa_0 R_0 \simeq 0.046227$, with a relative deviation of 5×10^{-4} from Eq. 2.64.

The choice of the hyperradial cutoff as a regulator is in principle arbitrary, and we need to verify the extent to which the universal properties of Efimov trimers are modified. For a trimer with binding momentum κ , the effect of the three-body cutoff on the wave function in Eq. 2.58 depends on κR_0 . For the ground-state trimer, this parameter is ≈ 0.046 , while for the n -th excited state it is approximately $0.046/22.7^n$. This guarantees that highly-excited states have a large overlap with the universal wave function in Eq. 2.58. The deviation from universality can be measured through the relative difference of κ_n/κ_{n+1} from the scaling factor $\exp(\pi/s_0) \approx 22.7$, which reads [72]:

$$\text{diff}_n = \frac{\frac{\kappa_n}{\kappa_{n+1}} - e^{\pi/s_0}}{e^{\pi/s_0}} \approx (5.297 \times 10^{-4}) \times e^{-6.244n}. \quad (2.69)$$

This is already small for the ground state ($\text{diff}_0 \simeq 0.053\%$), and negligible for highly excited states (for instance, $\text{diff}_4 < 10^{-14}$).

We also compare universal Efimov trimers with the ground-state trimer of the three-body-cutoff model. For the latter, the hyperradial correlation function $P_3(R)$ and the single-particle momentum distribution $n(\mathbf{k})$ are computed through the QMC method (see Chapter 3), which gives access to thermal-equilibrium properties. Therefore, the only accessible trimer state is the ground state, which is the dominating state when the thermal energy $k_B T$ is much smaller than the energy gap ΔE to the first excited state. This condition reads

$$1 \ll \beta \Delta E = \beta |E_T| \left(1 - e^{-2\pi/s_0}\right) \approx \beta |E_T|, \quad (2.70)$$

where E_T is the energy of the ground-state trimer (cf. Eq. 2.65). A technical aspect of our QMC simulations for the ground-state trimer is that they are performed for three bosons belonging to a single permutation cycle [51]. This is necessary to regulate the accessible volume, which is then set to be of the order of λ_{th}^3 . An alternative option would be to include a shallow harmonic trap. Fixing the permutation-cycle structure does not introduce a severe bias on the trimer state realized in the QMC simulations. The paths of the three particles come at extremely short distance, as seen in the divergence of $g^{(2)}(\mathbf{r})$ at small r , so that a different permutation structure could be considered at no cost (see Section 3.2.2.2). The only effect of the co-cyclicity condition is then to modify observables which involves length scales larger than $\approx \lambda_{\text{th}}$, or momenta smaller than $\approx 1/\lambda_{\text{th}}$.

The hyperradial distribution function $P_3(R)$ for a universal trimer is obtained directly as $|f_0(R)|^2$, via Eq. 2.58. In a QMC simulation which includes the three-body cutoff, $P_3(R)$ is obtained as a histogram of the hyperradii in several samples (cf. Section 3.3.1). To compare these two curves, we need to estimate κ_0 for the trimer obtained through QMC, which can be done by measuring the average hyperradius $\langle R^2 \rangle$ and using Eq. 2.62. This also provides a well-defined way to calibrate our QMC scheme, as described in Section 2.2.2.1. The two curves for $P_3(R)$ shown in Fig. 2.6 (for the universal trimer and for the ground-state trimer of the model with a hyperradial cutoff)

are indistinguishable, for $R > R_0$. This shows that even the ground-state trimer of the three-body-cutoff model is only weakly non-universal.

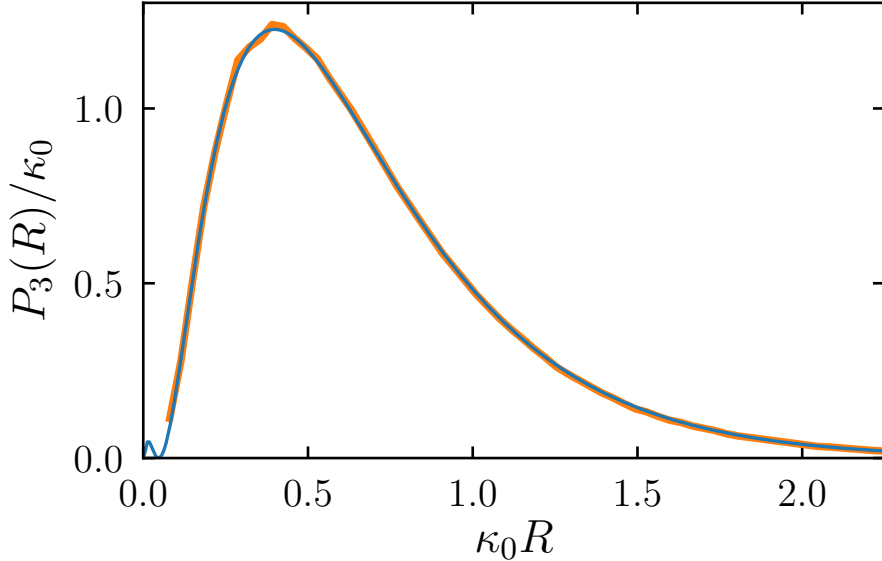


Figure 2.6: Hyperradial probability distribution $P_3(R)$ for a universal Efimov trimer (thin blue line, obtained as the squared modulus of $f_0(R)$, cf. Eq. 2.58), and for the ground-state trimer of the model in Eq. 2.66 (thick orange line, through the QMC method described in Chapter 3). The QMC simulation is performed at $\beta|E_T| \approx 4$, with imaginary-time discretization $\lambda_s = 1.52 \times R_0$ (see Section 3.2.1). The binding momentum κ_0 is extracted from the QMC data through Eqs. 2.64 and 2.74 (cf. Section 2.2.2.1).

The QMC method also yields the single-particle momentum distribution $n(\mathbf{k})$ (see Section 3.3.4). For a universal trimer, the numerically exact expression of $n(\mathbf{k})$ has been computed [73]. As for $N = 2$, $n(\mathbf{k})$ has a power-law tail, C_2/k^4 , at large-momentum. Tan's contact parameter reads

$$C_2 = \kappa \times 53.09722846\dots, \quad (2.71)$$

where κ is the trimer binding momentum [73]. Furthermore, $n(\mathbf{k})$ includes the subleading term

$$\frac{C_3}{k^5} \cos \left(2s_0 \log \left(\frac{\sqrt{3}k}{\kappa} \right) + \phi \right), \quad (2.72)$$

where C_3 is the three-body analogous of the two-body contact C_2 , and

$$\begin{aligned} C_3 &\simeq -89.26260 \times \kappa^2, \\ \phi &\simeq -0.8727976. \end{aligned} \quad (2.73)$$

This term is a consequence of the Efimov effect, and it has also been predicted for a many-body system of unitary bosons [62] (see Section 4.3.1). In Fig. 2.7 we compare the momentum distribution of a universal Efimov trimer with the one for the ground-state trimer of the three-body-cutoff model, obtained through our QMC simulations. The binding momentum κ_0 is extracted through Eqs. 2.64 and 2.74, so that the QMC data do not rely on any fitting parameter. $n(\mathbf{k})$ shows some weak deviation from the universal curve for $k \lesssim 2/\lambda_{\text{th}}$, as a consequence of the finite temperature and of our choice for the volume regulation. For $k\lambda_{\text{th}} \gtrsim 2$, however, the two curves are in agreement over at least three orders of magnitude in $n(\mathbf{k})$ (cf. Fig. 2.7a). For large momenta, however, the statistical noise prevents the accurate determination of the QMC curve (cf. Fig. 2.7b). This is a known issue of the naive method to measure $n(\mathbf{k})$, which could be improved with dedicated QMC estimators (see discussion in Section 3.4.2). Nevertheless, it is possible to track the first part of the universal oscillations in $k^4 n(\mathbf{k})$ (cf. Fig. 2.7b and Eq. 2.72). For even larger momenta (that is, for $k \gtrsim 1/R_0$), the momentum distribution of the three-body hard-core model is expected to deviate from the universal curve.

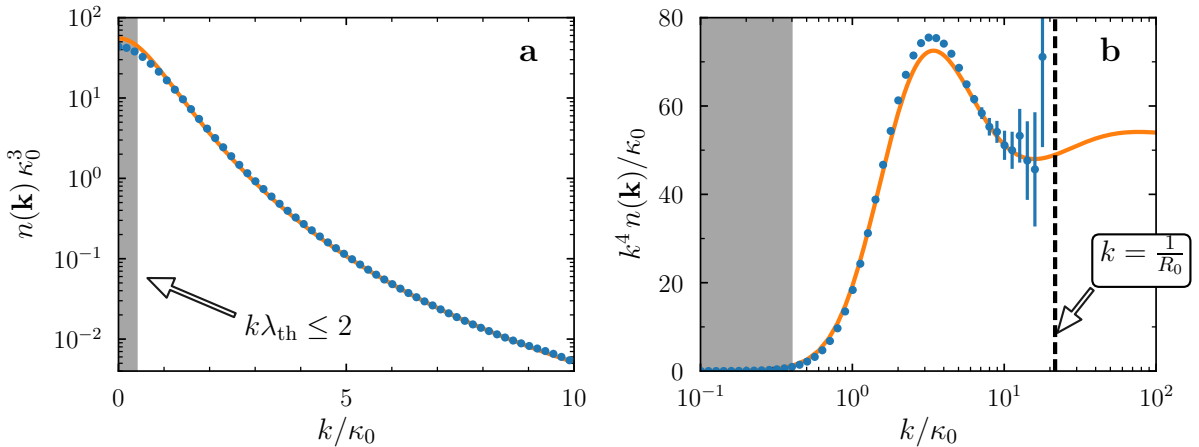


Figure 2.7: Momentum distribution of a universal trimer (orange solid line, from Ref. [73]) and of the ground-state trimer in the presence of a three-body cutoff (blue points, through QMC method, cf. Fig. 2.6). The shaded area corresponds to $k\lambda_{\text{th}} \leq 2$, where our choice to regulate the volume in QMC simulations induce deviations from the universal curve.

2.2.2.1 Ground-state trimer through quantum Monte Carlo

The results for the ground-state trimer of the three-body-cutoff model (see Figs. 2.6 and 2.7) are obtained through the QMC method described in Chapter 3. An important detail of these calculations is that there exists a discrepancy between the value of R_0 which is imposed as an input (R_0^{input}) and the actual value of R_0 which is realized in the simulation. This discrepancy follows from the fact that the QMC method is based on an

approximate form of the three-body density matrix, which incorporates the three-body cutoff through the Trotter approximation (see Section 3.2.1). The effective value of R_0 is obtained through this procedure [51]:

1. We set a certain R_0^{input} , which enters the approximate three-body density matrix via the Trotter approximation.
2. We extract the average hyperradius $\langle R^2 \rangle$ from the QMC simulation and obtain the trimer binding momentum through Eq. 2.62.
3. We extract the effective value of R_0 through Eq. 2.64.

The Trotter approximation depends on τ (the imaginary-time discretization interval), and its validity requires a small value of this parameter. At low temperature, the only available length scales are R_0^{input} and $\sqrt{\hbar^2\tau/m}$, so that they should also determine the deviation of R_0 from the input value R_0^{input} . This is confirmed by the QMC results in Fig. 2.8, which collapse on the single curve

$$\frac{R_0}{R_0^{\text{input}}} \simeq 1 - 0.588 \frac{\sqrt{\hbar^2\tau/m}}{R_0^{\text{input}}}. \quad (2.74)$$

This expression becomes invalid in the physically uninteresting regime where $\sqrt{\hbar^2\tau/m} \approx R_0^{\text{input}}$. For all other cases, it provides a method to correct the Trotter approximation, in a way which is consistent with the universal Efimov theory for three particles (*cf.* Figs. 2.6 and 2.7, where the correction in Eq. 2.74 is already taken into account). Furthermore, Eq. 2.74 can be used also to determine the value of R_0 in a dilute many-body system (see Section 4.1).

2.3 Ultracold atoms with strong interactions

After the theoretical prediction of the Efimov effect, four decades passed before its first experimental signatures were observed [8]. This observation was achieved with ultracold atomic systems, where the Feshbach-resonance technique provides an extreme control of the interaction strength and allows to reach the unitary regime (see Section 2.3.1). Following the first observation, several results were obtained in connection with few-body Efimov physics. Not only trimers of identical bosons were identified, but also four-body resonances and the Efimov effect for atomic mixtures. In most experiments, the central observable is the three-body recombination rate, the main contribution to losses of atoms from the confining potential, which has resonances corresponding to specific features of Efimov states (see Section 2.3.2).

While being useful to study few-body physics, three-body losses also constitute a severe obstacle towards the realization of a quantum-degenerate many-body state with unitary interactions. Both conditions (quantum degeneracy for a strongly-interacting

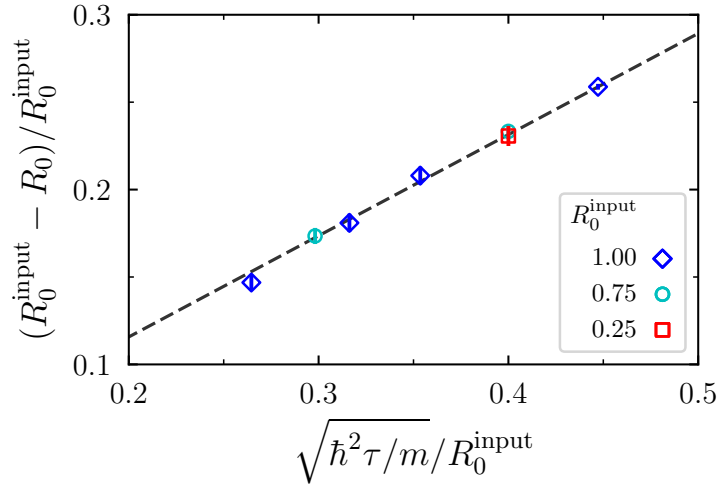


Figure 2.8: Discrepancy between R_0 and R_0^{input} , as a function of the dimensionless ratio $\sqrt{\hbar^2 \tau / m} / R_0^{\text{input}}$. Different symbols correspond to different choices of R_0^{input} (cf. legend, in arbitrary units), and all points are obtained in the low-temperature regime, $\beta|E_T| > 2.5$ (cf. Eq. 2.70). The black dashed line corresponds to the linear fit in Eq. 2.74.

system, and the unitary limit for interactions) have been independently obtained in experiments [33, 74, 75, 76, 77]. A single experiment has been realized at low temperature and with unitary interactions [78], but its interpretation has not yet reached a consensus (see Section 2.3.2.1).

2.3.1 Feshbach resonances

The square-well model potential has a set of resonances for the s-wave scattering length, taking place for specific combinations of its range and depth (see Fig. 2.1b). More generally, scattering resonances also exist for higher partial waves. Shape resonances take place when the centrifugal barrier (cf. Eq. 2.5) generates a quasibound state at short distance (see for instance Refs [79] and [80]). If the energy of the incoming pair of particle is close to the quasibound state, this induces a resonance, with an enhanced cross section. In this case, the control parameter is the collision energy.

Both these examples involve a single channel, and their control parameters (the range and depth of the potential, or the collision energy) are not easily tunable. Around a Feshbach resonance, in contrast, the scattering properties can be modified through a magnetic field, allowing to tune a across a wide interval [5]. This technique was first demonstrated with gases of Na and Rb atoms [81, 82], and it is the method of choice to produce strongly-interacting atomic clouds. The basic physics of a Feshbach resonance can be understood within a two-channels model. The atomic gas is prepared in a given hyperfine state, with the hyperspin quantum number resulting from the combination

of electronic and nuclear spins. The interparticle potential for atoms in this state defines an open channel, $V_{\text{open}}(r)$, for the low-energy scattering of two particles. Another potential $V_{\text{closed}}(r)$, for particles in a higher hyperfine state, defines the closed channel. This has a higher energy, and only its lowest bound states are accessible during a low-energy collision (see Fig. 2.9a). Due to the hyperfine coupling between the two channels, transitions between an open-channel scattering state and a closed-channel bound state are allowed. The two channels have different magnetic moments, due to their different

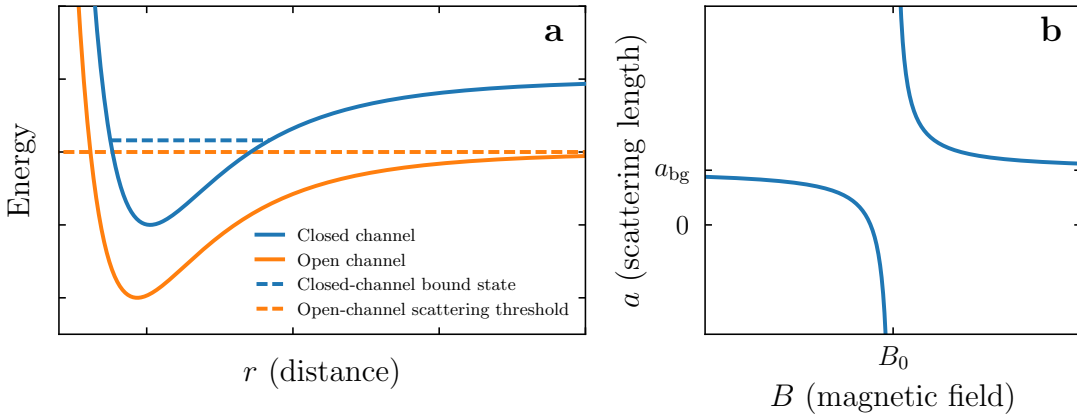


Figure 2.9: Panel **a**: Sketch of the open and closed interaction channels. The Feshbach resonance takes place when the closed-channel bound state corresponds to the open-channel scattering threshold. Panel **b**: Dependence of the scattering length on the magnetic field, *cf.* Eq. 2.75.

hyperspin state. Thus their energy difference can be tuned by means of the Zeeman shift induced by an external magnetic field. A Feshbach resonance takes place when the closed-channel bound state reaches the open-channel scattering threshold. In this case, the scattering length is drastically enhanced, due to the vanishing gap between these two states. For a magnetic field B close to the resonance value B_0 , an approximate expression for a reads

$$a(B) \approx a_{\text{bg}} \left(1 + \frac{\Delta}{B - B_0} \right), \quad (2.75)$$

where a_{bg} is the background scattering length and Δ characterizes the resonance width (*cf.* Fig. 2.9b). This provides a strong control on a , which can be tuned to both positive and negative large values, or even made close to zero

2.3.2 Signatures of the Efimov effect

In Section 2.2.1, we described Efimov theory in the unitary limit, and its infinite tower of scale-invariant states (*cf.* Eq. 2.60). This theory can be extended to the case of large, finite $|a|$, and the corresponding spectrum of Efimov states is represented in Fig. 2.10. In the

chosen coordinate system (that is, $\text{sign}(E)\sqrt{|E|}$ vs. $1/a$), the shallow dimer (*cf.* Eq. 2.19) corresponds to a straight line, forming an angle of $-\pi/4$ with the $1/a$ axis. When $|a| \rightarrow \infty$, the Efimov spectrum has an accumulation point at zero energy. For finite $|a|$, in contrast, there exist only a finite number of trimers (assuming that the Thomas collapse is not present, *cf.* Section 2.2.2). At negative a , the n -th trimer state disappears when $a = a_n^-$, where its energy reaches the threshold for a system of three unbound atoms. At positive a , the trimer becomes unstable at scattering length a_n^+ , where it dissociates into a dimer and a single atom.

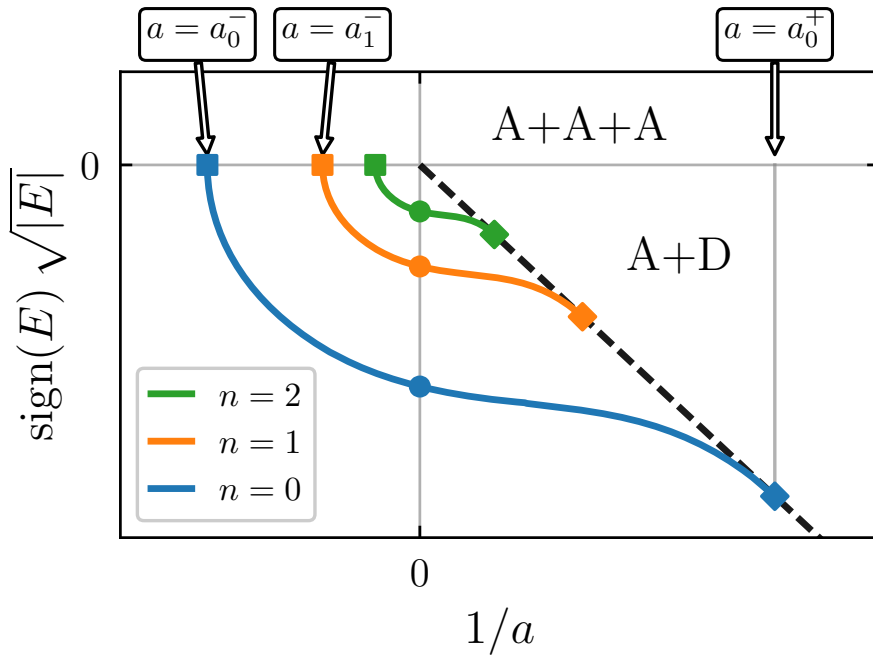


Figure 2.10: Energy spectrum for three identical bosons. For positive energy (“A+A+A” region), the three particles are unbound, while for $a > 0$ they form a dimer+atom system (“A+D” region, with the *black dashed line* corresponding to the dimer energy). Thick solid lines mark the energy of the first three trimer states, which touch the zero-energy threshold at negative scattering lengths a_n^- (*squares*). For positive scattering length a_n^+ (*diamonds*), the n -th trimer state disappears through the atom-dimer threshold. This figure is based on the parametrization of the Efimov spectrum from Ref. [10], and it has been deformed to make the first three states clearly visible.

In the universal regime, which is always reached for highly-excited trimer states, the Efimov spectrum in Fig. 2.10 has a geometric scale invariance which is also valid at finite scattering length (*cf.* the scale invariance at $|a| = \infty$, Eq. 2.60). This does not imply that the ratio between the binding energies of two subsequent trimers is constant and equal to ≈ 515 , which is only true in the unitary limit (*cf.* for instance the energies for $n = 0$ and $n = 1$ states at $a \lesssim a_1^-$, in Fig. 2.10). Nevertheless, the values of a_n^- and a_n^+

satisfy the universal scaling relation

$$a_{n_2}^\pm = \left(e^{-\pi/s_0} \right)^{n_2 - n_1} \times a_{n_1}^\pm, \quad (2.76)$$

This corresponds to the fact that a_n^- and a_n^+ are proportional to the inverse binding momentum of the n -th Efimov trimer, with prefactors which do not depend on n [10].

The number of Efimov states which can be identified in a single experiment is limited by several factors. Excited trimers have a large spatial extension and small binding energy, which require a large sample and a very low temperature. Even the observation of the first excited state requires exceptional experimental conditions, with a weak trapping potential and temperatures as low as $T \approx 10$ nK [83]. Moreover, the Efimov spectrum is universal only for binding energies smaller than $\hbar^2/(mr_0^2)$, where r_0 is the range of two-body interactions. In practice, the simultaneous identification of more than two trimer states has not been achieved with systems of identical bosonic atoms.

The three-body recombination rate represents the central observable for experiments aimed at identifying Efimov states. When a three-body recombination event (or three-body loss) takes place, two atoms bind into a dimer state, and the third carries away the released momentum and energy. The dimer state can be a deep molecular state, with large binding energy, or a shallow universal dimer, for large and positive scattering length. This process generally causes the loss of all three particles from the confining trap, and thus represents an instability mechanism for an ultracold atomic gas. The strength of three-body losses is characterized by the rate L_3 , defined through

$$\frac{\dot{N}}{N} = -L_3 \langle \rho^2 \rangle, \quad (2.77)$$

where N is the number of atoms in the system, \dot{N} is its time derivative, and $\langle \rho^2 \rangle$ is the mean square density (averaged over the density profile). Far from Feshbach resonances, the three-body loss rate is small, being for instance equal to $L_3 \simeq 4 \times 10^{-29}$ cm 6 s $^{-1}$ for non-condensed ^{87}Rb [84]. This corresponds to a decay rate below 1/minute, for a trap-center density lower than 5×10^{13} cm $^{-3}$ [45]. For large scattering length, however, L_3 is greatly enhanced, and this is a severe obstacle towards a realization of the quantum-degenerate, unitary Bose gas (*cf.* Section 2.3.2.1).

At low temperature and close to a Feshbach resonance, the three-body recombination rate can be factorized as [85, 86, 10]

$$L_3 = \frac{\hbar a^4}{m} f_\eta(\kappa_* a), \quad (2.78)$$

where f_η is a periodic function of $s_0 \log(\kappa_* a)$, κ_* is the binding momentum of a given Efimov trimer, and η is related to the lifetime of the Efimov trimer (a typical value for alkali atoms is $\eta \approx 0.1$ [9]). Considering negative scattering length and starting from vanishing $|a|$, f_η resonantly increases each time that a is equal to a_n^- , that is, each time

that a new Efimov trimer exists (*cf.* Fig. 2.10). The observation of these resonances in L_3 (and of the analogous features for positive a) provided the first unambiguous signature of the existence of Efimov states, obtained in 2006 with a gas of Cs atoms [8]. More recent experiments with ^7Li , ^{39}K and ^{133}Cs [87, 88, 83] allowed to identify features corresponding to two trimer states, and the resulting estimates for the scaling factor were partially consistent with the universal value, $\exp(\pi/s_0) \simeq 22.7$. Following these original observations, the experimental and theoretical study of Efimov physics greatly increased (see Ref. [89] for a review). A notable example is the study of heteronuclear mixtures, where the scaling factor can be much smaller than its value of 22.7 for identical bosons. For a Fermi-Bose mixture of ^6Li and ^{133}Cs this scaling factor is ≈ 5 , which allowed the simultaneous observation of three consecutive Efimov resonances [90].

As described in Section 2.2, the universal properties of Efimov trimers depend on an additional three-body length scale. In our model, this is represented by the hyperradial cutoff R_0 , while an alternative choice is the experimentally observable value of a_0^- . This length scale depends on all the details of the microscopic interactions which are not simply encoded in the scattering length. For an open-channel dominated Feshbach resonance, the only relevant length scale of the two-body interaction is the van der Waals length l_{vdW} (*cf.* Eq. 2.13), so that it is interesting to study its connection with the three-body parameter [89]. A surprising discovery is that the ratio $|a_0^-| / l_{\text{vdW}}$ has very small fluctuations: For a total of ten different Feshbach resonances in systems of ^7Li , ^{85}Rb , ^{133}Cs , and ^{39}K , this ratio takes values in the interval 8–10 [91]. Several theoretical studies addressed this universal property [92, 93, 94, 95], and also the more complex study of a_0^+ [96]. In Refs [92] and [94], it has been proposed that the universality of $|a_0^-| / l_{\text{vdW}}$ follows from a strong effective repulsion for hyperradii of the order of l_{vdW} , which suppresses the importance of short-range non-universal features. This barrier takes place at⁵ $R \approx 2.6 \times l_{\text{vdW}}$, which can be used to map our theoretical value of R_0 onto the van der Waals length.

To conclude this brief account of Efimov physics, we note that $N = 3$ is special, and that no Efimov effect exists for more than three identical particles [97]. For the case of $N = 4$, it has been predicted that two tetramer bound states are tied to each Efimov trimer [98, 99]. As for the $N = 3$ case, the experimental observation of these four-body states was based on resonance features in the recombination rate [100]. The extension to $N > 4$ is connected with the existence of a many-body Efimov liquid [71, 12], as discussed in Section 4.2,

2.3.2.1 Stability of the unitary Bose gas

The three-body recombination rate in Eq. 2.78 increases as a^4 , implying that this mechanical instability would prevent the experimental observation of the unitary Bose

⁵The definitions of the hyperradius in Refs [92] and [94] differ from each other, and from Eq. 2.51 (see footnote 1 in Ref. [94]).

gas, where $|a| \rightarrow \infty$. At finite temperature, however, a saturation of L_3 takes place when $|a| \approx \lambda_{\text{th}}$, setting an upper bound for the recombination rate. The corresponding expression at unitarity reads [74]

$$L_3 \simeq \frac{\hbar^5}{m} 36\sqrt{3}\pi^2 \frac{1 - e^{-4\eta}}{(k_B T)^2}. \quad (2.79)$$

The T^{-2} scaling of L_3 has been accurately measured in experiments with Li and Cs atoms, for temperatures spanning two orders of magnitude [74, 76].

The realization of a degenerate unitary gas would simultaneously require $\rho|a|^3$ and $\rho\lambda_{\text{th}}^3$ to be large, which could be achieved by two experimental paths, depending on which limit is taken first [101, 9]. In both cases, L_3 would diverge in the limit of large $|a|$ and λ_{th} (*cf.* Eqs. 2.78 and 2.79). A way out of this unphysical prediction consists in the conjecture that the only relevant length scale in this regime is set by the density, so that an alternative expression for L_3 should be used. Several steps have already been taken towards a degenerate unitary Bose gas, by partially relaxing one of its two defining conditions (large $|a|$ and λ_{th}). In the degenerate non-unitary regime, beyond-mean-field features [32] have been experimentally identified by measuring the equation of state [33] and Tan's contact parameter [102]. In a non-degenerate regime, several experiments reached unitary interactions, with measurements centered on the three-body recombination rate [74, 75, 76] or on the two- and three-body contact parameters [77].

A single experiment has addressed the low-temperature, unitary regime, by starting from a weakly-interacting Bose-Einstein condensate of Rb atoms and quickly ramping up the interaction strength [78]. A lifetime of the order of $600 \mu\text{s}$ is observed, long enough for the momentum distribution $n(\mathbf{k})$ to equilibrate, at least at large k . Measurements at different densities suggest a universal behavior, depending only on the interparticle distance. Consensus on the interpretation of this experiment has not been reached, especially concerning the effect of the fast ramp on the final temperature. On one side, it has been suggested that the experiment is in a degenerate state, with a universal dependence on the density, and that the observed momentum distributions is well fitted by the zero-temperature Efimovian prediction [62]. On the other side, the same curve has been fitted by high-temperature expansions, assuming that only local equilibrium is reached, and suggesting that the system is not degenerate [103, 63]. In Section 4.4, we provide more details about some theoretical descriptions of the degenerate unitary Bose gas, and compare our results to the experimental curve of Ref. [78].

In all aforementioned experiments, the atomic cloud is confined through a harmonic trap. The study of strongly-interacting Bose gases might benefit also from the recent advances in the use of homogeneous-box confinement [27]. Because of the uniform density profile, this set-up avoids the problem of having three-body recombination events taking place preferentially at the trap center, thus mitigating the effect of losses.

Conclusion

In this chapter, we have described the physical properties of two or three strongly-interacting bosons. For $N = 2$, the exact density-matrix is known for unitary, zero-range interactions. This allows to derive analytical approximate expressions for the key correlation functions, $g^{(1)}(\mathbf{r})$ and $g^{(2)}(\mathbf{r})$, which show the peculiar features for this kind of interactions. Their validity, in the high-temperature limit, has been verified through the QMC method.

For $N = 3$, we studied the Efimov trimers obtained within the three-body-cutoff model. Through QMC simulations for the ground-state trimer, we confirmed that the hyperradial distribution function agrees with the universal theory, for hyperradii larger than R_0 . This is also true for the momentum distribution of the ground-state trimer, for momenta approximately smaller than $1/R_0$. For the QMC calculations, the trimer binding momentum is extracted from the numerical data, so that no fitting parameter enters the results for $P(R)$ or $n(\mathbf{k})$.

CHAPTER 3

Path-Integral quantum Monte Carlo

In this chapter we discuss the quantum Monte Carlo (QMC) algorithm which is at the basis of the results shown in Chapters 2 and 4, for strongly-interacting bosonic systems. We start with Monte Carlo sampling (Section 3.1), which also applies to the study of classical systems (*cf.* Chapter 5), and then focus on the path-integral QMC approach (see Section 3.2). For particles interacting through a zero-range unitary potential, we introduce a novel algorithm which constitutes the optimal solution for the two-body problem, and can be generalized to many-body simulations (*cf.* Section 3.2.2.3). In Section 3.3 we describe the main observables which can be measured, with a stress on their relevance for bosonic systems. We conclude with Section 3.4, where two practical aspects of QMC simulations are discussed.

3.1 Monte Carlo sampling

Given a probability distribution $p(x)$ for x in a configuration space X , the task of statistical sampling (or Monte Carlo sampling) consists in choosing a sequence of samples $x_1, x_2, \dots \in X$ in such a way that their observed probability corresponds to $p(x)$ in the limit of a large number of samples. This allows to estimate properties of $p(x)$ which might not be accessible analytically, the simplest example being the average of a function of x (*cf.* Eqs. 3.1 and 3.2). For a selected class of probability distributions, direct-sampling algorithms are available (*cf.* Section 3.1.1), that is, algorithms which can sample the target distribution without approximations. Most distribution can however not be sampled directly, and one must to resort to Markov-chain Monte Carlo methods (MCMC) [104, 105, 39], typically based on the Metropolis algorithm (*cf.* Section 3.1.2). This algorithm starts with a given configuration x and produces a new sample x' which

is correlated with x . By repeating this operation, the sequence x_1, x_2, \dots is constructed, with elements which are distributed according to $p(x)$, in the limit of an infinite sequence.

Monte Carlo sampling has a direct application the study of a physical system in thermodynamic equilibrium, at an inverse temperature $\beta = 1/(k_B T)$. Each possible configuration of the system is assigned a statistical weight which depends only on its energy E_x , and is proportional to its Boltzmann weight $e^{-\beta E_x}$. Thus the average value of any static observable $O(x)$ (like the energy, or an n -points correlation function) is defined as

$$\langle O \rangle = \frac{\sum_x O(x) p(x)}{Z} \quad (3.1)$$

where $Z \equiv \sum_x p(x)$ is the partition function of the system, and where the sum has to be replaced by an integral for systems with continuous degrees of freedom. The connection with Monte Carlo sampling results from the fact that an average observable can be estimated through the law of large numbers,

$$\langle O \rangle = \lim_{t \rightarrow \infty} O_t \equiv \lim_{t \rightarrow \infty} \left(\frac{1}{t} \sum_{t=1}^t O(x_t) \right) \quad (3.2)$$

where x_1, \dots, x_t are samples drawn from $p(x)$ and O_t is the average over a finite number t of samples. It is essential that the partition function Z does not enter the estimator in Eq. 3.2, as this quantity is not directly accessible, in general. The choice of the sampling algorithm does not affect the validity of Eq. 3.2, but it affects the interpretation of O_t when the number of samples t is finite, which is always the case in a practical application. A large part of the research in the Monte Carlo field consists in designing algorithms with a fast convergence of O_t to $\langle O \rangle$.

3.1.1 Direct sampling

Direct-sampling algorithms generate independent samples from a given probability distribution. This basic feature has to be confronted with other methods (notably Markov-chain Monte Carlo, *cf.* Section 3.1.2), which rather produce correlated samples. Naive direct-sampling algorithms can be designed for a broad class of problems, but they often become unpractical in several relevant cases, a typical example being the case of physical systems with a large number of microscopic constituents.

In this work, we make use of several direct-sampling techniques, embedded inside more general Markov-chain schemes. For simple distributions, standard methods as a change of variable (*cf.* Section 3.1.1.1), rejection sampling (*cf.* Section 3.1.1.2), and tower sampling (*cf.* Section 3.1.1.3) are available. The Lévy reconstruction of a quantum path (*cf.* Section 3.2.2.1) is a direct-sampling algorithm to generate the discrete path of intermediate points connecting two given endpoints. Also the quantum paths of two particles interacting via a unitary zero-range potential can be sampled directly, through the novel algorithm described in Section 3.2.2.3.

3.1.1.1 Change of variable

The simplest direct sampling reduces the problem to the task of sampling a simpler probability distribution, for which direct sampling is already available. We consider a probability distribution $p(x)$ for $x \in \mathbb{R}$, and assume that the indefinite integral

$$f(x) = \int dx p(x) \quad (3.3)$$

is known, and its inverse function f^{-1} can be obtained explicitly. A concrete example is an exponential distribution,

$$p(x) = \begin{cases} \frac{1}{\xi} \exp\left(-\frac{x}{\xi}\right) & \text{if } x \geq 0 \\ 0 & \text{else} \end{cases}, \quad (3.4)$$

where $\xi > 0$ is a constant parameter. In this case, the integral in Eq. 3.3 is $f(x) = -\exp(-x/\xi)$, and its inverse is $f^{-1}(z) = -\xi \log(-z)$. Through the change of variable $z = f(x)$, we can write

$$\int_{\mathbb{R}} dx p(x) = \int_{f(0)}^{f(\infty)} dz = \int_{-1}^0 dz = \int_{\mathbb{R}} dz q(z) \quad (3.5)$$

where we have introduced $q(z)$, the uniform distribution

$$q(z) = \begin{cases} 1 & \text{if } -1 \leq z < 0 \\ 0 & \text{else} \end{cases}. \quad (3.6)$$

Therefore, a sample x^* from $p(x)$ can be obtained by drawing a sample z^* from $q(z)$ and using the inverse transformation $x^* = f^{-1}(z^*)$. Assuming that $q(z)$ can be sampled directly, this scheme constitutes a direct-sampling algorithm for $p(x)$. The generalization to more complex choices of $p(x)$ (for instance a higher-dimensional distribution) relies on the possibility of computing $\int dx p(x)$.

3.1.1.2 Rejection sampling

The rejection-sampling algorithm [106] also allows to samples $p(x)$ directly. Its first step is to choose an auxiliary distribution, $p'(x)$, such that

$$p'(x) \geq p(x) \quad \forall x, \quad (3.7)$$

where neither $p(x)$ nor $p'(x)$ need to be normalized. The distribution $p'(x)$ is chosen such that it can be sampled directly. Then $p(x)$ can be sampled as follows:

1. Draw a sample x^* from $p'(x)$.

2. Draw a uniform random number η between 0 and 1.
3. If $\eta \leq p(x^*)/p'(x^*)$, accept x^* , otherwise restart from step 1.

The average rejection rate in step 3 is given by

$$1 - \int dx \left(\frac{p'(x)}{\int dy p'(y)} \right) \frac{p(x)}{p'(x)} = \frac{\int dx [p'(x) - p(x)]}{\int dx p'(x)} \leq 1, \quad (3.8)$$

which is strictly larger than 0 (apart from the trivial case of $p'(x) = p(x)$). The value of this rate determines the practical applicability of rejection-sampling to a specific case. The strategy to optimize this algorithm is to construct the upper bound $p'(x)$ that minimizes $p'(x) - p(x)$ (cf. Fig. 3.1). In Section 3.2.2.3, we describe an application of rejection-sampling to the two-body density matrix of unitary quantum particles, and explain how $p'(x)$ is chosen.

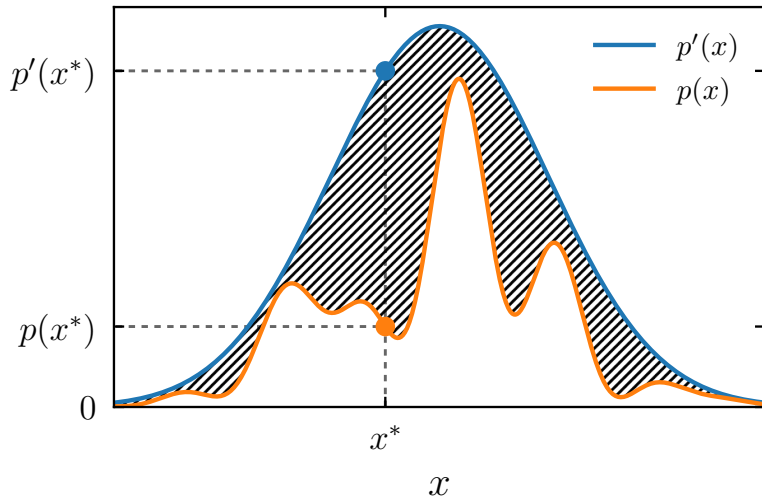


Figure 3.1: Rejection-sampling scheme, in which a Gaussian upper bound $p'(x)$ is used for the target distribution $p(x)$. The hatched area marks the difference between the two curves.

3.1.1.3 Tower sampling

While rejection sampling can be easily adapted to a probability distribution over a discrete configuration space, tower sampling represents an improved, rejection-free, method for this case. The probabilities $\{p_i\}_{i=1,\dots,M}$ are given, and we assume that the partition function $Z = \sum_{i=1}^M p_i$ is known. Then a sample can be drawn with the following scheme [39]:

1. Draw a sample η from the uniform distribution between 0 and Z .

2. Construct the cumulative distribution $c_j = \sum_{i=1}^j p_i$, for $j = 1, \dots, M$.
3. Find the value of j such that $c_j \leq \eta < c_{j+1}$.

This value of j represents a sample from the distribution $\{p_i\}$. For large M , the most computationally expensive part is the last step, namely the search of the value of j for a given η . The naive algorithm (sequentially checking whether $c_j \leq \eta < c_{j+1}$, for all $j = 1, 2, \dots$) requires a number of operations which scales linearly with M , while this scaling is reduced to $\log_2 M$ by using the bisection-search method [39]. More efficient methods are available for the case in which several samples have to be drawn from a given distribution: At the price of an initialization of the order of M operations, Walker's algorithm [107] allows to draw a sample in a fixed number of operation, independent on M .

3.1.2 Markov-chain Monte Carlo

The direct-sampling methods described above allow to obtain a sequence of statistically independent samples. In this section, in contrast, we present the Markov-chain Monte Carlo (MCMC) algorithm, which produces correlated samples. While this is a disadvantage with respect to direct sampling, MCMC algorithms have a much broader applicability. Here, we describe the case of a Markov chain with states in a discrete space X , and which evolves in discrete time steps. The main idea is to consider the required sequence of samples as the trajectory of a random walk of t steps in the configuration space: $x_1, \dots, x_t \in X$. Starting from a given initial state x_1 , all other states are constructed via a sequential stochastic method: Any new state x_{i+1} (for $i > 1$) is randomly sampled from a distribution which depends on the previous state x_i . The fact that x_{i+1} does not depend on the entire history x_1, \dots, x_i is a defining property of a Markov chain. The formal definition of this random walk consists in choosing its transition matrix, \mathcal{T}_{yx} . This is the probability to pass from a configuration x to a configuration y in one step, that is, the conditional probability for $x_{i+1} = y$ under the constraint that $x_i = x$. This leads to a distribution $p_i(x)$ for the i -th state being equal to x , which in general evolves with the Monte Carlo time step i : The probability that the $(i+1)$ -th sample is equal to x reads

$$p_{i+1}(x) = p_i(x) + \sum_{y \in X} p_i(y) \mathcal{T}_{xy} - p_i(x) \sum_{y \in X} \mathcal{T}_{yx}. \quad (3.9)$$

A MCMC algorithm is defined through its transition matrix. Given a set of conditions for \mathcal{T}_{yx} (namely irreducibility, aperiodicity, and stationarity, see below), the distribution $p_t(x)$ converges to the target distribution $p(x)$ which we want to sample, in the large- t limit [108]. The first condition is the irreducibility of the transition matrix: For any pair of states $x, y \in X$, there exists a positive integer t_0 such that $(\mathcal{T}^{t_0})_{x,y} > 0$, where \mathcal{T}^{t_0} is the t_0 -th power of the matrix with elements \mathcal{T}_{yx} . This condition guarantees that there does not exist a partition of the configuration space into subsets such that the

probability of passing from one to another subset is zero. The second condition is aperiodicity. For an irreducible Markov chain, this consists in the following statement: For any pair of states $x, y \in X$, there exists a positive integer t_0 such that $(\mathcal{T}^t)_{x,y} > 0$ for any $t > t_0$. An obvious violation of this condition would be a chain with an oscillatory behavior, such that $x_t \in X_1 \subset X$ for t odd and $x_t \in X \setminus X_1$ for t even. The third condition concerns the existence of a stationary distribution $peq(x)$ for \mathcal{T}_{yx} , that is, a distribution which is invariant under time evolution:

$$peq(x) = \sum_{y \in X} peq(y) \mathcal{T}_{xy}, \quad (3.10)$$

for all $x \in X$. Eq. 3.10 is known as the global-balance condition, and it corresponds to setting $p_{i+1}(x) = p_i(x) = peq(x)$ in Eq. 3.9. The three conditions mentioned here (irreducibility, aperiodicity and global balance) guarantee that the Markov-chain has a unique stationary distribution [108]. In a typical application of Markov-chain Monte Carlo algorithm, the stationary distribution has to correspond to a given target distribution, determined by the problem under study. In this case, one has to replace $peq(x)$ in Eq. 3.10 (or in Eq. 3.11 below) with the known target distribution $p(x)$. The global-balance condition corresponds to the fact that the net balance of probability flow on a single configuration x (that is, the difference between the incoming and outgoing probability fluxes) is equal to zero. A stricter condition consists in requiring that the net balance of probability flow between any two states x and y is equal to zero. This is the detailed-balance condition,

$$peq(y) \mathcal{T}_{xy} = peq(x) \mathcal{T}_{yx}, \quad (3.11)$$

which clearly implies Eq. 3.10, since one property of \mathcal{T} is that $\sum_y \mathcal{T}_{yx} = 1$. All the algorithms presented in this work satisfy this more strict condition.

The aforementioned criteria on the transition matrix are necessary for the convergence of the Markov-chain Monte Carlo algorithm, but they leave a large freedom in the choice of a valid transition matrix. Among the possible constructions, the Metropolis algorithm [109, 110] stands out as the most frequently used. We start by splitting the evolution during one time step in two parts: The proposal of a new state, and its acceptance or rejection. This corresponds to factorizing \mathcal{T}_{yx} into two parts:

$$\mathcal{T}_{yx} = \mathcal{A}_{x \rightarrow y} \times p_{\text{acc}}^{x \rightarrow y}. \quad (3.12)$$

The first term ($\mathcal{A}_{x \rightarrow y}$) is the a-priori probability for proposing y as the state at time $t + 1$, provided that the state at time t is x . This needs to be a distribution from which y can be obtained via a direct-sampling algorithm. The second factor ($p_{\text{acc}}^{x \rightarrow y}$) represents the acceptance probability: The new proposed state is accepted with probability $p_{\text{acc}}^{x \rightarrow y}$, while with probability $1 - p_{\text{acc}}^{x \rightarrow y}$ the move is rejected and the new state is equal to the previous state. In the Metropolis algorithm, the acceptance probability is chosen as

$$p_{\text{acc}}^{x \rightarrow y} = \min \left(1, \frac{p(y) \mathcal{A}_{y \rightarrow x}}{p(x) \mathcal{A}_{x \rightarrow y}} \right), \quad (3.13)$$

which satisfies the detailed-balance condition in Eq. 3.11, with $p_{eq}(x) = p(x)$. When the a-priori probability is symmetric ($\mathcal{A}_{y \rightarrow x} = \mathcal{A}_{x \rightarrow y}$), the acceptance probability takes the simpler form

$$p_{\text{acc}}^{x \rightarrow y} = \min \left(1, \frac{p(y)}{p(x)} \right). \quad (3.14)$$

The Metropolis acceptance probability in Eq. 3.13 highlights one of the ideas behind the factorization in Eq. 3.12: If we had a direct-sampling algorithm for the target distribution p , we could set $\mathcal{A}_{x \rightarrow y} = p(y)$, and make the acceptance probability in Eq. 3.13 equal to one. The presence of a finite rejection probability, in contrast, reflects the fact that we are generally not able to sample directly from p .

Any Monte Carlo algorithm (either direct-sampling or MCMC) produces a sequence of samples $\{x_1, \dots, x_t\}$ which gives access to the following estimator for the average value of an observable O :

$$O_t = \frac{1}{t} \sum_{i=1}^t O(x_i). \quad (3.15)$$

In the $t \rightarrow \infty$ limit, the standard deviation $\sigma_{\text{MC}}(t)$ of O_t (measured for instance through several independent realizations of the sequence x_1, \dots, x_t) decays to zero, while O_t converges to $\langle O \rangle$ (cf. Eq. 3.1). If the samples $\{x_1, \dots, x_t\}$ are statistically independent (which is the case if they are produced via a direct sampling algorithm), the standard deviation of O_t is equal to

$$\sigma_{\text{MC}}(t) = \sigma_{\text{MC}}^{\text{indept}}(t) = \sqrt{\frac{\langle O^2 \rangle - \langle O \rangle^2}{t}}. \quad (3.16)$$

Eq. 3.16 follows from the central limit theorem [39], and $\sigma_{\text{MC}}(t)$ provides a confidence interval to be assigned to the average-value estimator in Eq. 3.15¹. In contrast, Eq. 3.16 does not hold if the samples are statistically correlated, which is generally true when they are obtained through a MCMC algorithm. Several methods are available to estimate $\sigma_{\text{MC}}(t)$ in this case (see for instance Ref. [104]), including those based on integrated autocorrelation time, binning analysis, and bootstrap/jackknife techniques [111]. Apart from providing a confidence interval for O_t , $\sigma_{\text{MC}}(t)$ is also used to measure the efficiency of a given Monte Carlo algorithm, through the ratio

$$\frac{\sigma_{\text{MC}}^{\text{indept}}(t)}{\sigma_{\text{MC}}(t)}. \quad (3.17)$$

This quantity is equal to one (its maximum value) for statistically independent data, while it is smaller than one for correlated samples. A quantity directly related to the ratio in Eq. 3.17 is the autocorrelation function at equilibrium. In a MCMC algorithm, the

¹The $\sigma_{\text{MC}}(t)$ confidence interval only includes statistical fluctuations, and not systematic errors. In a MCMC simulation, for instance, the value of O_t at small t is biased by the choice of the initial configuration. However, when considering large values of t this bias becomes smaller than the statistical fluctuations of O_t .

statistical correlation between the values of an observable O at two time steps differing by a time lag $dt \ll t$ reads

$$C_O(dt) = \frac{\frac{1}{t-dt} \sum_{i=1}^{t-dt} O(x_{i+dt})O(x_i) - \left(\frac{1}{t-dt} \sum_{i=1}^{t-dt} O(x_i) \right)^2}{\frac{1}{t-dt} \sum_{i=1}^{t-dt} O^2(x_i) - \left(\frac{1}{t-dt} \sum_{i=1}^{t-dt} O(x_i) \right)^2}, \quad (3.18)$$

where t should be large enough that the Markov chain has reached its asymptotic stationary distribution. $C_O(dt)$ is equal to one for $dt = 0$ and decays to zero at large dt . The standard deviation $\sigma_{\text{MC}}(t)$ for a sequence of correlated samples is related to $C_O(dt)$ through

$$\sigma_{\text{MC}}(t) = \sigma_{\text{MC}}^{\text{indept}}(t) \times \sqrt{1 + 2 \sum_{dt>0} C_O(dt)}. \quad (3.19)$$

This leads to the definition of the integrated autocorrelation time for O ,

$$\tau_{\text{int}} = 1 + 2 \sum_{dt>0} C_O(dt), \quad (3.20)$$

which corresponds to the dt time scale over which the values of $O(x_i)$ and $O(x_{i+dt})$ are significantly correlated. If $C_O(dt)$ takes a simple exponential form $\exp(-dt/\tau^*)$, and if $\tau^* \gg 1$, we have

$$\tau_{\text{int}} = 1 + 2 \sum_{dt>0} e^{-dt/\tau^*} \simeq 1 + 2 \int_1^\infty dt e^{-dt/\tau^*} \simeq 2\tau^*. \quad (3.21)$$

This makes the correspondence evident between τ_{int} and the time scale for the decay of correlations.

Due to its simplicity and generality, the Metropolis algorithm represents the workhorse for a vast range of applications, in several scientific fields. One of the practical limiting factors is the presence of large correlations between subsequent samples, which sets a limit for the size of the problems for which accurate calculations are feasible. In physical application, this reflects into a limit on the maximum number of constituents that can be included in the system, which may represent a severe issue in the study of critical phenomena [104]. Several extensions of the Metropolis algorithm, either general or model-specific, have been proposed, to mitigate this problem. Among others, a class of irreversible algorithms (not satisfying the detailed-balance condition) have recently been shown to provide an efficiency gain for classical particle systems [112, 113, 114, 115] and spin models [116, 117].

3.1.3 Variable-dimensionality sampling

In Section 3.2, we describe how a quantum system can be mapped onto a classical representation and treated with a MCMC algorithm. A key feature of the sampling algorithm

employed in that case is that it draws samples from an extended configuration space (*cf.* Section 3.2.1). This space is partitioned into two sectors, and configurations in different sectors have a different number of degrees of freedom. The general MCMC scheme described in Section 3.1.2 can be applied also to this case, as described in this section. The resulting algorithm allows to estimate the ratio between the partition functions corresponding to the two sectors, which is a key observable (*cf.* Section 3.3.3). There exist several other applications of MCMC sampling in an extended space:

- The diagrammatic Monte Carlo technique consists in sampling from the sequence of terms which arise when a physical property is expressed through a series expansion. The main example is the Feynman-diagram expansion for observables of a quantum system [118, 119], where diagrams corresponding to different orders are associated with different numbers of variables.
- The Monte Carlo method of Ref. [120] aims at measuring Rényi entropies in a quantum many-body system. This is achieved by simulating two replicas of the same system, and computing the Rényi entropy through the ratio between two partition functions: The ordinary partition function of the two independent replicas, and an ad hoc partition function for the joint system in the presence of additional couplings.
- In the field of Bayesian inference, a similar algorithm is named reversible-jump Markov-chain Monte Carlo [121, 122]. Among its first applications, there has been the task of sampling from a mixture of different probability distributions, defined on spaces with different dimensionalities [123].

In this section we describe a general example from the class of variable-dimension algorithms. We consider a sequence of probability distributions p_n defined on \mathbb{R}^n . The integral of p_n over \mathbb{R}^n is denoted by Z_n , and it may differ from one (which is the relevant case for statistical-physics applications with unknown partition functions). The dimension-changing algorithm samples configurations contributing to the extended partition function,

$$Z_{\text{tot}} \equiv \sum_{n=0}^{\infty} Z_n = p_0 + \sum_{n=1}^{\infty} \int dx_1 \dots dx_n p_n(x_1, \dots, x_n), \quad (3.22)$$

where Z_n should decrease fast enough for large n , so that Z_{tot} is finite. MC moves between two configurations with the same n are constructed in the same way as in usual MCMC algorithms (*cf.* Section 3.1.2), while the sector-changing moves have some specific features. We consider moves between sectors n and $n+1$, and denote configurations in these two sectors with $\mathbf{x} \in \mathbb{R}^n$ and $\mathbf{y} \in \mathbb{R}^{n+1}$. The detailed-balance condition for a $n \leftrightarrow (n+1)$ move reads

$$p_n(\mathbf{x}) \mathcal{A}_{n \rightarrow n+1}(\mathbf{x}, \mathbf{y}) p_{\text{acc}}^{n \rightarrow n+1}(\mathbf{x}, \mathbf{y}) = p_{n+1}(\mathbf{y}) \mathcal{A}_{n+1 \rightarrow n}(\mathbf{x}, \mathbf{y}) p_{\text{acc}}^{n+1 \rightarrow n}(\mathbf{x}, \mathbf{y}), \quad (3.23)$$

where $\mathcal{A}_{n \rightarrow n+1}(\mathbf{x}, \mathbf{y})$ and $\mathcal{A}_{n+1 \rightarrow n}(\mathbf{x}, \mathbf{y})$ are normalized probability distributions for \mathbf{y} and \mathbf{x} , respectively. The condition in Eq. 3.23 is automatically satisfied if $p_{\text{acc}}^{n \rightarrow n+1}$ and $p_{\text{acc}}^{n+1 \rightarrow n}$ are chosen according to the Metropolis rule:

$$p_{\text{acc}}^{n \rightarrow n+1}(\mathbf{x}, \mathbf{y}) = \min \left[1, \frac{p_{n+1}(\mathbf{y}) \mathcal{A}_{n+1 \rightarrow n}(\mathbf{x}, \mathbf{y})}{p_n(\mathbf{x}) \mathcal{A}_{n \rightarrow n+1}(\mathbf{x}, \mathbf{y})} \right], \quad (3.24)$$

$$p_{\text{acc}}^{n+1 \rightarrow n}(\mathbf{x}, \mathbf{y}) = \min \left[1, \frac{p_n(\mathbf{x}) \mathcal{A}_{n \rightarrow n+1}(\mathbf{x}, \mathbf{y})}{p_{n+1}(\mathbf{y}) \mathcal{A}_{n+1 \rightarrow n}(\mathbf{x}, \mathbf{y})} \right]. \quad (3.25)$$

When proposing a move from $\mathbf{x} \in \mathbb{R}^n$ to $\mathbf{y} \in \mathbb{R}^{n+1}$, the a-priori probability $\mathcal{A}_{n \rightarrow n+1}(\mathbf{x}, \mathbf{y})$ also determines how to choose the $(n+1)$ -th coordinate of \mathbf{y} . A simple choice for the a-priori probabilities is to have them only acting on the last component of \mathbf{y} :

$$\begin{cases} \mathcal{A}_{n+1 \rightarrow n}(\mathbf{x}, \mathbf{y}) = [\prod_{i=1}^n \delta(x_i - y_i)], \\ \mathcal{A}_{n \rightarrow n+1}(\mathbf{x}, \mathbf{y}) = [\prod_{i=1}^n \delta(x_i - y_i)] \mathcal{A}_{\text{last}}(y_{n+1}), \end{cases} \quad (3.26)$$

with $\int dy_{n+1} \mathcal{A}_{\text{last}}(y_{n+1}) = 1$. In this case, the scheme for a $n \rightarrow n+1$ move consists in constructing \mathbf{y} (by setting $y_i = x_i$ for $i = 1, \dots, n$ and sampling y_{n+1} from $\mathcal{A}_{\text{last}}$), and accepting the move with probability $p_{\text{acc}}^{n \rightarrow n+1}(\mathbf{x}, \mathbf{y})$. The reverse move consists in setting $\mathbf{x} = \{y_i\}_{i=1, \dots, n}$ and accepting the move to \mathbf{x} with probability $p_{\text{acc}}^{n+1 \rightarrow n}(\mathbf{x}, \mathbf{y})$. If this $n+1 \rightarrow n$ move is accepted, no memory of y_{n+1} is conserved.

As a concrete example, we set

$$p_n(\mathbf{x}) = \frac{1}{(n+1)^3} \frac{1}{(2\pi\sigma^2)^{n/2}} \exp\left(-\frac{\mathbf{x}^2}{2\sigma^2}\right), \quad (3.27)$$

for $\mathbf{x} \in \mathbb{R}^n$ and $n \geq 0$. The corresponding partition functions read

$$Z_n = \frac{1}{(n+1)^3}. \quad (3.28)$$

By using the algorithm described in this section², we estimate the ratio Z_n/Z_0 through the ratio between the number of samples in the n -th and 0-th sectors. The results are in agreement with the expected analytic values (*cf.* Fig. 3.2).

3.2 Sampling quantum paths

The density-matrix approach to the thermodynamics of quantum particles has been introduced for non-interacting particles (*cf.* Section 1.3), and used to study two bosons

²A python implementation of this algorithm is available at https://github.com/tcompa/cross_dimensional_monte_carlo.

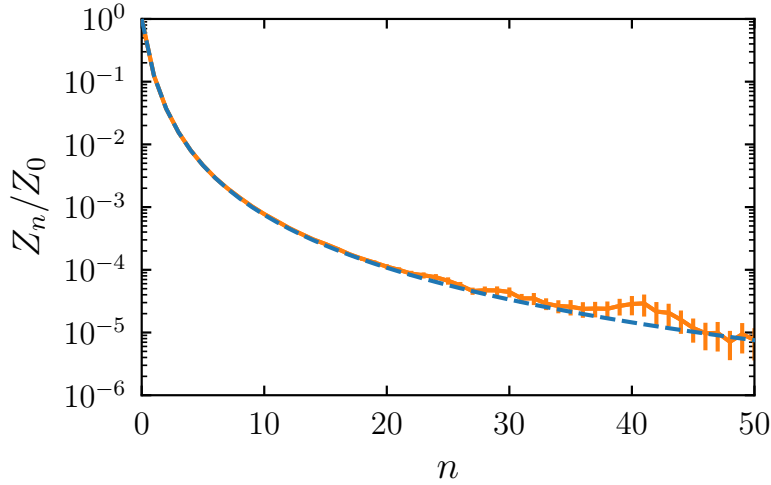


Figure 3.2: Statistical weight of the n -th sector for the extended probability distribution defined by Eq. 3.27, estimated via MC sampling (orange solid line, with error bars representing the standard error of the mean for 100 independent runs of 5×10^6 MC steps each). Full agreement is obtained with the analytical expression (dashed blue line, cf. Eq. 3.28).

interacting through a zero-range potential (cf. Section 2.1.2). To obtain results for non-trivial cases, this approach must be complemented with Monte Carlo algorithms. This is the case for most of the results shown in Chapter 2 (cf. Figs. 2.4 and 2.3) and Chapter 4. In view of the applications in Chapters 2 and 4 for quantum particles with unitary interactions, the current section includes a detailed description of our path integral Monte Carlo algorithm.

3.2.1 Path integrals and Monte Carlo

The density matrix ρ_N for N distinguishable particles and its generalization ρ_N^{bos} for N bosons have been introduced in Section 1.3. It is convenient to rewrite $\rho_N(\mathbf{X}, \mathbf{X}'; \beta)$ as a convolution of high-temperature density matrices $\rho_N(\mathbf{X}, \mathbf{X}'; \tau)$, where $\tau = \beta/S$ is the imaginary-time discretization and we are using the shorthands $\mathbf{X} = \{\mathbf{x}_1, \dots, \mathbf{x}_N\}$ and $\mathbf{X}' = \{\mathbf{x}'_1, \dots, \mathbf{x}'_N\}$. This rewriting is expressed as

$$\rho_N(\mathbf{X}, \mathbf{X}'; \beta) = \int d\mathbf{X}^1 \dots d\mathbf{X}^{S-1} [\rho_N(\mathbf{X}, \mathbf{X}^1; \tau) \rho_N(\mathbf{X}^1, \mathbf{X}^2; \tau) \dots \rho_N(\mathbf{X}^{S-1}, \mathbf{X}'; \tau)], \quad (3.29)$$

where \mathbf{X}^s corresponds to $\{\mathbf{x}_1^s, \dots, \mathbf{x}_N^s\}$, and $d\mathbf{X}$ is a shorthand for $d\mathbf{x}_1 \dots d\mathbf{x}_N$. A given value of $s = 0, \dots, S-1$ defines an imaginary-time slice, and the positions \mathbf{x}_i^s on each slice are named beads. Eq. 3.29 is exact, independently of interparticle interactions or

external potentials. The choice of S introduces a length scale

$$\lambda_s = \sqrt{\frac{2\pi\hbar^2\tau}{m}} = \sqrt{\frac{2\pi\hbar^2\beta}{mS}}, \quad (3.30)$$

which is the thermal wavelength corresponding to the inverse-temperature interval of a single slice. The decomposition in Eq. 3.29 does not affect the way in which the bosonic density matrix is constructed, as the average of $\rho_N(\mathbf{X}, P\mathbf{X}'; \beta)$ over all permutations P (*cf.* Eq. 1.27).

While the discretization in Eq. 3.29 is exact, it is introduced because it allows to devise useful approximation schemes. By increasing S , the interval $\tau = \beta/S$ can be made arbitrarily small. Thus the term $\rho_N(\mathbf{X}^s, \mathbf{X}^{s-1}; \tau)$ in Eq. 3.29 corresponds to the density matrix for a system of N particles at temperature $(k_B/\beta) \times S$, which can be made arbitrarily large. In this case, approximated expressions for ρ_N are available. The Trotter break-up [124] can be used for any Hamiltonian formed by a kinetic term and a general potential term $\tilde{V}(\mathbf{X})$, possibly including terms at any order (an external one-body potential, two-body interactions, three-body interactions, \dots). The approximation reads:

$$\rho_N(\mathbf{X}^s, \mathbf{X}^{s+1}; \tau) \simeq \exp\left(-\frac{\tau\tilde{V}(\mathbf{X}^s)}{2}\right) \left[\prod_{i=1}^N \rho_1(\mathbf{x}_i^s, \mathbf{x}_i^{s+1}; \tau) \right] \exp\left(-\frac{\tau\tilde{V}(\mathbf{X}^{s+1})}{2}\right) \quad (3.31)$$

The error in this approximation scales as τ^3 . An alternative approximation scheme is the pair-product approximation (PPA), relevant for the cases where the potential energy is the sum of two-body terms $V_2(\mathbf{x}_i - \mathbf{x}_j)$ for particles i and j [125, 11]. The single-slice thermal wavelength $\lambda_s \propto 1/\sqrt{S}$ can be made much smaller than the typical interparticle distance $\rho^{1/3}$, where $\rho = N/V$ is the density. If $\rho\lambda_s^3 \ll 1$, the probability of having three close-by particles (that is, in a region of volume λ_s^3) is strongly suppressed with respect to the probability of having two close-by particles. For this reason, it is sufficient to only consider two-body terms in ρ_N , which leads to the following approximated expression

$$\rho_N(\mathbf{X}^s, \mathbf{X}^{s+1}; \tau) \simeq \prod_{i=1}^N \rho_1(\mathbf{x}_i^s, \mathbf{x}_i^{s+1}; \tau) \prod_{j < i} g^{\text{rel}}(\mathbf{x}_i^s - \mathbf{x}_j^s, \mathbf{x}_i^{s+1} - \mathbf{x}_j^{s+1}; \tau). \quad (3.32)$$

This approximation is most useful when g^{rel} is known exactly, including the hard-sphere potential [126, 47] and the zero-range potential used in this work (*cf.* Section 2.1.2.1).

The QMC algorithm used in this thesis for the unitary-gas Hamiltonian (*cf.* Eq. 2.66) is based on a combination of Trotter and PPA approximations: The interparticle interactions are included via Eq. 3.32, while the Trotter break-up is used for the three-body cutoff. For a given imaginary-time discretization, we extract a τ -dependent effective value of R_0 from three-particle simulations, which correctly reproduces Efimov physics for small but finite τ (*cf.* Section 2.2.2). As shown in Section 4.1, this approach allows to reduce the number of necessary imaginary-time slices, compared to the plain use of the

Trotter break-up. Therefore, it reduces the difficulty of treating hard-core interactions within this approximation, which in other works required to replace the three-body cutoff with a soft repulsive potential [72].

Independently of the choice for the approximation scheme used, we can write the N -body bosonic partition function as the integral of the corresponding density matrix:

$$Z_{\text{closed}} = \int d\mathbf{X} \rho_N^{\text{bos}}(\mathbf{X}, \mathbf{X}; \beta). \quad (3.33)$$

For bosons, this can be directly interpreted as the integral of a non-normalized probability distribution, where $\rho_N^{\text{bos}}(\mathbf{X}, \mathbf{X}; \beta)$ is the statistical weight of the configuration \mathbf{X} . For a general N -fermions system, in contrast, the integrand can take negative values, as a consequence of anticommutation relations. This greatly complicates the use of QMC, often requiring additional approximations. The integral in Eq. 3.33 only includes closed paths. To extract information about off-diagonal properties as the one-body-reduced density matrix (*cf.* Section 3.3.3), we introduce a second partition function,

$$Z_{\text{open}} = \frac{1}{\xi_0^3} \int d\mathbf{r} \int d\mathbf{X} \rho_N^{\text{bos}}(\{\mathbf{x}_1 + \mathbf{r}, \mathbf{x}_2, \dots, \mathbf{x}_N\}, \{\mathbf{x}_1, \mathbf{x}_2, \dots, \mathbf{x}_N\}; \beta), \quad (3.34)$$

which includes one open path. Also the integrand of Z_{open} can be interpreted as a statistical weight, but in this case the configuration is given by $(N + 1)$ vectors: The N positions $\mathbf{x}_1, \dots, \mathbf{x}_N$ and the relative vector \mathbf{r} between the two ends of the open path. This also justifies the presence of the prefactor ξ_0^{-3} in Eq. 3.34 (where ξ_0 has the units of a length), to make Z_{open} dimensionless. The QMC algorithm described below is based on an extended partition function,

$$Z_{\text{tot}} = Z_{\text{closed}} + Z_{\text{open}}, \quad (3.35)$$

which includes both open and closed path-integral configurations. The relative weights of the closed and open sectors are $Z_{\text{closed}}/Z_{\text{tot}}$ and $Z_{\text{open}}/Z_{\text{tot}}$, and they can be modified by tuning ξ_0 , which is a free parameter of the QMC algorithm. Physical observables do not depend on the choice of ξ_0 , but this value enters in the Monte Carlo moves that change sector – *cf.* Section 3.2.4.

The path-integral formulation needs to be modified when the system consists of N particles in a cubic box with periodic boundary conditions (PBC). In this case, the first and last bead of a closed path (which can be formed by one or more bosons) have to be periodic images of each other, but not necessarily coincide. As an example, if $\mathbf{x}_j^0, \dots, \mathbf{x}_j^S$ is the path of particle j , then \mathbf{x}_j^0 and \mathbf{x}_j^S can differ by $L\mathbf{w}$, where L is the linear size of the box. The vector $\mathbf{w} \in \mathbb{Z}^3$ is the winding-number vector of the path, as it counts the number of times that the paths winds around the periodic box, in each one of the three directions. For one particle in a periodic box, the density matrix $\rho_1(\mathbf{x}, \mathbf{x}'; \beta)$ reads [39]

$$\rho_1^{\text{PBC}}(\mathbf{x}, \mathbf{x}'; \beta) = \sum_{\mathbf{w} \in \mathbb{Z}^3} \rho_1(\mathbf{x}, \mathbf{x}' + L\mathbf{w}; \beta). \quad (3.36)$$

When $L \gg \lambda_{\text{th}}$ (that is, at high temperature), all terms with non-zero \mathbf{w} in the right-hand side of Eq. 3.36 are exponentially suppressed, so that $\rho_1^{\text{PBC}}(\mathbf{x}, \mathbf{x}'; \beta) \simeq \rho_1(\mathbf{x}, \mathbf{x}'; \beta)$. This is the case when we consider a single imaginary-time slice, corresponding to a thermal wavelength λ_s much smaller than L (cf. Eq. 3.30). For this reason, we do not need to explicitly use ρ_1^{PBC} in the partition functions with discretized imaginary time (cf. Eqs. 3.37 and 3.38 below).

The QMC scheme described in this chapter and used in this thesis is local: All moves take place on a small imaginary-time interval, and a change of the winding number can only take place through a closing move (cf. Section 3.2.4). This choice is made in view of treating large systems of interacting particles. In other cases (for small N , or for non-interacting particles), the optimal choice would be to use QMC moves acting on a large imaginary-time slice.

Once the integrand of the partition function (in Eq. 3.33 or Eq. 3.34) is identified with the statistical weight of a configuration (\mathbf{X} , for Z_{closed} , or $\{\mathbf{X}, \mathbf{r}\}$, for Z_{open}), the MC approach described in Section 3.1 can be used to sample a sequence of configurations distributed from this statistical weight. This gives access to several diagonal or off-diagonal observables (see Section 3.3). In a practical application, an approximate version of the statistical weight ρ_N^{bos} is used (like the Trotter break-up or the PPA), which requires the discretization of the imaginary-time interval $[0, \beta]$. Thus the actual problem for which a QMC algorithm is designed is the one defined by the closed-sector partition function

$$Z_{\text{closed}} = \int d\mathbf{X}^0 \dots d\mathbf{X}^{S-1} \prod_{s=0}^{S-1} \rho_N^{\text{bos}}(\mathbf{X}^s, \mathbf{X}^{s+1}; \tau), \quad (3.37)$$

where $\mathbf{X}^S \equiv \mathbf{X}^0$, and where $\rho_N^{\text{bos}}(\mathbf{X}^s, \mathbf{X}^{s+1}; \tau)$ is replaced by a suitable high-temperature approximation. The open-sector partition function takes an analogous form:

$$Z_{\text{open}} = \frac{1}{\xi_0^3} \int d\mathbf{r} \int d\mathbf{X}^0 \dots d\mathbf{X}^{S-1} \left\{ \left[\prod_{s=0}^{S-2} \rho_N^{\text{bos}}(\mathbf{X}^s, \mathbf{X}^{s+1}; \tau) \right] \times \rho_N^{\text{bos}} \left(\{\mathbf{x}_1^{S-1}, \mathbf{x}_2^{S-1}, \dots, \mathbf{x}_N^{S-1}\}, \{\mathbf{x}_1^0 + \mathbf{r}, \mathbf{x}_2^0, \dots, \mathbf{x}_N^0\}; \tau \right) \right\}. \quad (3.38)$$

As mentioned above, the periodic-box density matrix can be replaced with its free-space counterpart when it is evaluated on a small imaginary-time interval. The same reasoning allows to approximate ρ_N^{bos} with ρ_N , in the integrands of Eqs. 3.37 and 3.38, provided that the discretization interval is small enough (that is, $\lambda_s \rho^{1/3} \ll 1$).

Eqs. 3.37 and 3.38 can be interpreted as a classical partition function: Each bead corresponds to a classical three-dimensional particle, with the number of particles being NS for a closed configuration and $NS + 1$ for an open one. This mapping implies that similar MC techniques can be developed to treat the equilibrium thermodynamics of classical and quantum systems. The idea of sampling path-integral configurations through the Monte Carlo technique [127, 125, 128, 129, 130, 131, 23] has evolved

into the method of choice for the finite-temperature quantum many-body problem, at least for the case of bosons in more than one dimension [11, 119]. The study of low-temperature liquid ^4He is connected with many technical advances in the design of PIMC algorithms [130, 23, 11]. More recently, further developments of this method [47, 132, 133, 134, 135, 136, 137, 138] (see Ref. [119] for a review) have allowed high-precision comparisons with the results of experiments in ultracold-atomic systems, for two-dimensional [139, 140] and three-dimensional [33, 141] continuous systems and for optical-lattice set-ups [142, 143]. In particular, the use of the extended partition function Z_{tot} (*cf.* Eq. 3.35) in the context of path-integral QMC was originally proposed for lattice systems [133, 134], and it has later been generalized to the continuous-space case which we treat here [136, 137].

Following Section 3.1 (and in particular Section 3.1.3), a MC algorithm for the partition function Z_{tot} consists in a sequence of updates of the path-integral configuration (that is, a sequence of Monte Carlo moves). In each move, a new configuration is sampled from the a-priori distribution, and it is accepted or rejected according to the Metropolis rule (which depends on the statistical weights of the previous and new configurations). The proposed new configuration only partially differs from the previous one, to avoid extremely small acceptance probabilities. In a path-integral QMC simulation, we include several update schemes, aimed at modifying configuration in different ways. The QMC algorithm proceeds by iteratively proposing updates: At each step, moves are selected randomly, with fixed frequencies which are part of the algorithm free parameters. When the move cannot take place (e.g. an swap move cannot be proposed for a configuration in the closed sector, see Section 3.2.3.2), the loop continues as if the move had been rejected. Provided that all these moves satisfy the criteria discussed in Section 3.1, the resulting configurations are distributed according to their statistical weight (given by the integrands of Eq. 3.37 and Eq. 3.38), in the limit of large number of samples. In particular, all moves described below are designed so that they satisfy the detailed-balance condition. In some cases (open/close and advance/recede move pairs) this condition is only fulfilled through a pair of complementary moves.

In the following sections, we review the details of several standard QMC moves, and we describe the novel two-body direct-sampling move (*cf.* Section 3.2.2.3), which is introduced specifically for the unitary interaction used in this work. When not specified, QMC simulations for the unitary Bose gas (*cf.* Chapter 2 and Chapter 4) are based on the Lévy-reconstruction, two-body direct-sampling, advance/recede, swap, and open/close moves.

3.2.2 Closed-sector moves

3.2.2.1 Lévy reconstruction

The simplest move that we include is a Lévy reconstruction of a portion of a single path [144, 11, 39]. Given two fixed beads \mathbf{x}^{s_1} and \mathbf{x}^{s_2} at imaginary-time slices s_1 and

$s_2 = s_1 + \Delta_s$, this move samples the probability distribution for the positions of the $\Delta_s - 1$ intermediate beads, given by

$$p(\mathbf{x}^{s_1+1}, \dots, \mathbf{x}^{s_2-1}) \propto \prod_{s=s_1}^{s_2-1} \rho_1(\mathbf{x}^s, \mathbf{x}^{s+1}; \tau). \quad (3.39)$$

The intermediate beads are sampled sequentially. First, \mathbf{x}_{s_1+1} is sampled from

$$p(\mathbf{x}^{s_1+1}) \propto \rho_1(\mathbf{x}^{s_1}, \mathbf{x}^{s_1+1}; \tau) \rho_1(\mathbf{x}^{s_1+1}, \mathbf{x}^{s_2}; (\Delta_s - 1)\tau), \quad (3.40)$$

which is a Gaussian distribution for \mathbf{x}^{s_1+1} , with mean

$$\langle \mathbf{x}^{s_1+1} \rangle = \frac{\Delta_s - 1}{\Delta_s} \mathbf{x}^{s_1} + \frac{1}{\Delta_s} \mathbf{x}^{s_2}, \quad (3.41)$$

and variance

$$\langle (\mathbf{x}^{s_1+1})^2 \rangle - \langle \mathbf{x}^{s_1+1} \rangle^2 = \frac{\Delta_s - 1}{\Delta_s} \tau. \quad (3.42)$$

Given the sampled value of \mathbf{x}^{s_1+1} , the probability distribution of \mathbf{x}^{s_1+2} reads

$$p(\mathbf{x}^{s_1+2}) \propto \rho_1(\mathbf{x}^{s_1+1}, \mathbf{x}^{s_1+2}; \tau) \rho_1(\mathbf{x}^{s_1+2}, \mathbf{x}^{s_2}; (\Delta_s - 2)\tau), \quad (3.43)$$

which is also a Gaussian, so that \mathbf{x}^{s_1+2} can be readily sampled. The scheme continues in the same way, until the position \mathbf{x}^{s_2-1} of the last bead is sampled. Paths constructed in this way are distributed as in Eq. 3.39. This sampling scheme relies on the fact that the probability distributions for intermediate bead positions are Gaussian. The same is true when particles are confined through an external harmonic potential, so that the Lévy construction can be adapted to this case [39].

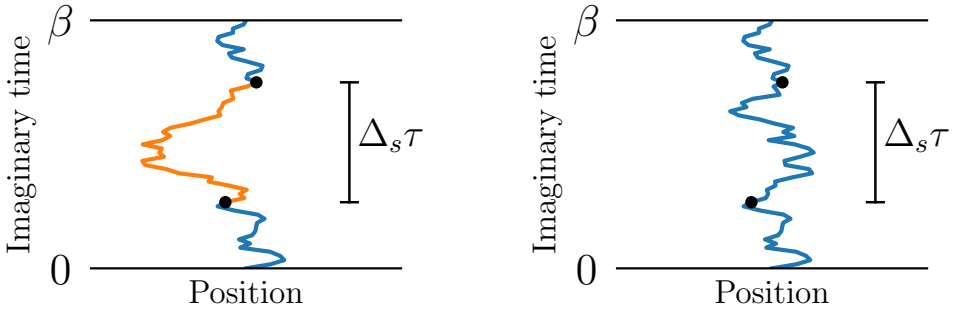


Figure 3.3: Lévy reconstruction of a portion of a single-particle path: Given two fixed endpoints, the intermediate beads (*orange path*, in the left panel) are sampled.

This move directly samples a single path. For a many-body non-interacting system, it is rejection-free. In the presence of interactions the Metropolis rule is used to accept

or reject the move, based on the statistical weights of the current and proposed configurations. While it can be naturally applied to any portion of a closed path (see Fig. 3.3), the Lévy-reconstruction move can also be used to modify an open configuration, provided that it only acts on a portion not including the two open ends. As it provides the direct-sampling solution for a single-particle path between two given endpoints, this sampling method is also an essential ingredient in all other QMC moves presented in this work.

3.2.2.2 Exchange move

Lévy reconstruction directly samples the single-particle density matrix, but it does not modify bosonic permutation cycles. This can be obtained through the exchange move, depicted in Fig. 3.4. We start by choosing two beads on a given imaginary-time slice s_1 : $\mathbf{x}_1^{s_1}$ and $\mathbf{x}_2^{s_1}$. This defines two path portions in the imaginary-time interval $[s_1, s_2]$, where $s_2 = s_1 + \Delta_s$ (*cf.* Fig. 3.4). The proposed move consists in exchanging the identity of the endpoints of these two paths, by connecting $\mathbf{x}_1^{s_1}$ with $\mathbf{x}_2^{s_2}$ and $\mathbf{x}_2^{s_1}$ with $\mathbf{x}_1^{s_2}$. The new connections, comprising $\Delta_s - 1$ intermediate beads each, are sampled through the Lévy construction. The acceptance probability for this exchange reads

$$p_{\text{acc}} = \min \left[1, \frac{\rho_1(\mathbf{x}_1^{s_1}, \mathbf{x}_2^{s_2}; \tau \Delta_s) \rho_1(\mathbf{x}_2^{s_1}, \mathbf{x}_1^{s_2}; \tau \Delta_s)}{\rho_1(\mathbf{x}_1^{s_1}, \mathbf{x}_1^{s_2}; \tau \Delta_s) \rho_1(\mathbf{x}_2^{s_1}, \mathbf{x}_2^{s_2}; \tau \Delta_s)} \frac{W_{\text{new}}}{W_{\text{old}}} \right], \quad (3.44)$$

where W_{old} and W_{new} are the contribution to the statistical weights of the old and new configurations given by two- and three-body interactions (*cf.* Section 3.2.1).

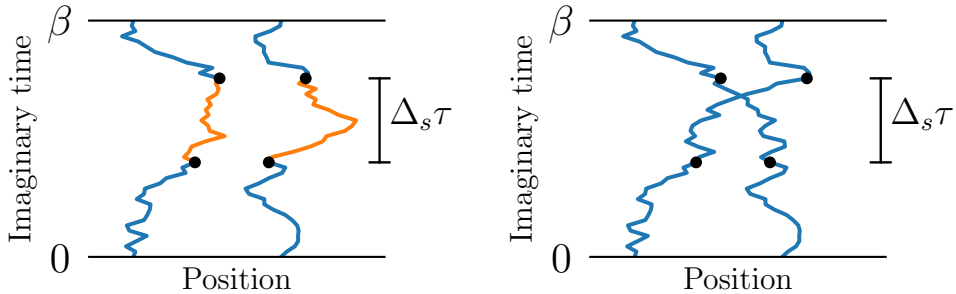


Figure 3.4: Exchange move for a diagonal two-particle configuration, modifying the structure of bosonic permutations.

This move is valid for an arbitrary pair of particles, but it has a very small acceptance probability when the distance between $\mathbf{x}_1^{s_1}$ and $\mathbf{x}_2^{s_1}$ is much larger than $\lambda_s \sqrt{\Delta_s}$. One way to avoid this problem is to restrict this move to close-by particles. Several criteria can be implemented, like setting a maximum-distance cutoff, or choosing $\mathbf{x}_2^{s_1}$ to be the bead closest to $\mathbf{x}_1^{s_1}$. Since the move does not change the starting points $\mathbf{x}_1^{s_1}$ and $\mathbf{x}_2^{s_1}$, it is simple

to design a symmetric a-priori probability based on one of these criteria, so that the simplified Metropolis acceptance probability in Eq. 3.14 can be used.

3.2.2.3 Direct-sampling two-body move

For a simulation restricted to the closed sector, the combination of Lévy reconstruction and exchange moves constitutes a valid QMC algorithm. However, this algorithm performs very poorly for the case of strong, short-ranged interactions. As described in Section 2.1.2.1, the probability distribution for a path-integral configuration diverges as $1/r^2$ whenever the distance r between two particles on the same slice goes to zero. In this situation, the configuration gains a very large statistical weight, and any MC update which would move the two particles away from each other has a small acceptance probability. We refer to this situation as pinning between the two particles. While the QMC algorithm is formally correct, the presence of pinned configurations dramatically increases the correlation time. Previous studies of bosonic or fermionic systems with zero-range interactions used ad-hoc Monte Carlo moves [12, 53, 54], in which the new distance between two particles on the same slice is sampled from an a-priori distribution proportional to $1/r^2$. In other cases, a two-body potential with small but finite range was used [59, 145, 146], at the cost of an additional extrapolation towards the zero-range limit. In this section we describe a novel QMC move which performs direct sampling of the two-body density matrix. This optimal algorithm for a system of two particles constitutes the building block of our many-body simulations (*cf.* Chapter 4).

We consider the paths of two particles, which have separation vectors $\mathbf{r}^{s_1} = \mathbf{x}_1^{s_1} - \mathbf{x}_2^{s_1}$ and $\mathbf{r}^{s_2} = \mathbf{x}_1^{s_2} - \mathbf{x}_2^{s_2}$ at imaginary-time slice s_1 and $s_2 = s_1 + \Delta_s$. As described in Section 2.1, the two-body problem can be separated into the center-of-mass and relative-motion independent problems. The center-of-mass part corresponds to the problem of a single particle with reduced mass equal to $2m$, for which the Lévy reconstruction algorithm is optimal, thus we concentrate on how to sample the relative-motion path.

For fixed \mathbf{r}_{s_1} and \mathbf{r}_{s_2} , our novel move reconstructs the path of intermediate relative vectors $\{\mathbf{r}^{s_1+1}, \dots, \mathbf{r}^{s_2-1}\}$ (see Fig. 3.5) through a direct-sampling algorithm for their probability distribution:

$$P_{\text{path}}(\mathbf{r}^{s_1+1}, \dots, \mathbf{r}^{s_2-1}) = \prod_{s=s_1}^{s_2-1} \rho_2^{\text{rel}}(\mathbf{r}^s, \mathbf{r}^{s+1}; \tau), \quad (3.45)$$

where ρ_2^{rel} is the two-body relative-motion density matrix (*cf.* Eqs. 2.29 and 2.35). The basic ingredient to sample a path from P_{path} is the ability to draw a sample \mathbf{r} from

$$P(\mathbf{r}|\mathbf{r}_a, \mathbf{r}_b, \tau_a, \tau_b) = \rho_2^{\text{rel}}(\mathbf{r}_a, \mathbf{r}; \tau_a) \rho_2^{\text{rel}}(\mathbf{r}, \mathbf{r}_b; \tau_b), \quad (3.46)$$

for given values of \mathbf{r}_a , \mathbf{r}_b , τ_a , and τ_b . The full path can then be sampled sequentially, as in the usual Lévy construction (*cf.* Section 3.2.2.1): First \mathbf{r}^{s_1+1} is drawn from

$$P(\mathbf{r}^{s_1+1}|\mathbf{r}^{s_1}, \mathbf{r}^{s_2}, \tau, (\Delta_s - 1)\tau), \quad (3.47)$$

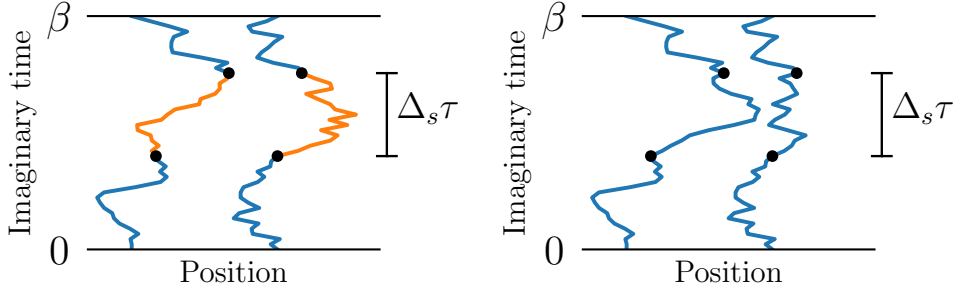


Figure 3.5: Scheme of the two-body direct-sampling move.

then \mathbf{r}^{s_1+2} is drawn from

$$P(\mathbf{r}^{s_1+2} | \mathbf{r}^{s_1+1}, \mathbf{r}^{s_2}, \tau, (\Delta_s - 2)\tau), \quad (3.48)$$

and so on until \mathbf{r}^{s_2-1} is sampled.

The distribution $P(\mathbf{r} | \mathbf{r}_a, \mathbf{r}_b, \tau_a, \tau_b)$ is conveniently rewritten as

$$P(\mathbf{r} | \mathbf{r}_a, \mathbf{r}_b, \tau_a, \tau_b) \propto \exp\left(-\frac{m(\mathbf{r} - \mathbf{r}^*)^2}{4\hbar^2\tau^*}\right) g^{\text{rel}}(\mathbf{r}_a, \mathbf{r}; \tau_a) g^{\text{rel}}(\mathbf{r}, \mathbf{r}_b; \tau_b), \quad (3.49)$$

where we have introduced

$$\mathbf{r}^* = \frac{\tau_b \mathbf{r}_a + \tau_a \mathbf{r}_b}{\tau_a + \tau_b}, \quad \tau^* = \frac{\tau_a \tau_b}{\tau_a + \tau_b}, \quad (3.50)$$

and neglected prefactors not depending on \mathbf{r} . To draw samples from the distribution in Eq. 3.49, we use rejection sampling (*cf.* Section 3.1.1.2). Given a distribution $Q(\mathbf{r})$ which can be sampled directly and such that $Q(\mathbf{r}) \geq P(\mathbf{r} | \mathbf{r}_a, \mathbf{r}_b, \tau_a, \tau_b)$, the scheme to draw a sample from $P(\mathbf{r} | \mathbf{r}_a, \mathbf{r}_b, \tau_a, \tau_b)$ is the following:

1. Draw a sample \mathbf{r} from $Q(\mathbf{r})$.
2. With probability $P(\mathbf{r} | \mathbf{r}_a, \mathbf{r}_b, \tau_a, \tau_b) / Q(\mathbf{r})$, accept the sample, otherwise go back to step 1.

We consider the expression for P in Eq. 3.49, for which we have

$$P(\mathbf{r} | \mathbf{r}_a, \mathbf{r}_b, \tau_a, \tau_b) \leq \exp\left(-\frac{m(\mathbf{r} - \mathbf{r}^*)^2}{4\hbar^2\tau^*}\right) \left[1 + \frac{2\tau_a\hbar^2}{mr\tau_a}\right] \left[1 + \frac{2\tau_b\hbar^2}{mr\tau_b}\right]. \quad (3.51)$$

The right-hand side of Eq. 3.51 is governed by two scalings: A divergent r^{-2} term close to the origin (core region), and an exponential decay for large distance from the origin (tail region). Thus we choose the following piecewise function (where $r = |\mathbf{r}|$):

$$Q(\mathbf{r}) = \begin{cases} K_{\text{core}} r^{-2} & \text{if } r \leq r_{\text{core}} \\ K_{\text{tail}} \exp\left(-\frac{m(\mathbf{r} - \mathbf{r}^*)^2}{4\hbar^2\tau^*}\right) & \text{if } r > r_{\text{core}} \end{cases}. \quad (3.52)$$

The prefactors,

$$K_{\text{core}} = \left(r_{\text{core}} + \frac{2\tau_a \hbar^2}{mr_a} \right) \left(r_{\text{core}} + \frac{2\tau_b \hbar^2}{mr_b} \right), \quad (3.53)$$

$$K_{\text{tail}} = \left(1 + \frac{2\tau_a \hbar^2}{mr_a r_{\text{core}}} \right) \left(1 + \frac{2\tau_b \hbar^2}{mr_b r_{\text{core}}} \right), \quad (3.54)$$

are chosen so that $P(\mathbf{r}|\mathbf{r}_a, \mathbf{r}_b, \tau_a, \tau_b) \leq Q(\mathbf{r})$. The value of r_{core} , which determines the boundary of the core and tail regions, is a free parameter of the algorithm, and this choice may affect the overall efficiency of this move. A typical choice is to set r_{core} equal to a small multiple of $\sqrt{\tau^* \hbar^2 / m}$, like $2\sqrt{\tau^* \hbar^2 / m}$. As part of the rejection-sampling scheme, we need to draw samples from the piecewise distribution $Q(\mathbf{r})$. This requires the computation of W_{core} and W_{tail} , the integrals of $Q(\mathbf{r})$ in the two regions, which gives

$$\frac{W_{\text{core}}}{K_{\text{core}}} = 4\pi r_{\text{core}}, \quad (3.55)$$

and

$$\frac{W_{\text{tail}}}{K_{\text{tail}}} = 4 \left(\frac{\pi \tau^* \hbar^2}{m} \right)^{3/2} \left\{ \operatorname{erfc}(x_-) + \operatorname{erfc}(x_+) + \frac{2}{r^*} \sqrt{\frac{\hbar^2 \tau^*}{\pi m}} \left[e^{-(x_-)^2} - e^{-(x_+)^2} \right] \right\}, \quad (3.56)$$

where $r^* = |\mathbf{r}^*|$, and $x_{\pm} \equiv (r_{\text{core}} \pm r^*) / (2\sqrt{\tau^* \hbar^2 / m})$. Given the weights W_{core} and W_{tail} , a fraction $W_{\text{core}} / (W_{\text{core}} + W_{\text{tail}})$ of samples are drawn in the core region, and the rest are drawn in the tail region. In the core region, we independently sample the direction of \mathbf{r} (by drawing three samples from a one-dimensional Gaussian distribution) and its radius (uniformly in the $[0, r_{\text{core}}]$ interval). In the tail region, we draw the vector \mathbf{r} from the distribution

$$\exp \left(-\frac{m(\mathbf{r} - \mathbf{r}^*)^2}{4\hbar^2 \tau^*} \right) \times \theta(|\mathbf{r}| - r_{\text{core}}), \quad (3.57)$$

which is done by iteratively drawing samples from the Gaussian part, until one of them has radius larger than r_{core} and is accepted. This concludes the description of how to draw one sample \mathbf{r} from the probability distribution in Eq. 3.49, which then leads to the sequential algorithm to sample a path $\{\mathbf{r}^{s_1+1}, \dots, \mathbf{r}^{s_2-1}\}$ from P_{path} (cf. Eq. 3.45 and subsequent paragraph).

This direct-sampling Monte Carlo move for the relative positions of a particle pair constructs a completely new path of intermediate relative vectors, rather than proposing a small modification to an existing one. For $N = 2$ particles, this algorithm defines a rejection-free random walk in configuration space (only an internal rejection rate is present, due to the use of rejection sampling). For $N \geq 3$, in contrast, the new configuration is accepted or rejected with the Metropolis rule. The interactions of the two

particles involved in this move is taken care of by the a-priori probability, so that it only interacts with the other $N - 2$ particles enter in the acceptance probability (*cf.* Eq. 3.13).

To verify the correctness of this move, we set up a closed-sector-only QMC simulation two bosons, which are restricted to be in a single permutation cycle. The probability distribution for the pair distance r is proportional to the average of $\rho_2^{\text{rel}}(\mathbf{r}, -\mathbf{r}; \beta)$ over the solid-angle (*cf.* Eqs. 2.29 and 2.35), which can be performed analytically. The perfect agreement of the QMC and analytic curves in Fig. 3.7 validates the two-body direct-sampling move.

With this novel move, the pinning problem is greatly reduced. As a relevant observable, we consider the fraction of distances smaller than a given threshold,

$$f = \frac{2}{N(N-1)} \sum_{i=1}^N \sum_{j=1}^{i-1} \theta(r_{\max} - r_{ij}), \quad (3.58)$$

where r_{ij} is the distance between particles i and j on a given slice, and θ is the Heaviside step function. We set a small distance threshold ($r_{\max} = \lambda_{\text{th}}/5$), as we are interested in whether the QMC algorithm is able to quickly modify the number of pinned particles. For several physical parameters, we perform QMC simulations of the Hamiltonian in Eq. 2.68 (that is, with zero-range unitary two-body potential and three-body hard-core cutoff), for N distinguishable particles, by using either the single-particle Lévy reconstruction move or the novel two-body move. We compute the autocorrelation function $C_f(dt)$ (*cf.* Eq. 3.18), which encodes the efficiency of the algorithm in producing decorrelated samples, with a faster decay representing a better algorithm. The advantage of the novel two-body move over the single-particle Lévy reconstruction is clear (see Fig. 3.6). Both moves display a rapid decay of $C_f(dt)$ from 1 to approximately 0.5 at small dt , while at larger time lag the Lévy reconstruction is significantly slower than the two-body move in decorrelating the observable f .

3.2.3 Open-sector moves

For path-integral configurations in the open sector, we modify the commonly used moves [136, 137], and adapt them so that they keep the number of particles fixed. The advance/recede move (*cf.* Section 3.2.3.1) is the open-sector equivalent of the Lévy reconstruction move described in Section 3.2.2.1, as it acts on a single-particle path. The swap move (*cf.* Section 3.2.3.2) provides a way to change the permutation-cycles structure. In the following, we denote by head and tail (or \mathbf{h} and \mathbf{t}) the two ends of the open path (see Fig. 3.8). The imaginary-time slice of these two beads is denoted by s_{cut} .

3.2.3.1 Advance/recede move

The basic way of modifying a path-integral configuration in the open sector is to act on the open path, without modifying the others. This path has two beads at imaginary-time

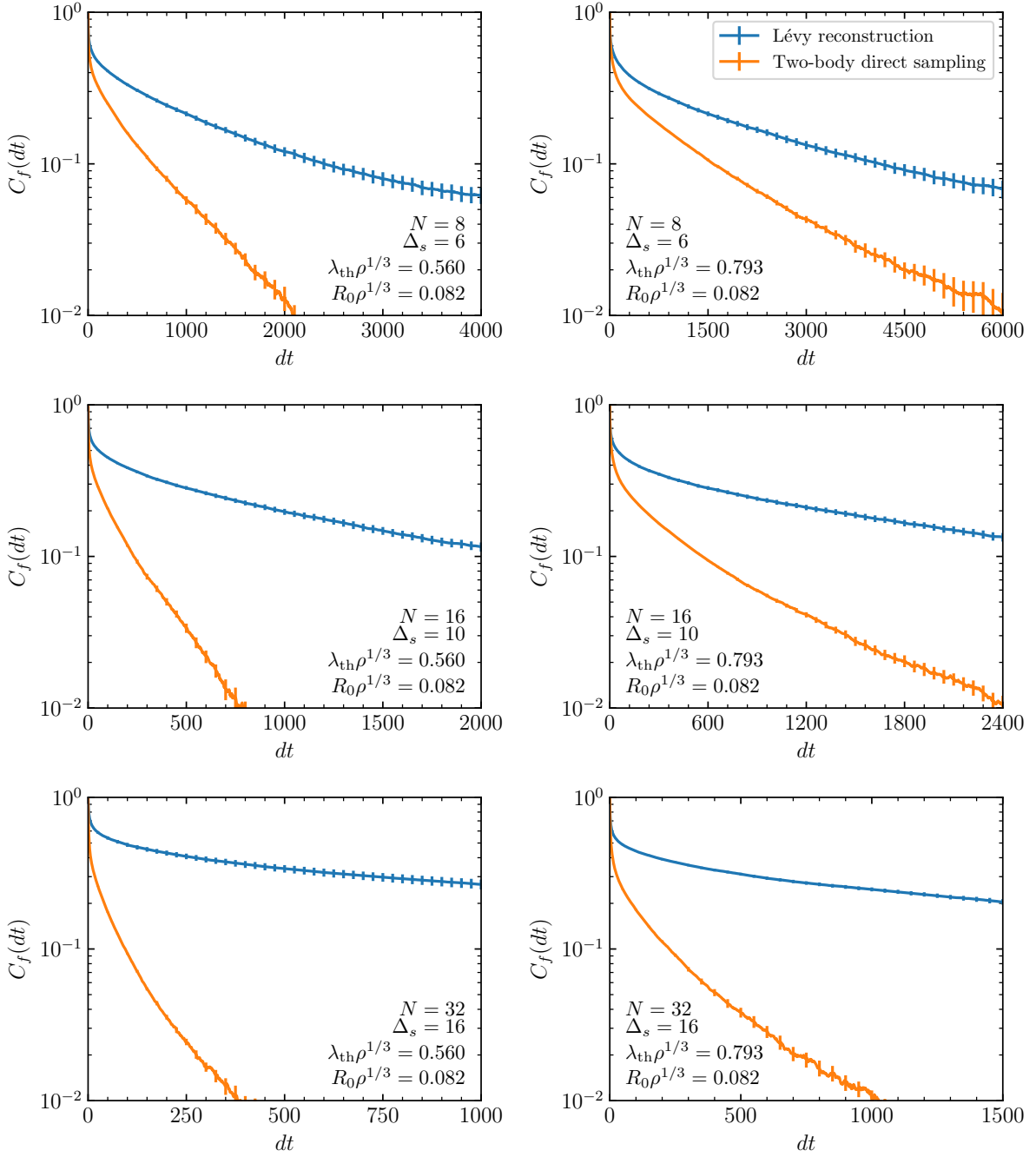


Figure 3.6: Autocorrelation function $C_f(dt)$ for the fraction f of distances smaller than $\lambda_{\text{th}}/5$. Simulations for distinguishable quantum particles (with different system size, temperature, and number of reconstructed slices Δ_s) are based on a single QMC move each: Either the Lévy reconstruction (blue line) or the two-body direct-sampling move (orange line). For all panels, $\lambda_s \rho^{1/3} \simeq 0.08$, and the time lag dt is in units of $N \times S$ proposed single-bead moves. The two-body direct-sampling move has a significantly faster decay of $C_f(dt)$.

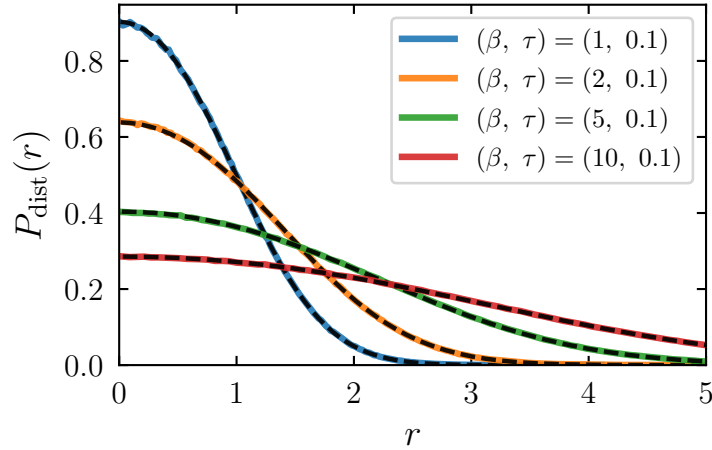


Figure 3.7: Normalized probability distribution for the pair distance r between two co-cyclical unitary bosons. QMC results obtained with the two-body direct-sampling move (solid lines, inverse temperature and imaginary-time interval reported in the legend, in units of m/\hbar^2) are in perfect agreement with the analytic expression (dashed black lines).

slice s_{cut} : The tail \mathbf{t} (connected to another bead on slice $s_{\text{cut}} + 1$), and the head \mathbf{h} (which follows a bead on slice $s_{\text{cut}} - 1$). In the advance move, the path ending in \mathbf{h} grows by Δ_s additional beads, determining a new head \mathbf{h}_{new} on the imaginary-time slice $s_{\text{cut}} + \Delta_s$. Moreover, the Δ_s beads following \mathbf{t} (included) are erased, so that the new tail is on the same slice as \mathbf{h}_{new} (cf. Fig. 3.8). The position of the new head \mathbf{h}_{new} is sampled from

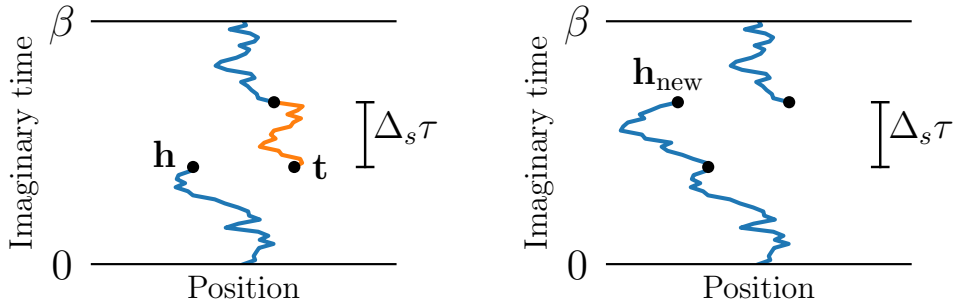


Figure 3.8: Advance move in a single-particle off-diagonal configuration.

$$P(\mathbf{h}_{\text{new}}) \propto \rho_1(\mathbf{h}, \mathbf{h}_{\text{new}}; \Delta_s \tau), \quad (3.59)$$

and a set of $\Delta_s - 1$ intermediate beads is obtained through the Lévy construction, with endpoints \mathbf{h} and \mathbf{h}_{new} .

The acceptance probability for this move is equal to one for a non-interacting system. In the presence of interactions, the statistical weight of old and new configurations is

computed, and the proposed update is accepted or rejected according to the Metropolis rule. The one described here is the canonical-ensemble version of the advance move, where the total number of beads remains fixed. If the number of beads changes, then the acceptance probability also depends on the chemical potential (*cf.* Eq. 2.20 in Ref. [137]). To satisfy the detailed-balance condition, we also introduce a complementary move (the recede move, where $s_{\text{cut}} \rightarrow s_{\text{cut}} - \Delta_s$), and choose one of the two moves with 50% probability.

The advance/recede moves also constitutes the basic move of the Reptation QMC technique [147], used to compute ground-state observables for a quantum system. For that algorithm, efficiency improves with the following modification: Instead of randomly choosing between the advance and recede moves, as many steps as possible are performed in the same direction, which is changed only when one of these steps is rejected [148]. This is a general approach for MC algorithms, known as lifting [149, 150], which could be added on top of our current QMC scheme.

3.2.3.2 Swap move

The swap move [136, 137] is a local move which modifies the structure of bosonic permutation cycles for path-integral configurations in the open sector. We first describe it in a simplified version, considering two non-interacting bosons, and discretizing the $[0, \beta]$ imaginary-time interval in two intervals of size $\tau = \beta/2$. The swap update allows to move between the two open configurations in Fig. 3.9, denoted with old (left panel) and new (right panel). Their statistical weights W_{old} and W_{new} are given by

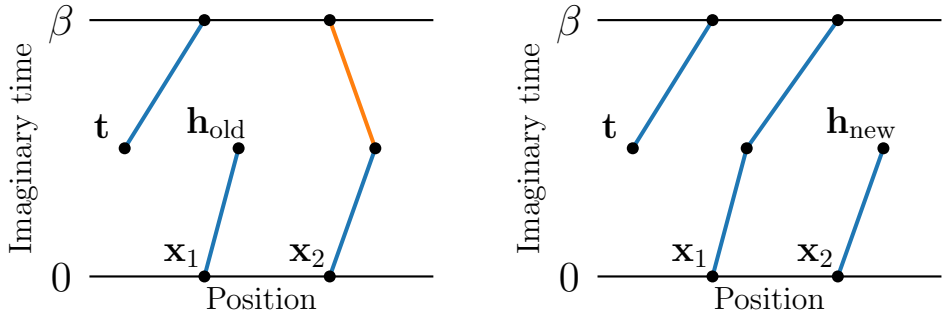


Figure 3.9: Old and new configurations for a swap move, in the case of two bosons with $S = 2$ imaginary-time slices.

$$W_{\text{old}} = \rho_1(\mathbf{h}_{\text{new}}, \mathbf{x}_2; \tau), \quad (3.60)$$

$$W_{\text{new}} = \rho_1(\mathbf{h}_{\text{old}}, \mathbf{x}_2; \tau), \quad (3.61)$$

up to common prefactors. The scheme of the swap move is the following:

1. We propose the move that connects \mathbf{h}_{old} to $\mathbf{x} \in \{\mathbf{x}_1, \mathbf{x}_2\}$, with a-priori probability

$$\mathcal{A}_{\text{old} \rightarrow \text{new}}(\mathbf{x}) = \frac{\rho_1(\mathbf{h}_{\text{old}}, \mathbf{x}; \tau)}{\sum_{i \in \{1,2\}} \rho_1(\mathbf{h}_{\text{old}}, \mathbf{x}_i; \tau)}. \quad (3.62)$$

2. We accept the move with probability

$$p_{\text{acc}}^{\text{old} \rightarrow \text{new}}(\mathbf{x}) = \begin{cases} 0 & \text{if } \mathbf{x} = \mathbf{x}_1, \\ \min \left[1, \frac{\sum_{i \in \{1,2\}} \rho_1(\mathbf{h}_{\text{old}}, \mathbf{x}_i; \tau)}{\sum_{i \in \{1,2\}} \rho_1(\mathbf{h}_{\text{new}}, \mathbf{x}_i; \tau)} \right] & \text{if } \mathbf{x} = \mathbf{x}_2. \end{cases} \quad (3.63)$$

3. If the move is accepted, the link between \mathbf{h}_{new} and \mathbf{x}_2 is erased, and a new connection is added between \mathbf{h}_{old} and \mathbf{x}_2 .

This move satisfies the detailed balance condition

$$W_{\text{old}} \mathcal{A}_{\text{old} \rightarrow \text{new}}(\mathbf{x}) p_{\text{acc}}^{\text{old} \rightarrow \text{new}}(\mathbf{x}) = W_{\text{new}} \mathcal{A}_{\text{new} \rightarrow \text{old}}(\mathbf{x}) p_{\text{acc}}^{\text{new} \rightarrow \text{old}}(\mathbf{x}), \quad (3.64)$$

for any $\mathbf{x} \in \{\mathbf{x}_1, \mathbf{x}_2\}$, where the definitions of $\mathcal{A}_{\text{new} \rightarrow \text{old}}(\mathbf{x})$ and $p_{\text{acc}}^{\text{new} \rightarrow \text{old}}(\mathbf{x})$ are analogous to the ones in Eqs. 3.62 and 3.63. It is often convenient to restrict this move to the case where \mathbf{h}_{old} and \mathbf{x}_2 are not too far apart, to avoid exceedingly small acceptance probabilities. This is implemented by setting $\mathcal{A}_{\text{old} \rightarrow \text{new}}(\mathbf{x})$ and $p_{\text{acc}}^{\text{old} \rightarrow \text{new}}(\mathbf{x})$ to zero when $|\mathbf{h}_{\text{old}} - \mathbf{x}|$ is larger than a given cutoff distance, and restricting the sum in the denominator of Eq. 3.62 accordingly.

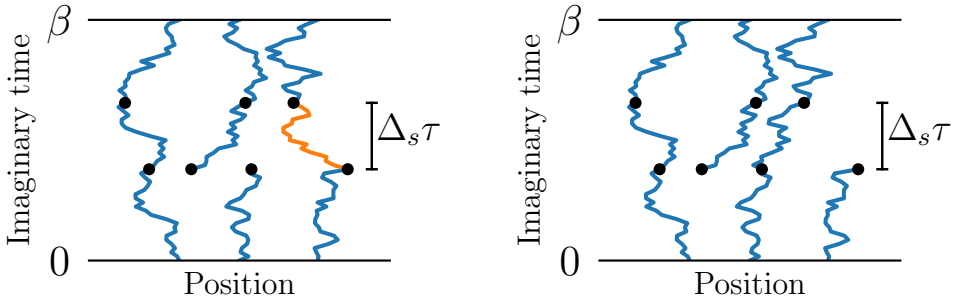


Figure 3.10: Swap move in a three-particle configuration, modifying the structure of bosonic permutations.

The actual swap move (see Fig. 3.10) differs from the simplified version in three ways: It takes place on several imaginary-time slices, it involves more than two particles, and it also includes the interaction part of the statistical weight. Here is the scheme of this move, in the version which includes a distance cutoff to avoid extremely low acceptance probabilities:

1. Given the slice s_{cut} where the head and tail of the open path are, we identify the set of all beads on slice $s_{\text{cut}} + \Delta_s$ which are at distance from \mathbf{h}_{old} smaller than a given cutoff. This set is denoted as $\mathcal{B} = \{\mathbf{b}_1, \mathbf{b}_2, \dots\}$.

2. We sample one element \mathbf{b}_j from \mathcal{B} , with probability

$$P(\mathbf{b}_j) = \frac{\rho_1(\mathbf{h}_{\text{old}}, \mathbf{b}_j; \Delta_s \tau)}{\sum_{\mathbf{b} \in \mathcal{B}} \rho_1(\mathbf{h}_{\text{old}}, \mathbf{b}; \Delta_s \tau)}, \quad (3.65)$$

which is performed via tower sampling (*cf.* Section 3.1.1.3).

3. Starting from \mathbf{b}_j , we follow the path backwards for Δ_s imaginary-time slices, to identify the bead \mathbf{h}_{new} (the head, in the proposed new configuration). We identify the set \mathcal{B}' of the beads on imaginary-time slice $s_{\text{cut}} + \Delta_s$ at distance from \mathbf{h}_{new} smaller than the chosen cutoff.
4. We finally construct the new configuration, by removing the links on the path portion connecting \mathbf{h}_{new} to \mathbf{b}_j , and by adding those between \mathbf{h}_{old} and \mathbf{b}_j (via the Lévy construction). We compute the interaction contributions $W_{\text{old}}^{\text{int}}$ and $W_{\text{new}}^{\text{int}}$ to the statistical weights of the old and new configuration, and set the acceptance probability for this move to [136, 137]

$$p_{\text{acc}} = \min \left[1, \frac{W_{\text{new}}^{\text{int}}}{W_{\text{old}}^{\text{int}}} \times \frac{\sum_{\mathbf{b} \in \mathcal{B}} \rho_1(\mathbf{h}_{\text{old}}, \mathbf{b}; \Delta_s \tau)}{\sum_{\mathbf{b} \in \mathcal{B}'} \rho_1(\mathbf{h}_{\text{new}}, \mathbf{b}; \Delta_s \tau)} \right], \quad (3.66)$$

with the additional constraint that p_{acc} is equal to zero if $|\mathbf{h}_{\text{new}} - \mathbf{b}_j|$ is larger than the chosen distance cutoff. This additional constraint is needed to guarantee that the move is always reversible.

The combination of the swap and advance/recede moves constitutes a complete algorithm for sampling configurations which contributes to the open-sector partition function, *cf.* Eq. 3.38.

3.2.4 Sector-changing moves

Here we describe the QMC moves between the open and closed sectors. Configurations in these two sectors include $3NS$ and $3N(S+1)$ spatial degrees of freedom, respectively. Thus the opening and closing moves are an example of the sampling scheme for subspaces of configurations with different dimensionality (see Section 3.1.3). We describe these QMC moves in three steps: For a single particle at high temperature, for a single particle at low temperature, and for N interacting particles.

We first consider the path corresponding to one quantum particle at inverse temperature β , confined in a large periodic cubic box of volume $V \gg \lambda_{\text{th}}^3$ (corresponding to the high-temperature limit). The statistical weights of open and closed configurations read

$$P_{\text{closed}}(\mathbf{x}^0, \dots, \mathbf{x}^{S-1}) = \left[\prod_{s=0}^{S-2} \rho_1(\mathbf{x}^s, \mathbf{x}^{s+1}; \tau) \right] \rho_1(\mathbf{x}^{S-1}, \mathbf{x}^0; \tau), \quad (3.67)$$

$$P_{\text{open}}(\mathbf{x}^0, \dots, \mathbf{x}^S) = \left[\prod_{s=0}^{S-2} \rho_1(\mathbf{x}^s, \mathbf{x}^{s+1}; \tau) \right] \rho_1(\mathbf{x}^{S-1}, \mathbf{x}^S; \tau) \frac{1}{\xi_0^3}, \quad (3.68)$$

where S is the total number of imaginary-time slices³, and the head and tail of the open path are on the imaginary-time slice S . The length scale ξ_0 is a free parameter of the algorithm, corresponding to the choice of a relative factor between the Z_{open} and Z_{closed} (cf. Eq. 3.34 and Section 3.2.1). We choose

$$\xi_0 = \sqrt{\frac{2\pi\hbar^2\Delta_s\tau}{m}}, \quad (3.69)$$

where Δ_s is the number of imaginary-time slices over which the closing and opening moves take place.

For the opening and closing moves, we choose an intermediate slice $s_1 = S - \Delta_s$, and we propose a new configuration which differs from the old one only on imaginary-time slices $s_1 + 1, \dots, S$ (cf. Fig. 3.11). As a-priori probabilities, we choose

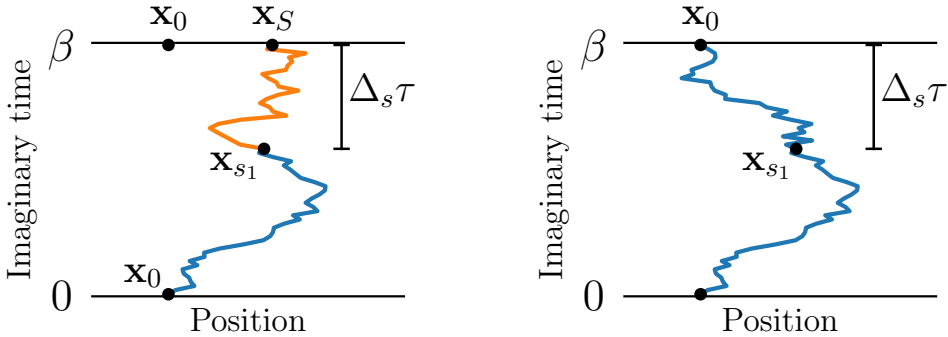


Figure 3.11: Scheme of the closing move for a single-particle path, passing from an off-diagonal configuration (*left panel*) to a diagonal one (*right panel*). The linear size L of the box (not shown) is much larger than λ_{th} .

$$\mathcal{A}_{\text{open} \rightarrow \text{closed}}(\mathbf{x}^{s_1+1}, \dots, \mathbf{x}^S) = \left[\prod_{s=s_1}^{S-2} \rho_1(\mathbf{x}^s, \mathbf{x}^{s+1}; \tau) \right] \rho_1(\mathbf{x}^{S-1}, \mathbf{x}^0; \tau) \left(\frac{2\pi\hbar^2\Delta_s\tau}{m} \right)^{3/2}, \quad (3.70)$$

$$\mathcal{A}_{\text{closed} \rightarrow \text{open}}(\mathbf{x}^{s_1+1}, \dots, \mathbf{x}^S) = \left[\prod_{s=s_1}^{S-1} \rho_1(\mathbf{x}^s, \mathbf{x}^{s+1}; \tau) \right] \rho_1(\mathbf{x}^{S-1}, \mathbf{x}^S; \tau). \quad (3.71)$$

³The imaginary-time discretization is used in view of the generalization to the N -body case, even though it would not be necessary for $N = 1$.

so that the acceptance probabilities

$$p_{\text{acc}}^{\text{open} \rightarrow \text{closed}} = \min \left[1, \frac{P_{\text{closed}}(\mathbf{x}^0, \dots, \mathbf{x}^{S-1}) \mathcal{A}_{\text{closed} \rightarrow \text{open}}(\mathbf{x}^{s_1+1}, \dots, \mathbf{x}^{S-1})}{P_{\text{open}}(\mathbf{x}^0, \dots, \mathbf{x}^S) \mathcal{A}_{\text{open} \rightarrow \text{closed}}(\mathbf{x}^{s_1+1}, \dots, \mathbf{x}^S)} \right] = 1, \quad (3.72)$$

$$p_{\text{acc}}^{\text{closed} \rightarrow \text{open}} = \min \left[1, \frac{P_{\text{open}}(\mathbf{x}^0, \dots, \mathbf{x}^S) \mathcal{A}_{\text{open} \rightarrow \text{closed}}(\mathbf{x}^{s_1+1}, \dots, \mathbf{x}^S)}{P_{\text{closed}}(\mathbf{x}^0, \dots, \mathbf{x}^{S-1}) \mathcal{A}_{\text{closed} \rightarrow \text{open}}(\mathbf{x}^{s_1+1}, \dots, \mathbf{x}^{S-1})} \right] = 1, \quad (3.73)$$

are both equal to one. This corresponds to rejection-free moves. At variance with the algorithm described in Section 3.1.3, one of the a-priori probabilities in Eqs. 3.70 and 3.71 is not normalized:

$$\int d\mathbf{x}^{s_1+1} \dots d\mathbf{x}^{S-1} \mathcal{A}_{\text{open} \rightarrow \text{closed}}(\mathbf{x}^{s_1+1}, \dots, \mathbf{x}^{S-1}) = \left(\frac{2\pi\hbar^2\Delta_s\tau}{m} \right)^{3/2} \rho_1(\mathbf{x}^{s_1}, \mathbf{x}^0, \Delta_s\tau), \quad (3.74)$$

$$\int d\mathbf{x}^{s_1+1} \dots d\mathbf{x}^S \mathcal{A}_{\text{closed} \rightarrow \text{open}}(\mathbf{x}^{s_1+1}, \dots, \mathbf{x}^S) = 1. \quad (3.75)$$

The definition of $\mathcal{A}_{\text{open} \rightarrow \text{closed}}$ could be modified to make its integral equal to one, but this would change the acceptance probabilities in Eqs. 3.72 and 3.73, introducing rejections. A more convenient way to proceed is to introduce an intermediate stopping probability for the closing move, given by

$$P_{\text{stop}} = 1 - \frac{\int d\mathbf{x}^{s_1+1} \dots \mathbf{x}^{S-1} \mathcal{A}_{\text{open} \rightarrow \text{closed}}(\mathbf{x}^{s_1+1}, \dots, \mathbf{x}^{S-1})}{\int d\mathbf{x}^{s_1+1} \dots \mathbf{x}^S \mathcal{A}_{\text{closed} \rightarrow \text{open}}(\mathbf{x}^{s_1+1}, \dots, \mathbf{x}^S)} = 1 - \exp \left(-\frac{m(\mathbf{x}^{s_1} - \mathbf{x}^0)^2}{2\hbar^2\Delta_s\tau} \right). \quad (3.76)$$

Therefore, the first step of a closing move consists in the choice of whether the move is proposed (which has probability $1 - P_{\text{stop}}$). If this is the case, the move continues in the usual way: A new configuration is proposed, and its acceptance or rejection is decided with the probability in Eq. 3.72. No change is needed for the opening move, which has zero stopping probability.

The description above is for a quantum particle in a periodic box. If λ_{th} is much smaller than the box linear size L , the presence of the box does not influence the statistical weights. At low temperature, however, the thermal wavelength λ_{th} becomes larger than L , and even a single path spreads over a region of volume comparable with L^3 . In this case, the choice of the boundary conditions becomes crucial. We use periodic boundary conditions, implying that a closed path may have a non-zero winding number (*cf.* Section 3.2.1). We include this possibility in the QMC algorithm through the closing move, which can introduce a non-zero winding-number vector \mathbf{w}^* (*cf.* Fig. 3.12).

The choice of which winding-number vector \mathbf{w}^* has to be assigned to a new configuration is simplified by the assumption

$$\sqrt{\frac{2\pi\hbar^2\Delta_s\tau}{m}} \ll L. \quad (3.77)$$

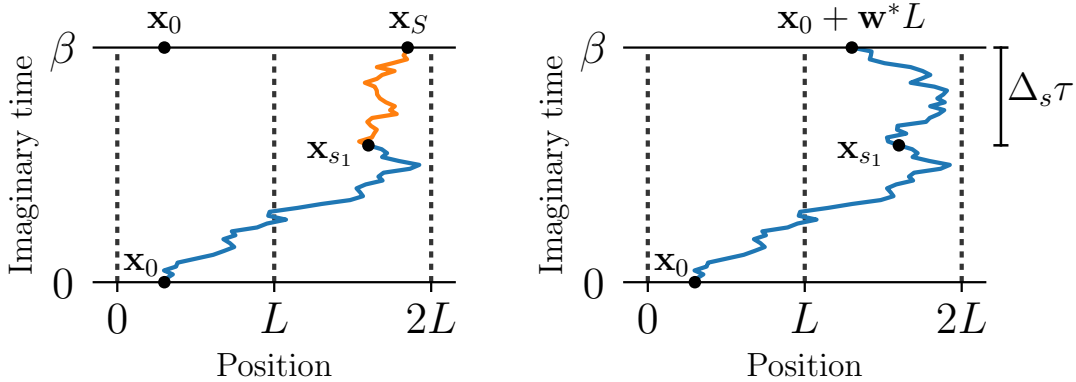


Figure 3.12: Closing move for a single-particle path in a periodic box of linear size L , passing from an off-diagonal configuration (*left panel*) to a diagonal one (*right panel*), and introducing a non-zero winding number (compare with Fig. 3.11).

This corresponds to the fact that the typical spread of the portion of path reconstructed during a sector-changing move is much smaller than the box size. Under the assumption in Eq. 3.77, there is no ambiguity in the choice of \mathbf{w}^* , which is given by

$$\mathbf{w}^* = \operatorname{argmin}_{\mathbf{w} \in \mathbb{Z}^3} |\mathbf{x}^{s_1} - (\mathbf{x}^0 + L\mathbf{w})|. \quad (3.78)$$

That is, the closing move connects the bead \mathbf{x}^{s_1} with the periodic image of \mathbf{x}^0 at smallest distance. This simple choice of \mathbf{w}^* is a consequence of Eq. 3.77, whereas without this assumption, we would have to randomly choose \mathbf{w}^* from the distribution $P(\mathbf{w}) \propto \rho_1(\mathbf{x}^{s_1}, \mathbf{x}^0 + \mathbf{w}L; \Delta_s\tau)$. The requirement in Eq. 3.77 is easily satisfied for a system with large N , where L is also large. In contrast, imposing this condition for a small- N simulation is typically sub-optimal, as it requires very small values of Δ_s .

It is instructive to determine the regime where winding has a negligible effect, since this is also the criterion for the superfluid transition (see Section 3.3.2). In the large-temperature limit ($\lambda_{\text{th}} \ll L$), the closed- and open-sector partition functions can be obtained analytically, by direct integration of P_{closed} and P_{open} , resulting in

$$Z_{\text{closed}} = \frac{V}{\lambda_{\text{th}}^3}, \quad Z_{\text{open}} = V \left(\frac{m}{2\pi\hbar^2\Delta_s\tau} \right)^{3/2}. \quad (3.79)$$

Therefore the relative statistical weight of the closed sector at high temperature reads

$$\frac{Z_{\text{closed}}}{Z_{\text{closed}} + Z_{\text{open}}} = \left[1 + \left(\frac{\Delta_s}{S} \right)^{3/2} \right]^{-1} = \left[1 + \Delta_s^{3/2} \left(\frac{\lambda_s}{\lambda_{\text{th}}} \right)^3 \right]^{-1}. \quad (3.80)$$

This expression includes the QMC parameter Δ_s , as a consequence of our choice for the length scale ξ_0 . Eq. 3.80 can be compared with the exact QMC calculation (valid

at any temperature), in which $Z_{\text{closed}}/(Z_{\text{closed}} + Z_{\text{open}})$ is estimated as the fraction of MC samples in the closed sector. We find that Eq. 3.80 is valid for $(\lambda_{\text{th}}/L)^3 \lesssim 1$ (see

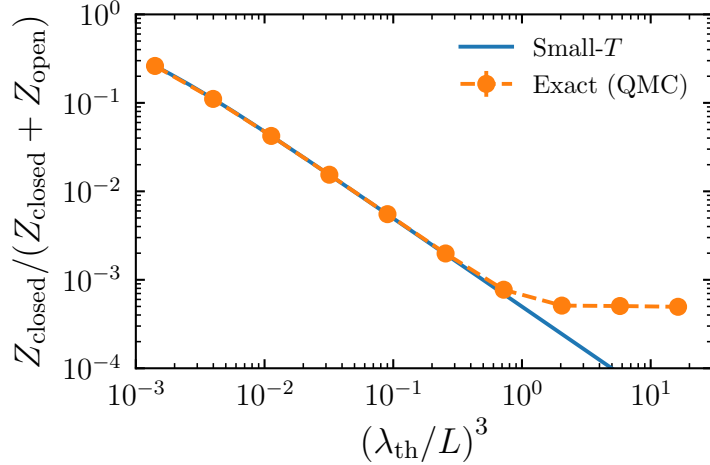


Figure 3.13: Relative weight of Z_{closed} , for one quantum particle in a periodic cubic box of volume L^3 . The high-temperature expansion (blue line, cf. Eq. 3.80) is compared with the exact curve (orange dots), obtained through QMC simulations (with $\lambda_s \rho^{1/3} = 0.03545$ and $\Delta_s = 5$).

Fig. 3.13). For smaller temperatures, the contribution of paths with non-zero winding cannot be neglected.

The opening and closing moves can be simply generalized to the case of N interacting bosons, by making it act on the two ends of the open path. The stopping probability (cf. Eq. 3.76) does not change, but the contributions of two- and three-body interactions to the statistical weight modify the acceptance probabilities in Eqs. 3.73 and 3.72, introducing a finite rejection probability. Furthermore, the condition in Eq. 3.77 is simple to satisfy for a system with large N , since L grows proportionally to $N^{1/3}$.

The scheme of the open/close QMC algorithm consists in repeating a certain amount of same-sector moves before proposing a sector switch, through the opening or closing moves. During the MC evolution in the open sector, the two ends of the open path can get at distance significantly larger than $\sqrt{2\pi\hbar^2\Delta_s\tau/m}$. In this case, the stopping probability (cf. Eq. 3.76) becomes close to one, and the chance that the closing move takes place is small, until the distance between the two open ends decreases. The typical number of open-sector MC steps between two accepted closing moves depends on the temperature (see Fig. 3.14). At low temperature, the distance between the two open ends becomes large more often, so that more open-sector steps are needed before a closing move is accepted. This is not simply a technical feature of the QMC algorithm, but it is directly connected with the concept of ODLRO for the one-body-reduced density matrix, cf. Section 3.3.3.

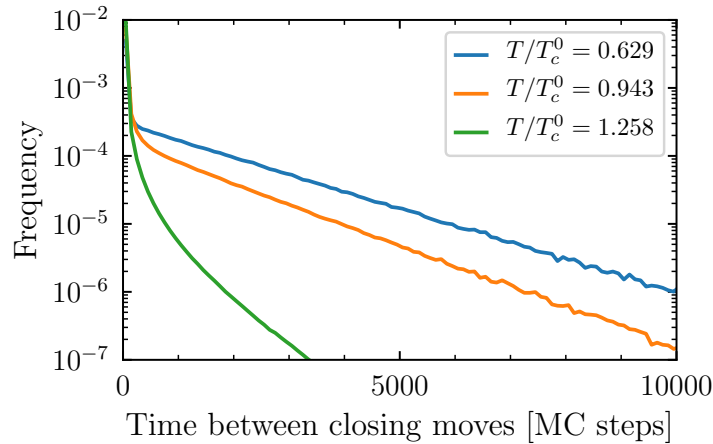


Figure 3.14: Histogram of the number of open-sector MC steps required before a closing move is accepted, for QMC simulations of $N = 10^3$ non-interacting bosons in a periodic box, at different temperatures (see legend). One MC step corresponds to moving $N \times S$ beads, on average. For the fixed-sector MC evolution, the Lévy-construction, advance/recede and swap moves are used.

3.3 Observables

In the following sections, we describe three kinds of observables: The closed-sector observables which also exist for classical particles (*cf.* Section 3.3.1), the closed-sector observables which are specific to quantum systems (*cf.* Section 3.3.2), and the most relevant open-sector observable, namely the one-body-reduced density matrix (*cf.* Sections 3.3.3 and 3.3.4). The latter is an off-diagonal observable, but its normalization includes the ratio of the open- and closed-sector partition functions (*cf.* Section 3.3.3). None of the observable estimators described in this section depends on the choice of the interaction potential. On the contrary, the improved momentum-distribution estimator (*cf.* Section 3.4.2) is specific for the unitary-bosons model under study.

For some observables, we include in this section a comparison of QMC data for the ideal Bose gas and results based on the recursion relations for the canonical partition function (*cf.* Section 1.4). Their agreement provides a validation of the QMC algorithm for systems without interactions.

3.3.1 Spatial correlation functions

For closed path-integral configurations, several observables can be expressed as functions of the positions $\mathbf{X} = \{\mathbf{x}_1^s, \dots, \mathbf{x}_N^s\}$ of the N beads on the imaginary-time slice s . The

normalized probability distribution for these positions is

$$P_{\text{pos}}(\mathbf{x}_1, \dots, \mathbf{x}_N) = \frac{\rho_N^{\text{bos}}(\{\mathbf{x}_1, \dots, \mathbf{x}_N\}, \{\mathbf{x}_1, \dots, \mathbf{x}_N\}; \beta)}{Z_{\text{closed}}}, \quad (3.81)$$

where we dropped the superscript s since P_{pos} does not depend on the imaginary-time slice. Independently of its quantum origin, P_{pos} can be interpreted as the probability distribution for N classical particles, and we can introduce some observables which are standard for classical systems [151]. The simplest of these observables is the density profile,

$$\left\langle \sum_{i=1}^N \delta(\mathbf{x}_i - \mathbf{x}) \right\rangle = \int d\mathbf{x}_1 \dots d\mathbf{x}_N P_{\text{pos}}(\mathbf{x}_1, \dots, \mathbf{x}_N) \sum_{i=1}^N \delta(\mathbf{x}_i - \mathbf{x}), \quad (3.82)$$

which gives the average local density at position \mathbf{x} . For a homogeneous system, this is a constant function of \mathbf{x} , while its value depends on the position when the system is non-homogeneous, for as for instance due to an external potential. Recording a histogram of particle-position samples during a QMC simulation gives direct access to the density profile.

In a similar way, we can define the pair-correlation function at positions \mathbf{x} and \mathbf{x}' as

$$g^{(2)}(\mathbf{x}, \mathbf{x}') = \sum_{i=1}^N \sum_{j \neq i} \langle \delta(\mathbf{x} - \mathbf{x}_i) \delta(\mathbf{x}' - \mathbf{x}_j) \rangle, \quad (3.83)$$

where the average is taken for $\{\mathbf{x}_1, \dots, \mathbf{x}_N\}$ distributed as in Eq. 3.81. For a homogeneous system, $g^{(2)}(\mathbf{x}, \mathbf{x}')$ is a function of the relative vector $\mathbf{r} = \mathbf{x} - \mathbf{x}'$ only. In QMC, we have direct access to the histogram of the interparticle distances, $P_{\text{dist}}(r)$, normalized as

$$\int dr P_{\text{dist}}(r) = 1. \quad (3.84)$$

This histogram is related to the pair-correlation function through

$$g^{(2)}(\mathbf{r}) = \frac{N(N-1)}{V} \frac{P_{\text{dist}}(r)}{4\pi r^2}, \quad (3.85)$$

which is valid for an isotropic system and for distances smaller than $L/2$ (where L is the edge of the cubic box where particles are confined). At larger distances, P_{dist} has a dependence on the presence of the box, and it vanishes at $r = \sqrt{3}L/2$. For a bosonic system with zero-range interactions, the pair-correlation functions is connected to the contact density c_2 through

$$\lim_{|\mathbf{r}| \rightarrow 0} (r^2 g^{(2)}(\mathbf{r})) = \frac{c_2}{(4\pi)^2}, \quad (3.86)$$

as described in Section 2.1.3.

Other n -point density correlation functions can be defined in the same way as the pair-correlation function. In Section 2.2.2, we compute the three-body correlation function for three unitary bosons at low temperature (*cf.* Fig. 2.6), which provides a signature of the Efimov effect.

3.3.2 Permutation cycles and superfluid density

Unlike the density profile and n -point correlation functions, which are also defined for a classical particle system, other diagonal observables are specific to quantum systems. This is reflected in the fact that they depend on degrees of freedom located at different imaginary-time slices.

Bosonic quantum statistics enters the path-integral formulation through permutation cycles (see Section 1.3), with the presence of long cycles being connected to the BEC transition. In the large-temperature limit ($\lambda_{\text{th}}^3 \rho \simeq 0$), any permutation P different from the identity permutation $\{1, \dots, N\}$ has vanishing statistical weight, so that particles are effectively distinguishable.

As the temperature is lowered, the statistical weight of permutations including long cycles becomes non-negligible, and in the zero-temperature limit a particle has the same probability for being in a cycle of any length. QMC simulation allow to directly measure the average number of particles on cycles of a given length. For an ideal Bose gas, this quantity can be computed exactly also through the recursion method for the canonical partition functions. With the notation of Section 1.4 for a system of N bosons in a periodic box, the average number of bosons on cycles of length k reads

$$\frac{k}{N} \times \frac{z(k\beta)Z_{N-k}(\beta)}{Z_N(\beta)}, \quad (3.87)$$

which can be computed numerically for any choice of N , V , and T . As shown in Fig. 3.15, the same result is obtained with an open/close QMC simulation for the ideal Bose gas, in which the swap move is used to change the structure of permutation cycles. This validates the QMC algorithm, for the non-interacting case.

The study of permutation cycles is directly related to the BEC transition. For ideal bosons the condensate fraction can be extracted from the quantity in Eq. 3.87 [39], which gives a quantitative connection between the statistics of permutation cycles and the BEC transition. This is not available for the case of interacting systems [42], although permutation cycles keep providing a useful ingredient for an heuristic study of the transition. In contrast with the condensate fraction, the superfluid fraction is directly connected to these cycles, both for ideal and interacting systems. A closed path in a periodic box can have a non-zero winding-number vector $\mathbf{w} \in \mathbb{Z}^3$, which is computed by counting how many times it winds around the periodic box along each direction (cf. Section 3.2.1). The total winding-number vector \mathbf{W} of a configuration is the sum of the winding-number vectors corresponding to all bosonic cycles,

$$\mathbf{W} = \sum_{\text{cycles}} \mathbf{w}_{\text{cycle}}, \quad (3.88)$$

where the sum of the number of bosons belonging to each cycle is equal to N . The symmetry of the system with respect to spatial inversion implies that $\langle \mathbf{W} \rangle = 0$, where

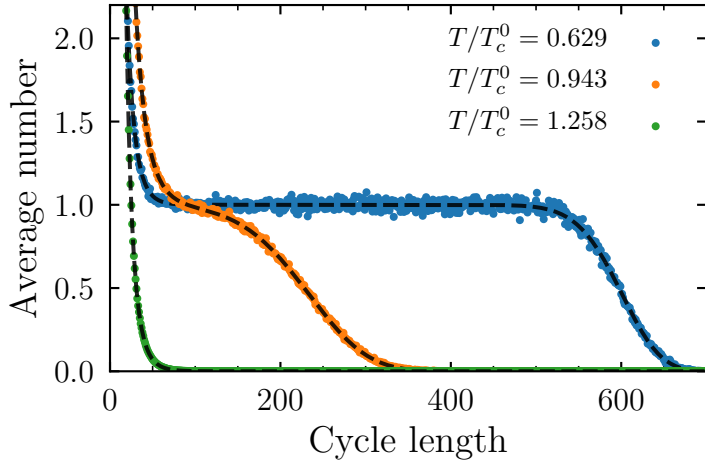


Figure 3.15: Average number of particles on cycles of a given length, for a system of $N = 10^3$ non-interacting bosons in a three-dimensional periodic box. Full agreement is obtained between the exact results obtained through the QMC algorithm described in this section (*dots*) and the exact recursion of Section 1.4 (*dashed black lines*).

the average is taken over configurations distributed according to ρ_N^{bos} . The average of \mathbf{W}^2 , in contrast, can be non-zero, and it gives direct access to the superfluid fraction ρ_s/ρ , via

$$\frac{\rho_s}{\rho} = \frac{m}{\hbar^2 \beta} \frac{\langle \mathbf{W}^2 \rangle L^2}{3N}, \quad (3.89)$$

where L is the linear size of the cubic box. This relation was first introduced in Ref. [23], based on connection of the superfluid density with the helicity modulus (*cf.* Section 1.1), and it does not depend on whether bosons are interacting. In a QMC simulation, we can collect statistics for W_x (note that $\langle W_x^2 \rangle = \langle W_y^2 \rangle = \langle W_z^2 \rangle = \langle \mathbf{W}^2 \rangle / 3$, due to the symmetry under permutations of $\{x, y, z\}$), and then obtain ρ_s through Eq. 3.89. At high temperature, the probability of winding numbers $W_x \neq 0$ is strongly suppressed (below 2%, for the left panel of Fig. 3.16), while it becomes significant at low temperature (*cf.* Fig. 3.16, middle and right panels). This is a direct consequence of the appearance of long permutation cycles, which can wind several times around the box. Computing $\langle \mathbf{W}^2 \rangle$ in QMC requires algorithms which can efficiently modify the structure of permutation cycles. This is best achieved with simulations in the extended configuration space (*cf.* Section 3.2.1 and Refs [136] and [137]), while the permutation-sampling algorithm originally devised for liquid helium are not optimal (see for instance Ref. [152]).

For the case of N non-interacting bosons, the exact value of ρ_s can also be obtained

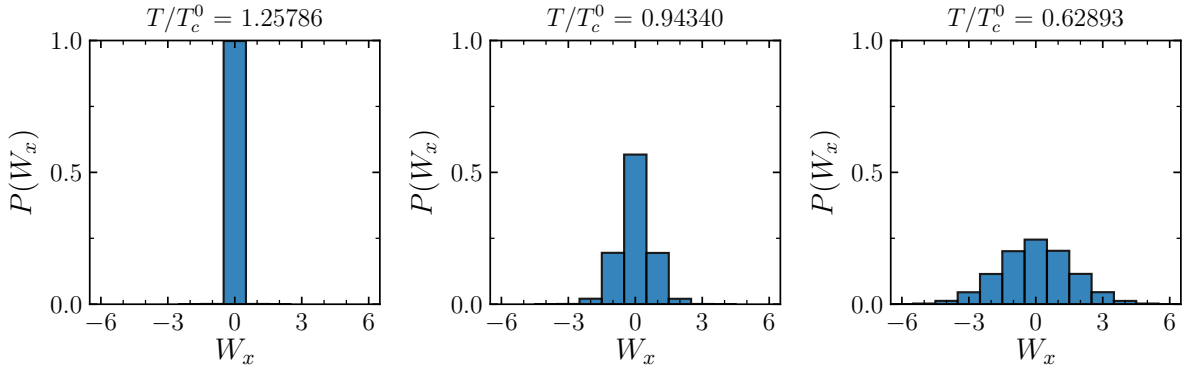


Figure 3.16: Winding-number distribution for $N = 10^3$ non-interacting bosons at different temperatures (*cf.* panel titles), computed through QMC simulations. For high temperature (*left panel*), the distribution is more narrowly peaked at $W_x = 0$, while it becomes broader as the temperature decreases. The corresponding superfluid fractions are reported in Table 3.1.

through the recursive method of Section 1.4, as described in Ref. [40]. By introducing

$$f_{k,w} = \frac{L}{\sqrt{2\pi\hbar^2\beta k/m}} \exp\left(-\frac{mL^2w^2}{2k\beta\hbar^2}\right), \quad (3.90)$$

we can rewrite $z(k\beta)$ (*cf.* Eq. 1.28) as

$$z(k\beta) = \left(\sum_{w \in \mathbb{Z}} f_{k,w}(\beta) \right)^3. \quad (3.91)$$

Given a cycle of length k , the average of its squared winding number along x reads

$$\langle w_x^2 \rangle_k = \frac{\sum_{w \in \mathbb{Z}} f_{k,w}(\beta) w^2}{\sum_{w \in \mathbb{Z}} f_{k,w}(\beta)}, \quad (3.92)$$

and it is a monotonically increasing function of $k \in \{1, \dots, N\}$. Given the probability distribution π_k for a particle to be on a cycle of length k (*cf.* Eq. 1.33), the variance of the x -component of \mathbf{W} is

$$\langle W_x^2 \rangle = \sum_{k=1}^N \pi_k \langle w_x^2 \rangle_k = \sum_{k=1}^N \frac{1}{N} \frac{z(k\beta) Z_{N-k}(\beta)}{Z_N(\beta)} \langle w_x^2 \rangle_k. \quad (3.93)$$

By combining this result with Eq. 3.89, we can compute ρ_s . This quantity agrees with QMC results for the ideal Bose gas with relative errors $\leq 0.7\%$ (*cf.* Table 3.1), which represents an additional verification for our algorithm.

T/T_c^0	ρ_s/ρ (Eqs. 3.89 and 3.93)	ρ_s/ρ (QMC and Eq. 3.89)	Relative error (QMC)
1.25786	0.000799	0.000806 ± 0.000006	0.7 %
0.94340	0.1781	0.1787 ± 0.0004	0.2 %
0.62893	0.5639	0.5619 ± 0.0013	0.2 %

Table 3.1: Superfluid fraction for $N = 10^3$ non-interacting bosons in a cubic periodic box, with the parameters of Fig. 3.16. The values obtained through Eqs. 3.89 and 3.93 are consistent with the QMC results.

3.3.3 One-body-reduced density matrix

For a translation-invariant system, the one-body-reduced density matrix $g^{(1)}(\mathbf{r})$ is defined as

$$g^{(1)}(\mathbf{r}) = \frac{N}{V} \times \frac{\int d\mathbf{x}_1 \dots d\mathbf{x}_N \rho_N^{\text{bos}}(\{\mathbf{x}_1, \mathbf{x}_2, \dots, \mathbf{x}_N\}, \{\mathbf{x}_1 + \mathbf{r}, \mathbf{x}_2, \dots, \mathbf{x}_N\}; \beta)}{Z_{\text{closed}}}, \quad (3.94)$$

which is normalized so that $g^{(1)}(\mathbf{r}) \rightarrow \rho$ for $|\mathbf{r}| \rightarrow 0$. $g^{(1)}(\mathbf{r})$ is proportional to the marginal probability distribution for a relative vector \mathbf{r} between the two ends of the open path, and it is connected with the statistics of permutation cycles. For an ideal Bose gas at high temperature ($\lambda_{\text{th}}^3 \rho \ll 1$), the probability for cycles of more than one particle is strongly suppressed. In this regime, the density matrix ρ_N^{bos} is approximately equal to the density matrix of N non-interacting distinguishable particles, which is the product of N single-particle terms. Thus the expression in Eq. 3.94 becomes

$$g^{(1)}(\mathbf{r}) = \frac{N}{V} \times \frac{\int d\mathbf{x}_1 \rho_1(\mathbf{x}_1, \mathbf{x}_1 + \mathbf{r}; \beta)}{\int d\mathbf{x}_1 \rho_1(\mathbf{x}_1, \mathbf{x}_1; \beta)} = \frac{N}{V} \times \exp\left(-\frac{m\mathbf{r}^2}{2\hbar^2\beta}\right). \quad (3.95)$$

Thus $g^{(1)}(\mathbf{r})$ decays exponentially for large r , with a characteristic length scale much smaller than L . This corresponds to the physical regime in which the winding of paths around the periodic box is suppressed, since the presence of non-zero winding would require the two open ends to reach a distance of the order of the box size. At low temperature, in contrast, the thermal wavelength λ_{th} becomes comparable to $\rho^{-1/3}$, and the probability of longer cycles increases. The distribution of the end-to-end vector of an isolated open path formed by k particles is proportional to $\rho_1(0, \mathbf{r}; k\beta)$. The corresponding length scale for the large- r decay is \sqrt{k} times larger than the one in Eq. 3.95. Thus an open cycle made by a macroscopic number of particles can reach an end-to-end distance of the order of $\sqrt{N}\lambda_{\text{th}}$, which is comparable or larger than the linear box size $L = (N/\rho)^{1/3}$ (cf. Fig. 3.17). It is then clear how the ODLRO criterion for Bose-Einstein condensation (cf. Section 1.1) is related to permutation cycles: $g^{(1)}(\mathbf{r})$ decays to zero on the length scale set by λ_{th} , unless the system has a relevant probability of including long cycles.

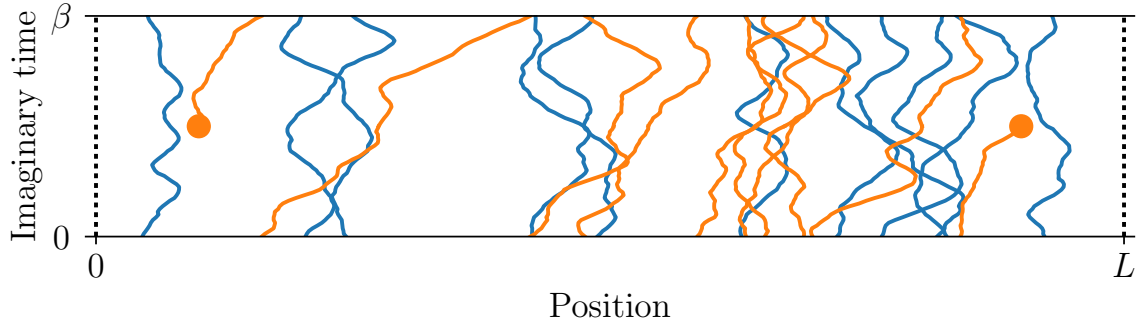


Figure 3.17: Schematic representation of ODLRO for $N = 20$ bosons in a box of linear size L : Due to the presence of a long cycle (orange line), the head and tail (orange dots) can be at a macroscopic distance, while short-cycle paths (blue lines) have a linear size of the order of λ_{th} .

The definition of $g^{(1)}(\mathbf{r})$ (cf. Eq. 3.94) can be rewritten as

$$g^{(1)}(\mathbf{r}) = \frac{N}{V} \frac{Z_{\text{open}} \xi_0^3}{Z_{\text{closed}}} \times P(\mathbf{r}), \quad (3.96)$$

by making use of Eqs. 3.33 and 3.34), and by introducing

$$P(\mathbf{r}) = \frac{\int d\mathbf{x}_1 \dots d\mathbf{x}_N \rho_N^{\text{bos}}(\{\mathbf{x}_1 + \mathbf{r}, \mathbf{x}_2 \dots, \mathbf{x}_N\}, \{\mathbf{x}_1, \mathbf{x}_2 \dots, \mathbf{x}_N\}; \beta)}{Z_{\text{open}} \xi_0^3}. \quad (3.97)$$

This distribution $P(\mathbf{r})$ is normalized ($\int d\mathbf{r} P(\mathbf{r}) = 1$), and can be directly accessed in a QMC simulation, by constructing a histogram for the separation vector \mathbf{r} between head and tail. Eq. 3.96 links the raw histogram $P(\mathbf{r})$ to the one-body-reduced density matrix. This requires the knowledge of ξ_0 (a free parameter in the QMC algorithm, chosen as in Eq. 3.69), and of $Z_{\text{open}}/Z_{\text{closed}}$. The general scheme for MC sampling in different dimensions (cf. Section 3.1.3) gives access to this ratio. For the QMC case, it is directly estimated as the ratio of the number of configurations in the closed and open sectors.

3.3.4 Momentum distribution and condensate fraction

The momentum distribution $n(\mathbf{k})$ is defined as the Fourier transform of $g^{(1)}(\mathbf{r})$,

$$n(\mathbf{k}) = V \int d\mathbf{r} g^{(1)}(\mathbf{r}) \exp(-i\mathbf{k} \cdot \mathbf{r}), \quad (3.98)$$

for a translation-invariant system. In a periodic box of linear size L , $n(\mathbf{k})$ has to be computed for a discrete set of momenta, given by $\mathbf{k}_{\mathbf{q}} = (2\pi/L)\mathbf{q}$, with $\mathbf{q} \in \mathbb{Z}^3$. Its normalization is such that

$$\sum_{\mathbf{q} \in \mathbb{Z}^3} n(\mathbf{k}_{\mathbf{q}}) = NV. \quad (3.99)$$

so that the condensate fraction reads⁴

$$\frac{N_0}{N} = \frac{n(\mathbf{k} = 0)}{NV}, \quad (3.100)$$

where N_0 is the average number of condensed particles. The average number N_{th} of thermal particles is $N_{\text{th}} = N - N_0$. For a large system in the normal-gas phase, the normalization in Eq. 3.99 can be approximated as

$$\int d\mathbf{k} n(\mathbf{k}) = N \times (2\pi)^3, \quad (3.101)$$

while this breaks down in the presence of a finite condensate fraction (*cf.* Section 1.1). At large temperature, the momentum distribution for non-interacting bosons is obtained from Eq. 3.95, and it reads

$$n(\mathbf{k}) = N \times \left(\frac{2\pi\hbar^2\beta}{m} \right)^{3/2} \times \exp \left(-\beta \frac{\hbar^2 k^2}{2m} \right), \quad (3.102)$$

which is the Boltzmann factor of an energy $\hbar^2 k^2 / (2m)$, that is, the result for distinguishable non-interacting particles.

In QMC, one could directly estimate $g^{(1)}(\mathbf{r})$ as a histogram and then use the definition in Eq. 3.98 to compute $n(\mathbf{k})$. This is not optimal, as it involves a Fourier transform of noisy data. In contrast, we use a method where $n(\mathbf{k})$ for a given momentum \mathbf{k} is obtained directly [131, 153]. By using the expression for $g^{(1)}(\mathbf{r})$ given in Eq. 3.96, the definition of $n(\mathbf{k})$ can be rewritten as

$$n(\mathbf{k}) = N \frac{Z_{\text{open}} \xi_0^3}{Z_{\text{closed}}} \times \int d\mathbf{r} P(\mathbf{r}) e^{-i\mathbf{k}\cdot\mathbf{r}}. \quad (3.103)$$

The integral in the right-hand side corresponds to the statistical average of $e^{-i\mathbf{k}\cdot\mathbf{r}}$. In QMC, samples of \mathbf{r} are distributed as $P(\mathbf{r})$, so that the average of $e^{-i\mathbf{k}\cdot\mathbf{r}}$ is directly available. We denote this measure of $n(\mathbf{k})$ the naive estimator, to be compared with the estimator described in Section 3.4.2 below. The open/close QMC algorithm gives access to the correctly-normalized one-body-reduced density matrix and momentum distribution ($g^{(1)}(\mathbf{r})$ and $n(\mathbf{k})$), as it allows to estimate the ratio $Z_{\text{open}}/Z_{\text{closed}}$ [137, 136]. By setting $\mathbf{k} = 0$ in Eq. 3.103, we obtain

$$\frac{N_0}{N} = \frac{\xi_0^3}{V} \frac{Z_{\text{open}}}{Z_{\text{closed}}}. \quad (3.104)$$

To conclude this section, we describe a peculiar property of the BEC phase, related to the fluctuations of the number of particles in the condensate (*cf.* Ref. [15], §3.3). N_0 and

⁴Here and in Chapter 4, N_0 is the average occupation number of the $\mathbf{k} = 0$ level, which in Chapter 1 is denoted by $\langle N_0 \rangle$.

N_{th} are the average numbers of condensed and non-condensed particles, and they have physical fluctuations, at any given temperature. This is the case both in the canonical ensemble (where $N = N_0 + N_{\text{th}}$ is fixed) and in the grand canonical ensemble (where N itself can fluctuate). For a typical extensive observable O , the variance $\sigma^2(O)$ is expected to scale linearly with the system size N . The relative importance of fluctuation (that is, $\sigma(O)/\langle O \rangle$) vanishes in the large- N limit, since $\sigma(O) \propto N^{1/2}$ and $\langle O \rangle \propto N$. For a system of non-interacting bosons in the normal-gas phase, the number N_{th} of non-condensed particles has fluctuations with the ordinary linear scaling (that is, $\sigma^2(N_{\text{th}}) \propto N$), both in the canonical and grand canonical ensembles [15]. In the BEC phase, however, the variance of N_{th} scales as

$$\sigma^2(N_{\text{th}}) \propto N^{4/3}. \quad (3.105)$$

This superlinear scaling differs from the typical case of extensive variables, and it is a consequence of the small- k behavior of $n(\mathbf{k})$ [15]. While this scaling holds both in the canonical and grand canonical ensembles, the corresponding scaling of $\sigma^2(N_0)$ shows a clear difference between the two ensembles. If the total number of particles $N = N_0 + N_{\text{th}}$ is constant, then the fluctuations of $N_0 = N - N_{\text{th}}$ scale in the same way as those of N_{th} , namely $\sigma^2(N_0) \propto N^{4/3}$. In the grand canonical ensemble, in contrast, the fluctuations of N_0 for an ideal BEC scale as $\sigma^2(N_0) \propto N^2$, meaning that their relative importance does not vanish in the $N \rightarrow \infty$ limit. This anomaly is a pathological feature of the ideal Bose gas, when treated via the grand canonical ensemble. The results mentioned here (notably the fact that $\sigma(N_0) \propto N^{2/3}$, in the BEC phase) also hold in the presence of interactions [154].

3.4 Additional aspects related to PIMC

In this section we describe two additional aspects of the path-integral QMC study presented in this work. The first concerns a common problem for most Monte Carlo studies of phase transition: Most MC methods give access to the properties of finite-size system, while the critical behavior close to phase transitions is best characterized in the infinite-size limit. This is addressed by the finite-size scaling technique – *cf.* Section 3.4.1. Section 3.4.2, in contrast, concerns a specific issue in the study of systems with zero-range interactions, as the model for the unitary Bose gas used in this work. The naive estimator for the momentum distribution (*cf.* Section 3.3.4) becomes unpractical at the large momenta, and we describe an approximate scheme to overcome this problem.

3.4.1 Superfluid transition and finite-size scaling

In this section, we describe the finite-size scaling technique to characterize the BEC phase transition. An example is provided by the case of the ideal Bose gas in a periodic box, for which we have an explicit expression of the superfluid density (*cf.* Eq. 3.89).

This quantity has a strong dependence on the system size (*cf.* Fig. 3.18), especially in the intermediate-temperature region close to T_c^0 . Even for the largest system considered in Fig. 3.18 ($N = 4096$), a clear deviation from the infinite-size result is visible. Moreover, the smoothness of the finite-size curves makes it hard to define a critical temperature for a system at a given $N \lesssim 10^3$.

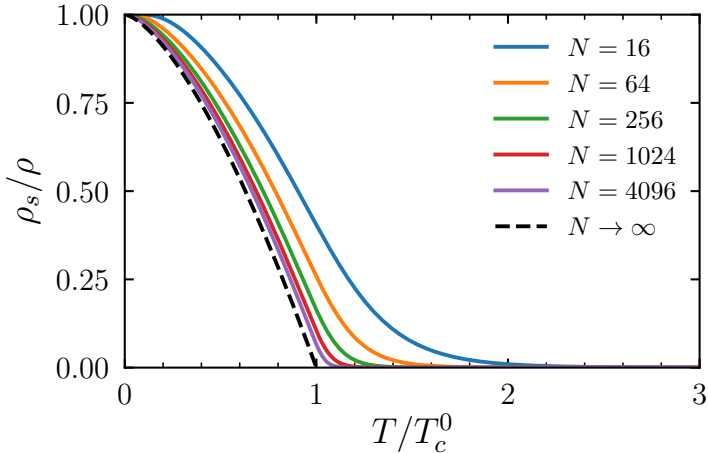


Figure 3.18: Superfluid fraction of N ideal bosons in a periodic box, as a function of the rescaled temperature, and for different values of N (*solid lines*, obtained through Eq. 3.89 and Eq. 3.93). Also shown is the exact result [20, 21] for an infinite system below T_c^0 (*dashed black line*, *cf.* Eq. 1.21).

The fact that the transition is smeared out and only becomes sharper for large systems can be understood in terms of the correlation-length behavior. We consider a BEC transition in three dimensions, with critical temperature T_c . The rescaled temperature is defined as $t = (T - T_c)/T_c$. At the transition point ($t = 0$), the superfluid fraction and correlation length⁵ of an infinite system have a power-law scaling, with exponents v and ν , that is

$$\xi \sim \frac{1}{t^\nu}, \quad \text{for } t \rightarrow 0^+, \quad (3.106)$$

and

$$\frac{\rho_s}{\rho} \sim t^v, \quad \text{for } t \rightarrow 0^-. \quad (3.107)$$

The value of these exponents depends on which universality class the transition belongs to. In three dimensions, the ideal Bose gas belongs to the complex Gaussian model class, which has $\nu = 1$ [20, 21]. The three-dimensional weakly-interacting Bose gas, in

⁵ For $T > T_c$, the correlation length ξ is defined via $\Delta F \sim e^{-L/\xi}$, where the twist free energy ΔF is the change in free energy corresponding to a change from periodic to antiperiodic boundary conditions along one direction [155]. For the extension of this definition below T_c , *cf.* Ref. [20].

contrast, is in the 3D XY class, with $\nu \simeq 0.67$ [156] (corresponding to the value measured for ${}^4\text{He}$ [157]). In a finite system, there exists a temperature region in which the infinite-system correlation length ξ exceeds the maximum length scale of the finite system, that is, the linear size L of the box. The finite-size scaling hypothesis is formulated in this temperature region, and states that the free energy (or any derived observable) is a universal function of $L/\xi \sim Lt^\nu$. When expressed for the superfluid fraction, this hypothesis reads [22, 155]

$$\frac{\rho_s}{\rho} = L^{-1}Q(L^{1/\nu}t) \quad (3.108)$$

where $Q(x)$ is a unknown universal function (which is analytic for any finite argument), and where we have assumed that $v = \nu$ [155]. The hypothesis in Eq. 3.108 provides a powerful technique to estimate T_c from finite-system results. The expansion of $Q(x)$ close to the transition point ($x \simeq 0$) gives

$$L \times \frac{\rho_s}{\rho} = Q(0) + Q'(0)L^{1/\nu}t + \dots, \quad (3.109)$$

so that $L \times (\rho_s/\rho)$ becomes independent on the system size at $t = 0$. Therefore, we

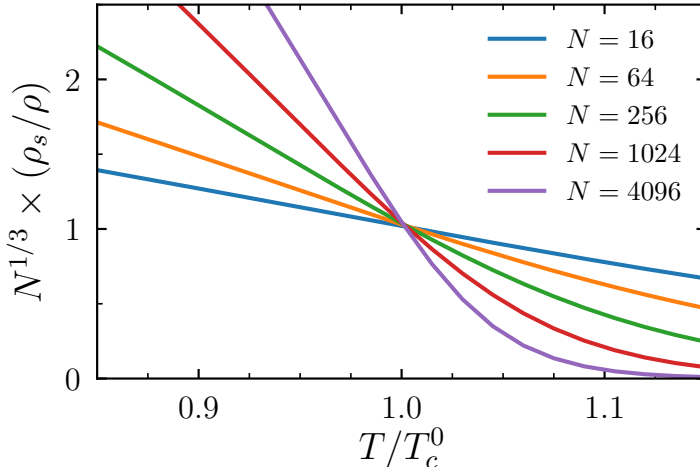


Figure 3.19: Rescaled superfluid fraction as a function of the temperature, for a system of N non-interacting bosons in a cubic periodic box (computed through Eq. 3.93, cf. Ref. [40]).

can plot $L \times (\rho_s/\rho)$ (or, equivalently, $N^{1/3}\rho_s/\rho$) as a function of temperature for several values of N , and the crossing point of these lines provides an estimate of T_c . An example for the ideal Bose gas is shown in Fig. 3.19, where the crossing point takes place near $T = T_c^0$. For small N , corrections to the scaling law in Eq. 3.108 cannot be neglected [155], introducing a systematic deviation of the estimates of the critical temperature from its actual value (not visible on the scale of Fig. 3.19).

Similar versions of the finite-size scaling idea constitute fundamental tools in the study of critical phenomena for several other cases, including magnetic systems [158, 159] and zero-temperature quantum phase transitions [160]. In the context of path-integral QMC, examples of this analysis are found in Ref. [161] (for ideal and interacting bosons) and Ref. [162] (for interacting bosons in the presence of an external potential). In Section 4.4.1, this method is used to determine the critical temperature of the unitary Bose gas.

3.4.2 Large-momentum tail of $n(\mathbf{k})$

The standard method to measure the momentum distribution in a QMC simulation is described in Section 3.3.4. In this section, for simplicity, we consider the observable $\bar{n}(\mathbf{k})$ (rather than the actual momentum distribution $n(\mathbf{k})$), defined through a rewriting of Eq. 3.103:

$$\bar{n}(\mathbf{k}) = \frac{1}{N} \frac{Z_{\text{closed}}}{Z_{\text{open}} \xi_0^3} \times n(\mathbf{k}) = \int d\mathbf{r} P(\mathbf{r}) e^{i\mathbf{k} \cdot \mathbf{r}}. \quad (3.110)$$

$P(\mathbf{r})$ is the normalized probability distribution for the separation vector \mathbf{r} between the head and tail of the open path (*cf.* Eq. 3.97). It corresponds to the distribution of the samples for \mathbf{r} in a QMC simulation, so that we can estimate $\bar{n}(\mathbf{k})$ as

$$\bar{n}(\mathbf{k}) \simeq \frac{1}{N_{\text{steps}}} \sum_{j=1}^{N_{\text{steps}}} \exp(-i\mathbf{k} \cdot \mathbf{r}_j) \quad (3.111)$$

where $\mathbf{r}_1, \dots, \mathbf{r}_{N_{\text{steps}}}$ are the samples of \mathbf{r} obtained through QMC. We refer to this method of measuring $\bar{n}(\mathbf{k})$ (or, equivalently, the momentum distribution) as the naive estimator. At $\mathbf{k} = 0$, $\bar{n}(\mathbf{k})$ is equal to one, and its physical fluctuations vanish. The relative fluctuations of $\bar{n}(\mathbf{k})$, in contrast, become very large in the large- k regime, where $\bar{n}(\mathbf{k})$ itself decays to zero. In this regime, the naive estimator gives a very poor estimate of $\bar{n}(\mathbf{k})$, as it consists of the average of strongly-oscillating terms. For the study of the BEC transition, the small- k part of the momentum distribution is the most relevant, so that this limitation of the naive estimator does not represent a practical issue. However, the large- k behavior of the momentum distribution is of key importance for systems with strong, short-ranged, interactions (which is the case for the unitary Bose gas, *cf.* Chapters 2 and 4), as it is connected to universal properties. The naive estimator is formally correct at any \mathbf{k} , and it can be used in the absence of alternative methods (see for instance Fig. 4.15), but it is not practical to address large- k regime. In the following paragraphs, we describe an improved estimator, explicitly designed to solve this issue.

The estimator derived in this section is specific for particles interacting through the zero-range unitary potential, unlike the generally applicable observable estimators of Section 3.3. For an open two-particles configuration, with head x and tail y on imaginary-time slice s_{cut} , we introduce the notation in Fig. 3.20 for a given set of

points $\mathcal{C} = \{\mathbf{A}, \mathbf{B}, \mathbf{C}, \mathbf{D}, \mathbf{E}\}$. The free parameter Δ_s determines the region of interest, which corresponds to the portion of the configuration with imaginary-time slices between $(s_{\text{cut}} - \Delta_s)$ and $(s_{\text{cut}} + \Delta_s)$.

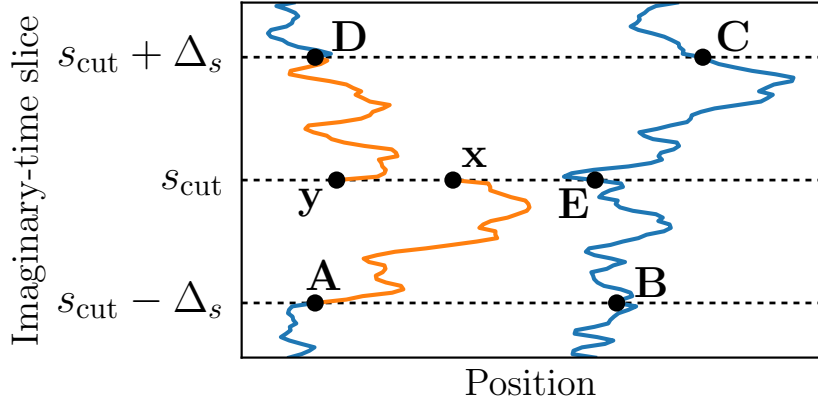


Figure 3.20: Open configuration for two particles, with open ends \mathbf{x} and \mathbf{y} in the vicinity of the imaginary-time slice s_{cut} .

We formally rewrite $\bar{n}(\mathbf{k})$ as

$$\bar{n}(\mathbf{k}) = \int d\mathcal{C} p^*(\mathcal{C}) \int d\mathbf{x} \int d\mathbf{y} P_{\text{end}}(\mathbf{x}, \mathbf{y} | \mathcal{C}) e^{-i\mathbf{k} \cdot (\mathbf{x} - \mathbf{y})}, \quad (3.112)$$

with the shorthand $d\mathcal{C} = d\mathbf{A} d\mathbf{B} d\mathbf{C} d\mathbf{D} d\mathbf{E}$. $p^*(\mathcal{C})$ is the (unknown) probability distribution for \mathcal{C} , and $P_{\text{end}}(\mathbf{x}, \mathbf{y} | \mathcal{C})$ is the conditional probability distribution for the endpoints \mathbf{x} and \mathbf{y} , for a given value of \mathcal{C} . We define

$$\bar{n}(\mathbf{k} | \mathcal{C}) = \int d\mathbf{x} \int d\mathbf{y} P_{\text{end}}(\mathbf{x}, \mathbf{y} | \mathcal{C}) e^{-i\mathbf{k} \cdot (\mathbf{x} - \mathbf{y})}, \quad (3.113)$$

so that $\bar{n}(\mathbf{k})$ is equal to the average of $\bar{n}(\mathbf{k} | \mathcal{C})$ over \mathcal{C} , if \mathcal{C} is distributed according to $p^*(\mathcal{C})$. $\bar{n}(\mathbf{k} | \mathcal{C})$ will be computed analytically. Thus one can use a QMC simulation to sample a sequence $\mathcal{C}_1, \dots, \mathcal{C}_{N_{\text{steps}}}$ of values of \mathcal{C} , and obtain an alternative estimator for $\bar{n}(\mathbf{k})$,

$$\bar{n}(\mathbf{k}) \simeq \frac{1}{N_{\text{steps}}} \sum_{j=1}^{N_{\text{steps}}} \bar{n}(\mathbf{k} | \mathcal{C}_j). \quad (3.114)$$

This estimator has improved convergence properties, especially in the large- k regime (corresponding to small distances between \mathbf{x} and \mathbf{y} , cf. Fig. 3.20), as it does not sample \mathbf{x} and \mathbf{y} , but the set \mathcal{C} .

We now turn to the analytic determination of $\bar{n}(\mathbf{k} | \mathcal{C})$. The conditional probability $P_{\text{end}}(\mathbf{x}, \mathbf{y} | \mathcal{C})$ is known explicitly, as it is proportional to the product of

$$\rho_1(\mathbf{A}, \mathbf{x}; \Delta_s \tau) \rho_1(\mathbf{B}, \mathbf{E}; \Delta_s \tau) \rho_1(\mathbf{E}, \mathbf{C}; \Delta_s \tau) \rho_1(\mathbf{y}, \mathbf{D}; \Delta_s \tau) \quad (3.115)$$

and

$$g^{\text{rel}}(\mathbf{A} - \mathbf{B}, \mathbf{x} - \mathbf{E}; \Delta_s \tau) g^{\text{rel}}(\mathbf{D} - \mathbf{C}, \mathbf{y} - \mathbf{E}; \Delta_s \tau). \quad (3.116)$$

Thus we can rewrite Eq. 3.113 as

$$\bar{n}(\mathbf{k}|\mathcal{C}) = \frac{h(\mathbf{k}, \mathbf{A}, \mathbf{B}, \mathbf{E}) h(-\mathbf{k}, \mathbf{D}, \mathbf{C}, \mathbf{E})}{h(0, \mathbf{A}, \mathbf{B}, \mathbf{E}) h(0, \mathbf{D}, \mathbf{C}, \mathbf{E})}, \quad (3.117)$$

with

$$\begin{aligned} h(\mathbf{k}, \mathbf{A}, \mathbf{B}, \mathbf{E}) \equiv & \left(\frac{2\pi\hbar^2\Delta_s\tau}{m} \right)^{3/2} \times \exp \left(\frac{m(\mathbf{B} - \mathbf{E})^2}{2\hbar^2\Delta_s\tau} \right) \times \\ & \times \int d\mathbf{x} \rho_2(\{\mathbf{A}, \mathbf{B}\}, \{\mathbf{x}, \mathbf{E}\}; \Delta_s \tau) e^{-i\mathbf{k}\cdot\mathbf{x}}. \end{aligned} \quad (3.118)$$

Eq. 3.117 is such that $\bar{n}(\mathbf{k} = 0|\mathcal{C}) = 1$. By writing ρ_2 as the sum of a non-interacting term plus a correction (cf. Eq. 2.29), we can split h into the sum of the two corresponding contributions, h_{ideal} and h_{corr} . The non-interacting term yields

$$h_{\text{ideal}}(\mathbf{k}, \mathbf{A}, \mathbf{B}, \mathbf{E}) = e^{-i\mathbf{k}\cdot\mathbf{A}} \exp \left(-\frac{\hbar^2\Delta_s\tau k^2}{2m} \right). \quad (3.119)$$

The term due to interactions reads

$$h_{\text{corr}}(\mathbf{k}, \mathbf{A}, \mathbf{B}, \mathbf{E}) = e^{-i\mathbf{k}\cdot\mathbf{E}} \frac{1}{b'v} \exp \left(-(e')^2 + \frac{(b')^2 + v^2}{4} \right) (I_+ - I_-), \quad (3.120)$$

with the shorthands

$$I_{\pm} = e^{\mp \frac{b'v}{2}} \operatorname{erfc} \left(\frac{b' \mp v}{2} \right), \quad (3.121)$$

and

$$\mathbf{b}' = \frac{\mathbf{A} - \mathbf{B}}{\sqrt{2\hbar^2\Delta_s\tau/m}} \quad (3.122)$$

$$\mathbf{e}' = \frac{\mathbf{A} - \mathbf{E}}{\sqrt{2\hbar^2\Delta_s\tau/m}} \quad (3.123)$$

$$v = \sqrt{(2\mathbf{e}' - \mathbf{b}')^2 - \frac{2\hbar^2\Delta_s\tau}{m} \mathbf{k}^2 - 2i\sqrt{\frac{2\hbar^2\Delta_s\tau}{m}} (2\mathbf{e}' - \mathbf{b}') \cdot \mathbf{k}}. \quad (3.124)$$

The result in Eq. 3.120 is obtained via the analytic continuation technique: The integration is first performed for an imaginary momentum $\mathbf{k} = \mathbf{k}^*/i$, and the replacement $\mathbf{k}^* \rightarrow i\mathbf{k}$ is used in the final result. To support the validity of this procedure, we have verified that the analytical result for h (the sum of h_{ideal} and h_{corr}) agrees to a high precision with a direct numerical quadrature based on the definition in Eq. 3.118.

The analytical knowledge of h gives direct access to $\bar{n}(\mathbf{k}|\mathcal{C})$, through Eq. 3.117, so that we can use the improved estimator in Eq. 3.114 to measure $\bar{n}(\mathbf{k})$. For the case of $N = 2$ particles in free space, the derivation of this estimator does not include any approximation. For particles in a periodic box, however, the derivation of h_{ideal} and h_{corr} only holds approximately. The approximation consists in replacing the integrals over the finite-box volume with the corresponding infinite-space integrals. This is a completely controlled approximation, since the factors in Eq. 3.115 decay exponentially for large $|\mathbf{x} - \mathbf{A}|$ or $|\mathbf{y} - \mathbf{D}|$, on a length scale given by

$$\lambda_{\text{ABCDE}} = \sqrt{\frac{2\pi\hbar^2\Delta_s\tau}{m}} \quad (3.125)$$

The approximation is valid for $\lambda_{\text{ABCDE}} \ll L$. As shown in Fig. 2.3, the improved estimator correctly captures the momentum distribution at all momenta. $\bar{n}(\mathbf{k}|\mathcal{C})$ already decays as k^{-4} , with a prefactor $\text{pref}(\mathcal{C})$. Thus the average of $\bar{n}(\mathbf{k}|\mathcal{C})$ over \mathcal{C} necessarily decays as k^{-4} , with the prefactor

$$\int d\mathcal{C} p^*(\mathcal{C}) \times \text{pref}(\mathcal{C}). \quad (3.126)$$

When the distances $|\mathbf{E} - \mathbf{A}|$ and $|\mathbf{E} - \mathbf{D}|$ are large, compared to λ_{ABCDE} , the effect of the interactions is suppressed, and $\text{pref}(\mathcal{C})$ is close to zero. If these distances are small, however, the presence of \mathbf{E} close to the open ends \mathbf{x} and \mathbf{y} causes $\text{pref}(\mathcal{C})$ to be significantly different from zero.

The calculation of $\bar{n}(\mathbf{k})$ above cannot be directly extended to more than two particles, thus we develop an approximate scheme to employ the improved estimator in a N -body simulation. We first split the open sector into the subsets L and NL of local and non-local configurations. These are defined through the following procedure:

1. The endpoints \mathbf{x} and \mathbf{y} of an open path are identified, as in Fig. 3.20.
2. \mathbf{A} is found by starting from \mathbf{x} and following the path backwards for Δ_s imaginary-time slices. \mathbf{B} is the bead closest to \mathbf{A} , on slice $s_{\text{cut}} - \Delta_s$.
3. \mathbf{D} is found by following the path that starts at \mathbf{y} for Δ_s slices, and \mathbf{C} is identified as the bead on slice $s_{\text{cut}} + \Delta_s$ which is closest to \mathbf{D} .
4. If \mathbf{B} and \mathbf{C} belong to the same path⁶, and if the five positions $\mathbf{A}, \mathbf{B}, \mathbf{C}, \mathbf{D}, \mathbf{E}$ are “close” to each other, then the configuration is part of the L sector, otherwise it is assigned to the NL sector.

The criterion for closeness, in point 4, is still to be defined. The separation into L and NL sectors naturally leads to the following exact rewriting of $\bar{n}(\mathbf{k})$:

$$\bar{n}(\mathbf{k}) = f_L \times \bar{n}_L(\mathbf{k}) + f_{NL} \times \bar{n}_{NL}(\mathbf{k}), \quad (3.127)$$

⁶This is always the case for the two-body configuration in Fig. 3.20, but it is not generally true for $N > 2$.

where f_L and f_{NL} are the fractions of configurations in the L and NL sectors. $\bar{n}_L(\mathbf{k})$ and $\bar{n}_{NL}(\mathbf{k})$ are the averages of $\exp(-i\mathbf{k} \cdot \mathbf{r})$ restricted to one of the two configuration subspaces, and they satisfy

$$\bar{n}_L(0) = \bar{n}_{NL}(0) = 1. \quad (3.128)$$

The L/NL separation is useful because, under certain conditions, only \bar{n}_L significantly contributes to the large- k tail of $\bar{n}(\mathbf{k})$. As assumed in the pair-product approximation (*cf.* Section 3.2.1), beyond-two-body physics has negligible effects at high temperature. If λ_{ABCDE} is small (as compared to the typical interparticle distance $\rho^{-1/3}$), the probability of finding two bosons in a region of volume $(\lambda_{ABCDE})^3$ is small, and the probability of finding three bosons is strongly suppressed. This implies that for a local configuration the probability distribution for \mathbf{x} and \mathbf{y} can be approximated by $P_{\text{end}}(\mathbf{x}, \mathbf{y}|\mathcal{C})$, which is the exact expression if only the two close-by bosons are considered. All the steps which lead to the improved estimator also hold (approximately) for N -body configurations in the L sector, and the expression for $\bar{n}(\mathbf{k})$ can be also used for $\bar{n}_L(\mathbf{k})$. However, this is not true for a non-local configuration, since in this case the effects due to more than two particles can be relevant. Therefore, $\bar{n}_{NL}(\mathbf{k})$ can only be computed through the naive estimator. We can then define the features that a “good” locality criterion (defined in practice by the definition of closeness, in point 4 above) should have:

1. It has to be inclusive enough, which is obtained by setting a large Δ_s , and by defining closeness (*cf.* point 4, at page 103) through a large length scale. In this case, the large- k part of $\bar{n}_{NL}(\mathbf{k})$ is approximately exponentially suppressed, and in a QMC calculation it is dominated by statistical noise. All configurations which significantly contribute to the k^{-4} tail are then counted in the L sector.
2. Δ_s and the leg n th scale for the definition of closeness have to be small enough, so that for all configurations in the L sectors the effect of a third particle on the probability of \mathbf{x} and \mathbf{y} can be neglected, and the two-body approximation is valid.

Given these two conditions, Eq. 3.127 is approximated by truncating the tail of $\bar{n}_{NL}(\mathbf{k})$, which we assume to include only statistical noise for k larger than a certain cutoff momentum. The existence of a good locality criterion is not guaranteed, and the validation of this approximation has to be performed a-posteriori, by comparing the contact parameter extracted from $n(\mathbf{k})$ with the unbiased value obtained from $g^{(2)}(\mathbf{r})$ (*cf.* Fig. 4.11b). If the former is significantly smaller, then the estimator described in this section cannot be used, and we have to fall back on the inefficient but unbiased naive estimator.

In Sections 4.3 and 4.4, we measure the momentum distribution for a large system of unitary bosons, across the whole phase diagram. The regime where the naive estimator performs worst (that is, where $n(\mathbf{k})$ has the strongest statistical fluctuations, at large k) is for high temperature, where the prefactor of the k^{-4} tail is small (*cf.* Figs. 4.10 and 4.11). In this regime, the improved estimator is only weakly biased, since the two-body approximation for the configurations in the L subspace is valid, at high temperature.

Therefore we are able to use it to measure $n(\mathbf{k})$ in this regime, for systems with large N (*cf.* Fig. 4.10). At intermediate or low temperatures, we do not find a satisfactory locality criterion, so that we have to fall back on the naive estimator. While this is an unbiased estimator, it requires a considerably longer simulations, and it cannot reach large momenta (see for instance Fig. 4.15).

Conclusion

This chapter concerns the path integral QMC technique, that gives access to the thermodynamics of bosonic systems. The open/close scheme (*cf.* Section 3.2.1), in particular, allows to measure key observables related to Bose-Einstein condensation and to the peculiar properties of the unitary gas. Some modifications to the ordinary path integral QMC method are necessary, to treat bosons with zero-range unitary interactions. These are made possible by the analytic knowledge of the two-body density matrix (*cf.* Section 2.1.2). As a main original contribution, we introduced a two-body direct-sampling move, which represents the optimal Monte Carlo solution at the $N = 2$ level (*cf.* Section 3.2.2.3). The same two-body move can be integrated in the many-body algorithm. This solves the technical problem of pinning, that is, the difficulty for the algorithm to separate two paths after they get at extremely short distance. Moreover, we designed an improved momentum-distribution estimator (*cf.* Section 3.4.2), which can properly capture the large- k tail of $n(\mathbf{k})$ (to be compared with the strong statistical fluctuations of the naive estimator in this regime). While being unbiased for $N = 2$, its generalization to the many-body case is only valid in a certain temperature regime (*cf.* Section 4.3.1).

CHAPTER 4

Many-body unitary bosons

In this chapter, we study the unitary Bose gas through the QMC method described in Chapter 3. By extending the considerations of Chapter 2 from $N = 2, 3$ to the full many-body problem, we construct the phase diagram for bosons in a homogeneous periodic box. In the unitary limit, the diverging scattering length does not provide a length scale. The phase behavior is then determined by three parameters: The thermal wavelength λ_{th} , the typical interparticle distance $\rho^{-1/3}$ and the three-body cutoff R_0 . Two dimensionless combinations of these parameters fix a state of the system, as schematically represented in Fig. 4.1. The phase diagram includes the three phases previously identified for trapped systems [12]: The normal gas at high temperature, and the BEC and Efimov-liquid phases at low temperature.

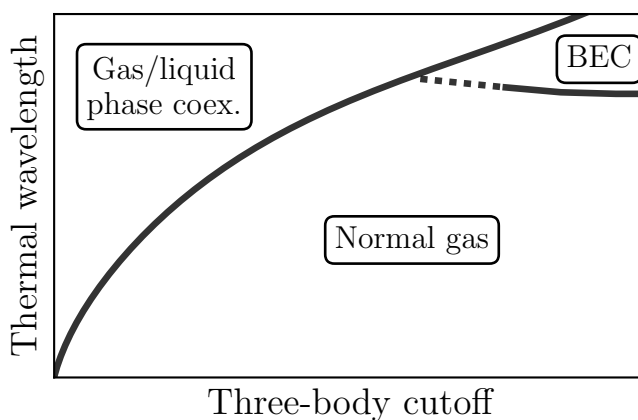


Figure 4.1: Phase diagram for unitary bosons in the NVT ensemble, at fixed density.

The Efimov liquid appears through phase separation, where a stable liquid droplet coexists with a low-density gas. In Section 4.2 we describe this coexistence, both through an analytic model and through the QMC method.

In the normal-gas and BEC phases the system remains homogeneous. For both these phases, we compute the momentum distribution $n(\mathbf{k})$ and the two-body contact parameter (*cf.* Sections 4.3 and 4.4). At low temperature, we compare our QMC results to the experimental momentum distribution [78] and to theoretical predictions for the ground-state contact density [163, 164, 165]. Moreover, we determine the critical temperature T_c for Bose-Einstein condensation.

In the construction of the many-body density matrix ρ_N , at the basis of the QMC method, two- and three-body interactions are included in an approximate way (*cf.* Chapter 3). Before studying the phase diagram of unitary bosons, we characterize these approximations, to validate the QMC scheme (*cf.* Section 4.1). The bias related to the approximate way to include the hyperradial cutoff in ρ_N is reduced by a calibration based on Efimov-trimmers properties.

4.1 Imaginary-time discretization revisited

Our QMC scheme is based on two approximations: The two-body zero-range potential is treated via the pair-product approximation (PPA), while the three-body cutoff is incorporated in the many-body density matrix through a Trotter break-up (*cf.* Section 3.2.1). Both approximations are exact in the limit of continuous paths, where the imaginary-time discretization τ vanishes. At density ρ , the PPA becomes exact in the limit $\lambda_s \rho^{1/3} \rightarrow 0$, while the Trotter scheme for the three-body cutoff requires $R_0 / \lambda_s \rightarrow 0$ (at a fixed value of $R_0 \rho^{1/3}$). In practice, these approximations are considered valid at a small-enough discretization interval $\tau = \beta/S$, where the physical observables show weak or no dependence on τ (within their statistical errors). For a given set of physical parameters (density, temperature and three-body cutoff), the largest valid value of τ (that is, the value for which observables become τ -independent) has to be determined explicitly. The goal of high-precision approximations is to allow the use of a larger τ , to speed up the numerical calculations.

The standard analysis consists in studying the dependence of observables on τ (or, equivalently, on the single-slice thermal wavelength λ_s). For the unitary Bose gas, this is shown in Fig. 4.2 (panels b and c), for the condensate and superfluid fractions and for the contact density. At the values of λ_s shown in the figure, these observables do not saturate towards a constant value, at small $\lambda_s \rho^{1/3}$. This means that an even larger number of slices would be needed. This strong dependence on τ is a consequence of the Trotter break-up for the three-body cutoff, rather than of the PPA. The first reason is that the PPA-validity parameter $\lambda_s^3 \rho$ reaches values smaller than 10^{-3} , where $\lambda_s^3 \rho \ll 1$ is clearly true. Furthermore, the explanation follows from the results obtained for the

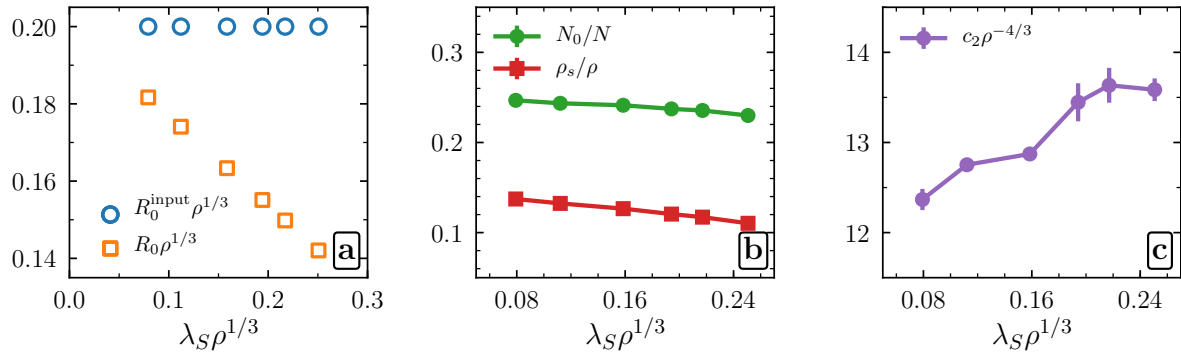


Figure 4.2: Effects of imaginary-time discretization, for fixed R_0^{input} . Panel **a**: Three-body cutoff given as an input (blue circles) and effective R_0 (orange squares, obtained through Eq. 2.74), for different values of the single-slice thermal wavelength λ_s . Panel **b**: Condensate fraction (green circles) and superfluid fraction (red squares), for $N = 48$ unitary bosons with the three-body cutoff values reported in panel **a**, at temperature $T = 1.0063 \times T_c^0$. Panel **c**: Contact density c_2 , obtained from the pair-correlation function $g^{(2)}(\mathbf{r})$ through Eq. 2.47. Physical parameters are the same as in panel **b**.

ground state of three unitary bosons (see Section 2.2.1). The input value R_0^{input} of the three-body cutoff is modified by the fact that the imaginary-time interval τ is finite. This leads to an effective cutoff R_0 , which is a function of τ and R_0^{input} (cf. Eq. 2.74). For the data shown in Fig. 4.2, the deviation of R_0 from R_0^{input} is relevant, remaining as large as the 10% of R_0^{input} for the smallest value of $\lambda_s \rho^{1/3}$ considered. Therefore, keeping R_0^{input} fixed and changing τ describes significantly different physical states, since these are defined by R_0 rather than by R_0^{input} . This confirms that the Trotter break-up is not efficient for the case of hard-core potentials, where it requires a large number of slices, and indeed it is rarely used in this context. For QMC simulation of hard spheres, this approximation can be replaced by the PPA, making use of the exact two-body density matrix [47]. In other studies of the unitary Bose gas, the three-body hard-core regulator is replaced by a power-law three-body repulsion, simpler to treat within a Trotter break-up [72, 53].

In this work, we use the exact knowledge of the Efimov-trimer wave function to be able to choose larger values of τ . The three-body simulations described in Sections 2.2.2 and 2.2.2.1 allow us to obtain the effective cutoff R_0 as a function of τ and R_0^{input} , through Eq. 2.74. For three particles, using the effective R_0 as a state variable is fully justified, as it leads to the agreement with some exact properties of Efimov trimers (cf. Figs. 2.6 and 2.7). In this way, the hyperradial cutoff is included exactly in the three-body density matrix. The remaining condition for the choice of τ only concerns the PPA validity, and not the three-body cutoff. The same approach can be generalized to the case of a homogeneous N -body system: To obtain the physical properties of the system with

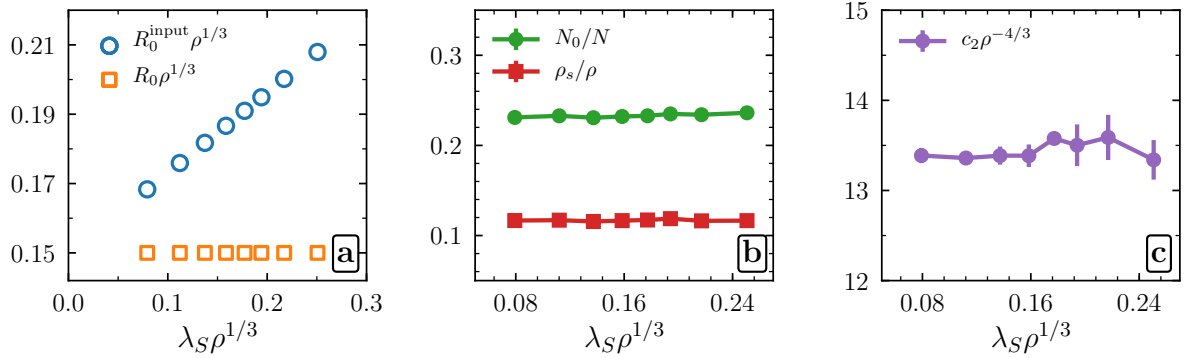


Figure 4.3: Effects of imaginary-time discretization, for fixed R_0 . Same notation as in Fig. 4.2, but the effective R_0 (rather than the input R_0^{input}) is kept constant (*cf.* panel a).

cutoff R_0 , we simulate an auxiliary system with cutoff R_0^{input} , chosen via Eq. 2.74 for a given value of τ . The corresponding analysis of the dependence on the imaginary-time discretization is shown in Fig. 4.3, where R_0 (rather than R_0^{input}) is kept constant. All three observables considered (superfluid and condensate fractions, and two-body contact) show an extremely weak dependence on λ_s , and they are essentially constant for $\lambda_s \rho^{1/3} \lesssim 0.2$. This justifies the use of the effective R_0 as a state variable. By lifting the requirement that $\lambda_s \ll R_0^{\text{input}}$, the only condition for the validity of the discretized N -body density matrix is the one for the validity of the PPA. The results in Fig. 4.3 show that this condition is clearly met.

4.2 Efimov liquid

Unitary bosons, defined by the Hamiltonian in Eq. 2.68, have two different transitions from the normal-gas phase, upon lowering the temperature [12]: When R_0 is large enough, a homogeneous BEC phase is formed (*cf.* Section 4.4), while for small R_0 the Efimov-liquid phase appears. This liquid phase has a large density (with the three-body cutoff preventing its collapse), and by the typical properties of a bosonic quantum-degenerate phase.

The existence of the liquid phase is connected to other theoretical predictions concerning clusters of N strongly-interacting bosons. In Ref. [71], up to $N = 13$ bosons were studied through Diffusion Monte Carlo, within a model including short-ranged two-body interactions with large scattering length, and the hard-core three-body regulator (*cf.* Eq. 2.67). The N -body cluster states which were obtained are tied to Efimov trimers, and inherit their universal character: Two cluster states tied to consecutive trimers at unitarity would have energies related through Eq. 2.60. At unitarity, the energies of the largest clusters ($N \gtrsim 9$) scale linearly with N . This suggests the existence of well-defined

phase, in the large- N limit, with constant energy per particle and with a bounded density (resulting from the balance between two- and three-body interactions). The QMC studies in Ref. [12] and in the current work provide additional evidence for the existence of this phase, which here is studied for finite temperature and larger system sizes ($N \approx 10^2$).

More recently, the ground state for clusters up to $N = 15$ were computed through path-integral Monte Carlo, for a similar model [72]. In this case, two-body zero-range unitary interactions were used (*cf.* Section 2.1), as in the current work. The hard-core three-body cutoff, however, was replaced by a power-law repulsive potential, $V_3(R) = C_p/R^p$. This turns into the hard-core regulator for $p \rightarrow \infty$. The ground states of Ref. [72] show a dependence on the power-law exponent p , which cannot be explained in terms of the three-body length scale $1/\kappa_0$ (*cf.* Section 2.2), therefore not fitting within Efimov universal systems. Nevertheless, a weaker kind of universality is observed, since the dependence on p is strongly reduced if the inverse N -body binding momentum is used as a length scale.

In this section we describe Efimov-liquid droplets at thermal equilibrium, which may be linked to the states computed in Refs [71] and [72]. After describing the instability towards the formation of liquid droplets via an analytical model (*cf.* Section 4.2.1), we present the direct observation of this instability through QMC calculations (*cf.* Section 4.2.2). A systematic comparison of the Efimov-liquid droplets with the states in Refs [71] and [72] is not pursued in this work.

4.2.1 Liquid/gas phase coexistence

In this section, we use an analytic model for unitary bosons, and compare its results with those obtained via QMC (*cf.* Section 4.2.2). In the NVT ensemble, the Efimov-liquid phase appears in the form of phase coexistence: Thermodynamically stable configurations consist of a liquid droplet at equilibrium with the surrounding gas. A clear distinction between the two coexisting phases is only obtained for large N . Small droplets are harder to describe, as their boundary is not sharply defined. The study the liquid and gas phases independently, without phase separation, would require using different ensembles, in which either N or V are allowed to fluctuate.

We consider an analytic model where the two coexisting phases (dilute gas and Efimov liquid) are treated separately [12]. For a system characterized by the (N, V, T) variables, we compute the free energy of a configuration where the N bosons are divided into a single small cluster with l particles and a gas of $N_{\text{gas}} = N - l$ particles. The density of the liquid is kept fixed and equal to $\rho_{\text{liq}} = (3.65R_0)^{-3}$ (*cf.* Section 4.2.2), where R_0 is the hyperradial cutoff. This implies that the gas density,

$$\rho_{\text{gas}} = \frac{N - l}{V - l/\rho_{\text{liq}}}, \quad (4.1)$$

depends on l . This dependence is negligible when $N \gg l$. For a liquid droplet, we assume that the free energy F_{liq} corresponds to

$$F_{\text{liq}}(l) \approx E_{\text{liq}}(l), \quad (4.2)$$

where E_{liq} is the energy of the droplet, and we neglect the entropic part of F_{liq} (which is valid at low temperature). The droplet is expected to be incompressible, with its properties not depending on temperature. The cluster energies $E_{\text{liq}}(l)$ are reported in Ref. [71], for $l \leq 13$, in units of the Efimov-trimer binding energy E_T (cf. Eq. 2.65). The extrapolation of these results for large- l reads

$$E_{\text{liq}}(l) = -|E_T| (-37.4 + 9.75 \times l). \quad (4.3)$$

The free energy of the dilute unitary Bose gas, in contrast, is estimated through the virial-expansion technique [166], which gives the physical properties of the system as an expansion in powers of $\lambda_{\text{th}}^3 \rho$. Within this scheme, the pressure at density ρ is expressed as

$$\frac{\beta P}{\rho} = \sum_{q=1}^{\infty} a_q \times (\lambda_{\text{th}}^3 \rho)^{q-1}. \quad (4.4)$$

The virial coefficients a_q entering Eq. 4.4 are related to the coefficients b_q of the cluster expansion, which is the analogous expansion of thermodynamic quantities in powers of the gas fugacity. The first three virial coefficients read

$$\begin{cases} a_1 &= 1, \\ a_2 &= -b_2, \\ a_3 &= 4b_2^2 - 2b_3. \end{cases} \quad (4.5)$$

The cluster coefficients up to b_3 were computed analytically for the unitary Bose gas [13]. The first non-trivial coefficient reads

$$b_2 = \frac{9}{2^{5/2}}, \quad (4.6)$$

while b_3 is obtained as an explicit function of βE_T . By using Eq. 4.4 and the fact that $P = -\partial F/\partial V$, we can compute the virial expression for the gas free energy, $F_{\text{gas}}(N, V, T)$. This is obtained by integrating the pressure for volumes between V and V_0 , and taking the limit of $V_0/\lambda_{\text{th}}^3 \rightarrow \infty$. The result reads

$$F_{\text{gas}}(N, V, T) = F_{\text{gas}}^0(N, V, T) + \frac{N}{\beta} \sum_{q>1} \frac{a_q}{q-1} (\rho \lambda_{\text{th}}^3)^{q-1}, \quad (4.7)$$

where F_{gas}^0 is the free energy of an ideal classical gas

$$\beta F_{\text{gas}}^0(N, V, T) = N \log \left(\frac{\lambda_{\text{th}}^3}{V} \right) + \log(N!). \quad (4.8)$$

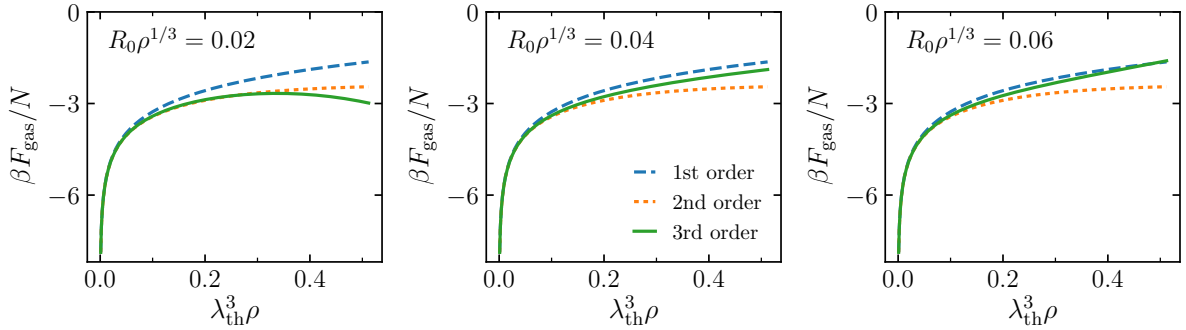


Figure 4.4: Rescaled free energy per particle, $\beta F_{\text{gas}}/N$, obtained through Eq. 4.7. The virial expansion is truncated at the first (blue dashed line), second (orange dotted line) or third (green solid line) order, and different panels correspond to different values of R_0 .

Through Eq. 4.7 and the explicit knowledge of b_3 , we have access to $F_{\text{gas}}(N, V, T)$ up to the third order in the virial expansion (*cf.* Fig. 4.4).

By combining Eqs. 4.2 and 4.7 for F_{liq} and F_{gas} , we can compute the free energy $F_{\text{coex}}^N(l)$ of a liquid droplet of l particles surrounded by a dilute gas of $N - l$ particles. This reads

$$F_{\text{coex}}^N(l) = E_{\text{liq}}(l) + F_{\text{gas}}(N - l, V - l/\rho_{\text{liq}}, T), \quad (4.9)$$

for given values of N , V and T . In particular, we consider the free-energy cost for nucleating a liquid droplet of l particles:

$$\Delta F(l) = F_{\text{coex}}^N(l, V, T) - F_{\text{coex}}^N(0, V, T), \quad (4.10)$$

The shape of $\Delta F(l)$ strongly depends on the temperature (*cf.* Fig. 4.5). At high temperature, $\rho \lambda_{\text{th}}^3 \ll 1$, the main contribution in $\Delta F(l)$ is $F_{\text{gas}}(N - l, V - l/\rho_{\text{liq}}, T) - F_{\text{gas}}(N, V, T)$, which is a monotonously increasing function of l . This situation corresponds to a stable homogeneous phase. At intermediate temperature, in contrast, $\Delta F(l)$ develops a maximum, at a critical droplet size $l = l^*$. In this case, the homogeneous phase (where $l = 0$) is only metastable, while the thermodynamically stable phase includes a liquid droplet with large l .

When considering dynamical properties of the system, the presence of a free-energy barrier $\Delta F(l^*) > 0$ implies that droplets are stable only when they are formed by $l > l^*$ particles. The corresponding nucleation rate per volume is proportional to $\exp(-\beta \Delta F(l^*))$, where $\Delta F(l^*)$ is the free-energy barrier to overcome the critical cluster size l^* . Since $l^* > 3$ (see Fig. 4.4), the presence of strong three-body losses would effectively destabilize liquid droplets before the critical nucleus size is reached. This is consistent with the fact that no signatures of the Efimov-liquid phase are found in current experimental realizations of the low-temperature unitary Bose gas (*cf.* Section 2.3.2.1).

For a given three-body cutoff R_0 , the liquid-instability temperature T_{liq} discriminates between a monotonous curve for $\Delta F(l)$ and one with a free-energy barrier. The phase

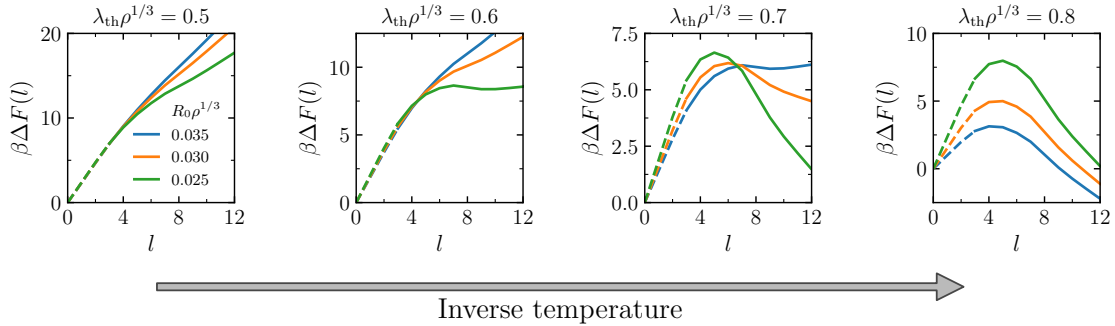


Figure 4.5: Free-energy cost $\Delta F(l)$ for a liquid droplet of l particles, at different temperatures (cf. panel titles), for large $N = 10^3$. In each panel, the three curves correspond to $R_0\rho^{1/3} = 0.025$ (green line), 0.03 (orange line), and 0.035 (blue line). The $l < 3$ portion of all curves (dashed line) is only qualitative, since liquid droplets of this size are not defined.

diagram corresponding to the Efimov-liquid transition includes two regions: A homogeneous dilute gas for $T > T_{\text{liq}}$, and phase coexistence of the gas with a liquid droplet for $T < T_{\text{liq}}$ (cf. Fig. 4.6) For a vanishing three-body cutoff ($R_0\rho^{1/3} \rightarrow 0$), the homogeneous gas is unstable at all temperatures (that is, T_{liq} becomes infinite). This is due to the fact that the liquid energy is proportional to $1/R_0^2$, and then diverges at small R_0 . Together with the fact that the liquid density (proportional to $1/R_0^3$) also diverges, this constitutes an alternative view on the Thomas collapse for bosons with zero-range pairwise interactions (cf. Section 2.2.1).

Since the virial expansion is valid at small $\rho\lambda_{\text{th}}^3$, the values of T_{liq} are not reliable for large R_0 , where the instability takes place at low temperature. It is instructive to compare the phase-boundary lines obtained through the virial expansion (as in the current work) and through the cluster expansion [51]¹. The latter is expected to be more accurate, since the cluster coefficient b_3 correctly describes the physics of up to three bosons. By a direct comparison (cf. Fig. 4.6), we find that the virial-expansion estimate of T_{liq} is valid for $R_0\rho^{1/3} \lesssim 0.04$.

4.2.2 QMC observation of the Efimov liquid

The instability towards the gas/liquid phase coexistence can also be observed directly through QMC simulations of N particles in a fixed volume V . At high temperature ($\lambda_{\text{th}}\rho^{1/3} \ll 1$), the system realizes a homogeneous phase, with a uniform density profile throughout the entire simulation box. As the temperature is lowered, before reaching T_{liq} , the effect of two-body interactions becomes more important, and small clusters of a few close-by particles appear. These clusters are not stable, and quickly dissolve as

¹The calculations in Ref. [51] are based on the incorrect expression from Ref. [10] (cf. footnote at page 45), which we have corrected to produce the curve in Fig. 4.6.

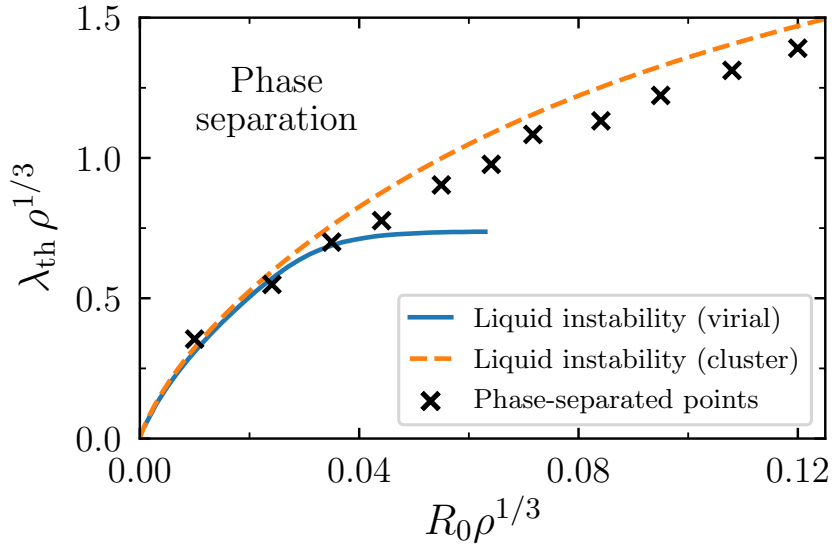


Figure 4.6: Phase diagram of the thermodynamic instability towards gas/liquid phase separation. At high temperature (small $\lambda_{\text{th}} \rho^{1/3}$) the system is a homogeneous gas, while phase separation takes place at low temperature. The instability line is computed by studying the free-energy barrier through the virial expansion (blue solid line, this work) or via the cluster expansion (orange dashed line, from Ref. [51]). In both cases, we set $\rho_{\text{liq}} = 1/(3.65 R_0)^3$. We also show points where a system of $N = 64$ bosons is positively identified as phase separated, through QMC simulations (black crosses, cf. Section 4.2.2).

the simulation proceeds. This leads to an increase of the contact density c_2 , which is well captured through a high-temperature expansion (cf. Section 4.3) and is not related to the existence of the Efimov-liquid phase. At lower temperature, in contrast, phase separation is directly observed in the QMC configurations, where we identify a dense liquid droplet surrounded by a dilute gas region which fills the remaining volume in the box (cf. Fig. 4.7).

During a QMC simulation for a point in the phase-separated region, it may happen that several small droplets form at different positions. The equilibrium configuration requires that these droplets move and eventually merge into a single one, which is directly observed for long simulation times. Our QMC scheme, however, is not optimal for this task, since moving a droplet of several bosons is a move suffering by high rejection probabilities. Other QMC methods are more appropriate to quantitatively characterize the two coexisting phases [167]. A method which partially solves the multiple-droplets issue is the simulated-annealing technique (described in Section 5.2.2). For the current case, it consists in reaching a given phase-diagram point through a sequence of successive simulations starting from high temperature. This allows us to observe the

nucleation process for systems of $N \approx 10^2$ particles, as shown in Fig. 4.7, reducing the chances of finding metastable multiple-droplets configurations. Nevertheless, a degree of uncertainty remains about the full equilibration of the QMC sampling at temperatures $T \lesssim T_{\text{liq}}$, which hinders the accurate identification of T_{liq} through QMC.

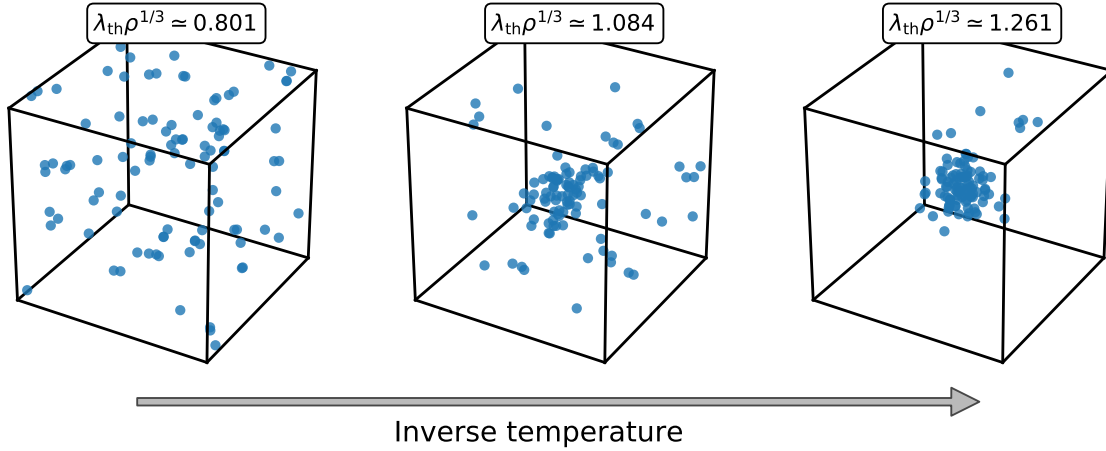


Figure 4.7: Nucleation sequence for $N = 100$, from a homogeneous gas (*left panel*) to the phase coexistence of a large droplet with a few particles in the surrounding region (*right panel*). The three-body cutoff is set to $R_0 \rho^{1/3} = 0.0717$, and the three configurations are part of a single QMC simulation with decreasing temperature.

To estimate the phase-separation instability line (*cf.* Section 4.2.1) we assume that the liquid droplet has a well-defined shape and a constant density, which is not valid for small N_{liq} . We estimate the liquid density ρ_{liq} by studying the structure of a liquid droplet through the pair-correlation function $g^{(2)}(\mathbf{r})$ (see Fig. 4.8). $r^2 g^{(2)}(\mathbf{r})$ has a peak at $r = r_{\text{peak}}$. For a spherical droplet of constant density, this peak would be at a distance close to the sphere radius (*cf.* Fig. 4.9). Thus we use the peak position in Fig. 4.8 as a fitting parameter, and identify $r_{\text{peak}}/1.05$ with the radius of the liquid droplet. The droplet volume V_{liq} is then estimated as $(4\pi/3) \times (r_{\text{peak}}/1.05)^3$. At finite distances $r \lesssim r_{\text{peak}}$, the pair-correlation function of the unitary-bosons system and of a homogeneous sphere agree (*cf.* Fig. 4.8)², justifying the assumption that Efimov-liquid droplets have a uniform density. At larger distances ($r \gtrsim r_{\text{peak}}$), the pair-correlation function of a perfectly spherical droplet rapidly decreases, and vanishes when r equals the sphere diameter. This is not the case for the observed correlation function in Fig. 4.8, as due to two reasons: The interface is not sharp, so that the distance between two particles in the droplet is not restricted to be smaller than the diameter, and the presence of the other particles (in the surrounding gas) modifies $g^{(2)}(\mathbf{r})$, increasing the probability of

²The two curves differ at vanishing distances, where the pair-correlation function of unitary bosons diverges as $1/r^2$, with a prefactor proportional to the contact density c_2 for the liquid phase.

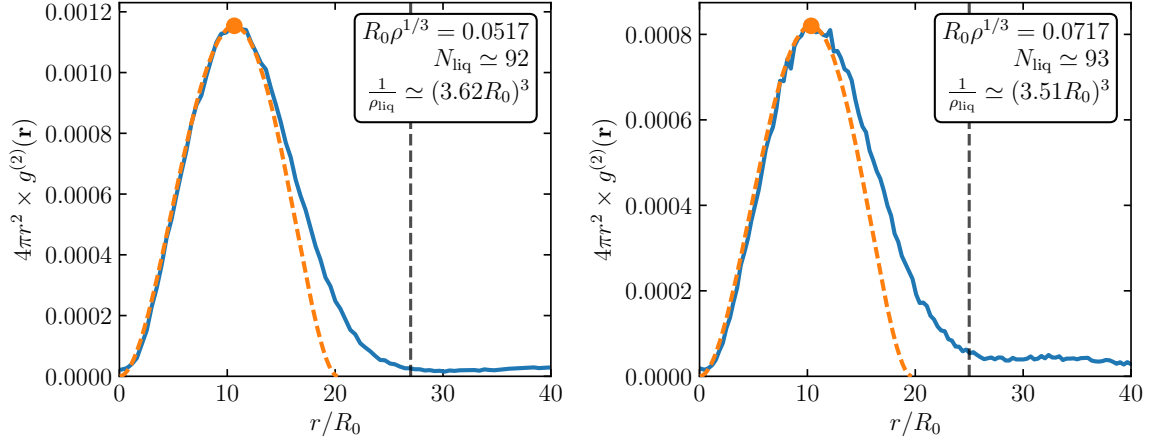


Figure 4.8: Pair-correlation function for $N = 100$ bosons in the phase-coexistence region (solid blue lines, through QMC simulation), and for a spherical droplet of constant density (orange dashed line, cf. Fig. 4.9) The two panels correspond to phase-diagram points $(R_0\rho^{1/3}, \lambda_{\text{th}}\rho^{1/3}) = (0.0517, 1.049)$ and $(R_0\rho^{1/3}, \lambda_{\text{th}}\rho^{1/3}) = (0.0717, 1.261)$. Curves in this figure are in arbitrary units, as the normalization of $g^{(2)}(\mathbf{r})$ introduced in Section 3.3.1 is only valid for a homogeneous system.

observing large distances. The fitting procedure provides an estimate of the radius and volume of the liquid droplet. To estimate ρ_{liq} , we compute the number of particles in the droplet as

$$N_{\text{liq}} = N \times \frac{\int_{r < r_{\max}} d\mathbf{r} g^{(2)}(\mathbf{r})}{\int d\mathbf{r} g^{(2)}(\mathbf{r})}. \quad (4.11)$$

The threshold r_{\max} is set at a distance where the peak in $r^2 g^{(2)}(\mathbf{r})$ is suppressed (cf. vertical dashed lines in Fig. 4.8). For the two values of R_0 considered in Fig. 4.8, the liquid fractions N_{liq}/N is approximately 0.9. The liquid density obtained in this way reads

$$\rho_{\text{liq}} = \frac{N_{\text{liq}}}{V_{\text{liq}}} = \frac{1}{(\alpha R_0)^3} \quad (4.12)$$

This quantity has strong run-to-run fluctuations, related to the imprecise definitions for N_{liq} and V_{liq} , since the boundary effects are important for the small droplet sizes considered ($N_{\text{liq}} \lesssim 100$). We have performed 56 QMC runs, at the four phase-diagram points defined by $(R_0\rho^{1/3}, \lambda_{\text{th}}\rho^{1/3}) = (0.0517, 1.0486), (0.0717, 1.2608), (0.0817, 1.3729)$, and $(0.1017, 1.418)$. The values of α vary between 3.3 and 3.9, with an average $\alpha \simeq 3.65$. The results do not depend on the three-body cutoff, implying that density is a universal property of the observed Efimov-liquid droplets. The small- r behavior of $g^{(2)}(\mathbf{r})$ for a phase-separated droplet is connected to the Efimov-liquid contact density, c_2^{liq} . The determination of c_2^{liq} , however, depends on the knowledge of N_{liq} and ρ_{liq} , which replace

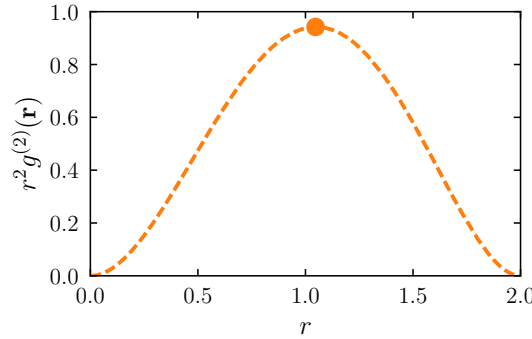


Figure 4.9: Pair-correlation function for points uniformly distributed in a sphere of unit radius, as a function of the distance r (normalized such that $\int d\mathbf{r} g^{(2)}(\mathbf{r}) = 4\pi$). The distribution has a peak at distance $r \simeq 1.05$. The curve is obtained by uniformly sampling points inside the sphere [39] and constructing the histogram of their distance.

N and ρ in Eq. 3.85. Therefore we cannot accurately quantify the contact density, due to the approximate definitions of N_{liq} and ρ_{liq} .

QMC simulations performed for several points in the phase diagram also give information about the location of the Efimov-liquid instability line, in addition to the results of the analytic models presented in Section 4.2.1. The precise curve for T_{liq} cannot be obtained from our simulations, due to a poor efficiency of our algorithm at $T \lesssim T_{\text{liq}}$. Nevertheless, we can use the QMC technique to map a sequence of points where a system with a given N is phase-separated – *cf.* Fig. 4.6. These points lie at temperatures slightly lower than the cluster-expansion instability line (*cf.* dashed line in Fig. 4.6). The shape of the line, however, is correctly captured by the analytic model.

The Efimov liquid is a quantum-coherent phase, with the same properties as a common BEC phase. This follows from the fact that its phase space density $\rho_{\text{liq}}\lambda_{\text{th}}^3$ is significantly larger than one. The coherence properties can also be observed directly in QMC simulations. The estimators described in Chapter 3 for the superfluid and condensate fractions cannot be applied directly to a phase-separated system. Measuring the average occupation for bosonic cycles of length k , we find that all lengths up to $k \approx N_{\text{liq}}$ have a finite occupation. Moreover, we observe that the one-body-reduced density matrix $g^{(1)}(\mathbf{r})$ decays to zero on a length scale which is comparable with the liquid-droplet size, which corresponds to the notion of off-diagonal long-range order (*cf.* Section 3.3.3). Both these properties are characteristic of BEC phase.

In conclusion, in Section 4.2 we have described several Efimov-liquid properties, and how this can be studied with the QMC technique. The possibility of forming and dissolving small liquid droplets, in particular, relies on the capability of both generating and removing configurations with pairs of particles at very short distance. This is the specific advantage of using our novel two-body direct-sampling move (*cf.* Section 3.2.2.3).

4.3 Normal-gas phase

The liquid instability described in the previous section is avoided if R_0 is large enough [12], which allows us to study the phase diagram of the homogeneous unitary Bose gas in all regions with $T > T_{\text{liq}}$. In this section, we consider the regime of large and intermediate temperatures, where the system is in the normal-gas phase. The low-temperature regime is then treated in Section 4.4.

4.3.1 Momentum distribution

As described in Chapter 3, our QMC algorithm allows to compute the momentum distribution $n(\mathbf{k})$ for a many-body system of unitary bosons. An example of the $n(\mathbf{k})$ curves is shown in Fig. 4.10, corresponding to three phase-diagram points with fixed three-body cutoff and different temperatures. In the following, we describe the different features present in these curves, and in particular the effect of unitary interactions.

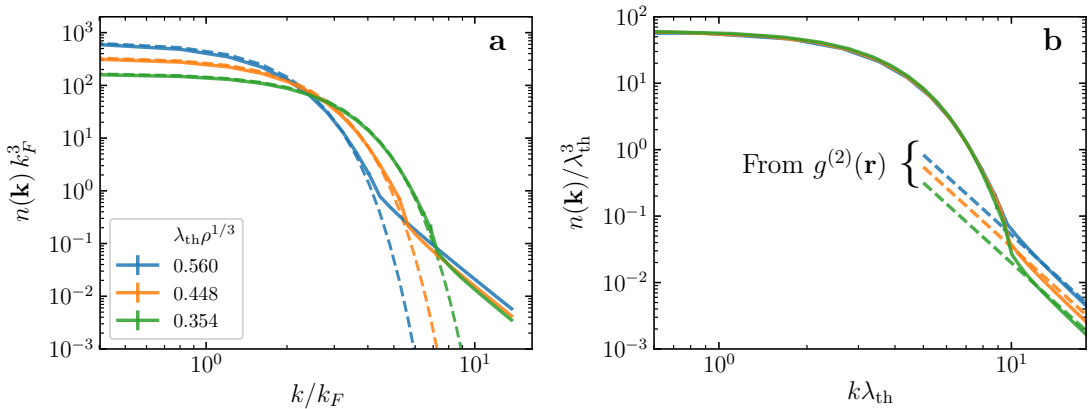


Figure 4.10: Momentum distribution for $N = 64$ unitary bosons, at fixed three-body cutoff ($R_0 \rho^{1/3} = 0.184$) and for variable temperatures (cf. legend). QMC results for $n(\mathbf{k})$ (solid lines, obtained through the improved estimator described in Section 3.4.2) are shown in different units in the two panels. Dashed lines in panel **a** correspond to the Boltzmann distribution (cf. Eq. 3.102), evaluated at the same temperatures as in the QMC simulations. In panel **b**, dashed lines mark the asymptotic tail of the momentum distribution, $n(\mathbf{k}) \simeq C_2/k^4$, with C_2 extracted from the QMC data for the pair-correlation function (cf. Eq. 2.47).

At large temperature, $\lambda_{\text{th}} \rho^{1/3} \rightarrow 0$, both quantum statistics and interparticle interactions have negligible effects on the momentum distribution, and this observable is given by the Boltzmann distribution (cf. Eq. 3.102, which is exact for non-interacting distinguishable particles). At any finite value of $\lambda_{\text{th}} \rho^{1/3}$, however, unitary zero-range

interactions lead to a qualitatively different momentum distribution: This curve develops a power-law asymptotic tail at large k , at variance with the Gaussian decay of the Boltzmann distribution (*cf.* Fig. 4.10a). For large enough temperature, the full momentum distribution is well described by the combination of a Gaussian decay at small k and a power-law decay at large k . We define k^* as the approximate momentum at which the crossover between the two curves takes place. In the high temperature regime, k^* is proportional to $1/\lambda_{\text{th}}$ ($k^* \approx 10/\lambda_{\text{th}}$, in Fig. 4.10a), meaning that for $\lambda_{\text{th}}\rho^{1/3} \rightarrow 0$ the power-law tail is only visible at exceedingly large momenta. This scaling of k^* is already observed in the momentum distribution of $N = 2$ unitary bosons, *cf.* Section 2.1.2. The two parts of $n(\mathbf{k})$, at small and large momenta, can be described independently. At small momentum, $n(\mathbf{k})$ has the same shape as for non-interacting distinguishable particles, as clearly visible in Fig. 4.10a. To compare curves at different temperatures, we express k in units of the Fermi momentum,

$$k_F = (6\pi^2\rho)^{1/3} \quad (4.13)$$

which is a scale defined at any temperature. Using the inverse thermal wavelength as a momentum unit, in contrast, directly shows that the small-momentum part of $n(\mathbf{k})$ has a universal shape (since it simply corresponds to the Boltzmann distribution), and that $k^* \approx 10/\lambda_{\text{th}}$ (*cf.* Fig. 4.10b). For large momentum, $n(\mathbf{k})$ falls off as C_2/k^4 . This is the momentum regime where the naive estimator of $n(\mathbf{k})$ has strong statistical fluctuations, thus we replace it with the improved estimator introduced in Section 3.4.2. The validity of this replacement is verified by independently computing C_2 through the pair-correlation function $g^{(2)}(\mathbf{r})$ (see Eq. 2.47). The two values of C_2 are in agreement only for $\lambda_{\text{th}}\rho^{1/3} \lesssim 0.5$. Further studies on the locality criterion (*cf.* Section 3.4.2) could improve this limitation. At lower temperature, a precise measure of the momentum distribution requires to fall back on the naive estimator (*cf.* Section 3.3.4).

Our results for $n(\mathbf{k})$ do not show signatures of subleading oscillations in the momentum distribution. For many-body states [168, 62], the predicted universal expression for the large-momentum tail of $n(\mathbf{k})$ reads

$$n(\mathbf{k}) \simeq \frac{C_2}{k^4} + \frac{C_3}{k^5} A \sin \left(2s_0 \log \left(\frac{k}{\kappa_0} \right) + \phi \right), \quad (4.14)$$

where A and ϕ are known constants, and κ_0 is the Efimov-trimer binding momentum (*cf.* Section 2.2.1). The three-body contact parameter C_3 is proportional to the probability of finding three bosons at small hyperradius. In our model, the hyperradius cannot be arbitrarily small, due to the three-body cutoff. Nevertheless, the subleading oscillations of Eq. 4.14 may appear in the momentum distribution for momenta smaller than $1/R_0$. For the curves in Fig. 4.10, the asymptotic tail in $n(\mathbf{k})$ kicks in at $k > 1/R_0$. Smaller R_0 would be required to observe subleading oscillations.

4.3.2 Contact density

We map the contact density c_2 across the entire phase diagram, by using the estimator based on the small- r limit of $g^{(2)}(\mathbf{r})$ (see Fig. 4.11a). The advantage of this estimator is that it remains practical for any temperature, unlike the computation of $\lim_{k \rightarrow \infty} k^4 n(\mathbf{k})$.

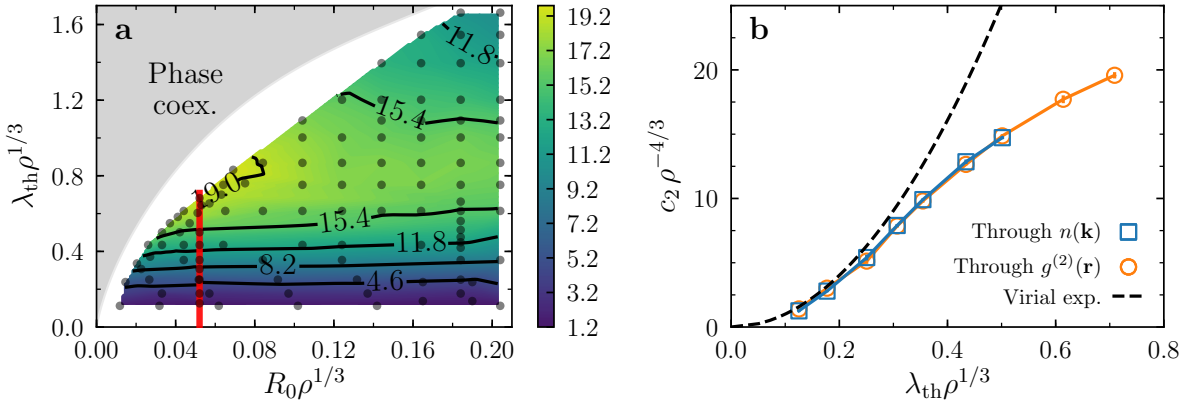


Figure 4.11: Contact-density $c_2\rho^{-4/3}$, obtained through QMC simulations of $N = 64$ unitary bosons. Panel a: The color code is a linear interpolation of $c_2\rho^{-4/3}$, which is computed at the points marked by black dots. The gray area is the phase-coexistence region (cf. cluster-expansion line in Fig. 4.6). Panel b: Contact density for fixed three-body cutoff ($R_0\rho^{1/3} = 0.0521$, red line in panel a), estimated from $n(\mathbf{k})$ (blue squares) or $g^{(2)}(\mathbf{r})$ (orange circles), and compared to the second-order virial expansion (black dashed line, cf. Eq. 4.15).

The contact density c_2 weakly depends on the three-body cutoff R_0 . This follows from the fact that constant- c_2 lines in Fig. 4.11a are almost horizontal. Exceptions to this general behavior are found only in specific regions: At the top-right corner of Fig. 4.11a, where the small number of QMC points may lead to a poor quality of the interpolation, and very close to the liquid-instability line, where the small system size ($N = 64$) might have a relevant effect. In the rest of the phase diagram, only a weak decrease of c_2 for increasing R_0 is present. This is due to the fact that the three-body repulsive potential effectively reduces the probability of two particles to be at short distance, causing a weak decrease of the contact density.

In Ref. [64], the contact density of the unitary Bose gas is computed within a theory based on the upper-branch idea and on the large- N expansion, not including any three-body regulator. The results for c_2 are compared to our QMC data in Ref. [169] (see Fig. 4.12), finding that the extrapolation of QMC data towards $R_0 = 0$ is qualitatively consistent with the upper-branch theory, at high temperature.

At large T , c_2 is given by the second-order virial expansion (see Appendix 4.A):

$$\frac{c_2}{\rho^{4/3}} = \frac{N-1}{N} \times 32\pi \left(\lambda_{\text{th}} \rho^{1/3} \right)^2. \quad (4.15)$$

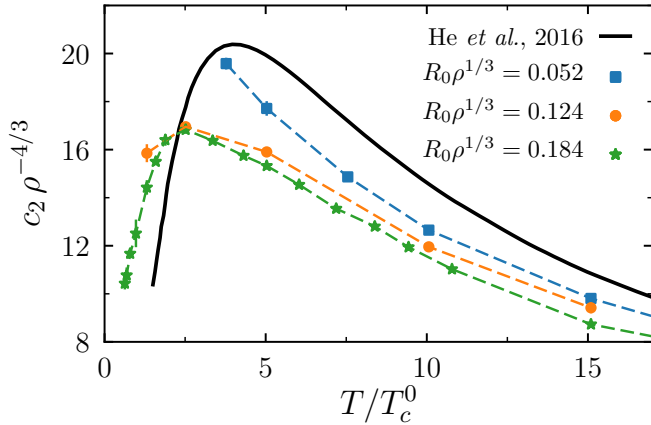


Figure 4.12: Contact-density $c_2 \rho^{-4/3}$ for three different hyperradial cutoffs (symbols, same QMC data as in Fig. 4.11a), compared with the large- N upper-branch theory [64, 169].

The comparison with QMC data (cf. Fig. 4.11b) shows that this is valid for $\lambda_{\text{th}} \rho^{1/3} \lesssim 0.3$, corresponding to $c_2 \rho^{-4/3} \lesssim 8$. For larger $\lambda_{\text{th}} \rho^{1/3}$ (that is, for lower temperature), the virial-expansion curve continues to increase, while the actual c_2 tend to saturate to a value smaller than $c_2 \rho^{-4/3} \approx 20$ (cf. Fig. 4.11a and Fig. 4.11b). For even lower temperatures, c_2 decreases again, as discussed more in detail in Section 4.4.3.

4.4 BEC phase

For large-enough three-body cutoff, the normal-gas phase is stabilized against the nucleation of an Efimov-liquid droplet. By lowering the temperature, a transition occurs towards a BEC phase, as we describe in this section. We identify the critical temperature of the transition (cf. Section 4.4.1), and study the momentum distribution and contact density inside the BEC phase (cf. Sections 4.4.2 and 4.4.3).

4.4.1 Critical temperature

The distinction between the normal-gas and BEC phases is formally defined for an infinite system, where the condensate fraction N_0/N is finite below the critical temperature T_c and vanishes for $T > T_c$. Since we consider a three-dimensional system, superfluidity and Bose-Einstein condensation are expected to take place simultaneously, so that either N_0/N or ρ_s/ρ can be chosen as an order parameter. To identify the critical temperature through the QMC results for finite systems, we use the finite-size scaling technique (cf. Section 3.4.1). For different system sizes N , we plot the rescaled superfluid fraction $N^{1/3}(\rho_s/\rho)$ as a function of temperature, and the crossing point of these curves provides

an estimate of the critical temperature T_c . For three different values of the three-body cutoff we obtain the T_c by this method (*cf.* Fig. 4.13a–c): At $R_0\rho^{1/3} = 0.164, 0.184$ and 0.204 , the critical temperature reads $T_c/T_c^0 = 0.87, 0.9$, and 0.91 (in units of the ideal-bosons critical temperature T_c^0). These quantities are consistently smaller than T_c^0 , with

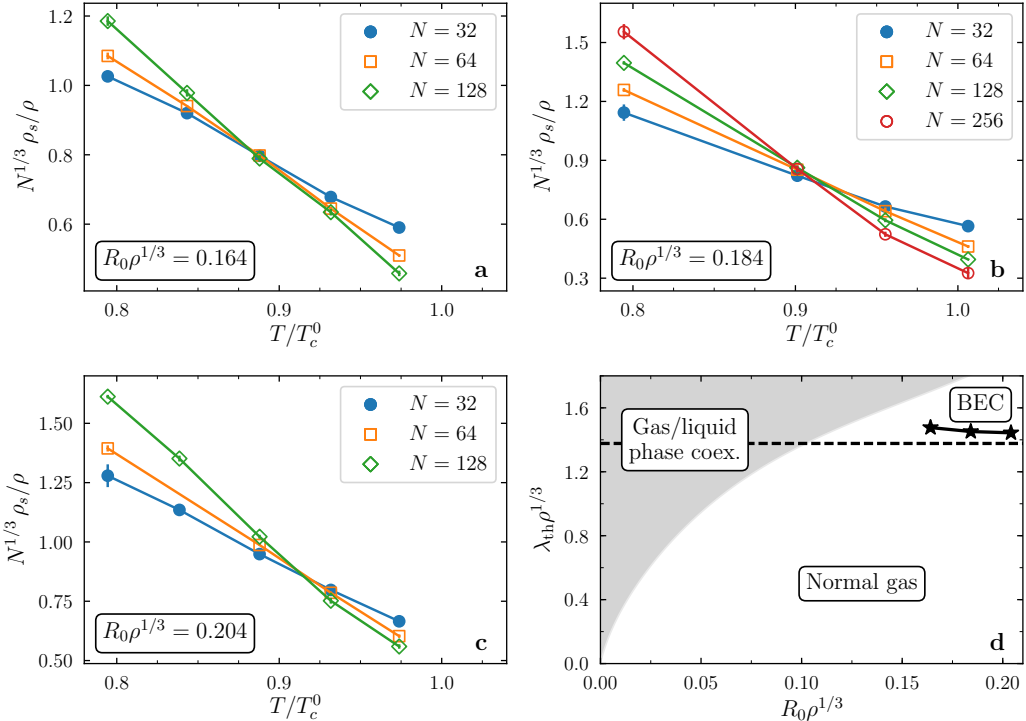


Figure 4.13: Panels a–c: Identification of the critical temperature for the superfluid transition, through the finite-size scaling of ρ_s/ρ . Different panels correspond to different three-body cutoff values, and temperatures are expressed in units of the ideal-bosons transition temperature T_c^0 (*cf.* Eq. 1.10). Panel d: Complete phase diagram for the unitary Bose gas (*cf.* Figs. 4.6 and 4.11a), including the superfluid-transition critical line (black stars). The horizontal dashed line marks the position of the BEC transition for a non-interacting Bose gas.

a relative deviation of approximately 10%. The dependence on the three-body cutoff is weak, and it consists in an increase of T_c with increasing R_0 . The fact that $T_c < T_c^0$ differs from the case of a homogeneous Bose gas with weak repulsive interactions, where the transition takes place at temperatures larger than T_c^0 [14]. The shift $T_c - T_c^0$ for the unitary Bose gas has the same sign as in liquid ${}^4\text{He}$ (*cf.* Section 1.2).

It has been predicted that the phase diagram of the unitary Bose gas also includes a triple point, where the three phases (Efimov liquid, normal gas, and BEC) coexist [12]. This could be studied by extending the normal-gas/BEC critical line (*cf.* stars in Fig. 4.13d) towards smaller values of $R_0\rho^{1/3}$, which we did not attempt in the present

work.

Two factors limit the precision of our estimate for T_c : The finite temperature grid (*cf.* Fig. 4.13) and the maximum system sizes considered ($N = 128$ or $N = 256$). Our results are not sufficient to compute the correlation-length critical exponent ν . Its estimation would be obtained by looking for the value that leads to a collapse of all QMC data onto a single universal curve, when plotting $N^{1/3}\rho_s/\rho$ vs. $(T - T_c)N^{1/(3\nu)}$ (see Section 3.4.1). Simulations of larger systems and on a denser temperature grid would be required for this task (*cf.* for instance Ref. [161]).

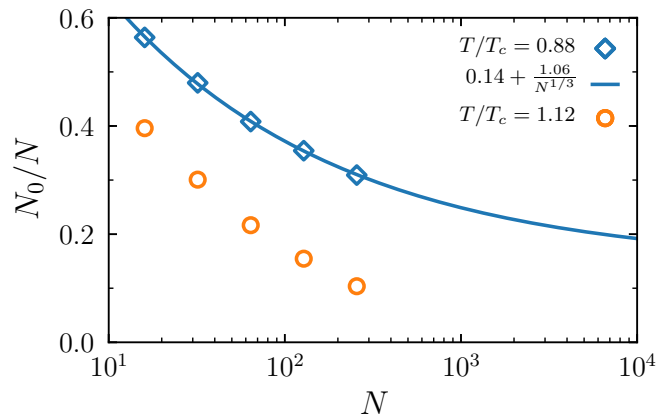


Figure 4.14: Scaling of the condensate fraction in a system of N unitary bosons, with fixed three-body cutoff ($R_0\rho^{1/3} = 0.184$). QMC results are shown for $T < T_c$ (blue diamonds) and $T > T_c$ (orange circles). At temperature $T = 0.88 T_c$, the condensate fraction tends to $N_0/N \simeq 0.14$ for $N \rightarrow \infty$, as obtained through a fit of the QMC data to Eq. 4.16 (blue solid line).

The critical temperature T_c identified above corresponds to the point such that for $T < T_c$ the superfluid density ρ_s/ρ of an infinite system becomes finite. To confirm that the phase below T_c is also a Bose-Einstein condensate, we compute the condensate fraction N_0/N . Through the current QMC algorithm, this is proportional to the ratio of the partition functions of the open and closed sectors, *cf.* Eq. 3.104. The finite-size corrections of N_0/N have different scaling with N in the normal-gas and BEC phase. In the BEC phase, one finds

$$\frac{N_0}{N} = n_0^\infty + \frac{\alpha_2}{N^{1/3}} \quad (T < T_c), \quad (4.16)$$

where n_0^∞ is the condensate fraction in the infinite-size limit. Eq. 4.16 follows from the assumption that, for a large system,

$$(g^{(1)}(\mathbf{r}) - n_0^\infty \rho) \propto \frac{1}{r}, \quad (4.17)$$

at large r . In three dimensions, Eq. 4.17 is the expected behavior for the correlation function of systems described by a two-dimensional order parameter [20], and it is valid for the one-body-reduced density matrix of a weakly-interacting Bose gas [15]. By using α_2 and n_0^∞ as fitting parameters, we find that our QMC data for finite systems are in good agreement with Eq. 4.16 (*cf.* Fig. 4.14), at $T < T_c$. This confirms that in the phase identified in this section the system is simultaneously a superfluid and a Bose-Einstein condensate.

For $T > T_c$, the system sizes addressed in our QMC calculations are insufficient to access the asymptotic large- N regime. Thus we cannot reliably extract a power-law behavior for N_0/N in this phase. Nevertheless, the data at $T = 1.12T_c$ (*cf.* Fig. 4.14) decay faster than $1/N^{1/3}$, confirming that the unitary gas is not Bose-condensed at this phase-diagram point.

4.4.2 Momentum distribution

To further characterize the BEC phase, we compute its momentum distribution (see Fig. 4.15), and describe how it differs from the momentum distribution of an ideal Bose gas. As mentioned in Section 4.3, the improved estimator for $n(\mathbf{k})$ cannot be used at

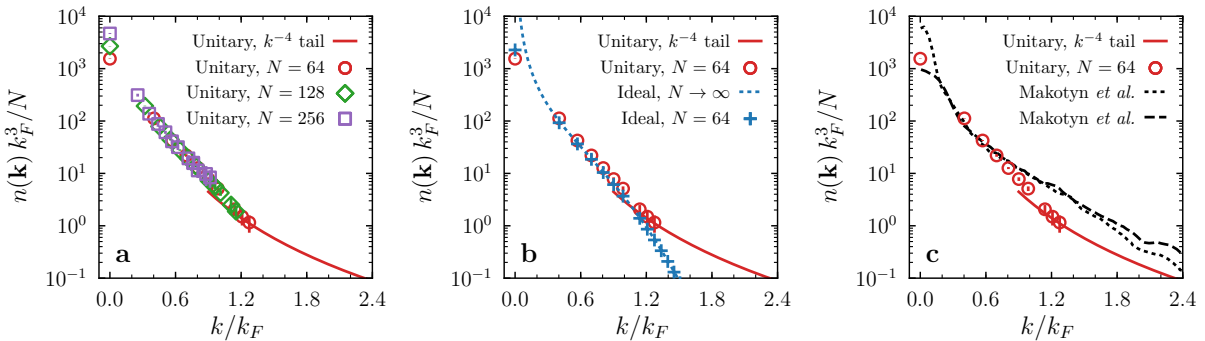


Figure 4.15: Momentum distribution of the unitary Bose gas in the BEC phase, at $R_0\rho^{1/3} = 0.184$ and $\lambda_{\text{th}}\rho^{1/3} = 1.545$. Panel **a**: $n(\mathbf{k})$ curves for different values of N (*symbols*), and asymptotic tail C_2/k^4 (*solid line*, with C_2 obtained from the pair-correlation function). Panel **b**: The $N = 64$ QMC data are compared with the curves for $N = 64$ and $N \rightarrow \infty$ ideal bosons (*plus symbols* and *dotted line*, respectively). Panel **c**: The $N = 64$ QMC data are compared with the experimental curves from Ref. [78], for average density equal to $5.5 \times 10^{18} \text{ m}^{-3}$ (*dotted line*) and $1.6 \times 10^{18} \text{ m}^{-3}$ (*dashed line*).

low temperature, and has to be replaced by the naive estimator in Eq. 3.103. This poses a limit on the largest k for which we can obtain a reasonable estimate of the momentum distribution, before statistical fluctuations become too strong, at large k . The issue becomes more relevant for large N . Nevertheless, we reach momenta large enough that the curves for $n(\mathbf{k})$ can be smoothly joined with the predicted tail C_2/k^4 , where

C_2 is obtained from the pair-correlation function (*cf.* Eq. 2.47). The two curves overlap at $k \approx 1.2k_F$ (*cf.* Fig. 4.15a). Therefore we obtain a QMC estimation for the whole momentum-distribution curve, by directly measuring $n(\mathbf{k})$ at $k \lesssim 1.2k_F$ and using the asymptotic tail for larger momenta.

In Fig. 4.15a, we show $n(\mathbf{k})$ curves for different system sizes. At finite momenta, corrections due to finite-size effects are already negligible for $N = 64$. At zero momentum, in contrast, the presence of a condensate is clearly visible in the divergence of $n(\mathbf{k} = 0)$ for large N , which is required to have a finite condensate fraction in the $N \rightarrow \infty$ limit.

We also compare the momentum distribution with the one of non-interacting bosons at the same phase-space density (*cf.* Fig. 4.15b). In the unitary Bose gas, interactions cause a depletion of the condensate, that is, a decrease of N_0/N with respect to the ideal-gas value. The fact that the condensate fraction is lowered in the presence of unitary interactions is consistent with the observed negative shift in the critical temperature, $T_c < T_c^0$. As the normalization of $n(\mathbf{k})$ is fixed, the $k = 0$ depletion needs to be compensated by the increase of the momentum distribution at other values of k . The slow-decaying power-law tail (to be compared with the exponential decay of $n(\mathbf{k})$ for the ideal Bose gas) partly contributes to this compensation. The remaining compensation consists in a larger weight of the unitary-gas momentum distribution in the intermediate- k region (*cf.* Fig. 4.15b). No additional features are observed, and in particular no signature of the universal subleading oscillations (see discussion below Eq. 4.14).

The asymptotic tail in $n(\mathbf{k})$ kicks in at $k^* \simeq 1.2k_F$, while $1/R_0$ is $1.4k_F$. The resolution of QMC results and the fact that $k^* \approx 1/R_0$ prevent us from observing the expected log-periodic oscillations (*cf.* Eq. 4.14). It is however interesting that these could be within reach, by slightly reducing T or R_0 .

We also compare our results with the experimental data of Ref. [78], the only study of the low-temperature unitary Bose gas currently available (see Section 2.3.2.1). The experimental and QMC curves are not in quantitative agreement (*cf.* Fig. 4.15c). The large-momentum tail from Ref. [78], in particular, lies systematically above our theoretical curve, approximately by a factor of two. This discrepancy is explained through the following remarks:

1. The degree of thermalization and the final temperature of the experiment are not clear (*cf.* Section 2.3.2.1), so that we cannot associate the experimental conditions to a specific point in the phase diagram. The QMC calculation, in contrast, has a well-defined temperature (which is chosen to lie in the BEC phase, for the comparison in Fig. 4.15c).
2. The experiment is performed in a harmonic trap, while the QMC curve is for a homogeneous system. The simplest approach to obtain the average contact density for a trapped system from the current QMC data would be the use of the local density approximation (see for instance Ref. [51]). The homogeneous-system c_2 has its maximum values in the normal-gas region of the phase diagram (*cf.* Fig. 4.11a),

thus the average trapped-system contact density may be larger than the one observed in Fig. 4.15c. It is then possible that combining the system inhomogeneity with our QMC data would reduce the discrepancy in the tail of $n(\mathbf{k})$.

4.4.3 Contact density

Our QMC calculations also yield the finite-temperature contact density c_2 , which can be compared with the several available predictions for its ground-state value. In Fig. 4.16, c_2 is shown for a fixed R_0 . The curve does not show any discontinuous feature at the critical temperature for the BEC transition. This is due to the fact that BEC appears in the long-range correlations (*cf.* Section 3.3.3), while c_2 is a short-range physical property. The main feature of c_2 , in contrast, is a smooth non-monotonic behavior, as already visible in Fig. 4.11a. In Ref. [64], the same feature was predicted with an approximate technique, with a peak of c_2 at $T \approx 4T_c^0$ (see also Ref. [169] for a comparison with the QMC results from the current work). No clear physical explanation for the decrease of c_2 at low temperature is currently available.

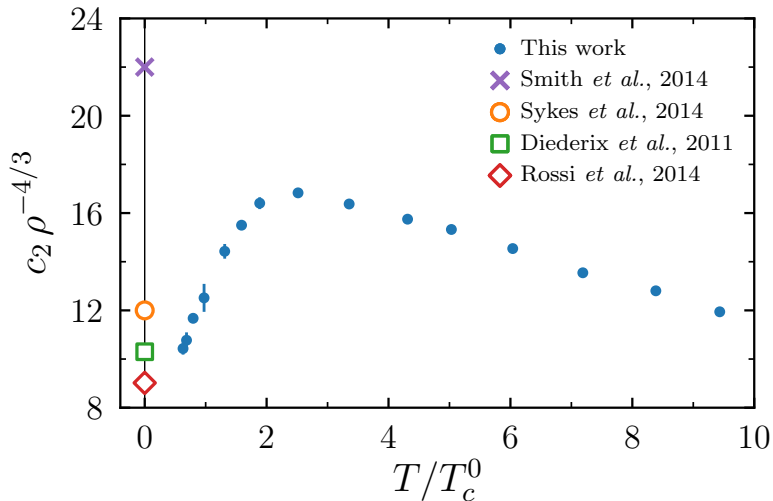


Figure 4.16: Exact results for the contact density for $R_0\rho^{1/3} = 0.184$ and low temperature (blue dots, same data as in Fig. 4.11a), and zero-temperature approximate results from Refs. [164, 163, 165]. The value from Ref. [62] is obtained through a fit of the experimental momentum distribution to the universal expression in Eq. 4.14.

Several approximate predictions exist for the ground-state value of $c_2 \rho^{-4/3}$, obtained via a Jastrow ansatz and hypernetted-chain approximation [164], a QMC calculations based on a Jastrow-Feenberg ansatz [165], and a time-dependent variational ansatz for the many-body state [163]. Our first principles low-temperature results are roughly compatible with these known values, although we did not attempt a systematic extrap-

olation towards zero temperature. In Ref. [62], a fit of the experimental momentum-distribution curve [78] with the universal zero-temperature prediction (*cf.* Eq. 4.14) leads to $c_2 \rho^{-4/3} \simeq 22$. As already mentioned in the comment of Fig. 4.15c, this value is significantly larger than the theoretical predictions (*cf.* Fig. 4.16).

Conclusion

In this chapter we have described the finite-temperature phase diagram of the model for unitary bosons which includes zero-range two-body interactions and a three-body cutoff. This was obtained with the QMC method described in Chapter 3. The direct observation of Efimov-liquid droplets (appearing as phase-separated states) allows to compute their density, which is found to be a universal property of this phase. In the remaining part of the phase diagram (corresponding to homogeneous phases), we studied the momentum distribution and its asymptotic tail. Upon decreasing the temperature from the $T \rightarrow \infty$ limit, the contact density has a non-monotonic behavior: It first increases (following its high-temperature expansion), then saturates at intermediate temperatures (with values $c_2 \rho^{-4/3} \lesssim 18$), and decreases at low temperature. The phase transition to the BEC phase has also been characterized, finding a critical temperature T_c approximately 10% smaller than the value for non-interacting bosons. The three-body cutoff R_0 is a crucial ingredient of the model, required to stabilize the homogeneous phase and prevent the nucleation of liquid droplets. In the homogeneous-phase region, however, changes due to R_0 are smooth and of a limited magnitude. This can be seen in c_2 and in T_c , and it justifies our use of the hard-core three-body regularization scheme

Appendix 4.A Contact density at high temperature

The high-temperature expansion for the contact parameter can be obtained through the pair-product ansatz for the many-body density matrix (*cf.* Eq. 3.32), and using the exact knowledge of the correction factor g^{rel} for unitary interactions (*cf.* Eq. 2.35). We consider N distinguishable quantum particles in a box of volume V , in the high-temperature regime ($\lambda_{\text{th}} \rho^{1/3} \ll 1$). Within the pair-product approximation for ρ_N , the pair-correlation function $g^{(2)}(\mathbf{x}, \mathbf{x}')$ reads

$$g^{(2)}(\mathbf{x}, \mathbf{x}') = \frac{\sum_{i=1}^N \sum_{j \neq i} \int d\mathbf{X} \delta(\mathbf{x}_i - \mathbf{x}) \delta(\mathbf{x}' - \mathbf{x}_j) \prod_{k=1}^N \left[\rho_1(\mathbf{x}_k, \mathbf{x}_k; \beta) \prod_{l>k} g^{\text{rel}}(\mathbf{x}_k - \mathbf{x}_l; \mathbf{x}_k - \mathbf{x}_l; \beta) \right]}{\int d\mathbf{X} \prod_{k=1}^N \left[\rho_1(\mathbf{x}_k, \mathbf{x}_k; \beta) \prod_{l>k} g^{\text{rel}}(\mathbf{x}_k - \mathbf{x}_l; \mathbf{x}_k - \mathbf{x}_l; \beta) \right]}. \quad (4.18)$$

The product of the $N(N - 1)/2$ terms including the correction factor g^{rel} can be expanded as

$$\prod_{k=1}^N \prod_{l>k} g^{\text{rel}}(\mathbf{x}_k - \mathbf{x}_l; \mathbf{x}_k - \mathbf{x}_l; \beta) \simeq 1 + \sum_{k=1}^N \sum_{l>k} \left[1 - g^{\text{rel}}(\mathbf{x}_k - \mathbf{x}_l; \mathbf{x}_k - \mathbf{x}_l; \beta) \right], \quad (4.19)$$

where we neglect terms involving higher powers of $(1 - g^{\text{rel}})$, which is valid for small $\rho^{1/3}\lambda_{\text{th}}$. Therefore the pair-correlation function can be rewritten as

$$g^{(2)}(\mathbf{x}, \mathbf{x}') \simeq N(N - 1) \frac{1 + f(\mathbf{x}, \mathbf{x}')/V^{N-2}}{1 + \sqrt{2}\lambda_{\text{th}}^3/V}, \quad (4.20)$$

where we have used

$$\int d\mathbf{y} \left[1 - g^{\text{rel}}(\mathbf{y}; \mathbf{y}; \beta) \right] \simeq \sqrt{2}\lambda_{\text{th}}^3, \quad (4.21)$$

and defined $f(\mathbf{x}, \mathbf{x}')$ as

$$f(\mathbf{x}, \mathbf{x}') \equiv \sum_{k=1}^N \sum_{l>k} \int d\mathbf{X} \delta(\mathbf{x}_i - \mathbf{x}) \delta(\mathbf{x}' - \mathbf{x}_j) \left[1 - g^{\text{rel}}(\mathbf{x}_k - \mathbf{x}_l; \mathbf{x}_k - \mathbf{x}_l; \beta) \right]. \quad (4.22)$$

This function reads

$$f(\mathbf{x}, \mathbf{x}') = V^{N-2} \left[\left(1 - g^{\text{rel}}(\mathbf{x} - \mathbf{x}'; \mathbf{x} - \mathbf{x}'; \beta) \right) + \frac{\lambda_{\text{th}}^3}{V} \sqrt{2} \frac{(N+1)(N-2)}{2} \right]. \quad (4.23)$$

By combining Eqs. 4.20 and 4.23, we obtain the full expression for $g^{(2)}(\mathbf{x}, \mathbf{x}')$ in the high-temperature regime. The contact parameter can then be evaluated through Eq. 2.48. For the contact density c_2^{dist} of N distinguishable particles with unitary zero-range interactions, we find

$$\rho^{-4/3} c_2^{\text{dist}} \simeq \frac{N-1}{N} \times 16\pi \left(\lambda_{\text{th}} \rho^{1/3} \right)^2, \quad (4.24)$$

at high temperature. The contact density c_2 for the unitary Bose gas is equal to $2 \times c_2^{\text{dist}}$. This follows from the doubling of the statistical weight for configurations where two bosons are at zero distance [61]. The resulting expression for c_2 (cf. Eq. 4.15) is the first contribution to the contact density in the virial expansion. The same expression is often reported without the $(N-1)/N$ prefactor [62, 63, 64], which is a valid approximation at large N . The correct prefactor is crucial, however, for the comparison with the few-body results in Section 2.1.3.

CHAPTER 5

Classical three-body hard-core model

In this chapter, we discuss the classical three-body hard-core model, which generalizes the hard-sphere model. The hard-sphere model deals with the thermodynamic properties of impenetrable objects like rod, disks or spheres in one, two, or three dimensions, respectively. For the case under study, the hard-core constraint consists in the three-body cutoff introduced in Section 2.2.2. In the original hard-sphere model, particles of radius σ interact through a hard-core repulsive potential,

$$V_2(\mathbf{x}_i, \mathbf{x}_j) = \begin{cases} \infty & \text{if } |\mathbf{x}_i - \mathbf{x}_j| < 2\sigma \\ 0 & \text{if } |\mathbf{x}_i - \mathbf{x}_j| > 2\sigma \end{cases}, \quad (5.1)$$

which does not include any attractive part. Despite its apparent simplicity, this model is a cornerstone of statistical mechanics since, among others, it has provided fundamental insight in the theory of phase transitions for continuous system, and especially on the melting transition. Already at their early stages, studies of this model have relied heavily on the most recent advances in computational techniques to treat statistical-physics systems, including the molecular dynamics and Monte Carlo techniques [170, 171, 109]. For two dimensions, in particular, these methods shed light on the debated topic of the existence of a transition. The occurrence of phase separation and the behavior of defects close to the transition greatly complicate this phenomenon [172, 173], motivating the development of improved algorithms.

Another important aspect of the hard-sphere model is its connection with the packing problem, i.e. the question of how to efficiently pack hard objects in a way that minimizes the fraction of void space. In dimensions up to $d = 3$, this has evident practical applications. More generally, the packing problem is connected to similar topics in geometry (e.g. the kissing-number problem and the covering problem), and its generalized form has been studied also in higher-dimensional spaces. Apart from purely

mathematical applications, it has direct connections with the information-theory problems of data transmission and storage [174].

The hard-sphere model has been generalized in multiple directions. Apart from the immediate generalization to non-spherical objects (see for instance Refs [175, 176]), the large- and infinite-dimensional cases have been considered, in connection with phase diagrams [177, 178, 179] and with the d -dimensional packing problem [180, 181]. More recently, systems of self-propelled hard particles have represented a useful simple model for the study of non-equilibrium statistical mechanics [182, 183, 184].

In this chapter, we describe a novel model, where the two-body hard-sphere potential is replaced by a three-body potential. For several cases, a complex physical behavior cannot be fully described by two-body interactions, as discussed in the context of nuclear forces [185]. Three-body terms are also explicitly used to describe spin glasses, as in the well-known p -spin model [186], but classical continuous systems with purely three-body forces have not been treated, to the best of our knowledge. Inspired by the unitary-gas phase diagram, we study the simplest possible many-body-interacting continuous system, the three-body hard-core model. This is defined by the following three-body potential

$$V_3(\mathbf{x}_i, \mathbf{x}_j, \mathbf{x}_k) = \begin{cases} \infty & \text{if } R_{ijk} < R_0 \\ 0 & \text{if } R_{ijk} > R_0 \end{cases}, \quad (5.2)$$

where the hyperradius R_{ijk} is defined as

$$R_{ijk} = \sqrt{\frac{(\mathbf{x}_i - \mathbf{x}_j)^2 + (\mathbf{x}_j - \mathbf{x}_k)^2 + (\mathbf{x}_k - \mathbf{x}_i)^2}{3}}. \quad (5.3)$$

This potentials impose that configurations have no triplet of particles with hyperradius smaller than R_0 . As for any hard-sphere model, the Boltzmann probability distribution takes only two values

$$p(\mathbf{x}_1, \dots, \mathbf{x}_N) = \begin{cases} 1 & \text{if legal configuration} \\ 0 & \text{else} \end{cases}, \quad (5.4)$$

where “legal” means that there exists no triplet $\{i, j, k\}$ with $R_{ijk} < R_0$. The properties of this model are determined by its single parameter, R_0 . Despite this simplicity, it includes counter-intuitive features, notably the structures that form at high-density. In $d = 2$, these are configurations hosting two particles on each site of a regular lattice, which is not forbidden by the three-body cutoff. Multiple occupancies can be justified by considering the k -body interacting model in d dimensions, and we find that they are mostly present in low-dimensional systems (see Section 5.2.1.4).

After describing the relevant computational tools to study this system (Section 5.1), we concentrate on the packing problem (how to obtain the densest possible structure) in Section 5.2. We propose a set of variational ansätze, which seem to obtain the correct

optimal solutions, as supported through the results of the simulated-annealing optimization algorithm. These solutions are then continued at finite pressure, in Section 5.3. Both in $d = 2$ and $d = 3$, we identify the transition between the fluid and solid phases, and explore the possibility of additional phases, employing several definitions of ordered phases. This chapter is based on Publication 1.

5.1 Sampling configurations at fixed pressure

In this section, we review several schemes which can be used to sample configurations from the NPT ensemble, where the pressure P is fixed and the system volume can fluctuate. We start by considering the probability distribution $p(\mathbf{x}_1, \dots, \mathbf{x}_N)$ for the positions of N particles in a volume V , at a given temperature T . This distribution corresponds to the Boltzmann weight of the configuration energy, and its partition function reads¹

$$Z_{NVT} = \int d\mathbf{x}_1 \dots \int d\mathbf{x}_N p(\mathbf{x}_1, \dots, \mathbf{x}_N). \quad (5.5)$$

For hard-core potentials, p takes only values zero or one, so that Z_{NVT}/V^N represents the fraction of configuration-space volume occupied by legal configurations. This ratio tends to one in the limit of zero density.

In the NPT ensemble, the pressure P is fixed, and fluctuations of the volume are allowed (NPT ensemble). The partition function corresponds to the average of Z_{NVT} over all possible volumes V , weighted by the additional factor $e^{-\beta PV}$ [151]:

$$Z_{NPT} = \int_0^\infty dV e^{-\beta PV} Z_{NVT} = \int_0^\infty dV \int d\mathbf{x}_1 \dots \int d\mathbf{x}_N e^{-\beta PV} p(\mathbf{x}_1, \dots, \mathbf{x}_N). \quad (5.6)$$

While the explicit knowledge of the partition function is not directly accessible for a general case, it is possible to sample configurations which contribute to the integrals (either in Eq. 5.5 or Eq. 5.6) according to the probability distribution determined by the integrand. For the NVT ensemble, this corresponds to sampling the set of positions $\mathbf{x}_1, \dots, \mathbf{x}_N$, while in the NPT ensemble one should draw samples from an extended configuration space which includes both the particle positions and the total volume V . These sampled configurations can then be used to compute estimates of the equilibrium average for thermodynamic quantities, like the average volume $\langle V \rangle$ or the density-density correlation function $g^{(2)}(\mathbf{r})$.

A Monte Carlo algorithm to sample the fixed-pressure configurations entering Z_{NPT} defines a random walk in the extended configuration space which includes both the

¹In this chapter, we only deal with the configuration partition function (also named configuration integral [151]), the integral over all spatial degrees of freedom of the Boltzmann factor for the total potential energy. The full partition function also includes the integral over momentum variables of the kinetic-energy Boltzmann factor, which is not relevant for the discussion in this chapter.

particle positions and the volume. We assume that this is achieved through two different Monte Carlo updates: “NVT” moves only change the particle positions, while “NPT” moves modify the volume of the system. We consider the standard choice for the NVT updates [39, 105] (where a random displacement of randomly-chosen particle is proposed, and accepted/rejected according to the Metropolis rule – *cf.* Section 3.1), and focus on two possible choices for NPT moves: A global rescaling of the system (Section 5.1.1) and the reshaping of the simulation box through the insertion or removal of void space (Section 5.1.2).

5.1.1 Box rescaling

Within the Monte Carlo method, the volume can be changed through a move which rescales the simulation box by a given factor, together with all particle positions [105]. We consider the case of a d -dimensional hypercubic box of edge L , with volume $V = L^d$, and introduce the scaled coordinates $\mathbf{s}_i = \mathbf{x}_i/L \in [0, 1]^d$. The partition function can be rewritten as

$$Z_{NPT} = \int_0^\infty dV \left(e^{-\beta PV} V^N \right) \int d\mathbf{s}_1 \dots \int d\mathbf{s}_N p(L\mathbf{s}_1, \dots, L\mathbf{s}_N). \quad (5.7)$$

where the integrals in $d\mathbf{s}_i$ are now on the unit box $[0, 1]^d$. The Monte Carlo move rescales the box size and all particle positions (see Fig. 5.1),

$$\begin{cases} V_{\text{old}} \rightarrow V_{\text{new}} = V_{\text{old}} + \Delta V \\ L_{\text{old}} \rightarrow L_{\text{new}} = (V_{\text{new}})^{1/d} \\ \mathbf{x}_{i,\text{old}} = L_{\text{old}} \mathbf{s}_i \rightarrow \mathbf{x}_{i,\text{new}} = L_{\text{new}} \mathbf{s}_i \end{cases}. \quad (5.8)$$

The statistical weight of the old and new configurations corresponds to the integrand in Eq. 5.7, so that the Metropolis acceptance probability (*cf.* Eq. 3.13) reads

$$p_{\text{acc}} = \min \left[1, \left(\frac{V_{\text{new}}}{V_{\text{old}}} \right)^N e^{-\beta P \Delta V} \frac{p(L_{\text{new}} \mathbf{s}_1, \dots, L_{\text{new}} \mathbf{s}_N)}{p(L_{\text{old}} \mathbf{s}_1, \dots, L_{\text{old}} \mathbf{s}_N)} \right], \quad (5.9)$$

where the factor $(V_{\text{new}}/V_{\text{old}})^N$ is associated with the rescaling of the N particle positions. This must be combined with NVT moves, as the volume rescaling is not sufficient to sample the entire configuration space, since the relative positions of the N particles are fixed. Such combination constitutes a valid Monte Carlo algorithm to sample the configurations contributing to the partition function in Eq. 5.6.

For systems in which $p(\mathbf{x}_1, \dots, \mathbf{x}_N)$ only takes values one or zero (as is the case for the hard-core potentials in Eq. 5.1 and Eq. 5.2), an optimized version of the box-rescaling move is available [187, 39]. In this case, we consider again the set of scaled particle positions \mathbf{s}_i , and define the value L_{cut} of the box edge such that

$$p(L\mathbf{s}_1, \dots, L\mathbf{s}_N) = \begin{cases} 0 & \text{if } L < L_{\text{cut}} \\ 1 & \text{if } L > L_{\text{cut}} \end{cases}. \quad (5.10)$$

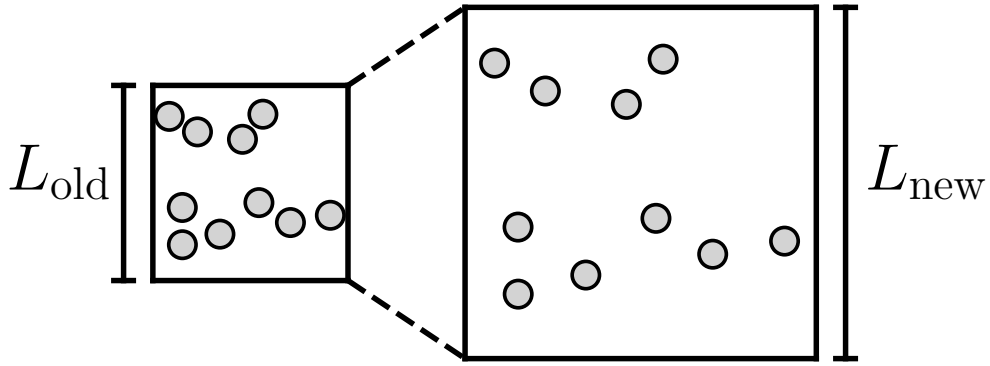


Figure 5.1: Volume-changing move for two-dimensional hard disks (*cf.* Eq. 5.1), in which all particle positions are rescaled by $L_{\text{new}}/L_{\text{old}}$.

The value of L_{cut} depends on the form of $p(\mathbf{x}_1, \dots, \mathbf{x}_N)$, and it is a function of the scaled coordinates: $L_{\text{cut}} = L_{\text{cut}}(\mathbf{s}_1, \dots, \mathbf{s}_N)$. The corresponding volume, $V_{\text{cut}} = L_{\text{cut}}^d$, represents the smallest volume that can be obtained for a given set of scaled positions $\mathbf{s}_1, \dots, \mathbf{s}_N$, without causing overlaps. For particles interacting through a pairwise hard-core potential of radius σ (*cf.* Eq. 5.1), L_{cut} is computed as

$$L_{\text{cut}} = \frac{2\sigma}{\min_{i,j} |\mathbf{s}_i - \mathbf{s}_j|}. \quad (5.11)$$

For $L > L_{\text{cut}}$, the set of positions $\mathbf{x}_i = L\mathbf{s}_i$ does not include any pair of points at distance smaller than 2σ . A similar definition holds for particles interacting through a three-body hard-core potential (Eq. 5.2). In this case, the value of L_{cut} for a given choice of $\{\mathbf{s}_i\}$ reads

$$L_{\text{cut}} = \frac{R_0}{\min_{i,j,k} \sqrt{\frac{|\mathbf{s}_i - \mathbf{s}_j|^2 + |\mathbf{s}_j - \mathbf{s}_k|^2 + |\mathbf{s}_k - \mathbf{s}_i|^2}{3}}}. \quad (5.12)$$

This definition guarantees that in the set of positions $\{L\mathbf{s}_i\}$ there exists no triplet of particles $\{i, j, k\}$ with hyperradius R_{ijk} smaller than R_0 , provided that $L > L_{\text{cut}}$. Given the value of L_{cut} (for a specific set of scaled positions), the NPT partition function in Eq. 5.7 reads

$$Z_{\text{NPT}}^{\text{hc}} = \int d\mathbf{s}_1 \dots d\mathbf{s}_N \int_{V_{\text{cut}}(\mathbf{s}_1, \dots, \mathbf{s}_N)}^{\infty} dV V^N e^{-\beta PV}, \quad (5.13)$$

for the case of hard-core potentials. An optimal version of the box-rescaling of Section 5.1.1 can be devised, based on Eq. 5.13, with acceptance probability equal to one. This requires drawing a sample from the distribution $p_{\text{cut}}(V)$, which corresponds to the integrand of Eq. 5.13,

$$p_{\text{cut}}(V) = \begin{cases} 0 & \text{if } V < V_{\text{cut}} \\ \left(\frac{V}{V_{\text{cut}}}\right)^N \exp[-\beta P(V - V_{\text{cut}})] & \text{if } V > V_{\text{cut}} \end{cases}' \quad (5.14)$$

where we have included the V -independent prefactor $V_{\text{cut}}^{-N} \exp(\beta P V_{\text{cut}})$ for convenience. The distribution

$$q(V) = \exp \left[\left(-\beta P + \frac{N}{V_{\text{cut}}} \right) (V - V_{\text{cut}}) \right]. \quad (5.15)$$

represents an upper-bound for $p_{\text{cut}}(V)$. For $q(V)$ to be normalizable, the condition $\beta P V_{\text{cut}} > N$ is required: If this condition is not met, the NPT update described here is not applied, and the simulation continues with a NVT move². Through a combination of the change-of-variable and rejection-sampling methods, we obtain the following scheme to draw a sample from $p_{\text{cut}}(V)$:

1. A random sample V_{new} is drawn from the exponential distribution $q(V)$, as explained in Section 3.1.1.1.
2. A random number η is drawn from the uniform distribution between 0 and $q(V_{\text{new}})$.
3. The new volume V_{new} is accepted if $\eta \leq p_{\text{cut}}(V_{\text{new}})$. If it is rejected, the move restarts from the first step (generating V_{new}), and we keep iterating this loop until a sample is accepted.

The sample V_{new} is sampled directly from p_{cut} , with acceptance probability equal to one. This is a clear advantage with respect to the (more general) move described above (see Eq. 5.9).

5.1.2 Insertion/removal move

The two NPT moves of Section 5.1.1 consist in a global rescaling of the system, so that the simulation-box aspect ratios (the length ratios of pairs of box edges) cannot change. This poses no problem in the simulation of a disordered (fluid) state, where the typical characteristic length scales are much smaller than the simulation box. However, it introduces a bias when the system can form ordered structures, as it favors the formation of lattice structures which have the same aspect ratio of the simulation box. This issue is particularly relevant when the high-density structure of the system is not known beforehand, but is rather the goal of the NPT calculations (see Section 5.2.2). More general NPT updates to overcome this limitation include the floppy-box Monte Carlo scheme [175] where both the box size and shape are modified during the Monte Carlo simulation. The simulation-box configuration is encoded in the vectors defining its edges: For a $d = 2$ rectangular box $[0, L_x] \times [0, L_y]$, for instance, these vectors are $\mathbf{e}_1 = (L_x, 0)$ and $\mathbf{e}_2 = (0, L_y)$. The NPT update is then designed to include changes of both the

² This condition corresponds to $V_{\text{cut}} > V_{\text{id}}$, where $V_{\text{id}} = N / (\beta P)$ is the average volume of a classical ideal gas at temperature $1/\beta$ and pressure P . We note that this does not constitute a severe issue in practical calculations for two-body or three-body hard-core models, for which the interesting regime is generally the one where clear deviations from the ideal gas volume are observed. This corresponds to large pressures and densities, so that the system typically includes at least one pair/triplet of close-by particles which make V_{cut} large enough.

magnitude and orientation of these vectors. This method has been used to predict the high-density structures for colloidal particles of several shapes [176, 188], by simulating small systems with $N \lesssim 12$.

Here, we introduce a simpler NPT move, in which the magnitudes of the d box-defining vectors are free to change, but their orientation remains fixed (that is, the simulation box remains a rectangular cuboid, with orthogonal edges). This method is then used for the calculations of Section 5.2.2 and Section 5.3. This update is composed by two parts: The insertion and removal moves. We describe them for the case

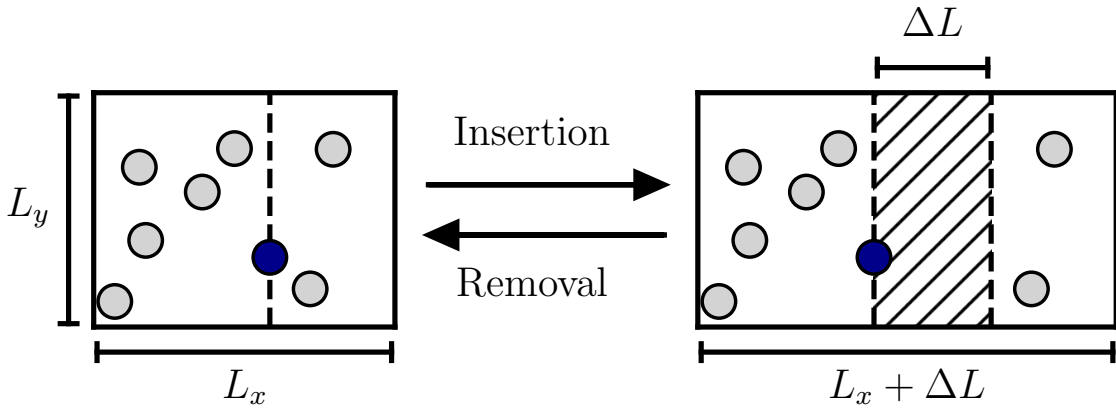


Figure 5.2: Insertion and removal NPT updates, adding or removing a void portion of space of area $\Delta L \times L_y$ (*hatched area*). This region is defined to have one boundary touching the position of a randomly-chosen particle, marked in blue in the figure.

of a $[0, L_x] \times [0, L_y]$ two-dimensional box, since their d -dimensional generalization is straightforward. The insertion move consists in changing one of the box edges by adding a random amount of void space (a rectangle aligned with the coordinate axes, constrained to touch a randomly chosen particle). If particle k and direction x are chosen, the insertion move corresponds to changing L_x into $L_x + \Delta L$ (where ΔL is chosen randomly in a given interval). This is obtained by adding a portion of void space with edges $\Delta L \times L_y$, starting from the x coordinate of the k -th particle. This move does not rescale the particle positions, which are only shifted to make space to the new void region (*cf.* Fig. 5.2). Therefore its acceptance probability is

$$p_{\text{acc}} = \min \left[1, e^{-\beta P \Delta V} \frac{p(\mathbf{x}'_1, \dots, \mathbf{x}'_N)}{p(\mathbf{x}_1, \dots, \mathbf{x}_N)} \right], \quad (5.16)$$

where $\Delta V = \Delta L \times L_y$ is the increase in volume, and the old and new coordinates are denoted with $\{\mathbf{x}_i\}$ and $\{\mathbf{x}'_i\}$, respectively. This differs from the case of the rescaling move described in Section 5.1.1, as there is no V^N factor in the acceptance probability (*cf.* Eq. 5.9). The complementary update is a removal move, in which it is proposed to remove the two-dimensional portion of space defined as

$$\{(x, y) : x \in [x_k, x_k + \Delta L]\}, \quad (5.17)$$

where ΔL is chosen randomly in a given interval, and x_k is the x component of the randomly-chosen particle \mathbf{x}_k . This move, which reduces L_x by an amount ΔL , is accepted with probability

$$p_{\text{acc}} = \min \left[1, e^{\beta P \Delta V} \frac{p(\mathbf{x}'_1, \dots, \mathbf{x}'_N)}{p(\mathbf{x}_1, \dots, \mathbf{x}_N)} \right], \quad (5.18)$$

and provided that it does not remove any particle (that is, if any particle lies in the region which should be removed, the move is rejected). In addition to the mentioned acceptance conditions, for both the insertion and removal moves, we reject moves leading to very elongated box shapes. This is common for MC methods where the box shape can change [175, 188, 189], to avoid strong finite-size effects. If the insertion and removal moves are proposed with the same frequency during the MC simulation, their combination satisfies the detailed balance condition, so that they represent a valid algorithm (when combined with an NVT move) to sample configurations contributing to Z_{NPT} .

The insertion/removal move has a specific difference with respect to the other NPT moves described above, which is important for the case where particles form an extended ordered structure. The rescaling move of Section 5.1.1 and the floppy-box MC algorithm are based on global changes of the simulation box, so that local structural properties (like the distance between two neighboring sites or the angle between two lattice bonds) are modified across the entire system, and the ordered structure is distorted. After such a move is accepted, it might take several NVT steps before the local structural properties re-equilibrate. In contrast, the insertion/removal move only changes the structural properties of a limited portion of the system. Moreover, this move can in principle add the void space necessary for a new lattice row (in two dimensions) or plane (in three dimensions) to form. The insertion of this void space has been advanced as a mechanism to change the number of lattice sites during a simulation [190], in connection with the known problem of equilibrating the number of lattice defects in a NPT simulation [173]. This motivated our choice of the insertion/removal move, although a systematic study of its performance for equilibrating the defects number has not been addressed in this work.

5.2 Packing problem

In this section we consider the packing problem, which consists in maximizing the density of a system subject to a hard-core constraint. In the traditional formulation of this problem, the constraint is that all pair distances must be larger than a given quantity 2σ (cf. Eq. 5.1). This corresponds to the problem of packing disks in two dimensions or spherical particles in three dimensions, which has evident practical applications [191].

For two-dimensional disks, the solution consists in placing their centers on a triangular lattice [174]. For this structure, the radius can be increased until the packing

fraction η (the fraction of the total area which is covered by disks) reaches

$$\eta_{\max}^{\text{tri}} = \frac{\pi}{2\sqrt{3}} \simeq 0.9069. \quad (5.19)$$

This situation is called close packing (*cf.* Fig. 5.3), and it corresponds to the largest density which can be reached for this chosen structure (the triangular lattice, in this case). The close-packing condition can be obtained for any structure. As an example, if disks are placed on a square lattice the close-packing fraction reads

$$\eta_{\max}^{\text{sq}} = \frac{\pi}{4} \simeq 0.7854. \quad (5.20)$$

which is indeed lower than the one for the triangular lattice.

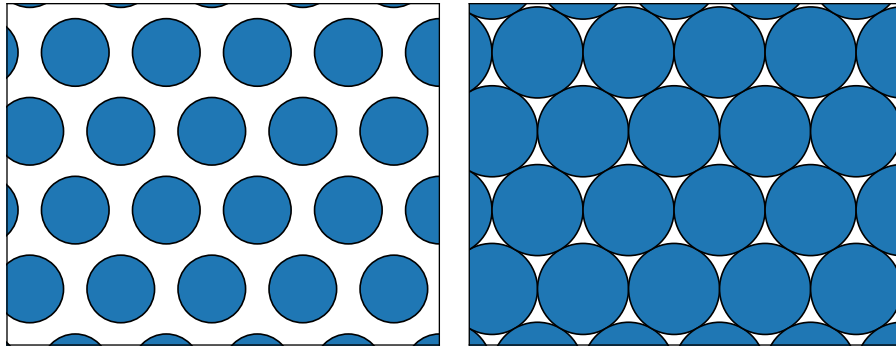


Figure 5.3: Disks forming a triangular lattice, away from close packing (*left*, packing fraction $\eta = 1/2$), or in the close-packed limit (*right*, packing fraction $\eta = \eta_{\max}^{\text{tri}}$).

For three dimensional spheres, the optimal packing fraction reads

$$\eta_{\max}^{d=3} = \frac{\pi}{3\sqrt{2}} \simeq 0.74048, \quad (5.21)$$

and is obtained by either the face-centered cubic (FCC) or the hexagonal close packed (HCP) structures [174]. The fact that this is the optimal value (known as Kepler conjecture) has been proved for the class of periodic structures (that is, lattice structures) by Gauss, in 1831, while the formal proof for the general case has been completed only in the 21st century [192, 193].

In this section we consider the packing problem for particles interacting via the three-body hard-core potential (Eq. 5.2), rather than disks or spheres. After the enumeration of several possible candidate structures (Section 5.2.1), in Section 5.2.2 we describe the simulated-annealing technique, a Monte Carlo algorithm for the unconstrained search of optimal structures.

d	Structure	Parameters	$\rho_{\max} R_0^d$
1	Regular spacing, <i>atoms</i>	–	$\sqrt{2}$
	Regular spacing, <i>dimers</i>	–	$2\sqrt{2/3}$
2	Oblique, <i>atoms</i>	$r = \sqrt{2}$ $\theta = 0$	$\sqrt{2}$
	Oblique, <i>dimers</i>	$r = 1$ $\theta = \pi/6$	$(2/\sqrt{3})^3$
3	Barlow ABA, <i>atoms</i>	$r = 1/2$	$\frac{13}{27}\sqrt{26/3}$
	Barlow ABA, <i>dimers</i>	$r = \sqrt{2/3}$	$(2/\sqrt{3})^3$
	Barlow ABC, <i>atoms</i>	$r = 1/\sqrt{6}$	$(2/\sqrt{3})^3$
	Barlow ABC, <i>dimers</i>	$r = \sqrt{2/3}$	$(2/\sqrt{3})^3$
	Tetragonal, <i>atoms</i>	$r = 1$	$(2/\sqrt{3})^3$
	Tetragonal, <i>dimers</i>	$r = 1$	$\sqrt{32/27}$
	Simple-hexagonal, <i>atoms</i>	$r = 1/\sqrt{2}$	$2\sqrt{2/3}$
	Simple-hexagonal, <i>dimers</i>	$r = 1$	$8\sqrt{2}/9$

Table 5.1: Densities of d -dimensional close-packed structures. The structure may include free parameters (aspect ratio r or angle θ), and the optimal values are indicated. For each value of d , the largest density is marked in bold.

5.2.1 Variational ansätze

As a first step towards finding high-density structures for the three-body hard-core model, we consider a set of variational ansätze, and compute their close-packing density. For each ansatz, we first maximize the density over the free parameters of the structure (angles and/or aspect ratios), obtaining the close-packing density ρ_{\max} . The next step consists in comparing different ansätze, to find the overall optimal density and structure. A structure is defined by a regular arrangement of some sites in space, and by the choice of how many particles should be placed on each site (one or two). The one-dimensional case is used as an example – *cf.* Section 5.2.1.1 – before treating the two- and three-dimensional cases (see Sections 5.2.1.2 and 5.2.1.3). The results of this section are summarized in Table 5.1.

5.2.1.1 One dimension

In $d = 1$, we consider an alternating spacing between single atoms, such that consecutive interparticle distances are $\dots, l, (Al), l, (Al), \dots$ (see Fig. 5.4), where $0 \leq A \leq 1$. The case $A = 1$ corresponds to a regular (equally spaced) lattice, while the other limit case, $A = 0$, gives an equally-spaced lattice where each site is filled by two particles (note that this is not forbidden by the three-body constraint). The former is a regular

lattice of atoms, while the latter is a lattice of dimers. For any value of A , the density of

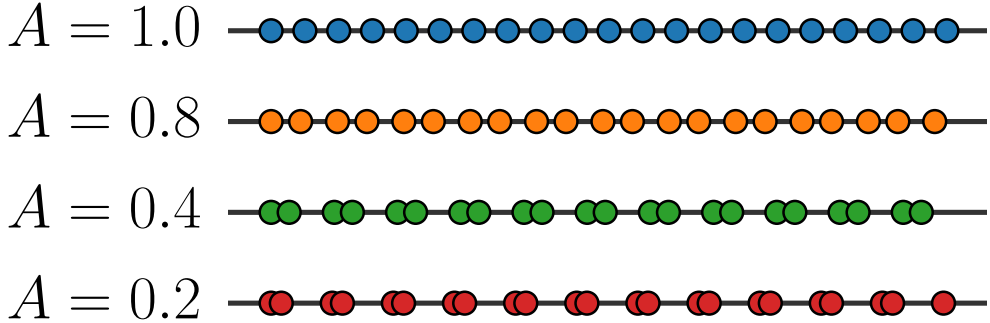


Figure 5.4: One-dimensional structures considered, for different values of A . The close-packing condition is enforced, that is, l is set to its minimum allowed value l_{\min} (cf. Eq. 5.24).

the structure reads

$$\rho = \frac{2}{(1+A)l'} \quad (5.22)$$

since there are two particles in any segment of length $(1+A)l$. Given any triplet of subsequent lattice sites, their distances are l , Al , and $(1+A)l$, so that the squared hyperradius reads

$$R^2 = \frac{1+A^2+(1+A)^2}{3} \times l^2. \quad (5.23)$$

The three-body constraint sets a lower bound on l , which reads

$$l_{\min}(A) = R_0 \times \sqrt{\frac{3}{1+A^2+(1+A)^2}}. \quad (5.24)$$

Thus the close-packing density for the variational ansatz under study reads

$$\rho_{\max}(A) = \frac{2}{(1+A)l_{\min}(A)} = \frac{1}{R_0} \frac{2\sqrt{2}}{\sqrt{3}} \sqrt{1 - \frac{A}{(1+A)^2}}. \quad (5.25)$$

This is maximum at $A = 0$, resulting in a density

$$\rho_{\text{best}}^{d=1} = \frac{1}{R_0} \frac{2\sqrt{2}}{\sqrt{3}} \simeq \frac{1.63299}{R_0}, \quad (5.26)$$

as reported in Table 5.1. The subscript “best” indicates the highest density attained with the variational ansatz considered³. The candidate optimal structure for $d = 1$ is

³For $d = 2$ and $d = 3$, this also indicates the maximum over different ansätze.

a lattice with two particles per site, which can be interpreted in more general terms – *cf.* Section 5.2.1.4. As an additional check, the close-packed density for a regular lattice with one particle per site (corresponding to $A = 1$) reads

$$\rho_{\max}(A = 1) = \frac{\sqrt{2}}{R_0} \simeq \frac{1.4142}{R_0}, \quad (5.27)$$

which is indeed smaller than ρ_{best} .

5.2.1.2 Two dimensions

In two dimensions, our ansatz distinguishes between two classes of structures, including either one or two particles per lattice site. We consider an oblique lattice, with spacing l along the x direction, and with aspect ratio r and angle θ , defined as in Fig. 5.5. The basis vectors read

$$\begin{aligned} \mathbf{e}_1 &= (l, 0), \\ \mathbf{e}_2 &= (rl \sin \theta, rl \cos \theta), \end{aligned} \quad (5.28)$$

so that the position of a lattice site is

$$\mathbf{x}_{n,m} = n\mathbf{e}_1 + m\mathbf{e}_2, \quad n, m \in \mathbb{Z}. \quad (5.29)$$

We may set $r \geq 1$ and $0 \leq \theta \leq \arcsin(1/(2r))$. Examples are the triangular lattice (with

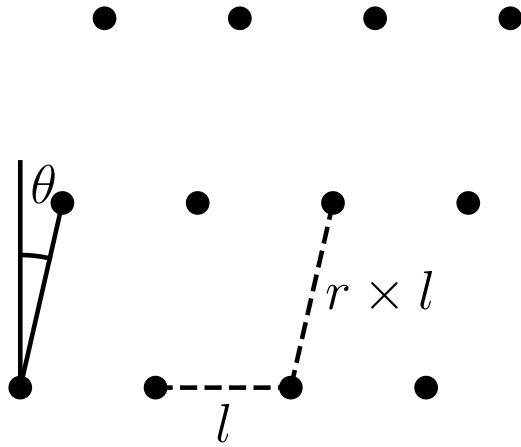


Figure 5.5: Oblique lattice with aspect ratio r and angle θ .

$r = 1$ and $\theta = \pi/6$) and the rectangular lattice (with $\theta = 0$).

We first consider an oblique lattice with one particle per site, which has a density equal to

$$\rho = \frac{1}{l^2 r \cos \theta}, \quad (5.30)$$

since there is one particle in every cell, and the cell area is $l \times rl \cos \theta$. In contrast with the one-dimensional case, here we have to apply the three-body cutoff to several different triplets, obtaining a combination of several constraints for l (which are all – in general – functions of r and θ). In particular, we find

$$l_{\min}^2(r, \theta) = R_0^2 \times \max \left(\frac{1}{2}, \frac{1}{2r^2}, \frac{3}{2(1 + r^2 - r \sin \theta)} \right). \quad (5.31)$$

The third element in the max function is the one corresponding to a triplet forming a triangle (for instance the triplet $\{\mathbf{x}_{0,0}, \mathbf{x}_{1,0}, \mathbf{x}_{0,1}\}$) while the first two concern three sites which are aligned along a straight line, either along \mathbf{e}_1 (e.g. sites $\{\mathbf{x}_{0,0}, \mathbf{x}_{1,0}, \mathbf{x}_{2,0}\}$) or along \mathbf{e}_2 (e.g. sites $\{\mathbf{x}_{0,0}, \mathbf{x}_{0,1}, \mathbf{x}_{0,2}\}$). Using the knowledge of l_{\min} , we can construct the close-packed version of an oblique lattice, for each r and θ – cf. Fig. 5.6. Among all the

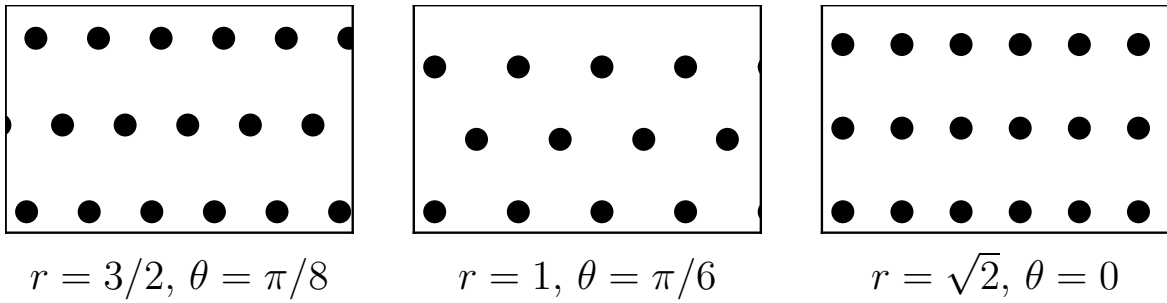


Figure 5.6: Three examples of close-packed oblique lattices, with a single particle per site. The three structures have different r and θ , and their densities read $\rho R_0^2 \simeq 1.287, 1.155$, and 1.414 .

possible oblique lattices with one particle per site, the one reaching the highest density is the rectangular one, with $r = \sqrt{2}$ and $\theta = 0$ (cf. left panel of Fig. 5.7).

The same strategy can be followed for an oblique lattice with two particles per site, which has density (cf. Eq. 5.30)

$$\rho = \frac{2}{l^2 r \cos \theta}. \quad (5.32)$$

In this case, the constraint on the hyperradius reads

$$l_{\min}^2(r, \theta) = R_0^2 \times \max \left(\frac{3}{2}, \frac{3}{2r^2}, \frac{3}{2(1 + r^2 - r \sin \theta)} \right), \quad (5.33)$$

where the third argument in the max function corresponds to the case of three particles distributed on sites $\mathbf{x}_{0,1}$ and $\mathbf{x}_{1,0}$. This expression for $l_{\min}(r, \theta)$ gives access to the close-packing density as a function of (r, θ) (cf. Eq. 5.32, and right panel of Fig. 5.7). The overall maximum density (maximized over r and θ) for the dimer oblique lattice is $\rho R_0^2 = (2/\sqrt{3})^3 \simeq 1.5396$, obtained with a triangular lattice ($r = 1$ and $\theta = \pi/6$).

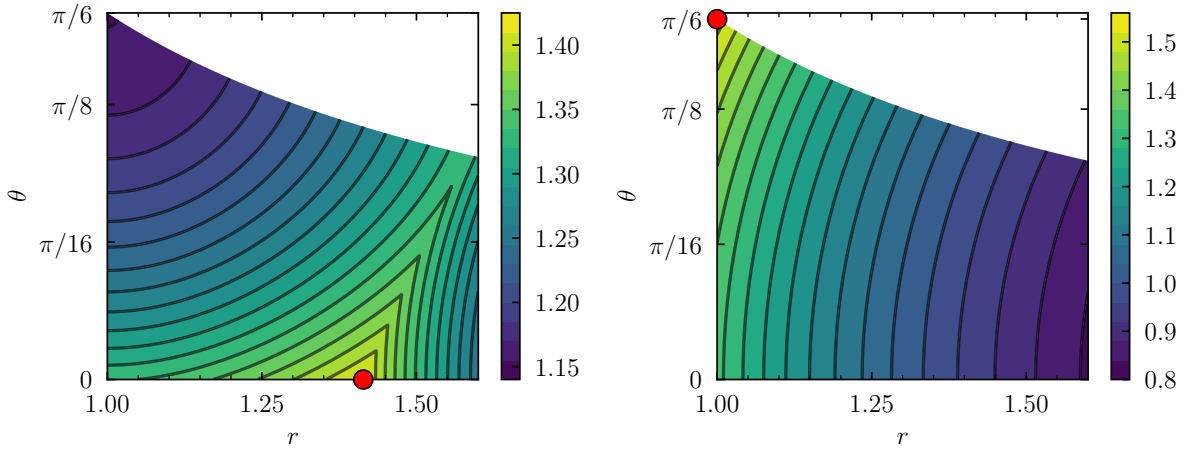


Figure 5.7: Close-packing density (in units of R_0^{-2}) as a function of (r, θ) , for the oblique lattice with one particle per site (*left panel*) or with one dimer per site (*right panel*). In each panel, the red dot marks the maximum density.

As reported in Table 5.1, the highest density found with our ansatz is for the triangular lattice with two particles per site,

$$\rho_{\text{best}}^{d=2} = \frac{1}{R_0^2} \left(\frac{2}{\sqrt{3}} \right)^3 \simeq \frac{1.5396}{R_0^2}. \quad (5.34)$$

In the class of oblique lattices with a single particle per site, the optimal structure is the rectangular lattice (with $\theta = 0$ and $r = \sqrt{2}$), which attains a density only 10% smaller than $\rho_{\text{best}}^{d=2}$.

5.2.1.3 Three dimensions

For the three-dimensional case, we consider several classes of structures:

1. Tetragonal lattices, obtained by stretching a cubic lattice along one direction by a factor r .
2. Simple-hexagonal lattice, obtained by an A-A-A stack of triangular-lattice layers (*cf.* Fig. 5.8). The aspect ratio r is defined as the ratio between the interplanar distance and the in-plane lattice constant.
3. Barlow structures [194, 191], obtained by A-B-A or A-B-C stack of triangular-lattice layers (see Fig. 5.9). The aspect ratio r is defined as for the simple-hexagonal case. For $r = \sqrt{2/3}$, the A-B-A and A-B-C classes reproduce the hexagonal close-packed and face-centered cubic structures, respectively [191].

All these cases correspond to the three-dimensional stacking of planar structures, so that they all share the free parameter r , defined as the ratio between the interplanar distance

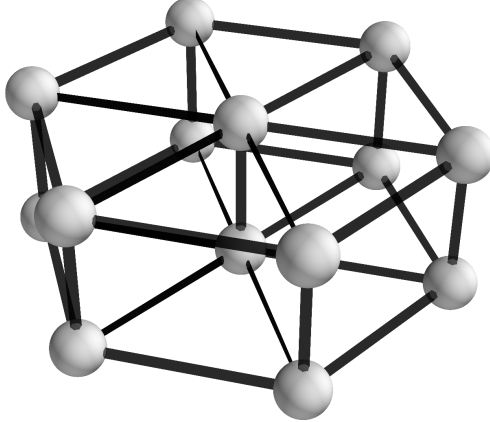


Figure 5.8: Simple-hexagonal lattice, obtained as an A-A stack of triangular lattices.

and the in-plane lattice. We shall now enumerate the close-packing densities for these eight cases (four structures, with the possibility of either one or two particles per site), obtaining the results shown in Table 5.1. As in Section 5.2.1.2, we first need to compute the lower bound $l_{\min} = l_{\min}(r)$ for the in-plane lattice constant l , that can be then used to compute the density as a function of r .

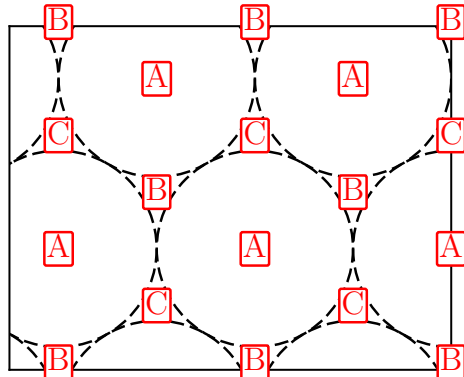


Figure 5.9: Scheme to construct Barlow structures. The first two layers of particles are placed on the sites marked by A and B , respectively. The third layer is then placed either on sites A (for the A-B-A stack) or on sites C (for the A-B-C stack).

For the tetragonal lattices, the minimum in-plane lattice constant reads

$$\frac{l_{\min}^2(r)}{R_0^2} = \begin{cases} \max\left(\frac{1}{2r^2}, \frac{3}{4}, \frac{3}{2(1+r^2)}\right), & \text{for one particle per site,} \\ \max\left(\frac{3}{2}, \frac{3}{2r^2}\right), & \text{for two particles per site,} \end{cases} \quad (5.35)$$

while for the simple-hexagonal lattice this is

$$\frac{l_{\min}^2(r)}{R_0^2} = \begin{cases} \max \left(1, \frac{1}{2r^2}, \frac{3}{2(1+r^2)} \right), & \text{for one particle per site,} \\ \max \left(\frac{3}{2}, \frac{3}{2r^2} \right), & \text{for two particles per site.} \end{cases} \quad (5.36)$$

The Barlow A-B-A structure gives

$$\frac{l_{\min}^2(r)}{R_0^2} = \begin{cases} \max \left(1, \frac{1}{8r^2}, \frac{9}{5+6r^2}, \frac{9}{2+18r^2} \right), & \text{for one particle per site,} \\ \max \left(\frac{3}{2}, \frac{3}{8r^2}, \frac{9}{2+6r^2} \right), & \text{for two particles per site,} \end{cases} \quad (5.37)$$

and the A-B-C stack has

$$\frac{l_{\min}^2(r)}{R_0^2} = \begin{cases} \max \left(1, \frac{1}{18r^2}, \frac{9}{5+6r^2}, \frac{3}{1+6r^2}, \frac{9}{2+42r^2} \right), & \text{for one particle per site,} \\ \max \left(\frac{3}{2}, \frac{1}{6r^2}, \frac{9}{2+6r^2} \right), & \text{for two particles per site.} \end{cases} \quad (5.38)$$

These expressions follow by imposing the three-body constraint on all relevant triplets of sites forming the structure. The knowledge of $l_{\min}(r)$ gives access to the minimum volume of the unit cell, so that we can directly compute the close-packing density for a given structure and at a given aspect ratio r . As shown in Fig. 5.10, the simple-hexagonal structure with one particle per site is the one reaching the maximum density, which reads

$$\rho_{\text{best}}^{d=3} = \frac{1}{R_0^3} \left(2 \sqrt{\frac{2}{3}} \right) \simeq \frac{1.63299}{R_0^3}. \quad (5.39)$$

This is reported in Table 5.1, together with the maximum densities for all the other three-dimensional structures considered.

5.2.1.4 Multiple occupancies with k -body hard-sphere interactions

As described in the previous sections, we find two different highest-density structures, among the ones we considered: For $d = 1$ and $d = 2$, these are structures with two particles per site, while in three dimensions the best candidate structure has only one particle per site. In this section we give an heuristic argument, suggesting that only in low dimensions the high-density structures have multiple particles per site. We consider a d -dimensional system with a k -body hard-core cutoff, where the k -body distance between positions $\mathbf{x}_1, \dots, \mathbf{x}_k$ is defined as

$$R^{(k)} \equiv \sqrt{\frac{2}{k(k-1)} \sum_{1 \leq i < j \leq k} (\mathbf{x}_i - \mathbf{x}_j)^2} \quad (5.40)$$

and it is set to be larger than a cutoff value R_0 . For $k = 2$ and $k = 3$, this corresponds to the hard-sphere and three-body hard-core models, respectively. We restrict our argument to a very specific class of structures, namely the ones that satisfy two properties:

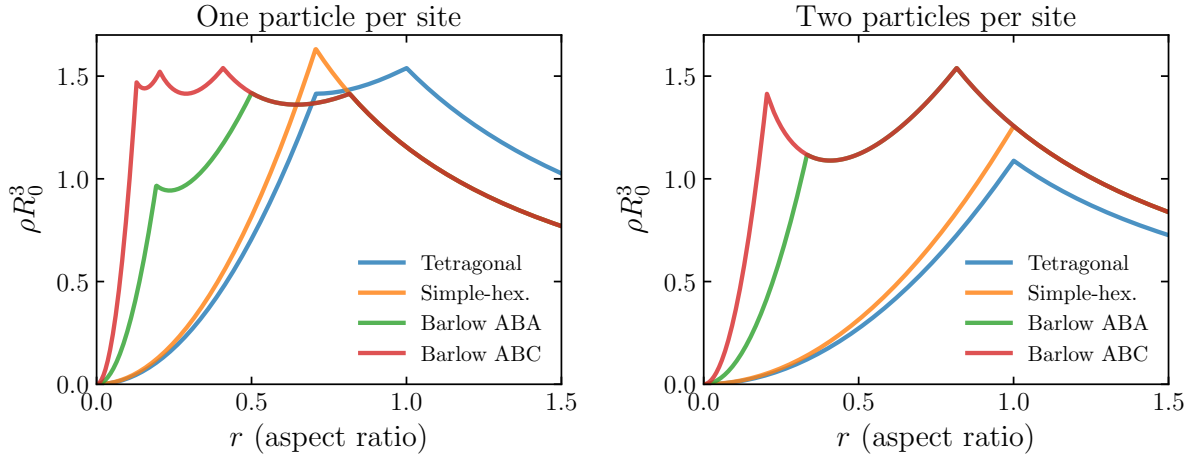


Figure 5.10: Maximum densities for a given structure as a function of the aspect ratio r . The two panels correspond to one (*left*) or two (*right*) particles per site.

1. All pairs of nearest-neighboring sites are at the same distance l .
2. Each site has at least $k - 1$ nearest neighbors which are also nearest neighbors with each other.

The existence of such a structure is not guaranteed, and depends on k and on the dimensionality d . Some examples are:

- For $d = 1$ and $k = 2$, the equally-spaced lattice.
- For $d = 2$ and $k \in \{2, 3\}$, the triangular lattice.
- For $d = 3$ and $k \in \{2, 3, 4\}$, any structure which includes groups of four particles placed on the vertices of a tetrahedron (e.g. the hexagonal close-packed structure, a specific case of the A-B-A stack described in Section 5.2.1.3).

For this kind of structures, it is simple to obtain the close-packing limit. Given a certain k , we consider k sites which are all nearest neighbors, as guaranteed by the definition of the structures we are considering, and look for different ways to place k particles on these k sites. In particular, we try to place m particles on each site (where m has to be smaller than k , due to the k -body constraint), as in these simple examples for $m \leq 2$:

- For $m = 1$, we place one particle on each site, independently of k .
- For $m = 2$ and k even, we place two particles per site on $k/2$ sites, and leave the remaining $k/2$ sites empty.
- For $m = 2$ and k odd, we place two particles per site on $(k - 1)/2$ sites and one particle on a specific site, and leave the remaining $(k - 1)/2$ sites empty.

For a general m , the k sites are partitioned into three classes:

1. Sites hosting exactly m particles: The number of such sites is $(k - Rm(k, m))/m$, where $Rm(k, m)$ is the remainder of the integer division k/m .

2. Sites hosting the remaining $Rm(k, m)$ particles: If $Rm(k, m) \neq 0$, then there is one such site, otherwise there is none.
3. The remaining sites hosting zero particles.

Given this partition, we can compute the number N_{zero} of particle pairs such that the two particles forming the pair are on the same site:

$$N_{\text{zero}}(k, m) = \frac{k - Rm(k, m)}{m} \frac{m(m-1)}{2} + \frac{Rm(k, m)(Rm(k, m)-1)}{2}. \quad (5.41)$$

This allows to write the k -body distance for these k particles (*cf.* Eq. 5.40) as

$$R^{(k)} = \sqrt{\frac{2}{k(k-1)} \left[\left(\frac{k(k-1)}{2} - N_{\text{zero}}(k, m) \right) l^2 \right]} \quad (5.42)$$

where l is the distance between two nearest neighbors, and

$$\left(\frac{k(k-1)}{2} - N_{\text{zero}}(k, m) \right) \quad (5.43)$$

is the total number of pairs at non-zero distance. By setting $R^{(k)} \geq R_0$ and inverting Eq. 5.42, we can determine a lower bound l_{\min} on the distance l . This in turn gives access to the scaling of the close-packing density for a given k , which reads

$$\rho \propto \frac{1}{R_0^d} \frac{m}{(k - N_{\text{zero}}(k, m))^{d/2}}, \quad (5.44)$$

where we neglected all prefactors not depending on d or m . This expression allows to compare, for a given k , the close-packing densities which can be obtained by placing m particles on each site – *cf.* Fig. 5.11. We observe the same qualitative behavior for all values of k : In low-dimensional cases, the largest density is reached by placing many particles on each site (given the constraint $m < k$), while for large d the dominating density is the one with $m = 1$ particles per site.

While this heuristic argument explains the qualitative difference between the candidate structures we have found for $d = 1, 2$ and 3 , it remains restricted to the specific class of structures considered in this section. As an example, the best known structure for $d = 3$ (the simple-hexagonal lattice of single particles, *cf.* Section 5.2.1.3) does not belong to this class. This explains why in the $k = 3$ panel of Fig. 5.11 the $m = 1$ density is the largest one for all $d \leq 3$, even though the simple-hexagonal lattice with one particle per site has a higher density for $d = 3$.

We note that the formation of regular structures with more than one particle per site (also known as microphases, or cluster phases) has been observed for realistic systems of penetrable particles, for example purely repulsive soft spheres [195] or branching polymers [196]. Also in these cases, as for the three-body hard-core model, the interparticle distance is allowed to vanish.

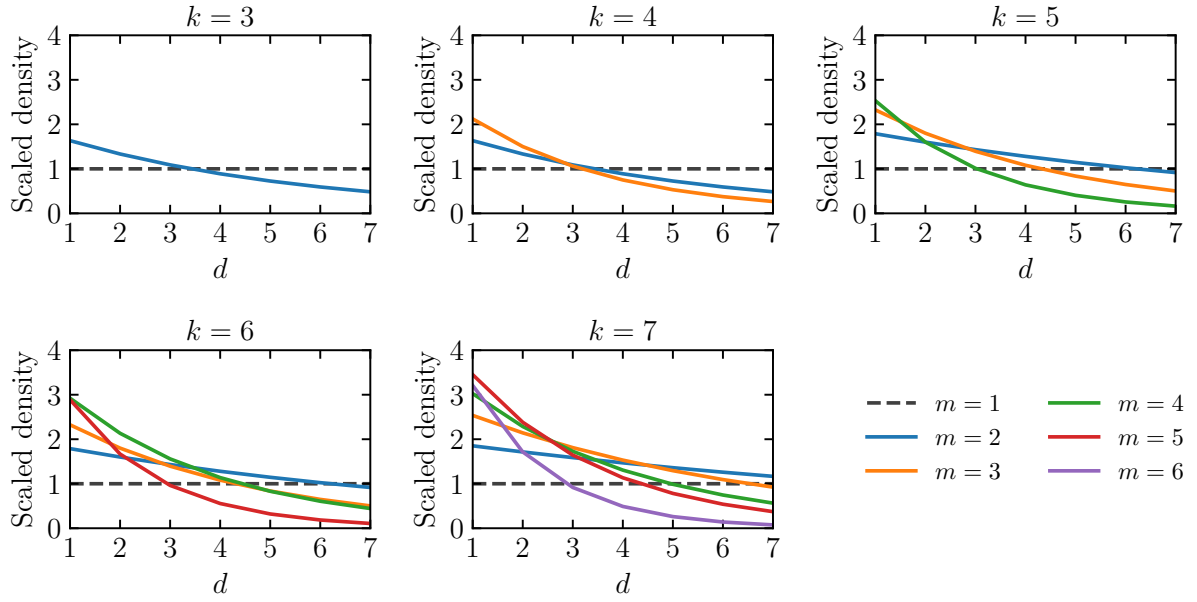


Figure 5.11: Density of the d -dimensional close-packed structure, for the k -body hardcore model. Each panel corresponds to a given k , while different lines correspond to different values of m (the number of particles per site). All densities are expressed in units of the $m = 1$ density.

5.2.2 Simulated annealing

In this section we describe the simulated annealing (SA) technique, and its application to finding high-density structures for the three-body hard-core model. Simulated annealing is an algorithm for the optimization of functions of many variables, inspired by the simulations of statistical-physics models [197, 198]. It corresponds to finding the ground state of a statistical-physics system, where the probability distribution for a configuration x at inverse temperature β is $p_\beta(x) = \exp(-\beta E(x))$. This can also be applied to more general cases, with $E(x)$ being the function to optimize and β a fictitious inverse temperature. The minimization proceeds as follows:

1. Select a random initial configuration x . This step depends on the precise form of the configuration space, but it can be generally achieved by assigning a random value to each degree of freedom of x .
2. Set β to a value close to zero, corresponding to the infinite-temperature limit.
3. Iterate the following steps, until a convergence condition is satisfied.
 - (a) Perform several steps of a Monte Carlo algorithm that samples the distribution $p_\beta(x)$.
 - (b) Increase β , according to a “cooling protocol”.

As the inverse temperature β increases, the probability distribution p_β becomes more peaked around the minima of $f(x)$, while it is strongly suppressed for all configurations at large distance from one of these minima. This change of p_β has a consequence in the dynamics of the Monte Carlo algorithm: At large β , the acceptance probability is suppressed for MC moves that increase the energy f . This is clear for instance if the Metropolis algorithm is used (*cf.* Eq. 3.13). In the $\beta \rightarrow \infty$ limit, the only accepted MC moves are those which lower the energy, so that eventually a local minimum of f is reached, after a large number of MC steps.

The local minimum is not guaranteed to be also global, for a given SA realization. Nevertheless, there is a degree of control on the algorithm, which provides hints at whether this is the case. The main control parameter for the SA algorithm is the cooling protocol, i.e. the choice of how the inverse temperature β increases during the optimization. This can be encoded in a function $\beta = h(t_{\text{MC}})$ giving the value of β in terms of the step t_{MC} of the MC simulation. An example is given in Eq. 5.45, where the parameter α represents the cooling velocity. This function typically starts at $h(0) \approx 0$, and it increases towards its large-time limit, $\lim_{t_{\text{MC}} \rightarrow \infty} h(t_{\text{MC}}) = \infty$. In a typical application, different cooling protocols are adopted (fast/slow, *cf.* Eq. 5.45 and Fig. 5.12), with several independent runs for each (with randomized initial conditions). If the SA algorithm is reaching the global optimum, its results should not depend on the precise choice of the cooling protocol, provided that it is slow enough. This constitutes a useful diagnostics on the SA results: If they show a clear dependence on the choice of h , this suggests that a slower cooling protocol should be used. Nevertheless, the independence on the cooling protocol is not sufficient to prove that the global optimum has been found.

Also due to its simplicity, the SA algorithm has been used for a broad and diverse set of applications (see for instance Ref. [199]), and in particular it has been proposed as a method to find optimal crystal structures [200] (*cf.* Ref. [201] for a review of the techniques used for this problem). This is the application which we are interested in, and which we describe more in detail.

We consider the finite-size version of the packing problem, where we look for the structure which maximizes the density of a system of N particles (rather than the infinite-system version discussed in Section 5.2.1), subject to the three-body hard-core constraint of Eq. 5.2. The NPT partition function (*cf.* Eq. 5.6) is expressed in a form which can be easily interpreted in view of the SA algorithm: The goal is to find the configuration that maximizes the quantity NR_0^d/V , and the SA approach to this minimization is to take the result of an MC simulation during which we let βPR_0^d become very large. Notice that in this case the probability distribution is already available from the physical model, rather than being a fictitious one. The artificial part of the SA algorithm is considering the $\beta PR_0^d \rightarrow \infty$ limit. The practical scheme for this minimization task is the following

1. Initialize the pressure to a very small value, $\beta PR_0^d \approx 0$.
2. Choose a large initial volume, and initialize the particle positions through direct sampling.

3. Iterate the following steps:

- Perform several steps of the fixed-pressure MC algorithm, alternating NVT moves and the insertion/removal NPT move.
- If necessary, iteratively adapt the parameters of the NVT and NPT moves, to keep a finite acceptance rate⁴.
- Increase $\beta P R_0^d$, according to the chosen cooling protocol.

As an example, we choose the following protocol for the evolution of the pressure:

$$\beta P R_0^d \propto h(t_{\text{MC}}) = (t_{\text{MC}})^\alpha, \quad (5.45)$$

where α determines the speed at which βP increases. The precise definition of one Monte Carlo time step (which corresponds to a certain number of proposed NPT and NVT moves) is not relevant for the current discussion, as long as we keep this definition fixed and we only deal with a fixed number of particles N . For this choice of the cooling

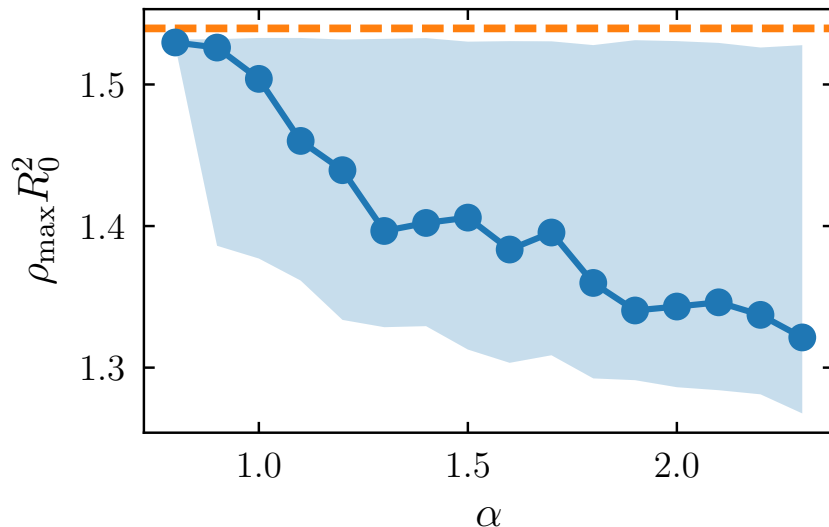


Figure 5.12: Results of simulated annealing for $N = 32$ particles in two dimensions, at annealing “velocity” α (cf. Eq. 5.45). The average maximum density (blue circles, averaged over 40 independent SA runs) is compared with the density of a close-packed triangular lattice of dimers (orange dashed line). The blue shaded area represents the full spread of the density (minimum to maximum), over all SA runs. One time unit corresponds to 50 sweeps (each one being formed by 32 single-particle NVT moves and 4 NPT updates), and all runs are stopped at $\beta P R_0^2 = 500$.

⁴Note that this adaptive adjustment can introduce a bias on the measure of average quantities in an equilibrium simulation, but the aim of SA is rather to obtain the maximum density, and not average observables.

protocol h , we can study the properties of the configurations obtained at large pressure, and their dependence on the rate α . This is shown in Fig. 5.12, for the specific case of a two-dimensional system of $N = 32$ particles, which is chosen so that a defect-free 4×4 triangular lattice of dimers (which has density $\rho R_0^2 \simeq 1.5396$ and is our best candidate for being the densest structure *cf.* Section 5.2.1.2) can be realized. This example then serves a double goal: It can support the heuristic notion that the triangular lattice of dimers is the optimal structure, and – once this is assumed to be true – it allows to study the SA performance as a function of α . As with any stochastic algorithm, the outcome can vary between different realizations, so that we need to study the statistical properties of a set of several runs. We find the following results (*cf.* Fig. 5.12):

- Across the entire range of α considered, at least one of the several runs reaches the dimer triangular-lattice structure, with density close to $\rho R_0^2 \simeq 1.5396$ (note that we only reach a finite $\beta P R_0^2$, so that a small deviation is to be expected).
- No density higher than $\rho R_0^2 \simeq 1.5396$ is observed, supporting the claim that the dimer triangular-lattice structure represents the global optimum.
- The average final density is a decreasing function of α : When the pressure is increased faster (that is, for larger α), there are more chances that particles form a non-optimal structure.
- The non-optimal structures generally belong to one of three classes: (1) Sub-optimal regular structures (including a rectangular lattice with one particle per site), (2) regular structures which are not aligned with the box axis, and (3) structures with localized defects. For the small system considered here ($N = 32$), the second and third cases correspond to a strong decrease of the density, with respect to the triangular lattice of dimers, but this effect would be smaller for system of larger size.

This example supports the claim that the best candidate structure identified by the enumeration in Section 5.2.1.2 is also the global optimum for $d = 2$. The same is confirmed with SA calculations for $N = 72$ particles. In the same way, the densest three-dimensional structure found with our SA calculations is a simple-hexagonal lattice with one particle per site, which is also the result of Section 5.2.1.3. At a finite cooling rate, the SA method only provides a lower bound for the global optimum of density, but we base the following part of this chapter on the assumption that the best candidate structures identified for $d = 2$ and $d = 3$ really represent the configurations that would form at infinite pressure.

5.3 Finite-pressure phase diagrams

In this section, we discuss the finite-pressure phase diagram of the three-body hard-core model, in two and three dimensions. Our main result is the equation of state (EOS) for a finite system, which expresses the density as a function of the pressure. At small pressure ($\beta P R_0^d \rightarrow 0$), the system is in a dilute disordered state. Due to the small density, the

three-body potential acts a small perturbation, and for any $\beta P R_0^d \gtrsim 0$ the virial expansion of the partition function ([39], §2.2.2) describes the deviations from the ideal-gas EOS (in which the density ρ is simply equal to βP). At infinite pressure ($\beta P R_0^d \rightarrow \infty$), in contrast, the system realizes the structure which gives the global maximum for the density. The full EOS gives the finite-pressure behavior of the system, which interpolates between these two limits. Both cases (the disordered state at small pressure and the high-density structure at infinite pressure) exist over finite pressure intervals, forming fluid and solid phases.

Concerning the solid-phase structure, we assume that this corresponds to the best candidate structure identified in Section 5.2 (namely the triangular dimer of lattice in two dimensions and the simple-hexagonal lattice of single particles in three dimensions). Thus we have a qualitative difference between the two- and three-dimensional cases: For $d = 2$, large-pressure configurations are made by tightly-bound dimers, while the solid phase for $d = 3$ is a lattice of single particles.

We focus on the existence of an intermediate phase, between the fluid and solid. In two dimensions, a hypothetical intermediate phase could be made either of dimers or of single particles. In three dimensions, we do not expect the formation of pairs, but in principle different solid phases (separated by solid-solid structural transitions) could exist. The search for additional phases leads us to use or introduce different criteria to identify ordered phases. These criteria include the characterization of orientational order, and of the magnetization of an effective spin system (for the two dimensional case). Neither for $d = 2$ nor for $d = 3$ we find evidence for an intermediate phase.

5.3.1 Two dimensions

The solid phase is characterized by the long-range decay of positional order, as encoded in the large-distance behavior of the density-density correlation function, $g^{(2)}(\mathbf{r})$. In the disordered phase, this function decays exponentially. In $d = 2$, the existence of a crystal with true long-range positional order is precluded by Mermin-Wagner theorem [202]. In this case, the solid-phase $g^{(2)}(\mathbf{r})$ decays algebraically.

Distinguishing between exponential and power-law decays of $g^{(2)}(\mathbf{r})$ is only possible through simulations of large systems sizes (for instance systems of $N \approx 10^6$ particles have been used, for the two-dimensional hard-disk model [112, 203]). For discontinuous phase transitions, a simpler approach consists in calculating the NPT equation of state, which does not involve the analysis of $g^{(2)}(\mathbf{r})$. In this case, the melting transition is identified as the point at which the density has a discontinuity. We follow this path, and use the Monte Carlo algorithm described in Section 5.1 to obtain the density at a given pressure. In particular, we consider systems with $N = 2 \times N_d^2$ particles (where N_d is the number of dimers), and we choose to always initialize the simulation from a defect-free configuration corresponding to the infinite-pressure limit (that is, a triangular lattice of dimers). This is due to the difficulty of obtaining defect-free configurations

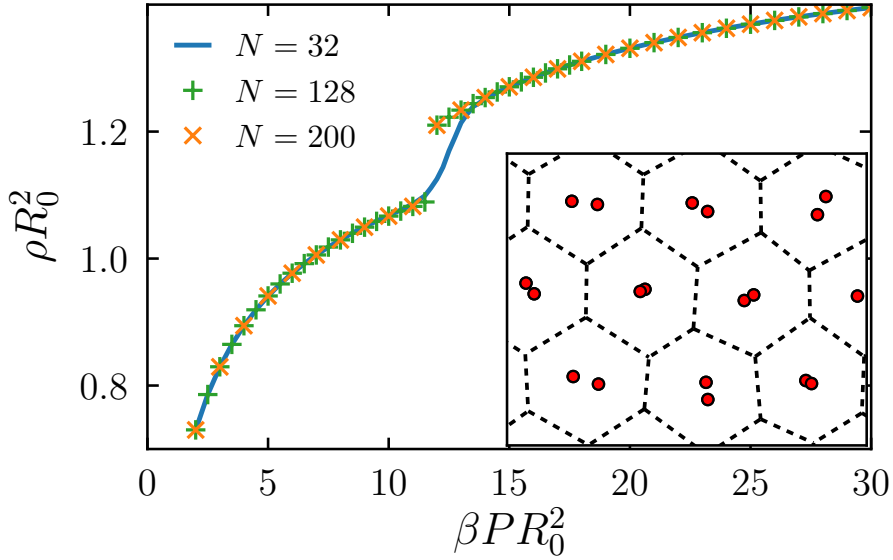


Figure 5.13: Equation of state (density *vs.* pressure) for the two-dimensional three-body hard-core model (*main panel*), computed for different system sizes. The inset represents a portion of a simulation snapshot at $\beta PR_0^2 = 13$, including the particle positions (*red circles*) and the Voronoi cells of dimer centers of mass (*dashed black lines*). Given a set of positions $\mathbf{x}_1, \mathbf{x}_2, \dots$, the Voronoi cell of \mathbf{x}_1 is defined as the region of points with distance from \mathbf{x}_1 smaller than the distance to any other \mathbf{x}_j .

starting from a disordered state, which can only be obtained through a careful use of simulated annealing (*cf.* Section 5.2.2). The alternative choice (that is, always starting from a disordered configuration) would lead to configurations with defects, in the solid phase. While these are legitimate configurations entering the partition function, their statistical weight has to be strongly suppressed (for the small system sizes considered here, $N \leq 200$), due to the fact that their volume is significantly larger than the defect-free configurations. This justifies the fact that we ignore them, so that our simulations of the solid are actually simulations of the defect-free solid (which has a slightly larger density). If larger systems were considered, the relative increase in volume due to a defect (including the case of the formation of a lattice non-aligned with the simulation box) would be smaller, so that this would not be an issue.

We find that the critical pressure P_c at which the solid melts is approximately $\beta P_c R_0^2 \simeq 11.75$ (*cf.* Fig. 5.13). For small system size ($N = 32$) the equation of state is smooth around P_c , while the density jump becomes sharper for larger systems ($N = 128, 200$). At finite N , the discontinuous transition is rounded because at $P \approx P_c$ the system oscillates between two kinds of configurations (high density and low density), so that the average density takes an intermediate value. The two peaks in the density distribution

are separated by a small-probability valley (*cf.* Fig. 5.14), corresponding to a free-energy barrier between the solid and fluid phases. As the number of particles N increases, the barrier is expected to increase proportionally to N , so that the probability of the intermediate states is strongly suppressed. The consequence of this suppression on the Monte Carlo dynamics is that the characteristic MC time scale for a change of phase to take place soon exceeds the total simulation time. This is the reason why the smoothing of the $N = 32$ EOS (related to frequent changes of phase) is not observed for larger N .

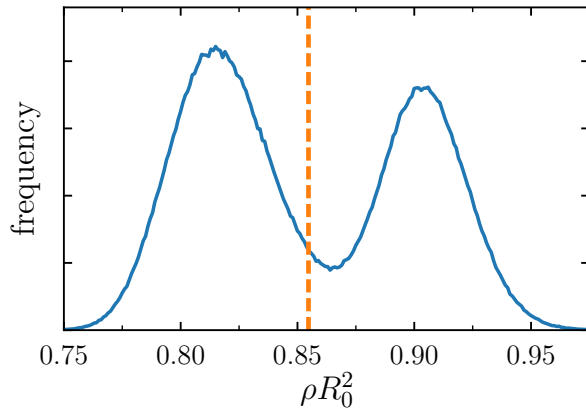


Figure 5.14: Histogram of the densities measured throughout the MC simulation with $N = 32$ (*blue solid line*), at pressure $\beta PR_0^2 = 12.5$ (slightly higher than the critical value). The vertical dashed line represents the average density.

Except for the density jump at P_c , the EOS does not suggest the presence of other phases. In particular, we do not find any pressure where the rectangular lattice of single atoms (the second densest structure from Section 5.2.1.2, with a close-packed density of $\rho R_0^2 = \sqrt{2}$) is stable. By directly looking at simulation snapshots for pressure close to the critical value, however, we do recognize the presence of small clusters with rectangular order (see Fig. 5.15). These are only metastable structures, which eventually transform into a dimer lattice, for instance by coalescence of two neighboring lattice rows.

The two-dimensional three-body hard-core model could be mapped onto at least two other systems (a hard-disk model and a spin model, described below) which we use to explore the possibility of an intermediate phase. In both cases, we need a quantitative definition of the term dimer, and we choose it to describe two particles that are each other's closest neighbor. In the solid phase, the number N_d of dimers equals $N/2$. This definition also applies to the disordered phase, where not all particles participate in tightly-bound pairs. The properties of the fluid-phase dimers, however, are significantly different from those in the solid: The dimer fraction N_d/N is smaller than 1/2 (*cf.* Fig. 5.16a), and the dimer size (the distance between the two paired particles) shows a jump at the critical pressure, being larger in the disordered phase (*cf.* Fig. 5.16b). Both these properties suggest that below the critical pressure, as the dimer solid melts, the

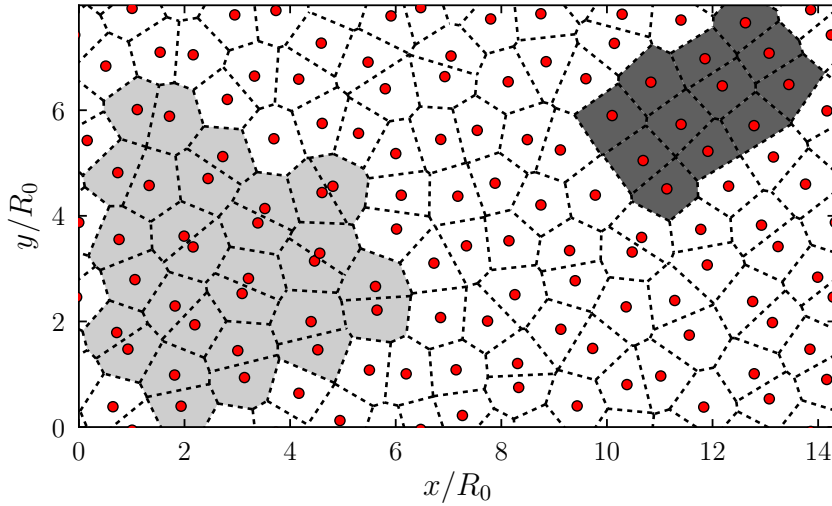


Figure 5.15: Snapshot for $N = 128$ and $\beta P R_0^2 = 14$ (started from a disordered configuration), with particle positions (red circles) and their Voronoi cells (dashed black lines). A patch with rectangular order (dark gray) and a nucleating dimer solid (light gray) are highlighted.

presence of tightly-bound dimers also disappears. This opposes the existence of a low-density phase which includes pre-formed dimers, for which we have no evidence.

As a further element of the behavior of dimers, we also consider the mapping to an effective hard-disk model, which can be defined starting from the infinite-pressure limit. We first consider two dimers of zero size, formed by particles (i, j) and (k, l) which satisfy $\mathbf{x}_i = \mathbf{x}_j$ and $\mathbf{x}_k = \mathbf{x}_l$. If two such dimers are placed at distance $|\mathbf{x}_i - \mathbf{x}_k| = r$, the hyperradius of any three positions in $\{i, j, k, l\}$ reads

$$R = \sqrt{\frac{r^2 + r^2}{3}} = \sqrt{\frac{2}{3}} r, \quad (5.46)$$

as two of the three particle pairs are at distance r , while the third has a vanishing distance. This quantity has to be larger than R_0 , which corresponds to

$$r > \sqrt{\frac{3}{2}} R_0 \equiv 2\sigma_{\text{eff}}. \quad (5.47)$$

Thus the interaction between two zero-size dimers is exactly the hard-disk potential of Eq. 5.1, with the effective hard-disk radius $\sigma_{\text{eff}} \equiv R_0 \sqrt{3/8}$. This mapping is only exact in the infinite-pressure limit, where the dimer size vanishes. Nevertheless, we can extend it to finite values of P , and compare it with the original three-body hard-core model. In particular, we compare the two equations of state, and the values of the orientational order parameter – see below.

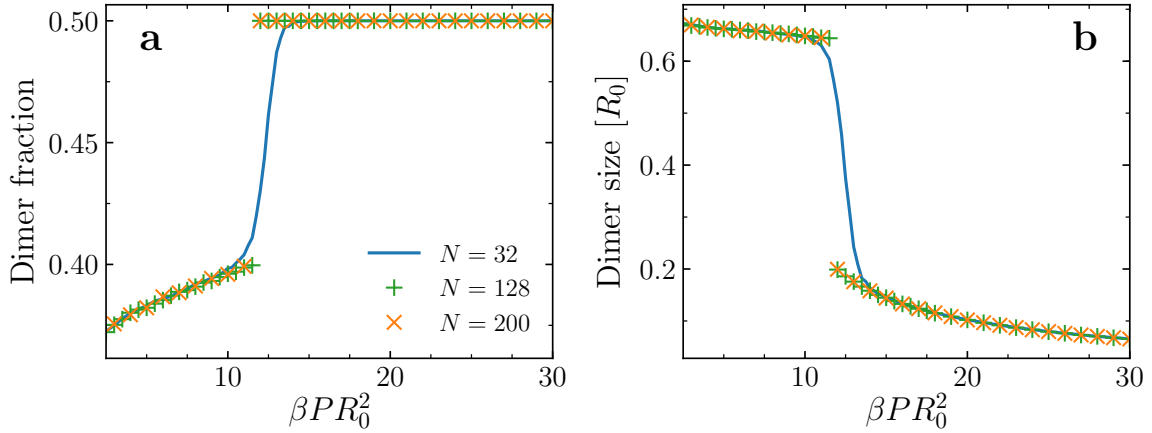


Figure 5.16: (a) Fraction of dimers in the system, N_d/N , as a function of the pressure and for different system sizes. (b) Average dimer size, in units of R_0 .

To make the mapping explicit, we need to define the transformation between the parameters of the two models: The effective hard-disk radius is already defined by Eq. 5.47, and we also need to multiply the pressure of the hard-disk model by a factor of two, stemming from the fact that the configuration space of three-body particles has $2N$ dimensions while these are only $2N_d = N$ for the hard-disk model. After this rescaling, we find that the EOS of the effective model agrees fairly well with the one for the three-body model, for all pressures above P_c (cf. Fig. 5.17a). The density of the hard-disk model is systematically larger than the one of the three-body model, which is due to the fact that finite-pressure dimers have a non-zero size, so that a larger pressure is required to reach the same number density. Below P_c , as expected, the two equations of state are clearly different.

In the hard-disk model, an intermediate phase exists between the fluid and the solid. This is the hexatic phase, which is distinct from the fluid due to the presence of orientational order [173, 112]. In the same way as the positional order is described through the large-distance behavior of the correlator between local densities, $g^{(2)}(\mathbf{r})$, the concept of orientational order relies on the local orientational order parameter, ψ_6 . We give its definition for a system of M particles (which can be the dimers of the three-body model or the hard disks of the effective model), with coordinates $\mathbf{x}_1, \dots, \mathbf{x}_M$ (for the dimers, this coordinate is defined as the middle point between the two particles). We first consider a Voronoi construction, in which each point \mathbf{x}_i is assigned to the cell corresponding to the region of space including points which are closer to \mathbf{x}_i than to any other \mathbf{x}_j . This introduces a notion of neighboring points: Points \mathbf{x}_i and \mathbf{x}_j are neighbors if their Voronoi cells share one edge, and we call the length of this edge W_{ij} . We can then define the local

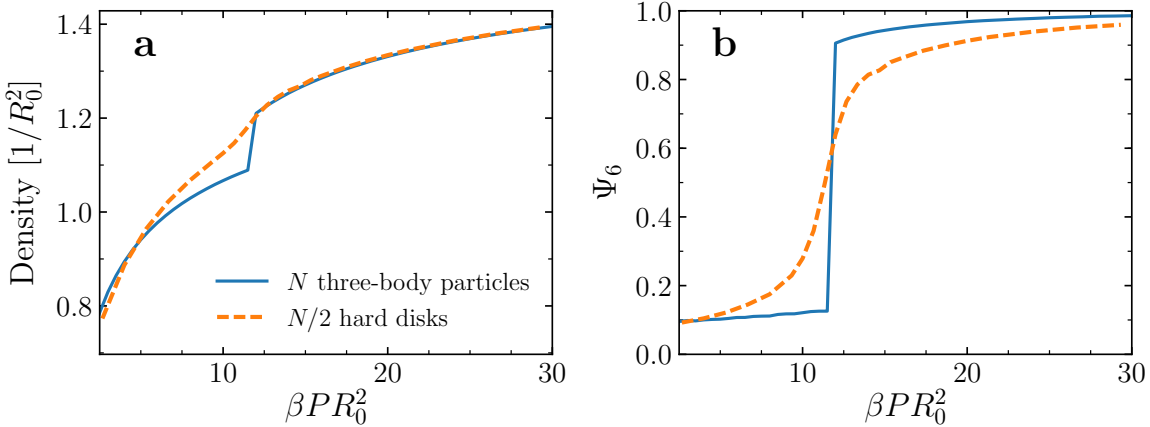


Figure 5.17: Density (a) and global orientational order parameter (b) of the three-body hard-core model with $N = 128$ particles (blue solid line, data corresponding to Fig. 5.13), compared to the same quantities for the effective hard-disk model (orange dashed line, with number of disks equal to $N/2$ – see text for the conversion rules for density and pressure).

orientational order parameter for particle i as

$$\psi_{6,i} = \frac{\sum_j W_{ij} \exp(6i\theta_{ij})}{\sum_j W_{ij}}, \quad (5.48)$$

where the sums are over all the neighbors of i , and where θ_{ij} is the angle between $\mathbf{x}_i - \mathbf{x}_j$ and a reference axis⁵. The absolute value of this quantity is exactly one if the points $\{\mathbf{x}_i\}$ form a perfect triangular lattice, while it is smaller than one for a disordered configuration. By knowing the quantity $\psi_{6,i}$ for all particles, a continuous local-orientation field $\psi_6(\mathbf{x})$ can be constructed by coarse graining over small regions of space, so that the orientational correlator can be defined as the statistical average $\langle \psi_6(\mathbf{x})\psi_6(\mathbf{x} + \mathbf{r}) \rangle$. As noted above, simulations of very large systems would be needed to compute this quantity to a degree where the nature of its large-distance decay (exponential or algebraic) can be identified. We rather consider the global orientational order parameter, Ψ_6 , which is the average of $\psi_{6,i}$ over all particles. The comparison of Ψ_6 for the dimers of the original three-body model and for the effective hard-disk model shows a qualitative agreement – see Fig. 5.17b.

⁵ The same quantity is often defined as

$$\psi_{6,i} = \frac{1}{6} \sum_j \exp(6i\theta_{ij}),$$

instead of using the weighted average of Eq. 5.48. As argued in Ref. [204], this definition lacks robustness against small changes of particle positions.

The key information enclosed in this comparison is that the decomposition of dimers and the melting of the effective hard disks take place at the same pressure, within our accuracy. An hypothetical hexatic phase of dimers (where they keep orientational order) would exist in the region of pressures larger than the dimer-decomposition pressure and smaller than the solid-melting pressure, where the latter can be approximated with the corresponding value for the effective hard-disk model. The fact that we do not observe a significant difference between these two critical pressures is an evidence against the hypothesis of an hexatic phase of dimers, although large-system simulations would be needed to truly prove this statement. Furthermore, we also verified that the curve for Ψ_6 decreases as $1/\sqrt{N_d}$ in the fluid phase, which is the expected scaling for a disordered system [205].

In the $P \gtrsim P_c$ regime, the dimer model may be mapped onto an effective system of continuous spins, and tested for the presence of magnetic order. The mapping from dimers to spins consists in neglecting the fluctuations in dimer sizes, and only considering the angle α_j between the j -th spin and a reference axis (cf. Fig. 5.18).

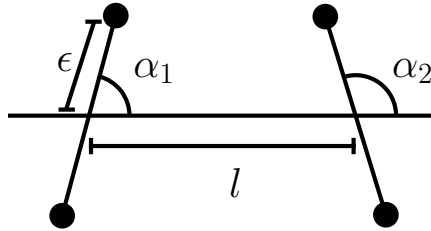


Figure 5.18: Mapping from a pair of dimers (with size 2ϵ and distance l) to a pair of spins (forming angles α_1 and α_2 with the dimer-dimer axis).

When the dimers form a lattice, which is the case for $P > P_c$, this is reminiscent of a continuous-spin model, with effective Hamiltonian

$$H_{\text{eff}} = \sum_{(i,j)} V_{\text{eff}}(\alpha_i, \alpha_j) \quad (5.49)$$

where the sum is over all bonds (i,j) between neighboring sites, and where V_{eff} is the effective spin-spin interaction potential. This potential depends on two parameters of the original three-body model: The distance l between neighboring dimers, and the dimer size 2ϵ . With the notation of Fig. 5.18, the effective potential between spins 1 and 2 depends on the positions of the four particles forming the two dimers, which are expressed as

$$\begin{cases} \mathbf{x}_{1,a} = (\epsilon \cos \alpha_1, \epsilon \sin \alpha_1), \\ \mathbf{x}_{1,b} = (-\epsilon \cos \alpha_1, -\epsilon \sin \alpha_1), \\ \mathbf{x}_{2,a} = (l + \epsilon \cos \alpha_2, \epsilon \sin \alpha_2), \\ \mathbf{x}_{2,b} = (l - \epsilon \cos \alpha_2, -\epsilon \sin \alpha_2). \end{cases} \quad (5.50)$$

In particular, $V_{\text{eff}}(\alpha_1, \alpha_2)$ is equal to 0 if all triplets p, q, r which can be chosen from the four positions in Eq. 5.50 have hyperradius larger than R_0 . If, in contrast, any of these triplets has hyperradius smaller than R_0 , then $V_{\text{eff}}(\alpha_1, \alpha_2) = \infty$. Therefore the three-body hard-core repulsion of the original model maps onto an effective hard-core spin-spin interaction, with this effective potential becoming relevant when l is comparable with R_0 and ϵ/l is not too small. In this regime, the favorable configurations are the ones where any two neighboring spins are aligned along the axis perpendicular to the dimer-dimer connection, so that $\alpha_1, \alpha_2 \approx \pi/2$.

Drawing an analogy with spin models, we introduce the average magnetization per spin, defined as

$$z = \frac{1}{N_d} \sum_j e^{2i\alpha_j}, \quad (5.51)$$

where α_j is the angle made by the j -th spin with a reference axis. The factor of two in the exponent reflects the twofold rotational symmetry of this effective model (the angles α_j are defined up to a rotation of π). This quantity is well defined across the whole range of pressures, but its behavior is mainly interesting for $P \gtrsim P_c$: For $P < P_c$, in the fluid phase, the dimers do not form a lattice and their fraction is smaller than 1/2, while for very large pressure the dimer size shrinks to zero and the α_i values have strong fluctuations. If a magnetically-ordered phase existed, $|z|$ would tend to a finite value for the system size going to infinity. In contrast, we find that the quantity $|z|\sqrt{N_d}$

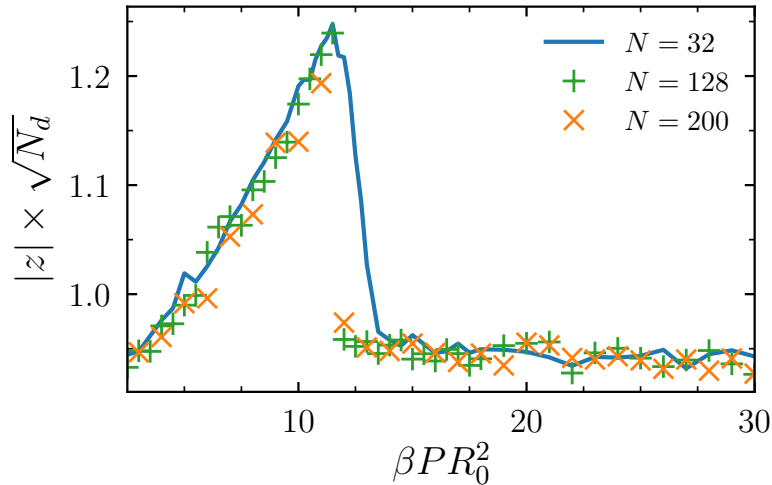


Figure 5.19: Rescaled magnetization $|z|\sqrt{N_d}$ of the effective spin model for dimers (cf. Eq. 5.51). The relation between the total number N of particles and the number N_d of dimers is given in Fig. 5.16a.

is independent on the number N_d of dimers (see Fig. 5.19), meaning that $|z|$ vanishes

as $1/\sqrt{N_d}$ as the system size is increased. This is the expected scaling for a disordered phase, thus ruling out the existence of a magnetic order for the dimers.

The lack of magnetic order is due to the effective interaction $V_{\text{eff}}(\alpha_i, \alpha_j)$ between neighboring spins, which leads to frustration, on the triangular lattice: Given three spins a, b, c placed on the vertices of a triangle, it is not possible to have simultaneously $V_{\text{eff}}(\alpha_a, \alpha_b) = V_{\text{eff}}(\alpha_b, \alpha_c) = V_{\text{eff}}(\alpha_c, \alpha_a) = 0$. The energy cost of a non-aligned pair would be infinite (due to the fact that this is a hard-core potential), so that the only remaining option is that the dimers shrink in size, effectively becoming non-interacting. This is the mechanism which breaks magnetic order for the triangular lattice of dimers.

5.3.2 Three dimensions

We now turn to the three-dimensional case, where the solid phase at large pressure is constituted by a simple-hexagonal lattice of single particles. As in the two-dimensional case, we compute the equation of state by Monte Carlo simulations at fixed pressure, always starting from the defect-free solid phase. The three-dimensional EOS also shows a density jump, at a critical pressure $\beta P_c R_0^3 = 18.5$: The lattice melts at $P = P_c$, and the system is liquid for smaller pressure (cf. Fig. 5.20).

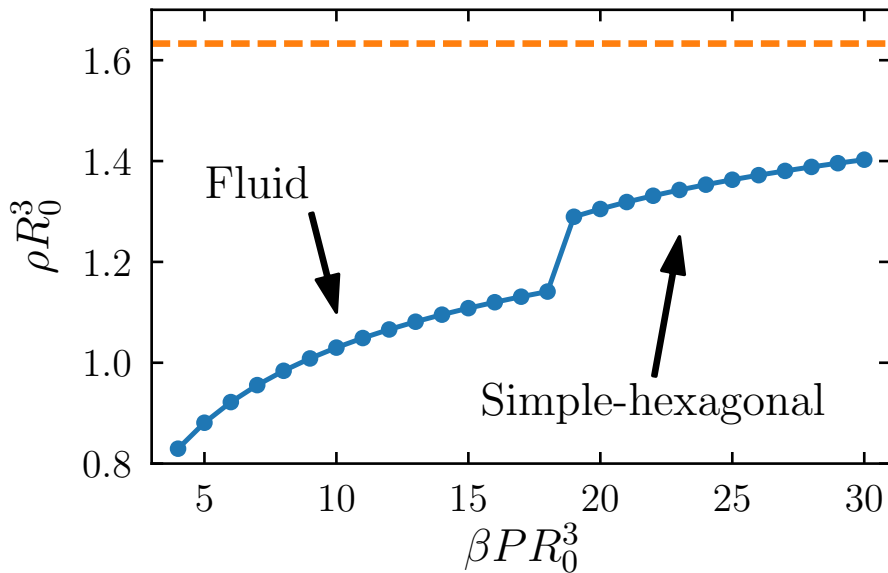


Figure 5.20: Equation of state (density *vs.* pressure) for the three-dimensional three-body hard-core model with $N = 64$ (*blue points*), compared with the density of the close-packed simple-hexagonal lattice (*orange dashed line*, corresponding to $\rho R_0^3 \simeq 1.63299$).

As the solid-phase structure does not include the formation of dimers, we do not map the $d = 3$ system onto effective hard-sphere or spin models. The main option for

an intermediate phase consists in the presence of a second solid phase, with different structure, separated by the simple-hexagonal solid phase by a structural transition.

The study of structural properties for three-dimensional systems is typically based on the use of bond-orientational order parameters (BOOP's) [206], which are a more general version of the sixfold orientational order parameter $\psi_{6,i}$ defined above for the two-dimensional case. Following Ref. [204], we rather consider the closely-related local Minkowski structure metrics, as the original BOOP's are known to have important shortcomings. The l -th order metric for particle i is defined as

$$q_{l,i} = \sqrt{\frac{4\pi}{2l+1} \sum_{m=-l}^l \left| \sum_{j \in \mathcal{F}_i} W_{ij} Y_{lm}(\theta_{ij}, \phi_{ij}) \right|^2}, \quad (5.52)$$

where Y_{lm} are the spherical-harmonics functions, evaluated for the solid angle determined by the bond unit vector

$$\frac{\mathbf{x}_i - \mathbf{x}_j}{|\mathbf{x}_i - \mathbf{x}_j|}. \quad (5.53)$$

The set \mathcal{F}_i of neighbors of particle i includes all particles j such that the i -th and j -th Voronoi cells share a facet, and the area W_{ij} of this facet (normalized so that $\sum_{j \in \mathcal{F}_i} W_{ij} = 1$) enters as a weight in the sum $\sum_{j \in \mathcal{F}_i}$, cf. Eq. 5.52. As for the two-dimensional case (cf. Eq. 5.48), we use this weighted sum of the contributions of all neighbors j : This is robust against the main shortcoming of the BOOP, namely the dependence on the definition of neighboring sites [204]. The local BOOP's and Minkowski structure metrics are largely used to identify regular structures (see references in Ref. [204]). In particular, the joint probability distribution of q_4 and q_6 has been employed to identify different crystalline structures for Lennard-Jones systems [207]. We compute this joint distribution from the MC data at several pressures, using available software tools [208], and find the following results (cf. Fig. 5.21):

- The distributions of q_4 and q_6 are broader for pressures below P_c , and become narrower in the solid phase.
- In the solid phase, the average values of q_4 and q_6 tend to the values computed for an ideal simple-hexagonal lattice as P is increased.
- In the fluid phase, q_4 and q_6 show no correlation. In the solid, they acquire a weak positive correlation, which is anyway hidden by the fact that both distributions become quite narrow, with their averages tending to the infinite-pressure values.

This calculation lacks any indication of an additional structural transition between two solid phases: For $P > P_c$, the equation of state is smooth, excluding the possibility of a stable intermediate phase.

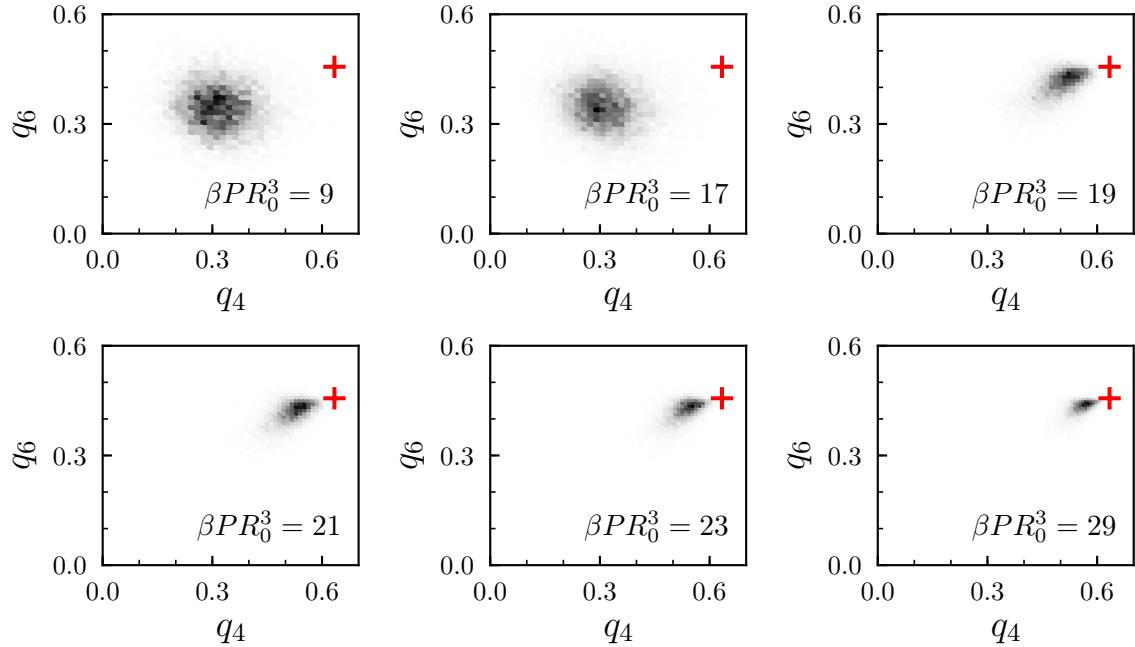


Figure 5.21: Joint histograms of the local Minkowski structure metrics (q_4, q_6) for different values of the pressure, below and above $\beta P_c R_0^3 \simeq 18.5$. The red cross marks the values of the perfect simple-hexagonal lattice, $q_4 \simeq 0.6339$ and $q_6 \simeq 0.4563$.

Conclusion

In this chapter, we have studied the classical three-body hard-core model, in two and three dimensions. We first considered the packing problem, by using several analytic ansätze. The best global-optimum candidates (the triangular lattice of dimers for $d = 2$, and the simple-hexagonal lattice of single particles for $d = 3$) are independently obtained through the simulated-annealing technique.

We extended these results to finite pressure via the NPT Monte Carlo technique, modified through the addition of the insertion/removal move. Both for $d = 2$ and $d = 3$, we observe a discontinuous melting transition between the solid and fluid phases, without signatures of intermediate phases. For $d = 2$, the closely-bound dimers which form the solid do not show any hidden order, when mapped onto effective hard-disk or spin models.

General conclusion

In this thesis, we address the quantum many-body problem for bosons at unitarity. The connection with the few-body properties of this system, in particular with the Efimov effect, is taken into account in our model, which reproduces the expected universal features. Starting from the exact solution of the two-body problem at finite temperature, we develop a novel QMC algorithm, which treats unitary interactions efficiently. In Chapter 4, we compute the phase diagram for a homogeneous system. The thermodynamic instability towards the Efimov liquid is observed in QMC simulations, and well captured by an approximate analytic model. Through the latter, we compute the barrier in the excitation free-energy, which sets a finite time scale for nucleation. In the remaining part of the phase diagram, the system is homogeneous. This allows us to identify the BEC critical temperature, which is reduced by approximately 10% from its non-interacting value. Furthermore, we compute the momentum distribution at different temperatures, observing the large-momentum power-law tail and the depletion of the condensate due to interactions. In the homogeneous regions of the phase diagram, physical properties have a weak dependence on the three-body cutoff R_0 , justifying our use of the hard-core three-body regularization scheme.

Our novel QMC algorithm is tailored to the unitary Bose gas, but its main ingredient (the two-body direct-sampling move) is more general. The core idea consists in combining the pair-product approximation with an optimal QMC move at the two-body level, which may be extended to systems in reduced dimensions or with different interaction potentials.

Efimov-liquid droplets do not show a strong dependence on temperature, and their structural properties, like the density, are mainly determined by R_0 . This is a first step towards the connection with the cluster ground states predicted for small systems of unitary particles [71, 72]. A comparison of the different current predictions would allow to better assess the universality of these states, which in this work are studied at thermal equilibrium. The study of a macroscopic liquid phase, however, would be best

performed in a homogeneous situation, rather than in the presence of phase separation. This can be obtained for instance within the grand canonical ensemble, for which QMC algorithms are already available [136].

While remaining in the homogeneous regions of the phase diagram, a further open question concerns the effect of Efimov trimers in a many-body equilibrium state. On one hand, it would be interesting to find a method to identify them and estimate their size. On the other hand, their presence could have noticeable effect on observables like the energy. The latter has not been measured in this study, and would certainly need to be addressed in a following work.

In Chapter 5, we consider the classical three-body hard-core model, which would represent the infinite-temperature limit of our unitary-gas model. We propose solutions for the packing problem in $d = 2$ and $d = 3$, which consist in a triangular lattice of pairs of particles and in a simple-hexagonal lattice with one particle per site, respectively. These counter-intuitive structures are a consequence of the purely three-body interactions, and it would be interesting to verify how they are modified in the presence of weak two-body interactions. To extend these results to finite pressure and identify the melting transition, we use the NPT Monte Carlo technique. A systematic study of our insertion/removal move could show whether this proposal provides a clear advantage in the notoriously hard study of the melting transition.

Acknowledgements

First of all, I wish to thank my PhD advisor, Werner Krauth. His main role was to push me forward, and there is no doubt that this has been constantly done. I also express my gratitude to the members of the PhD committee, Hans-Werner Hammer, Tommaso Roscilde, Christophe Salomon, and Patrizia Vignolo, for their careful scrutiny of my work and interesting comments.

Several people contributed directly to the research reported in this manuscript. The presence of Riccardo Rossi has been crucial, in the last three years, as he represents a perfect (and perfectionist) sparring partner. Also Kris van Houcke, Sebastian Kapfer, Xavier Leyronas, Swann Piatecki, and Félix Werner helped me to shape this work, with essential comments and suggestions. The big picture behind the unitary-gas project became more clear thanks to many other discussions, including those with Yvan Castin, Frédéric Chevy, Zoran Hadzibabic, and Youjin Deng.

The manuscript and defense preparation would have been harder without the generous help of those who spent their time in rereading the thesis and listening to the rehearsals. Juliane, Quentin, Vasileios, Volker, and Ze, thank you!

Finally, I whish to thank the large network of friends, colleagues, and family members, not only in Milan and Paris, but also in Lisbon and Concepción, in Utrecht and Trento, in Lyon and Florence, and in many other places. Their constant support and affection were fundamental in these last three years.

Bibliography

- [1] M. H. Anderson, J. R. Ensher, M. R. Matthews, C. E. Wieman, and E. A. Cornell. [Observation of Bose-Einstein Condensation in a Dilute Atomic Vapor](#). *Science*, 269(5221):198–201, 1995. doi: 10.1126/science.269.5221.198.
- [2] C. C. Bradley, C. A. Sackett, J. J. Tollett, and R. G. Hulet. [Evidence of Bose-Einstein Condensation in an Atomic Gas with Attractive Interactions](#). *Phys. Rev. Lett.*, 75: 1687–1690, 1995. doi: 10.1103/PhysRevLett.75.1687.
- [3] K. B. Davis, M. O. Mewes, M. R. Andrews, N. J. van Druten, D. S. Durfee, D. M. Kurn, and W. Ketterle. [Bose-Einstein Condensation in a Gas of Sodium Atoms](#). *Phys. Rev. Lett.*, 75:3969–3973, 1995. doi: 10.1103/PhysRevLett.75.3969.
- [4] I. Bloch, J. Dalibard, and S. Nascimbene. [Quantum simulations with ultracold quantum gases](#). *Nat. Phys.*, 8(4):267–276, 2012. doi: 10.1038/nphys2259.
- [5] C. Chin, R. Grimm, P. Julienne, and E. Tiesinga. [Feshbach resonances in ultracold gases](#). *Rev. Mod. Phys.*, 82(2):1225–1286, 2010. doi: 10.1103/RevModPhys.82.1225.
- [6] W. Zwerger, editor. *The BCS-BEC Crossover and the Unitary Fermi Gas*, volume 836 of *Lecture Notes in Physics*. Springer-Verlag Berlin Heidelberg, 2012. doi: 10.1007/978-3-642-21978-8.
- [7] V. Efimov. [Energy levels arising from resonant two-body forces in a three-body system](#). *Phys. Lett. B*, 33(8):563–564, 1970. doi: 10.1016/0370-2693(70)90349-7.
- [8] T. Kraemer, M. Mark, P. Waldburger, J. G. Danzl, C. Chin, B. Engeser, A. D. Lange, K. Pilch, A. Jaakkola, H.-C. Nägerl, and R. Grimm. [Evidence for Efimov quantum states in an ultracold gas of caesium atoms](#). *Nature*, 440:315–318, 2006. doi: 10.1038/nature04626.

- [9] F. Chevy and C. Salomon. [Strongly correlated Bose gases](#). *J. Phys. B: At. Mol. Phys.*, 49(19):192001, 2016. doi: 10.1088/0953-4075/49/19/192001.
- [10] E. Braaten and H.-W. Hammer. [Universality in few-body systems with large scattering length](#). *Phys. Rep.*, 428(5-6):259 – 390, 2006. ISSN 0370-1573. doi: 10.1016/j.physrep.2006.03.001.
- [11] D. M. Ceperley. [Path integrals in the theory of condensed helium](#). *Rev. Mod. Phys.*, 67(2):279–355, 1995. doi: 10.1103/RevModPhys.67.279.
- [12] S. Piatecki and W. Krauth. [Efimov-driven phase transitions of the unitary Bose gas](#). *Nat. Commun.*, 5:3503, 2014. doi: 10.1038/ncomms4503.
- [13] Y. Castin and F. Werner. [Le troisième coefficient du viriel du gaz de Bose unitaire](#). *Can. J. Phys.*, 91(5):382–389, 2013. doi: 10.1139/cjp-2012-0569. English version: arXiv:1212.5512.
- [14] J. O. Andersen. [Theory of the weakly interacting Bose gas](#). *Rev. Mod. Phys.*, 76: 599–639, 2004. doi: 10.1103/RevModPhys.76.599.
- [15] L. P. Pitaevskii and S. Stringari. [Bose-Einstein Condensation](#). Oxford University Press, Oxford, 2003.
- [16] A. J. Leggett. [Quantum Liquids: Bose Condensation and Cooper Pairing in Condensed-matter Systems](#). Oxford Graduate Texts. OUP Oxford, 2006. ISBN 9780198526438.
- [17] O. Penrose and L. Onsager. [Bose-Einstein Condensation and Liquid Helium](#). *Phys. Rev.*, 104:576–584, 1956. doi: 10.1103/PhysRev.104.576.
- [18] C. N. Yang. [Concept of Off-Diagonal Long-Range Order and the Quantum Phases of Liquid He and of Superconductors](#). *Rev. Mod. Phys.*, 34:694–704, 1962. doi: 10.1103/RevModPhys.34.694.
- [19] F. London. [The \$\lambda\$ -Phenomenon of Liquid Helium and the Bose-Einstein Degeneracy](#). *Nature*, 141:643–644, 1938. doi: 10.1038/141643a0.
- [20] M. E. Fisher, M. N. Barber, and D. Jasnow. [Helicity Modulus, Superfluidity, and Scaling in Isotropic Systems](#). *Phys. Rev. A*, 8:1111–1124, 1973. doi: 10.1103/PhysRevA.8.1111.
- [21] M. N. Barber. [Helicity modulus for an ideal Bose fluid](#). *J. Phys. A*, 10(8):1335, 1977. doi: 10.1088/0305-4470/10/8/012.
- [22] M. N. Barber. [Finite-size scaling](#). In C. Comb and J. L. Lebowitz, editors, *Phase transitions and Critical Phenomena*. Academic, New York, 1983.

- [23] E. L. Pollock and D. M. Ceperley. Path-integral computation of superfluid densities. *Phys. Rev. B*, 36:8343–8352, 1987. doi: 10.1103/PhysRevB.36.8343.
- [24] A. J. Leggett. BEC: The alkali gases from the perspective of research on liquid helium. *AIP Conf. Proc.*, 477(1):154–169, 1999. doi: 10.1063/1.59354.
- [25] D. Jervis and J. H. Thywissen. Making an Ultracold Gas, chapter 2, pages 5–32. Imperial College Press, 2015. doi: 10.1142/9781783264766_0002.
- [26] S. Baier, M. J. Mark, D. Petter, K. Aikawa, L. Chomaz, Z. Cai, M. Baranov, P. Zoller, and F. Ferlaino. Extended Bose-Hubbard models with ultracold magnetic atoms. *Science*, 352(6282):201–205, 2016. ISSN 0036-8075. doi: 10.1126/science.aac9812.
- [27] A. L. Gaunt, T. F. Schmidutz, I. Gotlibovych, R. P. Smith, and Z. Hadzibabic. Bose-Einstein Condensation of Atoms in a Uniform Potential. *Phys. Rev. Lett.*, 110: 200406, 2013. doi: 10.1103/PhysRevLett.110.200406.
- [28] L. Chomaz, L. Corman, T. Bienaimé, R. Desbuquois, C. Weitenberg, S. Nascimbène, J. Beugnon, and J. Dalibard. Emergence of coherence via transverse condensation in a uniform quasi-two-dimensional Bose gas . *Nat. Commun.*, 6:6162, 2015. doi: 10.1038/ncomms7162.
- [29] F. Dalfovo, S. Giorgini, L. P. Pitaevskii, and S. Stringari. Theory of Bose-Einstein condensation in trapped gases. *Rev. Mod. Phys.*, 71:463–512, 1999. doi: 10.1103/RevModPhys.71.463.
- [30] L. Chomaz, S. Baier, D. Petter, M. J. Mark, F. Wächtler, L. Santos, and F. Ferlaino. Quantum-Fluctuation-Driven Crossover from a Dilute Bose-Einstein Condensate to a Macrodroplet in a Dipolar Quantum Fluid. *Phys. Rev. X*, 6:041039, 2016. doi: 10.1103/PhysRevX.6.041039.
- [31] I. Ferrier-Barbut, H. Kadau, M. Schmitt, M. Wenzel, and T. Pfau. Observation of Quantum Droplets in a Strongly Dipolar Bose Gas. *Phys. Rev. Lett.*, 116:215301, 2016. doi: 10.1103/PhysRevLett.116.215301.
- [32] T. D. Lee, K. Huang, and C. N. Yang. Eigenvalues and Eigenfunctions of a Bose System of Hard Spheres and Its Low-Temperature Properties. *Phys. Rev.*, 106: 1135–1145, 1957. doi: 10.1103/PhysRev.106.1135.
- [33] N. Navon, S. Piatecki, K. Günter, B. Rem, T. C. Nguyen, F. Chevy, W. Krauth, and C. Salomon. Dynamics and Thermodynamics of the Low-Temperature Strongly Interacting Bose Gas. *Phys. Rev. Lett.*, 107:135301, 2011. doi: 10.1103/PhysRevLett.107.135301.
- [34] R. P. Feynman. Space-Time Approach to Non-Relativistic Quantum Mechanics. *Rev. Mod. Phys.*, 20:367–387, 1948. doi: 10.1103/RevModPhys.20.367.

- [35] R. P. Feynman. *Atomic Theory of the λ Transition in Helium*. *Phys. Rev.*, 91:1291–1301, 1953. doi: 10.1103/PhysRev.91.1291.
- [36] R. P. Feynman and A. R. Hibbs. *Quantum mechanics and path integrals*. International series in pure and applied physics. McGraw-Hill, New York, St. Louis, San Francisco, 1965. ISBN 0-07-020650-3.
- [37] P. T. Landsberg. *Thermodynamics: With Quantum Statistical Illustrations*. Monographs in Statistical Physics and Thermodynamics. Interscience Publishers, 1961.
- [38] P. Borrmann and G. Franke. *Recursion formulas for quantum statistical partition functions*. *J. Chem. Phys.*, 98(3):2484–2485, 1993. doi: 10.1063/1.464180.
- [39] W. Krauth. *Statistical Mechanics: Algorithms and Computations*. Oxford University Press, USA, 2006.
- [40] M. Holzmann and W. Krauth. *Transition Temperature of the Homogeneous, Weakly Interacting Bose Gas*. *Phys. Rev. Lett.*, 83:2687–2690, 1999. doi: 10.1103/PhysRevLett.83.2687.
- [41] M. Chevallier. *Bosons à basse température: des intégrales de chemin aux gaz quasi-bidimensionnels*. PhD thesis, Université Pierre et Marie Curie - Paris VI, 2009.
- [42] M. Chevallier and W. Krauth. *Off-diagonal long-range order, cycle probabilities, and condensate fraction in the ideal Bose gas*. *Phys. Rev. E*, 76:051109, 2007. doi: 10.1103/PhysRevE.76.051109.
- [43] W. van Dijk, C. Lobo, A. MacDonald, and R. K. Bhaduri. *Fisher zeros of a unitary Bose gas*. *Can. J. Phys.*, 0(0):1–6, 2014. doi: 10.1139/cjp-2014-0585.
- [44] L. D. Landau and E. M. Lifshitz. *Quantum Mechanics: Non-Relativistic Theory*. Pergamon Press, 3rd edition, 1991.
- [45] J. Dalibard. Collisional dynamics of ultra-cold atomic gases. In M. Inguscio, S. Stringari, C.E. Wieman (Eds): *Bose-Einstein Condensation in Atomic Gases*, volume 140, pages 321–349. IOP Press, Amsterdam, 1999.
- [46] Y. Castin and F. Werner. *The Unitary Gas and its Symmetry Properties*, pages 127–191. Springer Berlin Heidelberg, Berlin, Heidelberg, 2012. ISBN 978-3-642-21978-8. doi: 10.1007/978-3-642-21978-8_5.
- [47] W. Krauth. *Quantum Monte Carlo Calculations for a Large Number of Bosons in a Harmonic Trap*. *Phys. Rev. Lett.*, 77:3695–3699, 1996. doi: 10.1103/PhysRevLett.77.3695.

- [48] H. Bethe and R. Peierls. [Quantum Theory of the Diplon](#). *Proc. R. Soc. London, Ser. A*, 148(863):146–156, 1935. ISSN 0080-4630. doi: 10.1098/rspa.1935.0010.
- [49] F. Werner and Y. Castin. [General relations for quantum gases in two and three dimensions. II. Bosons and mixtures](#). *Phys. Rev. A*, 86:053633, 2012. doi: 10.1103/PhysRevA.86.053633.
- [50] M. Holzmann. [La transition de Bose-Einstein dans un gaz dilué](#). PhD thesis, Université Pierre et Marie Curie - Paris VI, 2000.
- [51] S. Piatecki. [The Bose gas at large scattering lengths](#). PhD thesis, École Normale Supérieure, Paris, 2014.
- [52] J. Carlson, S.-Y. Chang, V. R. Pandharipande, and K. E. Schmidt. [Dilute Fermi Gases with Large Scattering Lengths: Atomic Gases and Neutron Matter](#). *AIP Conf. Proc.*, 690(1):184–191, 2003. doi: 10.1063/1.1632128.
- [53] Y. Yan and D. Blume. [Incorporating exact two-body propagators for zero-range interactions into N-body Monte Carlo simulations](#). *Phys. Rev. A*, 91:043607, 2015. doi: 10.1103/PhysRevA.91.043607.
- [54] R. Pessoa, S. A. Vitiello, and K. E. Schmidt. [Monte Carlo Calculations for Fermi Gases in the Unitary Limit with a Zero-Range Interaction](#). *J. Low Temp. Phys.*, 180(1-2):168–179, 2015. ISSN 0022-2291. doi: 10.1007/s10909-015-1283-0.
- [55] R. Pessoa, S. Gandolfi, S. A. Vitiello, and K. E. Schmidt. [Contact interaction in a unitary ultracold Fermi gas](#). *Phys. Rev. A*, 92:063625, 2015. doi: 10.1103/PhysRevA.92.063625.
- [56] L. Viverit, S. Giorgini, L.P. Pitaevskii, and S. Stringari. [Momentum distribution of a trapped Fermi gas with large scattering length](#). *Phys. Rev. A*, 69:013607, 2004. doi: 10.1103/PhysRevA.69.013607.
- [57] S. Tan. [Generalized virial theorem and pressure relation for a strongly correlated Fermi gas](#). *Ann. Phys.*, 323(12):2987 – 2990, 2008. ISSN 0003-4916. doi: 10.1016/j.aop.2008.03.003.
- [58] F. Werner and Y. Castin. [General relations for quantum gases in two and three dimensions: Two-component fermions](#). *Phys. Rev. A*, 86:013626, 2012. doi: 10.1103/PhysRevA.86.013626.
- [59] D. Blume and K. M. Daily. [Universal relations for a trapped four-fermion system with arbitrary s-wave scattering length](#). *Phys. Rev. A*, 80:053626, 2009. doi: 10.1103/PhysRevA.80.053626.

- [60] M. J. Lighthill. *An Introduction to Fourier Analysis and Generalised Functions*. Cambridge Monographs on Mechanics. Cambridge University Press, 1964.
- [61] R. K. Pathria and P. D. Beale. *Statistical Mechanics*. Elsevier Science, 3rd edition, 2011. ISBN 9780123821898.
- [62] D. H. Smith, E. Braaten, D. Kang, and L. Platter. [Two-Body and Three-Body Contacts for Identical Bosons near Unitarity](#). *Phys. Rev. Lett.*, 112:110402, 2014. doi: 10.1103/PhysRevLett.112.110402.
- [63] M. Barth and J. Hofmann. [Efimov correlations in strongly interacting Bose gases](#). *Phys. Rev. A*, 92:062716, 2015. doi: 10.1103/PhysRevA.92.062716.
- [64] X.-J. Liu, B. Mulkerin, L. He, and H. Hu. [Equation of state and contact of a strongly interacting Bose gas in the normal state](#). *Phys. Rev. A*, 91:043631, 2015. doi: 10.1103/PhysRevA.91.043631.
- [65] V. Efimov. Weakly-bound states of three resonantly-interacting particles. *Sov. J. Nucl. Phys.*, 12(589):101, 1971.
- [66] Y. Nishida, Y. Kato, and C. D. Batista. [Efimov effect in quantum magnets](#). *Nat. Phys.*, 9(2):93–97, 2013. doi: doi:10.1038/nphys2523.
- [67] T. Pal, P. Sadhukhan, and S. M. Bhattacharjee. [Renormalization Group Limit Cycle for Three-Stranded DNA](#). *Phys. Rev. Lett.*, 110:028105, 2013. doi: 10.1103/PhysRevLett.110.028105.
- [68] L. H. Thomas. The Interaction Between a Neutron and a Proton and the Structure of H^3 . *Phys. Rev.*, 47:903–909, 1935. doi: 10.1103/PhysRev.47.903.
- [69] E. Nielsen, D. V. Fedorov, A. S. Jensen, and E. Garrido. [The three-body problem with short-range interactions](#). *Phys. Rep.*, 347(5):373 – 459, 2001. ISSN 0370-1573. doi: 10.1016/S0370-1573(00)00107-1.
- [70] P. Naidon and S. Endo. [Efimov Physics: a review](#). 2016. arXiv:1610.09805 [quant-ph].
- [71] J. von Stecher. [Weakly bound cluster states of Efimov character](#). *J. Phys. B*, 43(10): 101002, 2010. doi: 10.1088/0953-4075/43/10/101002.
- [72] Y. Yan and D. Blume. [Energy and structural properties of \$N\$ -boson clusters attached to three-body Efimov states: Two-body zero-range interactions and the role of the three-body regulator](#). *Phys. Rev. A*, 92:033626, 2015. doi: 10.1103/PhysRevA.92.033626.

- [73] Y. Castin and F. Werner. [Single-particle momentum distribution of an Efimov trimer](#). *Phys. Rev. A*, 83:063614, 2011. doi: 10.1103/PhysRevA.83.063614.
- [74] B. S. Rem, A. T. Grier, I. Ferrier-Barbut, U. Eismann, T. Langen, N. Navon, L. Khaykovich, F. Werner, D. S. Petrov, F. Chevy, and C. Salomon. [Lifetime of the Bose Gas with Resonant Interactions](#). *Phys. Rev. Lett.*, 110:163202, 2013. doi: 10.1103/PhysRevLett.110.163202.
- [75] R. J. Fletcher, A. L. Gaunt, N. Navon, R. P. Smith, and Z. Hadzibabic. [Stability of a Unitary Bose Gas](#). *Phys. Rev. Lett.*, 111:125303, 2013. doi: 10.1103/PhysRevLett.111.125303.
- [76] U. Eismann, L. Khaykovich, S. Laurent, I. Ferrier-Barbut, B. S. Rem, A. T. Grier, M. Delehaye, F. Chevy, C. Salomon, L.-C. Ha, and C. Chin. [Universal Loss Dynamics in a Unitary Bose Gas](#). *Phys. Rev. X*, 6:021025, 2016. doi: 10.1103/PhysRevX.6.021025.
- [77] R. J. Fletcher, R. Lopes, J. Man, N. Navon, R. P. Smith, M. W. Zwierlein, and Z. Hadzibabic. [Two and Three-body Contacts in the Unitary Bose Gas](#). 2016. arXiv 1608.04377 [cond-mat.quant-gas].
- [78] P. Makotyn, C. E. Klauss, D. L. Goldberger, E. A. Cornell, and D. S. Jin. [Universal dynamics of a degenerate unitary Bose gas](#). *Nat. Phys.*, 10(2):116–119, 2014. doi: 10.1038/nphys2850.
- [79] H. M. J. M. Boesten, C. C. Tsai, B. J. Verhaar, and D. J. Heinzen. [Observation of a Shape Resonance in Cold-Atom Scattering by Pulsed Photoassociation](#). *Phys. Rev. Lett.*, 77:5194–5197, 1996. doi: 10.1103/PhysRevLett.77.5194.
- [80] H. M. J. M. Boesten, C. C. Tsai, J. R. Gardner, D. J. Heinzen, and B. J. Verhaar. [Observation of a shape resonance in the collision of two cold \$^{87}\text{Rb}\$ atoms](#). *Phys. Rev. A*, 55:636–640, 1997. doi: 10.1103/PhysRevA.55.636.
- [81] S. Inouye, M. R. Andrews, J. Stenger, H.-J. Miesner, D. M. Stamper-Kurn, and W. Ketterle. [Observation of Feshbach resonances in a Bose–Einstein condensate](#). *Nature*, 392:151–154, 1998. doi: 10.1038/32354.
- [82] Ph. Courteille, R. S. Freeland, D. J. Heinzen, F. A. van Abeelen, and B. J. Verhaar. [Observation of a Feshbach Resonance in Cold Atom Scattering](#). *Phys. Rev. Lett.*, 81:69–72, 1998. doi: 10.1103/PhysRevLett.81.69.
- [83] B. Huang, L. A. Sidorenkov, R. Grimm, and J. M. Hutson. [Observation of the Second Triatomic Resonance in Efimov’s Scenario](#). *Phys. Rev. Lett.*, 112:190401, 2014. doi: 10.1103/PhysRevLett.112.190401.

- [84] E. A. Burt, R. W. Ghrist, C. J. Myatt, M. J. Holland, E. A. Cornell, and C. E. Wieman. **Coherence, Correlations, and Collisions: What One Learns about Bose-Einstein Condensates from Their Decay.** *Phys. Rev. Lett.*, 79:337–340, 1997. doi: 10.1103/PhysRevLett.79.337.
- [85] P. O. Fedichev, M. W. Reynolds, and G. V. Shlyapnikov. **Three-Body Recombination of Ultracold Atoms to a Weakly Bound s Level.** *Phys. Rev. Lett.*, 77:2921–2924, 1996. doi: 10.1103/PhysRevLett.77.2921.
- [86] T Weber, J. Herbig, M. Mark, H.-C. Nägerl, and R. Grimm. **Three-Body Recombination at Large Scattering Lengths in an Ultracold Atomic Gas.** *Phys. Rev. Lett.*, 91:123201, 2003. doi: 10.1103/PhysRevLett.91.123201.
- [87] M. Zaccanti, B. Deissler, C. D'Errico, M. Fattori, M. Jona-Lasinio, S. Müller, G. Roati, M. Inguscio, and G. Modugno. **Observation of an Efimov spectrum in an atomic system .** *Nat. Phys.*, 5:586–591, 2009.
- [88] S. E. Pollack, D. Dries, and R. G. Hulet. **Universality in Three- and Four-Body Bound States of Ultracold Atoms .** *Science*, 326:1683–1685, 2009. doi: 10.1126/science.1182840.
- [89] F. Ferlaino, A. Zenesini, M. Berninger, B. Huang, H. C. Nägerl, and R. Grimm. **Efimov Resonances in Ultracold Quantum Gases.** *Few-Body Syst.*, 51(2):113–133, 2011. ISSN 1432-5411. doi: 10.1007/s00601-011-0260-7.
- [90] S.-K. Tung, K. Jiménez-García, J. Johansen, C. V. Parker, and C. Chin. **Geometric Scaling of Efimov States in a ${}^6\text{Li}$ - ${}^{133}\text{Cs}$ Mixture.** *Phys. Rev. Lett.*, 113:240402, 2014. doi: 10.1103/PhysRevLett.113.240402.
- [91] Y. Wang, J. P. D’Incao, and B. D. Esry. **Ultracold Few-Body Systems.** In E. Arimondo, P. R. Berman, and C. C. Lin, editors, *Advances in Atomic, Molecular, and Optical Physics*, volume 62, chapter 1, pages 1 – 115. Academic Press, 2013. doi: 10.1016/B978-0-12-408090-4.00001-3.
- [92] J. Wang, J. P. D’Incao, B. D. Esry, and Chris H. Greene. **Origin of the Three-Body Parameter Universality in Efimov Physics.** *Phys. Rev. Lett.*, 108:263001, 2012. doi: 10.1103/PhysRevLett.108.263001.
- [93] R. Schmidt, S.P. Rath, and W. Zwerger. **Efimov physics beyond universality.** *Eur. Phys. J. B*, 85(11):1–6, 2012. ISSN 1434-6036. doi: 10.1140/epjb/e2012-30841-3.
- [94] P. Naidon, S. Endo, and M. Ueda. **Physical origin of the universal three-body parameter in atomic Efimov physics.** *Phys. Rev. A*, 90:022106, 2014. doi: 10.1103/PhysRevA.90.022106.

- [95] P. Naidon, S. Endo, and M. Ueda. **Microscopic Origin and Universality Classes of the Efimov Three-Body Parameter.** *Phys. Rev. Lett.*, 112:105301, 2014. doi: 10.1103/PhysRevLett.112.105301.
- [96] P. M. A. Mestrom, J. Wang, C. H. Greene, and J. P. D’Incao. **Efimov universality for ultracold atoms with positive scattering lengths.** 2016. arXiv 1609.02857 [physics.atom-ph].
- [97] R. D. Amado and F. C. Greenwood. **There Is No Efimov Effect for Four or More Particles.** *Phys. Rev. D*, 7:2517–2519, 1973. doi: 10.1103/PhysRevD.7.2517.
- [98] H. W. Hammer and L. Platter. **Universal properties of the four-body system with large scattering length.** *Eur. Phys. J. A*, 32(1):113–120, 2007. ISSN 1434-601X. doi: 10.1140/epja/i2006-10301-8.
- [99] J. von Stecher, J. P. D’Incao, and C. H. Greene. **Signatures of universal four-body phenomena and their relation to the Efimov effect .** *Nat. Phys.*, 5:417–421, 2009.
- [100] F. Ferlaino, S. Knoop, M. Berninger, W. Harm, J. P. D’Incao, H.-C. Nägerl, and R. Grimm. **Evidence for Universal Four-Body States Tied to an Efimov Trimer.** *Phys. Rev. Lett.*, 102:140401, 2009. doi: 10.1103/PhysRevLett.102.140401.
- [101] B. S. Rem. **The Road to the Unitary Bose Gas.** PhD thesis, École Normale Supérieure, Paris, 2013.
- [102] R. J. Wild, P. Makotyn, J. M. Pino, E. A. Cornell, and D. S. Jin. **Measurements of Tan’s Contact in an Atomic Bose-Einstein Condensate.** *Phys. Rev. Lett.*, 108:145305, 2012. doi: 10.1103/PhysRevLett.108.145305.
- [103] S. Laurent, X. Leyronas, and F. Chevy. **Momentum Distribution of a Dilute Unitary Bose Gas with Three-Body Losses.** *Phys. Rev. Lett.*, 113:220601, 2014. doi: 10.1103/PhysRevLett.113.220601.
- [104] M. E. J. Newman and G. T. Barkema. *Monte Carlo Methods in Statistical Physics.* Clarendon Press, 1999. ISBN 9780198517979.
- [105] D. Frenkel and B. Smit. *Understanding Molecular Simulation: From Algorithms to Applications.* Academic Press, San Diego, 2nd edition, 2002.
- [106] J. von Neumann. Various techniques used in connection with random digits. In *The Monte Carlo Method*, number 12 in National Bureau of Standards Applied Mathematics Series, pages 36–38. United States Government Printing Office, Washington, DC, 1951.

- [107] A. J. Walker. An efficient method for generating discrete random variables with general distributions. *ACM Transactions on Mathematical Software (TOMS)*, 3(3): 253–256, 1977. doi: 10.1145/355744.355749.
- [108] A. Sokal. *Monte Carlo Methods in Statistical Mechanics: Foundations and New Algorithms*, pages 131–192. Springer US, Boston, MA, 1997. ISBN 978-1-4899-0319-8. doi: 10.1007/978-1-4899-0319-8_6.
- [109] N. Metropolis, A. W. Rosenbluth, M. N. Rosenbluth, A. H. Teller, and E. Teller. Equation of State Calculations by Fast Computing Machines. *J. Chem. Phys.*, 21(6): 1087–1092, 1953. doi: 10.1063/1.1699114.
- [110] W. K. Hastings. Monte Carlo sampling methods using Markov chains and their applications. *Biometrika*, 57(1):97–109, 1970. doi: 10.1093/biomet/57.1.97.
- [111] B. Efron. Bootstrap Methods: Another Look at the Jackknife. *Ann. Statist.*, 7(1): 1–26, 1979. doi: 10.1214/aos/1176344552.
- [112] E. P. Bernard and W. Krauth. Two-Step Melting in Two Dimensions: First-Order Liquid-Hexatic Transition. *Phys. Rev. Lett.*, 107:155704, 2011. doi: 10.1103/PhysRevLett.107.155704.
- [113] M. Michel, S. C. Kapfer, and W. Krauth. Generalized event-chain Monte Carlo: Constructing rejection-free global-balance algorithms from infinitesimal steps. *J. Chem. Phys.*, 140(5):054116, 2014. doi: 10.1063/1.4863991.
- [114] S. C. Kapfer and W. Krauth. Two-Dimensional Melting: From Liquid-Hexatic Coexistence to Continuous Transitions. *Phys. Rev. Lett.*, 114:035702, 2015. doi: 10.1103/PhysRevLett.114.035702.
- [115] M. Isobe and W. Krauth. Hard-sphere melting and crystallization with event-chain Monte Carlo. *J. Chem. Phys.*, 143(8):084509, 2015. doi: 10.1063/1.4929529.
- [116] M. Michel, J. Mayer, and W. Krauth. Event-chain Monte Carlo for classical continuous spin models. *EPL (Europhysics Letters)*, 112(2):20003, 2015. doi: 10.1209/0295-5075/112/20003.
- [117] Y. Nishikawa, M. Michel, W. Krauth, and K. Hukushima. Event-chain algorithm for the Heisenberg model: Evidence for $z \simeq 1$ dynamic scaling. *Phys. Rev. E*, 92: 063306, 2015. doi: 10.1103/PhysRevE.92.063306.
- [118] K. Van Houcke, E. Kozik, N. Prokof'ev, and B. Svistunov. Diagrammatic Monte Carlo. *Phys. Procedia*, 6:95–105, 2010. doi: 10.1016/j.phpro.2010.09.034.

- [119] L. Pollet. Recent developments in quantum Monte Carlo simulations with applications for cold gases. *Rep. Progr. Phys.*, 75(9):094501, 2012. doi: 10.1088/0034-4885/75/9/094501.
- [120] S. Humeniuk and T. Roscilde. Quantum Monte Carlo calculation of entanglement Rényi entropies for generic quantum systems. *Phys. Rev. B*, 86:235116, 2012. doi: 10.1103/PhysRevB.86.235116.
- [121] P. J. Green. Reversible jump Markov chain Monte Carlo computation and Bayesian model determination. *Biometrika*, 82(4):711–732, 1995. doi: 10.1093/biomet/82.4.711.
- [122] Green P. J.. *Trans-dimensional Markov chain Monte Carlo*, pages 179–198. Oxford Statistical Science Series. Oxford University Press, 2003. ISBN 9780198510550.
- [123] S. Richardson and P. J. Green. On Bayesian Analysis of Mixtures with an Unknown Number of Components (with discussion). *Journal of the Royal Statistical Society: Series B (Statistical Methodology)*, 59(4):731–792, 1997. ISSN 1467-9868. doi: 10.1111/1467-9868.00095.
- [124] M. Suzuki. Relationship between d-Dimensional Quantal Spin Systems and (d+1)-Dimensional Ising Systems: Equivalence, Critical Exponents and Systematic Approximants of the Partition Function and Spin Correlations. *Prog. Theor. Phys.*, 56(5):1454–1469, 1976. doi: 10.1143/PTP.56.1454.
- [125] J. A. Barker. A quantum-statistical Monte Carlo method; path integrals with boundary conditions. *J. Chem. Phys.*, 70(6):2914–2918, 1979. doi: 10.1063/1.437829.
- [126] S. Y. Larsen. Quantum-Mechanical Pair-Correlation Function of Hard Spheres. *J. Chem. Phys.*, 48(4):1701–1708, 1968. doi: 10.1063/1.1668897.
- [127] T. Morita. Solution of the Bloch Equation for Many-Particle Systems in Terms of the Path Integral. *J. Phys. Soc. Jpn.*, 35(4):980–984, 1973. doi: 10.1143/JPSJ.35.980.
- [128] M. F. Herman, E. J. Bruskin, and B. J. Berne. On path integral Monte Carlo simulations. *J. Chem. Phys.*, 76(10):5150–5155, 1982. doi: 10.1063/1.442815.
- [129] G. Jacucci and E. Omerti. Monte Carlo calculation of the radial distribution function of quantum hard spheres at finite temperatures using path integrals with boundary conditions. *J. Chem. Phys.*, 79(6):3051–3054, 1983. doi: 10.1063/1.446134.
- [130] E. L. Pollock and D. M. Ceperley. Simulation of quantum many-body systems by path-integral methods. *Phys. Rev. B*, 30:2555–2568, 1984. doi: 10.1103/PhysRevB.30.2555.

- [131] D. M. Ceperley and E. L. Pollock. Path-integral computation of the low-temperature properties of liquid ^4He . *Phys. Rev. Lett.*, 56:351–354, 1986. doi: 10.1103/PhysRevLett.56.351.
- [132] B. B. Beard and U.-J. Wiese. Simulations of Discrete Quantum Systems in Continuous Euclidean Time. *Phys. Rev. Lett.*, 77:5130–5133, 1996. doi: 10.1103/PhysRevLett.77.5130.
- [133] N. V. Prokof'ev, B. V. Svistunov, and I. S. Tupitsyn. Exact, complete, and universal continuous-time worldline Monte Carlo approach to the statistics of discrete quantum systems. *J. Exp. Theor. Phys.*, 87(2):310–321, 1998. doi: 10.1134/1.558661.
- [134] N. V. Prokof'ev, B. V. Svistunov, and I. S. Tupitsyn. “Worm” algorithm in quantum Monte Carlo simulations. *Phys. Lett. A*, 238(4-5):253–257, 1998. doi: 10.1016/s0375-9601(97)00957-2.
- [135] N. Prokof'ev, O. Ruebenacker, and B. Svistunov. Critical Point of a Weakly Interacting Two-Dimensional Bose Gas. *Phys. Rev. Lett.*, 87:270402, 2001. doi: 10.1103/PhysRevLett.87.270402.
- [136] M. Boninsegni, N. Prokof'ev, and B. Svistunov. Worm Algorithm for Continuous-Space Path Integral Monte Carlo Simulations. *Phys. Rev. Lett.*, 96:070601, 2006. doi: 10.1103/PhysRevLett.96.070601.
- [137] M. Boninsegni, N. V. Prokof'ev, and B. V. Svistunov. Worm algorithm and diagrammatic Monte Carlo: A new approach to continuous-space path integral Monte Carlo simulations. *Phys. Rev. E*, 74:036701, 2006. doi: 10.1103/PhysRevE.74.036701.
- [138] M. Holzmann and W. Krauth. Kosterlitz-Thouless Transition of the Quasi-Two-Dimensional Trapped Bose Gas. *Phys. Rev. Lett.*, 100:190402, 2008. doi: 10.1103/PhysRevLett.100.190402.
- [139] S. P. Rath, T. Yefsah, K. J. Günter, M. Cheneau, R. Desbuquois, M. Holzmann, W. Krauth, and J. Dalibard. Equilibrium state of a trapped two-dimensional Bose gas. *Phys. Rev. A*, 82:013609, 2010. doi: 10.1103/PhysRevA.82.013609.
- [140] C.-L. Hung, X. Zhang, N. Gemelke, and C. Chin. Observation of scale invariance and universality in two-dimensional Bose gases . *Nature*, 470:236–239, 2011. doi: 10.1038/nature09722.
- [141] R. P. Smith, N. Tammuz, R. L. D. Campbell, M. Holzmann, and Z. Hadzibabic. Condensed Fraction of an Atomic Bose Gas Induced by Critical Correlations. *Phys. Rev. Lett.*, 107:190403, 2011. doi: 10.1103/PhysRevLett.107.190403.

- [142] F. Gerbier, S. Trotzky, S. Fölling, U. Schnorrberger, J. D. Thompson, A. Widera, I. Bloch, L. Pollet, M. Troyer, B. Capogrosso-Sansone, N. V. Prokof'ev, and B. V. Svistunov. [Expansion of a Quantum Gas Released from an Optical Lattice](#). *Phys. Rev. Lett.*, 101:155303, 2008. doi: 10.1103/PhysRevLett.101.155303.
- [143] S. Trotzky, L. Pollet, F. Gerbier, U. Schnorrberger, I. Bloch, N. V. Prokof'ev, B. Svistunov, and M. Troyer. [Suppression of the critical temperature for superfluidity near the Mott transition](#). *Nat. Phys.*, 6(12):998–1004, 2010. doi: 10.1038/nphys1799.
- [144] P. Lévy. Sur certains processus stochastiques homogènes. *Compos. Math.*, 7:283–339, 1939. ISSN 0010-437X; 1570-5846/e.
- [145] D. Blume and K. M. Daily. Trapped two-component Fermi gases with up to six particles: Energetics, structural properties, and molecular condensate fraction. *C. R. Phys.*, 12(1):86 – 109, 2011. ISSN 1631-0705. doi: 10.1016/j.crhy.2010.11.010.
- [146] X. Y. Yin and D. Blume. [Trapped unitary two-component Fermi gases with up to ten particles](#). *Phys. Rev. A*, 92:013608, 2015. doi: 10.1103/PhysRevA.92.013608.
- [147] S. Baroni and S. Moroni. [Reptation Quantum Monte Carlo: A Method for Unbiased Ground-State Averages and Imaginary-Time Correlations](#). *Phys. Rev. Lett.*, 82:4745–4748, 1999. doi: 10.1103/PhysRevLett.82.4745.
- [148] C. Pierleoni and D. M. Ceperley. [Computational Methods in Coupled Electron–Ion Monte Carlo Simulations](#). *ChemPhysChem*, 6(9):1872–1878, 2005. ISSN 1439-7641. doi: 10.1002/cphc.200400587.
- [149] F. Chen, L. Lovász, and I. Pak. Lifting Markov chains to speed up mixing. In *Proceedings of the thirty-first annual ACM symposium on Theory of computing*, pages 275–281. ACM, 1999.
- [150] P. Diaconis, S. Holmes, and R. M. Neal. [Analysis of a nonreversible Markov chain sampler](#). *Ann. Appl. Probab.*, 10(3):726–752, 2000. doi: 10.1214/aoap/1019487508.
- [151] J.-P. Hansen and I. R. McDonald. *Theory of Simple Liquids, Fourth Edition: with Applications to Soft Matter*. Academic Press, 4th edition, 2013. ISBN 0123870321.
- [152] D. M. Ceperley and B. Bernu. [Ring Exchanges and the Supersolid Phase of \${}^4\text{He}\$](#) . *Phys. Rev. Lett.*, 93:155303, 2004. doi: 10.1103/PhysRevLett.93.155303.
- [153] D. M. Ceperley and E. L. Pollock. [The momentum distribution of normal and superfluid liquid \${}^4\text{He}\$](#) . *Can. J. Phys.*, 65(11):1416–1420, 1987. doi: 10.1139/p87-222.
- [154] S. Giorgini, L. P. Pitaevskii, and S. Stringari. [Anomalous Fluctuations of the Condensate in Interacting Bose Gases](#). *Phys. Rev. Lett.*, 80:5040–5043, 1998. doi: 10.1103/PhysRevLett.80.5040.

- [155] E. L. Pollock and K. J. Runge. Finite-size-scaling analysis of a simulation of the ^4He superfluid transition. *Phys. Rev. B*, 46:3535–3539, 1992. doi: 10.1103/PhysRevB.46.3535.
- [156] M. Campostrini, M. Hasenbusch, A. Pelissetto, and E. Vicari. Theoretical estimates of the critical exponents of the superfluid transition in ^4He by lattice methods. *Phys. Rev. B*, 74:144506, 2006. doi: 10.1103/PhysRevB.74.144506.
- [157] A. Singasaas and G. Ahlers. Universality of static properties near the superfluid transition in ^4He . *Phys. Rev. B*, 30:5103–5115, 1984. doi: 10.1103/PhysRevB.30.5103.
- [158] D. P. Landau. Finite-size behavior of the Ising square lattice. *Phys. Rev. B*, 13:2997–3011, 1976. doi: 10.1103/PhysRevB.13.2997.
- [159] K. Binder. Critical Properties from Monte Carlo Coarse Graining and Renormalization. *Phys. Rev. Lett.*, 47:693–696, 1981. doi: 10.1103/PhysRevLett.47.693.
- [160] M. P. A. Fisher, P. B. Weichman, G. Grinstein, and Daniel S. Fisher. Boson localization and the superfluid-insulator transition. *Phys. Rev. B*, 40:546–570, 1989. doi: 10.1103/PhysRevB.40.546.
- [161] S. Pilati, S. Giorgini, and N. Prokof'ev. Critical Temperature of Interacting Bose Gases in Two and Three Dimensions. *Phys. Rev. Lett.*, 100:140405, 2008. doi: 10.1103/PhysRevLett.100.140405.
- [162] T. T. Nguyen, A. J. Herrmann, M. Troyer, and S. Pilati. Critical Temperature of Interacting Bose Gases in Periodic Potentials. *Phys. Rev. Lett.*, 112:170402, 2014. doi: 10.1103/PhysRevLett.112.170402.
- [163] A. G. Sykes, J. P. Corson, J. P. D’Incao, A. P. Koller, C. H. Greene, A. M. Rey, K. R. A. Hazzard, and J. L. Bohn. Quenching to unitarity: Quantum dynamics in a three-dimensional Bose gas. *Phys. Rev. A*, 89:021601, 2014. doi: 10.1103/PhysRevA.89.021601.
- [164] J. M. Diederix, T. C. F. van Heijst, and H. T. C. Stoof. Ground state of a resonantly interacting Bose gas. *Phys. Rev. A*, 84:033618, 2011. doi: 10.1103/PhysRevA.84.033618.
- [165] M. Rossi, L. Salasnich, F. Ancilotto, and F. Toigo. Monte Carlo simulations of the unitary Bose gas. *Phys. Rev. A*, 89:041602, 2014. doi: 10.1103/PhysRevA.89.041602.
- [166] K. Huang. *Statistical mechanics*. John Wiley & Sons, 2nd edition, 1987. ISBN 0471815187.

- [167] R. Fantoni and S. Moroni. [Quantum Gibbs ensemble Monte Carlo](#). *J. Chem. Phys.*, 141(11):114110, 2014. doi: 10.1063/1.4895974.
- [168] E. Braaten, D. Kang, and L. Platter. [Universal Relations for Identical Bosons from Three-Body Physics](#). *Phys. Rev. Lett.*, 106:153005, 2011. doi: 10.1103/PhysRevLett.106.153005.
- [169] L. He, X.-J. Liu, X.-G. Huang, and H. Hu. [Stoner ferromagnetism of a strongly interacting Fermi gas in the quasirepulsive regime](#). *Phys. Rev. A*, 93:063629, 2016. doi: 10.1103/PhysRevA.93.063629.
- [170] B. J. Alder and T. E. Wainwright. [Phase Transition for a Hard Sphere System](#). *J. Chem. Phys.*, 27(5):1208–1209, 1957. doi: 10.1063/1.1743957.
- [171] B. J. Alder and T. E. Wainwright. [Phase Transition in Elastic Disks](#). *Phys. Rev.*, 127: 359–361, 1962. doi: 10.1103/PhysRev.127.359.
- [172] J. A. Barker and D. Henderson. [What is "liquid"? Understanding the states of matter](#). *Rev. Mod. Phys.*, 48:587–671, 1976. doi: 10.1103/RevModPhys.48.587.
- [173] K. J. Strandburg. [Two-dimensional melting](#). *Rev. Mod. Phys.*, 60:161–207, 1988. doi: 10.1103/RevModPhys.60.161.
- [174] J. H. Conway and N. J. A. Sloane. *Sphere Packings, Lattices and Groups*. Springer-Verlag, New York, 1999.
- [175] L. Filion, M. Marechal, B. van Oorschot, D. Pelt, F. Smallenburg, and M. Dijkstra. [Efficient Method for Predicting Crystal Structures at Finite Temperature: Variable Box Shape Simulations](#). *Phys. Rev. Lett.*, 103:188302, 2009. doi: 10.1103/PhysRevLett.103.188302.
- [176] J. de Graaf, R. van Roij, and M. Dijkstra. [Dense Regular Packings of Irregular Nonconvex Particles](#). *Phys. Rev. Lett.*, 107:155501, 2011. doi: 10.1103/PhysRevLett.107.155501.
- [177] H. L. Frisch, N. Rivier, and D. Wyler. [Classical Hard-Sphere Fluid in Infinitely Many Dimensions](#). *Phys. Rev. Lett.*, 54:2061–2063, 1985. doi: 10.1103/PhysRevLett.54.2061.
- [178] M. Luban and J. P. J. Michels. [Equation of state of hard \$D\$ -dimensional hyperspheres](#). *Phys. Rev. A*, 41:6796–6804, 1990. doi: 10.1103/PhysRevA.41.6796.
- [179] R. Finken, M. Schmidt, and H. Löwen. [Freezing transition of hard hyperspheres](#). *Phys. Rev. E*, 65:016108, 2001. doi: 10.1103/PhysRevE.65.016108.

- [180] A. Scardicchio, F. H. Stillinger, and S. Torquato. Estimates of the optimal density of sphere packings in high dimensions. *J. Math. Phys.*, 49(4):043301, 2008. doi: 10.1063/1.2897027.
- [181] G. Parisi. On the Most Compact Regular Lattices in Large Dimensions: A Statistical Mechanical Approach. *J. Stat. Phys.*, 132(2):207–234, 2008. ISSN 1572-9613. doi: 10.1007/s10955-008-9539-6.
- [182] J. Palacci, S. Sacanna, A. P. Steinberg, D. J. Pine, and . M. Chaikin. Living Crystals of Light-Activated Colloidal Surfers. *Science*, 339(6122):936–940, 2013. ISSN 0036-8075. doi: 10.1126/science.1230020.
- [183] L. Berthier. Nonequilibrium Glassy Dynamics of Self-Propelled Hard Disks. *Phys. Rev. Lett.*, 112:220602, 2014. doi: 10.1103/PhysRevLett.112.220602.
- [184] K.-D. N. T. Lam, M. Schindler, and O. Dauchot. Self-propelled hard disks: implicit alignment and transition to collective motion. *New J. Phys.*, 17(11):113056, 2015. doi: 10.1088/1367-2630/17/11/113056.
- [185] E. Epelbaum, H.-W. Hammer, and Ulf-G. Meißner. Modern theory of nuclear forces. *Rev. Mod. Phys.*, 81:1773–1825, 2009. doi: 10.1103/RevModPhys.81.1773.
- [186] D. J. Gross and M. Mezard. The simplest spin glass. *Nucl. Phys. B*, 240(4):431 – 452, 1984. doi: 10.1016/0550-3213(84)90237-2.
- [187] W. W. Wood. Monte Carlo Calculations for Hard Disks in the Isothermal-Isobaric Ensemble. *J. Chem. Phys.*, 48(1):415–434, 1968. doi: 10.1063/1.1667938.
- [188] J. de Graaf, L. Filion, M. Marechal, R. van Roij, and M. Dijkstra. Crystal-structure prediction via the Floppy-Box Monte Carlo algorithm: Method and application to hard (non)convex particles. *J. Chem. Phys.*, 137(21):214101, 2012. doi: 10.1063/1.4767529.
- [189] E. Bianchi, G. Doppelbauer, L. Filion, M. Dijkstra, and G. Kahl. Predicting patchy particle crystals: Variable box shape simulations and evolutionary algorithms. *J. Chem. Phys.*, 136(21):214102, 2012. doi: 10.1063/1.4722477.
- [190] W. C. Swope and H. C. Andersen. Thermodynamics, statistical thermodynamics, and computer simulation of crystals with vacancies and interstitials. *Phys. Rev. A*, 46:4539–4548, 1992. doi: 10.1103/PhysRevA.46.4539.
- [191] T. Aste and D. Weaire. *The pursuit of perfect packing*. Institute of Physics Publishing, Bristol, 2000.
- [192] T. C. Hales. A proof of the Kepler conjecture. *Annals of Mathematics*, 162(3):1065–1185, 2005. doi: 10.4007/annals.2005.162.1065.

- [193] T. Hales, M. Adams, G. Bauer, D. Tat Dang, J. Harrison, T. Le Hoang, C. Kaliszyk, V. Magron, S. McLaughlin, T. Tat Nguyen, T. Quang Nguyen, T. Nipkow, S. Obua, J. Pleso, J. Rute, A. Solovyev, A. Hoai Thi Ta, T. N. Tran, D. Thi Trieu, J. Urban, K. Khac Vu, and R. Zumkeller. [A formal proof of the Kepler conjecture](#). 2015. arXiv 1501.02155 [math.MG].
- [194] W. Barlow. [Probable nature of the internal symmetry of crystals](#). *Nature*, 29:186–188, 1883. doi: 10.1038/029186a0.
- [195] B. M. Mladek, D. Gottwald, G. Kahl, M. Neumann, and C. N. Likos. [Formation of Polymorphic Cluster Phases for a Class of Models of Purely Repulsive Soft Spheres](#). *Phys. Rev. Lett.*, 96:045701, 2006. doi: 10.1103/PhysRevLett.96.045701.
- [196] B. M. Mladek, Gerhard Kahl, and Christos N. Likos. [Computer Assembly of Cluster-Forming Amphiphilic Dendrimers](#). *Phys. Rev. Lett.*, 100:028301, 2008. doi: 10.1103/PhysRevLett.100.028301.
- [197] M. P. Vecchi S. Kirkpatrick, C. D. Gelatt. [Optimization by Simulated Annealing](#). *Science*, 220(4598):671–680, 1983.
- [198] V. Černý. [Thermodynamical approach to the traveling salesman problem: An efficient simulation algorithm](#). *Journal of Optimization Theory and Applications*, 45(1):41–51, 1985. ISSN 1573-2878. doi: 10.1007/BF00940812.
- [199] R. Chibante, editor. *Simulated Annealing, Theory with Applications*. Global Optimization. Sciendo, 2010. ISBN 978-953-307-134-3.
- [200] J. Pannetier, J. Bassas-Alsina, J. Rodriguez-Carvajal, and V. Caignaert. [Prediction of crystal structures from crystal chemistry rules by simulated annealing](#). *Nature*, 346:343–345, 1990. doi: 10.1038/346343a0.
- [201] S. M. Woodley and R. Catlow. [Crystal structure prediction from first principles](#). *Nat. Mat.*, 7(12):937–946, 2008. doi: 10.1038/nmat2321.
- [202] N. D. Mermin and H. Wagner. [Absence of Ferromagnetism or Antiferromagnetism in One- or Two-Dimensional Isotropic Heisenberg Models](#). *Phys. Rev. Lett.*, 17:1133–1136, 1966. doi: 10.1103/PhysRevLett.17.1133.
- [203] M. Engel, J. A. Anderson, S. C. Glotzer, M. Isobe, E. P. Bernard, and W. Krauth. [Hard-disk equation of state: First-order liquid-hexatic transition in two dimensions with three simulation methods](#). *Phys. Rev. E*, 87:042134, 2013. doi: 10.1103/PhysRevE.87.042134.
- [204] W. Mickel, S. C. Kapfer, G. E. Schröder-Turk, and K. Mecke. [Shortcomings of the bond orientational order parameters for the analysis of disordered particulate matter](#). *J. Chem. Phys.*, 138(4):044501, 2013. doi: 10.1063/1.4774084.

- [205] M. D. Rintoul and S. Torquato. Computer simulations of dense hard-sphere systems. *J. Chem. Phys.*, 105(20):9258–9265, 1996. doi: 10.1063/1.473004.
- [206] P. J. Steinhardt, D. R. Nelson, and M. Ronchetti. Bond-orientational order in liquids and glasses. *Phys. Rev. B*, 28:784–805, 1983. doi: 10.1103/PhysRevB.28.784.
- [207] W. Lechner and C. Dellago. Accurate determination of crystal structures based on averaged local bond order parameters. *J. Chem. Phys.*, 129(11):114707, 2008. doi: 10.1063/1.2977970.
- [208] S. C. Kapfer. sphmink. <https://github.com/skapfer/sphmink>, 2013.

Publications

Publication 1: Liquid-solid transitions in the three-body hard-core model

Tommaso Comparin, Sebastian C. Kapfer and Werner Krauth, *EPL (Europhysics Letters)*, **109**, 20003 (2015).

This article presents our study of the three-body hard-core model, in two and three dimensions. We address the packing problem through a set of variational ansätze, finding that the maximum density is reached for a triangular lattice of particle pairs (in $d = 2$) and for a simple-hexagonal lattice of single particles (in $d = 3$). The Monte Carlo method is used to identify the melting transition, taking place upon lowering the pressure.

Liquid-solid transitions in the three-body hard-core model

TOMMASO COMPARIN^(a), SEBASTIAN C. KAPFER^(b) and WERNER KRAUTH^(c)

*Laboratoire de Physique Statistique, École Normale Supérieure/PSL Research University, UPMC,
Université Paris Diderot, CNRS - 24 rue Lhomond, 75005 Paris, France*

received 9 October 2014; accepted in final form 12 January 2015
published online 2 February 2015

PACS 05.20.Jj – Statistical mechanics of classical fluids

PACS 64.70.dj – Melting of specific substances

Abstract – We determine the phase diagram for a generalisation of two- and three-dimensional hard spheres: a classical system with three-body interactions realised as a hard cut-off on the mean-square distance for each triplet of particles. Quantum versions of this model are important in the context of the unitary Bose gas, which is currently under close theoretical and experimental scrutiny. In two dimensions, the three-body hard-core model possesses a conventional atomic liquid phase and a peculiar solid phase formed by dimers. These dimers interact effectively as hard disks. In three dimensions, the solid phase consists of isolated atoms that arrange in a simple-hexagonal lattice.

Copyright © EPLA, 2015

Introduction. – In many fields of physics, interactions between particles are accurately described through pair potentials. These potentials can be long range or short range, and may combine attractive and repulsive components, as in the Lennard-Jones interaction. The minimal model for pairwise-interacting systems is the hard-sphere potential, which has played a central role in statistical mechanics and computational physics, and is also a prominent topic in mathematical research [1–3].

In a number of cases, two-body potentials are insufficient to describe complex physical behaviour. A notorious example are nuclear forces, where three-body interactions have long been discussed [4,5]. Explicit three-body terms appear also in spin glasses, as in the well-known p -spin model [6].

Recently, three-body potentials were studied in cold atomic quantum gases. One proposed route to enhance their effects consists in suppressing the pair interactions [7]. The unitary Bose gas at low temperature represents another situation in which three-body physics is relevant. For some bosonic atoms, the Feshbach-resonance technique allows to reach the *unitary* regime, where the two-particle scattering length diverges, and an additional length scale is provided by a three-body parameter. Experiments in this regime have lead to direct evidence of the Efimov effect [8–11], a spectacular manifestation of

three-body physics in the quantum realm. This has triggered a massive experimental and theoretical effort on the study of this strongly interacting system [12–18].

The above considerations motivate the study of a minimal model of three-body interactions. In the current work, we consider a classical system in which each triplet (i, j, k) of particles interacts through the potential

$$V_3(R_{ijk}) = \begin{cases} \infty, & \text{if } R_{ijk} < R_0, \\ 0, & \text{if } R_{ijk} > R_0, \end{cases} \quad (1)$$

where $R_{ijk}^2 = (r_{ij}^2 + r_{jk}^2 + r_{ki}^2)/3$. The interaction term of eq. (1) explicitly appears in recent theoretical models of the unitary Bose gas [15,17], where it prevents the collapse [19] of the quantum-mechanical wave function. In the corresponding experimental system, the three-body parameter R_0 is related to the length scale of the van der Waals interactions [20–22].

Among the many generalisations of the hard-sphere model (*e.g.* to aspherical and polydisperse objects, or to dimensions different from three), the three-body hard-core model has not —to our knowledge— been studied before.

As for the hard-sphere model, the phase diagram of the three-body hard-core model is independent of temperature, and transitions are driven purely by entropy. The crucial distinction of the three-body hard-core model is that two particles can exist at zero distance from each other, and can bind into dimers.

We consider the classical three-body hard-core model in two and three dimensions. To obtain the infinite-pressure

^(a)E-mail: tommaso.comparin@ens.fr

^(b)E-mail: sebastian.kapfer@fau.de

^(c)E-mail: werner.krauth@ens.fr

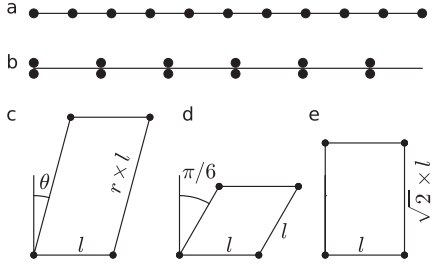


Fig. 1: Close-packed structures in 1D and 2D. (a) Linear array of isolated atoms and (b) of dimers with the smallest spacing allowed by the three-body cut-off. (c) General case of the 2D oblique lattice structure, (d) triangular lattice at $(r, \theta) = (1, \pi/6)$, (e) rectangular lattice with $(r, \theta) = (\sqrt{2}, 0)$.

limit, we first solve heuristically the three-body equivalent of the classic sphere-packing problem [3]: We maximise the packing fraction for several families of structures where the three-body constraint eq. (1) is tight. We support our result by simulated-annealing calculations which confirm our highest-density close-packed structures. In two dimensions, the densest structure is a triangular lattice of dimers, while in three dimensions it is a simple-hexagonal lattice of isolated atoms. Finally, we use Monte Carlo (MC) simulations in the NPT ensemble to determine the phase diagram at finite pressure. Both in 2D and 3D, we find no other stable thermodynamic phases besides the liquid and the high-density solid.

Close-packed structures. — We illustrate our procedure to compute densities of close-packed structures in the one-dimensional case. We consider evenly spaced lattice sites with lattice constant l . For a lattice with a single atom on every site —fig. 1(a)— the smallest triplet is composed by three subsequent sites and the hard-core condition in eq. (1) leads to the following bound on the lattice spacing:

$$R = \sqrt{\frac{l^2 + l^2 + (2l)^2}{3}} = l\sqrt{2} \geq R_0. \quad (2)$$

The corresponding upper bound on the density ρ reads $\rho \leq \rho_{\max} = \sqrt{2}/R_0$. On the other hand, for the lattice with every site occupied by a dimer of two atoms, the smallest triplet consists of a dimer and an additional atom on a neighbouring site; the root-mean-square distance is $R = l\sqrt{2}/3$ and the close-packed density is $\rho_{\max} = 2\sqrt{2}/3/R_0$. Thus, at high pressure, the dimer lattice is favoured (see table 1).

In two dimensions, we consider the family of oblique lattices —see fig. 1(c)— in which the unit cell is a parallelogram with edges l and $r \times l$, and where the smaller internal angle equals $\pi/2 - \theta$. Without loss of generality, we set $r \geq 1$ and $0 \leq \theta \leq \arcsin(1/(2r))$. This family includes the triangular and the rectangular lattices, as indicated in figs. 1(d) and (e). For isolated particles, close packing is obtained for a rectangular lattice with aspect ratio $\sqrt{2}$, while for dimers, the close-packed structure is

Table 1: Densities of D -dimensional close-packed structures. The structure may include free parameters (aspect ratio r or angle θ), and the optimal values are indicated. Labels a and d correspond to filling the lattice sites with atoms or dimers, respectively.

D	structure	param.	$\rho_{\max} R_0^D$	
1	regular spacing a	—	$\sqrt{2}$	1.41
	regular spacing d	—	$2\sqrt{2/3}$	1.63
2	oblique a	$r = \sqrt{2}$	$\sqrt{2}$	1.41
		$\theta = 0$		
	oblique d	$r = 1$	$(2/\sqrt{3})^3$	1.54
3	Barlow ABA a	$r = 1/2$	$\frac{13}{27}\sqrt{26/3}$	1.42
	Barlow ABA d	$r = \sqrt{2/3}$	$(2/\sqrt{3})^3$	1.54
	Barlow ABC a	$r = 1/\sqrt{6}$	$(2/\sqrt{3})^3$	1.54
	Barlow ABC d	$r = \sqrt{2/3}$	$(2/\sqrt{3})^3$	1.54
	tetragonal a	$r = 1$	$(2/\sqrt{3})^3$	1.54
	tetragonal d	$r = 1$	$\sqrt{32/27}$	1.09
	simple-hex. a	$r = 1/\sqrt{2}$	$2\sqrt{2/3}$	1.63
	simple-hex. d	$r = 1$	$8\sqrt{2}/9$	1.26

a triangular lattice. Again, high pressure favours the formation of dimers (see table 1).

In three dimensions, we consider three families of structures: Barlow, tetragonal, and simple-hexagonal. Barlow packings are the solutions of the conventional (two-body) sphere packing problem and include the fcc and hcp structures [3]. In our case, the lattice parameters are regulated by the three-body hard-core repulsion and not by the hard-sphere diameter. Within this class, we consider A-B-A and A-B-C stackings of triangular lattice planes, with a ratio r between the interplanar spacing and the in-plane lattice constant. For the tetragonal structures, we stretch the simple-cubic lattice along the z -direction by an aspect ratio r . Finally, we consider the simple-hexagonal structure, which is an A-A-A stacking of triangular lattice planes. As for the Barlow structures, the ratio r between the interplanar and in-plane spacings is a free parameter. Among the 3D structures considered, the highest density is achieved by single particles in a simple-hexagonal lattice with an aspect ratio $r = 1/\sqrt{2}$.

The formation of a structure with more than one particle per lattice site is a peculiarity of systems in which interparticle distances can vanish [23]. In the three-body hard-core model, close-packed systems with dimers are only favourable in low dimensions, as we now show by a heuristic argument: For lattices in which the three closest sites are all equidistant from each other (examples are the two-dimensional triangular lattice and the three-dimensional hcp or fcc lattices), we compute the scaling of the packing density with dimensionality D . We find $\rho_{\max}(\text{dimers})/\rho_{\max}(\text{atoms}) = 2(2/3)^{D/2}$. Thus, a lattice of dimers is favourable only for $D \leq 3$, while in higher

dimensions the density of the atomic lattice is larger. (This argument ignores next-nearest neighbours and non-uniform distances between lattice sites.) The same scaling argument can be generalised to a hard-core k -body model on a lattice in which the closest k sites are all at the same distance from each other. Up to $(k-1)$ particles can share a lattice site. As in the $k=3$ case, for large D the largest density is obtained for isolated atoms.

From the list of densities in table 1, we infer that the close-packed structures—in the classes considered here—of the three-body hard-core model are a regular lattice of dimers in $D=1$, a triangular lattice of dimers in $D=2$, and a simple-hexagonal lattice of single particles in $D=3$. Our approach is not exhaustive, and does not constitute a proof. In particular, mixtures of atoms and dimers remain to be explored. We support our results using a simulated-annealing procedure [24,25], in which we perform subsequent short MC simulations at slowly increasing pressure, starting from low-density disordered configurations. Simulated annealing runs for $N=100, 72, 64$ particles in $D=1, 2, 3$ dimensions, respectively, indeed yield the expected structures in the limit of infinite pressure.

Finite-pressure results.— We now consider the phase diagram of the three-body hard-core model at finite pressure. We use a Markov-chain MC scheme to simulate the system in the NPT ensemble (at fixed particle number N and pressure P). Our MC scheme involves two kinds of moves. The first is the standard local move, where a randomly chosen particle is displaced in its neighbourhood, and the move is accepted unless it violates any of the three-body constraints of eq. (1). The second move is a change of volume that also modifies the shape of the simulation box: For a D -dimensional box with edges L_1, \dots, L_D , the move modifies one of the L 's by adding or removing a random amount of void space (a rectangle aligned with the coordinate axes, constrained to touch a randomly chosen particle). This move does not alter the positions of the particles. As an example, if particle k and direction 1 are chosen, one move corresponds to removing the D -dimensional portion of space defined by $\{(x_1, \dots, x_D) \mid x_{k,1} < x_1 < x_{k,1} + \delta_1\}$, where δ_1 is chosen randomly in a fixed interval. This move, which changes L_1 into $L_1 - \delta_1$, is accepted only if it does not remove any particle and if the new configuration still satisfies the three-body constraint. The complementary move consists in extending L_1 to $L_1 + \delta_1$, by adding a portion of empty space with edges $\delta_1 \times L_2 \times \dots \times L_D$, starting from $x_{k,1}$. The acceptance probability for this insertion move is $p_{\text{acc}} = \exp(-\beta P \Delta V)$, where $\Delta V = \delta_1 \prod_{i=2}^D L_i$ is the change in volume; this differs from the conventional NPT move, which rescales the simulation box and the particle positions and requires an additional factor V^N in the statistical weight. In addition to the mentioned acceptance conditions, we reject moves that lead to very elongated box shapes, $\max_{i,j} (L_i/L_j) > 2$, as is common in MC methods

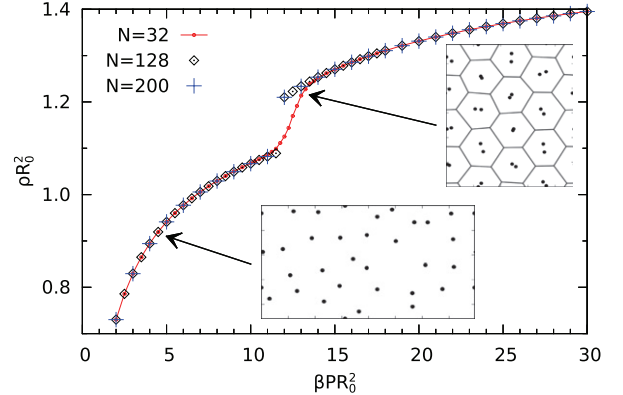


Fig. 2: (Colour on-line) Equation of state (density *vs.* pressure) for the 2D three-body hard-core system, with different system size N . The insets show snapshots of the $N=32$ system at pressures $\beta PR_0^2 = 4.5$ and $\beta PR_0^2 = 13$. Black lines in the inset indicate Voronoi cells of the dimer centres of mass.

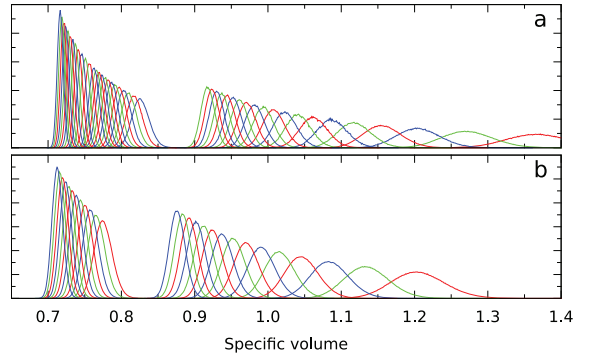


Fig. 3: (Colour on-line) Probability density function of the specific volume $V/(NR_0^D)$ at fixed pressure. (a) $N=128$ particles in $D=2$ dimensions, (b) $N=64$ particles in $D=3$ dimensions. Pressures are as in figs. 2 and 8, respectively.

based on variable box shape [26–28] to avoid strong finite-size effects.

Two-dimensional system.— For the $D=2$ system, we expect a disordered isotropic liquid phase at low pressure and a triangular solid phase of dimers at high pressure. We initialise the MC sampling with configurations in the solid phase, and observe melting for low values of P . Melting is indeed observed as a jump in the density, as shown in the equation of state (fig. 2). For small systems ($N=32$), there is an intermediate pressure regime where the system oscillates between the two phases. For larger systems, we only observe a single phase at each pressure, and the specific volume no longer has a bimodal distribution—see fig. 3(a). The density gap indicates a first-order phase transition, for the system sizes under study.

In the solid phase, defects are suppressed in our simulations due to the system sizes considered. The density in the equation of state, fig. 2, overestimates infinite-system value (with defects). In particular, vacancies are not observed on our simulation time scales, even though our

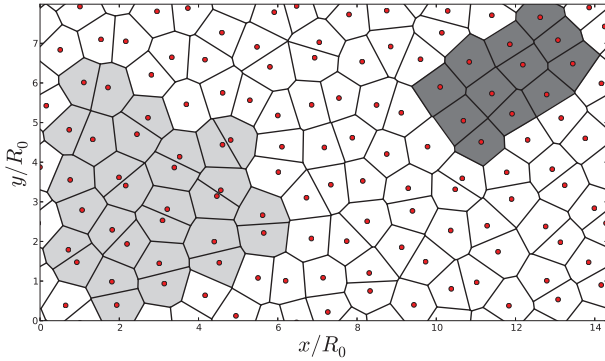


Fig. 4: (Colour on-line) Snapshot of $N = 128$ particles (red dots) at $\beta PR_0^2 = 14$, during the equilibration of a simulation started from a low-density disordered configuration. Black lines represent the particles' Voronoi cells. A patch with rectangular order is highlighted in dark gray, while a nucleating dimer solid is highlighted in light gray.

volume- and shape-changing move can in principle create the void space for a new lattice row to form (which has been advanced as a mechanism to change the number of lattice sites [29]).

Moreover, in two dimensions, the Mermin-Wagner theorem [30] precludes the existence of a crystal with truly long-ranged positional order, but allows for a solid phase with long-ranged orientational order and algebraically decaying positional order. 2D systems frequently exhibit an intermediate hexatic phase with short-ranged positional order, as has been recently shown for hard disks [31,32] and soft disks [33]. Since the dimers in our system effectively interact as hard disks (see below), an intermediate hexatic phase of dimers might also exist here, and could be observable in larger simulations.

From table 1 we identify a further candidate for an intermediate phase between the monomer liquid and the dimer solid: The rectangular close-packed structure of monomers attains a density only 10% below the close-packed triangular lattice of dimers. In our simulations, we observe transient patches with rectangular order: fig. 4 shows both the nucleating dimer solid and a rectangular patch. The aspect ratio of the rectangles is consistent with the close-packed structure, *i.e.*, $r = \sqrt{2}$. However, we find no pressure at which the rectangular structure is the equilibrium phase. Instead, the rectangular patches seem to decay by coalescence of two neighbouring lattice rows into a line of dimers, eventually forming a triangular dimer patch. Conversely, a dimer liquid was found to be unstable and to decompose.

Quantitatively, we define the term *dimer* to describe two particles that are each other's closest neighbour. This definition applies also to the disordered phase, where not all particles participate in tightly bound pairs. We measure the dimer fraction $2N_d/N$ according to this definition (where N_d is the number of dimers), and we show in fig. 5(a) that in the liquid, this quantity strongly deviates

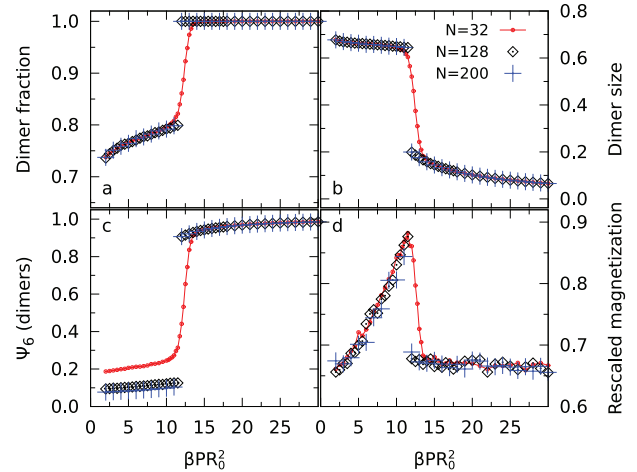


Fig. 5: (Colour on-line) Symbols and colours as in fig. 2. (a) Fraction $2N_d/N$ of dimers in the system. (b) Average dimer size, in units of R_0 . (c) Ψ_6 order parameter of dimers. (d) Dimer magnetisation m , multiplied by $\sqrt{N_d}$ (statistical uncertainties are comparable to symbol sizes).

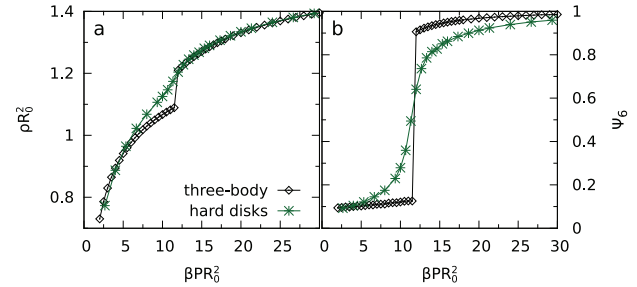


Fig. 6: (Colour on-line) The three-body hard-core solid compared to hard disks: (a) equation of state and (b) global orientational order parameter Ψ_6 for $N = 128$ three-body-interacting particles (black diamonds) and $N_{\text{disks}} = 64$ hard-disks (green stars). The conversion from hard-disk to three-body units follows from $\sigma = R_0 \sqrt{3}/8$; the density and packing fraction of the effective model read $\rho_{\text{disks}} = \rho/2$ and $\eta_{\text{disks}} = \rho_{\text{disks}} \pi \sigma^2 = \rho R_0^2 3\pi/16$, while the pressure is $P_{\text{disks}} \sigma^2 = 2(8/3)P R_0^2$. Data for the three-body model (ρ and Ψ_6) are the same as in figs. 2 and 5(c).

from its ideal-solid value of 1. Melting of the solid phase and decomposition of the dimers thus occurs in a single step.

The three-body model with all particles paired up into small dimers can be mapped to a conventional two-body hard-core system, containing composite particles (the dimers). In the infinite-pressure limit, dimers have zero extent and the dimer-dimer interaction makes them equivalent to hard disks with an effective radius $\sigma = R_0 \sqrt{3}/8$. At finite pressure, this mapping is approximate. In fig. 6(a), we compare the equation of state for 128 three-body-interacting particles and 64 hard disks. After rescaling the pressure by a factor of two stemming from the $2N$ -dimensional configuration space of the three-body particles *vs.* the $2N_{\text{disks}} = N$ dimensions for the hard disks, the equations of state agree fairly well in the solid

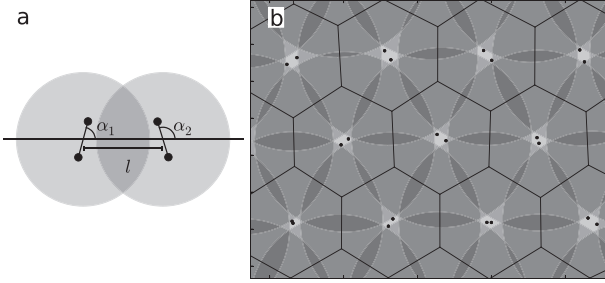


Fig. 7: (a) Representation of the configuration of four particles (dots) paired up in two dimers. Each shaded circle represents the excluded region generated by the two particles in a dimer. (b) Partial snapshot of the simulation of $N = 128$ particles at $\beta PR_0^2 = 20$. For each dimer, the excluded region is shaded. Black lines indicate Voronoi cells of the dimer centres of mass.

phase. The density of hard disks is systematically larger, as due to the non-zero extent of the dimers at finite pressure. This deviation decreases for increasing pressure.

In analogy with the hard-disk model, we define the orientational order parameter of the liquid-solid transition. We identify the N_j neighbours of the j -th dimer (where $N_j = 6$ in the ideal crystal) through a Voronoi tessellation. The *local* orientational order parameter is then [34]

$$\psi_{6,j} = \frac{\sum_{k=1}^{N_j} W_{jk} \exp(6i\theta_{jk})}{\sum_{k=1}^{N_j} W_{jk}}, \quad (3)$$

where θ_{jk} is the angle of the vector $\mathbf{r}_j - \mathbf{r}_k$ with respect to a reference axis and W_{jk} is the length of the Voronoi boundary between dimers j and k . The *global* orientational order parameter is $\Psi_6 = |\sum_{j=1}^{N_d} \psi_{6,j}|/N_d$. In the solid phase this quantity remains finite for increasing system sizes —fig. 5(c)— while in the fluid phase it decays as $1/\sqrt{N_d}$ and hexagonal order for the residual dimers is lost. In fig. 6(b), we show the global orientational order parameter Ψ_6 for the three-body hard-core system and its hard-disk analogue. Within our accuracy, the decomposition of dimers and the melting of the hard disks take place at the same pressure.

At finite pressure, the size of the dimers remains finite. It is thus interesting to study dimer orientation as an effective spin model. Dimers can rotate in 2D and have twofold rotational symmetry. We define the dimer magnetisation m as

$$m = \frac{1}{N_d} \left| \sum_{j=1}^{N_d} \exp(2i\alpha_j) \right|, \quad (4)$$

where α_j is the angle that the dimer forms with a reference axis.

We first consider four particles paired up into two dimers of fixed size, and free to rotate about their centres of mass, as shown in fig. 7(a). Each dimer generates a circular region around its centre of mass into which none of the two particles of the other dimer can penetrate. The radius of the excluded region depends on the dimer's

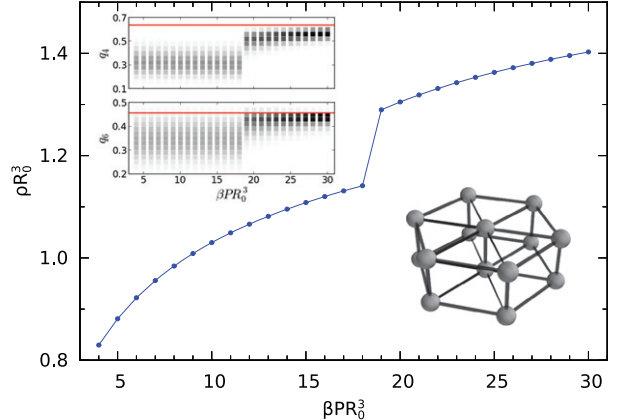


Fig. 8: (Colour on-line) Main panel: equation of state (density *vs.* pressure) for the 3D three-body hard-core model of $N = 64$ particles. Left inset: q_4 and q_6 histograms, for each pressure value (darker bins correspond to higher probability), and perfect-lattice limit (red line). Right inset: representation of the simple-hexagonal lattice (realised at high pressure).

size. When approaching each other, the dimers can no longer rotate freely and have to progressively align with each other, standing perpendicular to the dimer-dimer axis ($\alpha_1, \alpha_2 = \pi/2$). In the triangular lattice, this interaction is frustrated, since not all pairs of dimers in a triangle can align. The dimers then have to shrink to satisfy the three-body constraint (see fig. 7(b)). Effectively, the dimer spins are non-interacting, and their magnetisation vanishes as $1/\sqrt{N_d}$ as the system size increases. This is confirmed by the collapse of the $m\sqrt{N_d}$ curves —see fig. 5(d). In the thermodynamic limit, no magnetic order remains. In fig. 5(b) we show that the average size of dimers in the solid phase keeps decreasing, as required.

Three-dimensional system. Our simulations in three dimensions are analogous to the $D = 2$ simulations described above. Starting from the ideal simple-hexagonal solid, at low pressure the system melts into a disordered liquid phase; the equation of state is shown in fig. 8. As in the two-dimensional case, the gap in the specific-volume probability distribution shows that for this system size, the transition is discontinuous —see fig. 3(b).

We quantify local structure using bond order parameters [35], again following the construction of ref. [34] (*i.e.*, we weight the contribution of each bond between neighbours with the area of the shared Voronoi facet). In the solid phase, the distributions of q_4 and q_6 (see inset of fig. 8) are peaked, and their averages approach the perfect-lattice limit at high pressure. In the liquid phase, these distributions are broader, and give no indication for preferred local configurations. Except at the melting pressure, the distributions evolve smoothly with P , and there is no sign of further structural transformations.

Conclusions. — In this paper, we have studied the classical three-body hard-core model in two and three dimensions, and identified a unique solid phase in both cases.

In two dimensions, the transition involves simultaneous appearance of two types of order: particles form dimers, and the dimers order in a triangular solid that we expect to have quasi-long-range positional order.

The solid phase can be mapped to an effective hard-disk model, which reproduces the equation of state for large enough pressure. Dimers break up right at the melting transition of the effective hard-disks. The small system sizes considered here do not allow us to comment on the existence of an intermediate hexatic phase of dimers. Moreover, we note that the dimer solid phase does not show (magnetic) order of dimer orientations. We explain this feature through the frustration of the effective spin-spin interaction that results from the three-body cut-off.

In three dimensions, the close-packed structure is formed by isolated particles—rather than tightly bound dimers—placed on a simple-hexagonal lattice. This has an interest in connection with the model for the unitary Bose gas, since pairs of particles at very small distances would be pathological in the original quantum model [17]. Our equation of state enriches the phase diagram in ref. [17] at high temperature and pressure, and one might be able to link these two different regimes for the model.

More generally, the nature of the highest-density structure in the three-body hard-core model might represent a mathematically non-trivial generalisation of the classic Kepler problem [3], both in two and in three dimensions.

We thank RICCARDO ROSSI for helpful discussions.

REFERENCES

- [1] SzÁSZ D. (Editor), *Hard Ball Systems and the Lorentz Gas* (Springer-Verlag, Berlin, Heidelberg) 2000.
- [2] CONWAY J. H. and SLOANE N. J. A., *Sphere Packings, Lattices and Groups* (Springer-Verlag, New York) 1999.
- [3] ASTE T. and WEAIRE D., *The Pursuit of Perfect Packing* (Institute of Physics Publishing, Bristol) 2000.
- [4] GLÖCKLE W., WITALA H., HÜBER D., KAMADA H. and GOLAK J., *Phys. Rep.*, **274** (1996) 107.
- [5] EPELBAUM E., HAMMER H.-W. and MEISSNER ULF-G., *Rev. Mod. Phys.*, **81** (2009) 1773.
- [6] GROSS D. J. and MEZARD M., *Nucl. Phys. B*, **240** (1984) 431.
- [7] PETROV D. S., *Phys. Rev. Lett.*, **112** (2014) 103201.
- [8] EFIMOV V., *Phys. Lett. B*, **33** (1970) 563.
- [9] KRAEMER T., MARK M., WALDBURGER P., DANZL J. G., CHIN C., ENGESER B., LANGE A. D., PILCH K., JAAKKOLA A., NÄGERL H.-C. and GRIMM R., *Nature*, **440** (2006) 315.
- [10] ZACCANTI M., DEISSLER B., D'ERRICO C., FATTORI M., JONA-LASINIO M., MÜLLER S., ROATI G., INGUSCIO M. and MODUGNO G., *Nat. Phys.*, **5** (2009) 586.
- [11] POLLACK S. E., DRIES D. and HULET R. G., *Science*, **326** (2009) 1683.
- [12] REM B. S., GRIER A. T., FERRIER-BARBUT I., EISMANN U., LANGEN T., NAVON N., KHAYKOVICH L., WERNER F., PETROV D. S., CHEVY F. and SALOMON C., *Phys. Rev. Lett.*, **110** (2013) 163202.
- [13] FLETCHER R. J., GAUNT A. L., NAVON N., SMITH R. P. and HADZIBABIC Z., *Phys. Rev. Lett.*, **111** (2013) 125303.
- [14] MAKOTYN P., KLAUSS C. E., GOLDBERGER D. L., CORNELL E. A. and JIN D. S., *Nat. Phys.*, **10** (2014) 116.
- [15] VON STECHER J., *J. Phys. B: At. Mol. Opt. Phys.*, **43** (2010) 101002.
- [16] YAN Y. and BLUME D., *Phys. Rev. A*, **90** (2014) 013620.
- [17] PIATECKI S. and KRAUTH W., *Nat. Commun.*, **5** (2014) 3503.
- [18] ROSSI M., SALASNICH L., ANCILOTTO F. and TOIGO F., *Phys. Rev. A*, **89** (2014) 041602(R).
- [19] THOMAS L. H., *Phys. Rev.*, **47** (1935) 903.
- [20] BERNINGER M., ZENESINI A., HUANG B., HARM W., NÄGERL H. C., FERLAINO F., GRIMM R., JULIENNE P. S. and HUTSON J. M., *Phys. Rev. Lett.*, **107** (2011) 120401.
- [21] WILD R. J., MAKOTYN P., PINO J. M., CORNELL E. A. and JIN D. S., *Phys. Rev. Lett.*, **108** (2012) 145305.
- [22] WANG J., D'INCAO J. P., ESRY B. D. and GREENE C. H., *Phys. Rev. Lett.*, **108** (2012) 263001.
- [23] MLADEK B. M., GOTTLWALD D., KAHL G., NEUMANN M. and LIKOS C. N., *Phys. Rev. Lett.*, **96** (2006) 045701.
- [24] KIRKPATRICK S., GELATT C. D. jr. and VECCHI M. P., *Science*, **220** (1983) 671.
- [25] ČERNÝ V., *J. Optim. Theory Appl.*, **45** (1985) 41.
- [26] FILION L., MARECHAL M., VAN OORSCHOT B., PELET D., SMALLenburg F. and DIJKSTRA M., *Phys. Rev. Lett.*, **103** (2009) 188302.
- [27] DE GRAAF J., FILION L., MARECHAL M., VAN ROIJ R. and DIJKSTRA M., *J. Chem. Phys.*, **137** (2012) 214101.
- [28] BIANCHI E., DOPPELBAUER G., FILION L., DIJKSTRA M. and KAHL G., *J. Chem. Phys.*, **136** (2012) 214102.
- [29] SWOPE W. C. and ANDERSEN H. C., *Phys. Rev. A*, **46** (1992) 4539.
- [30] MERMIN N. D. and WAGNER H., *Phys. Rev. Lett.*, **17** (1966) 1307.
- [31] BERNARD E. P. and KRAUTH W., *Phys. Rev. Lett.*, **107** (2011) 155704.
- [32] ENGEL M., ANDERSON J. A., GLOTZER S. C., ISOBE M., BERNARD E. P. and KRAUTH W., *Phys. Rev. E*, **87** (2013) 042134.
- [33] KAPFER S. C. and KRAUTH W., *Phys. Rev. Lett.*, **114** (2015) 035702.
- [34] MICKE W., KAPFER S. C., SCHRÖDER-TURK G. E. and MECKE K., *J. Chem. Phys.*, **138** (2013) 044501.
- [35] STEINHARDT P., NELSON D. R. and RONCHETTI M., *Phys. Rev. B*, **28** (1983) 784.

Publication 2: Momentum Distribution in the Unitary Bose Gas from First Principles

Tommaso Comparin and Werner Krauth, *Physical Review Letters*, **117**, 225301 (2016).

This article presents our study of a finite-temperature, homogeneous system of unitary bosons, through a dedicated quantum Monte Carlo algorithm. Starting from the normal-gas, we identify the two distinct transitions that take place upon lowering the temperature. For small R_0 , we directly observe the formation of Efimov-liquid droplets. For large R_0 , we determine the critical temperature for the BEC transition through the finite-size-scaling analysis of QMC results. We also compute the momentum distribution, and map its large- k behavior in the homogeneous regions of the phase diagram.

Momentum Distribution in the Unitary Bose Gas from First Principles

Tommaso Comparin^{*} and Werner Krauth[†]

*Laboratoire de Physique Statistique, École Normale Supérieure/PSL Research University, UPMC,
Université Paris Diderot, CNRS, 24 rue Lhomond, 75005 Paris, France*

(Received 24 May 2016; published 22 November 2016)

We consider a realistic bosonic N -particle model with unitary interactions relevant for Efimov physics. Using quantum Monte Carlo methods, we find that the critical temperature for Bose-Einstein condensation is decreased with respect to the ideal Bose gas. We also determine the full momentum distribution of the gas, including its universal asymptotic behavior, and compare this crucial observable to recent experimental data. Similar to the experiments with different atomic species, differentiated solely by a three-body length scale, our model only depends on a single parameter. We establish a weak influence of this parameter on physical observables. In current experiments, the thermodynamic instability of our model from the atomic gas towards an Efimov liquid could be masked by the dynamical instability due to three-body losses.

DOI: [10.1103/PhysRevLett.117.225301](https://doi.org/10.1103/PhysRevLett.117.225301)

First predicted in 1970 [1], the Efimov effect describes the behavior of three strongly interacting bosons when any two of them cannot bind. At unitarity, when the scattering length diverges, the three-body bound states are scale invariant and they form a sequence up to vanishing binding energy and infinite spatial extension. Efimov trimers had been intensely discussed in nuclear physics, but it was in an ultracold gas of caesium atoms that they were finally discovered [2]. To observe Efimov trimers, experiments in atomic physics rely on Feshbach resonances [3], which allow one to instantly switch a gas between weak interactions and the unitary limit. Such a control of interactions is lacking in nuclear physics or condensed matter experiments, and singular interactions can be probed there only in the presence of accidental fine tuning [4]. Beyond the original system [2], Efimov trimers have now been observed for several multicomponent systems, including bosonic, fermionic, and Bose-Fermi mixtures [5–7]. These experimental findings are interpreted in terms of the theory of few-body strongly interacting quantum systems. For three identical bosons in three dimensions, a complete universal theory is available, on and off unitarity [4]. Further theoretical work is aimed at understanding bound states for more than three bosons, mixtures, and the effects of dimensionality.

Near-unitary interparticle interactions also impact the thermodynamics of the atomic gas, the description of which presents a challenge beyond the traditional theory of the Efimov effect. In addition, mean-field theory does not apply to infinite interactions [8], and the virial expansion [9] fails to describe the low-temperature state. Moreover, in atomic-physics experiments, strong interactions enhance the three-body loss rate, making the gas of bosons unstable. A characterization of the universal dynamics of these losses has been recently achieved [10–12]. On the other hand, a single breakthrough experiment [13] has addressed the

low-temperature thermodynamics for a unitary bosonic gas, coming to the conclusion that equilibrium was approached faster than the system lifetime. The importance of this system stems from its universal character: All differences between atomic species may be encoded in a single three-body parameter, related to the van der Waals length [14]. However, this prominent experiment could not be interpreted univocally, as first-principles theoretical predictions were lacking. In the present work, we obtain these predictions for a model which shares the experimental system's universality. We develop a novel quantum Monte Carlo algorithm [15] that overcomes the peculiar challenges posed by the infinite interactions. This allows us to compute the critical temperature for Bose-Einstein condensation, and the full momentum distribution $n(\mathbf{k})$ throughout the entire phase diagram, including its universal asymptotic behavior.

In the unitary limit, the scattering length diverges, and atomic pair interactions are powerful yet very short-ranged. The bosonic pair correlation function $g^{(2)}(\mathbf{r})$ diverges as $1/r^2$ at short distances $r = |\mathbf{r}|$, yet two isolated unitary bosons barely hold together: They form a molecule of infinite radius and vanishing binding energy. In thermodynamic equilibrium, three or more such bosons, with zero-range interactions, collapse into a single point, unless the unitary pair interactions are counterbalanced by a three-body repulsion. In experimental systems the latter is effectively realized by the van der Waals potential [14], so that the unitary Bose gas is stabilized against collapse. The divergence of $g^{(2)}(\mathbf{r})$ persists in the gas, with a finite contact density $c_2 = \lim_{r \rightarrow 0} (4\pi r)^2 g^{(2)}(\mathbf{r})$. The large- k asymptotics of the momentum distribution [16,17] is governed by Tan's contact parameter $C_2 = c_2 V$ (where V is the system volume), and it decays as $n(\mathbf{k}) \simeq C_2/k^4$ for $k \rightarrow \infty$.

We consider N bosons at temperature T in a periodic cubic box (thermodynamic NVT ensemble). Pair interactions are

of zero range and infinite depth, and the resonant two-body bound state realizes an infinite scattering length. In addition, any three particles a, b, c are subject to a hard cutoff $R > R_0$ on their hyperradius R , defined as the mean of their squared pair distances: $R^2 \equiv (r_{ab}^2 + r_{bc}^2 + r_{ac}^2)/3$. This realistic model describes ultracold atomic ensembles with an interaction range much smaller than the scattering length, the interparticle distance, and the thermal de Broglie wavelength. The two-body interactions, with their infinite scattering length, provide no scale. The model's phase diagram thus depends on two dimensionless numbers, namely, the thermal de Broglie wavelength $\lambda_{\text{th}}\rho^{1/3}$, and the three-body cutoff $R_0\rho^{1/3}$, both in units of the typical interparticle distance $\rho^{-1/3}$ [where $\lambda_{\text{th}} = \sqrt{2\pi\hbar^2\beta/m}$, $\beta = 1/(k_B T)$, and $\rho = N/V$]. At high temperature, three-particle effects are suppressed, and the model depends only on $\lambda_{\text{th}}\rho^{1/3}$. In experiments at low temperature, three-body correlations lead to strong recombination losses, with a loss rate scaling as $\sim T^{-2}$ [10–12], the predominant source of instability of the system. In contrast, our model conserves particle number.

Path-integral quantum Monte Carlo techniques allow us to solve this model from first principles, that is, without systematic errors. Computational challenges are posed by the divergence of $g^{(2)}(\mathbf{r})$ at contact [see Fig. 1(b)] and by the need to determine $n(\mathbf{k})$ for large momenta k [see Fig. 1(d)]. This corresponds to computing the single-particle correlation function $g^{(1)}(\mathbf{r})$ —the inverse Fourier transform of $n(\mathbf{k})$ —at small r , close to its cusp singularity at $r \rightarrow 0$ [see Fig. 1(c)]. Our path-integral quantum Monte Carlo algorithm [15,18–20] samples both closed and open path-integral configurations [cf. Fig. 1(a)]. The former give access to the superfluid fraction ρ_s/ρ (via the winding-number estimator [21]) and to the pair-correlation function $g^{(2)}(\mathbf{r})$ (from which we extract the contact density c_2). Open configurations, in contrast, sample the single-particle correlation function $g^{(1)}(\mathbf{r})$, and give access to the normalized momentum distribution [satisfying $\int d\mathbf{k}n(\mathbf{k})/(2\pi)^3 = N$ in the normal gas]. A dedicated estimator allows us to sample $n(\mathbf{k})$ for arbitrarily large momenta k [cf. Supplemental Material (i) [22]].

We include zero-range unitary interactions between two bosons through the exact two-body propagator [23,24], and treat them with a highly efficient direct-sampling approach [15]. The many-body density matrix is then built via the pair-product approximation. The hyperradial cutoff is included via the Trotter breakup [18], and an effective value of R_0 is obtained—for a finite imaginary-time discretization—through the comparison with the expression for the hyperradial wave function of a single universal trimer [15,23]. For three unitary bosons, the length scale R_0 sets a lower bound on the Efimov energy spectrum, and specifies a three-body ground state. At low temperature, our Monte Carlo simulations for $N = 3$ allow us to obtain excellent agreement of the hyperradial probability

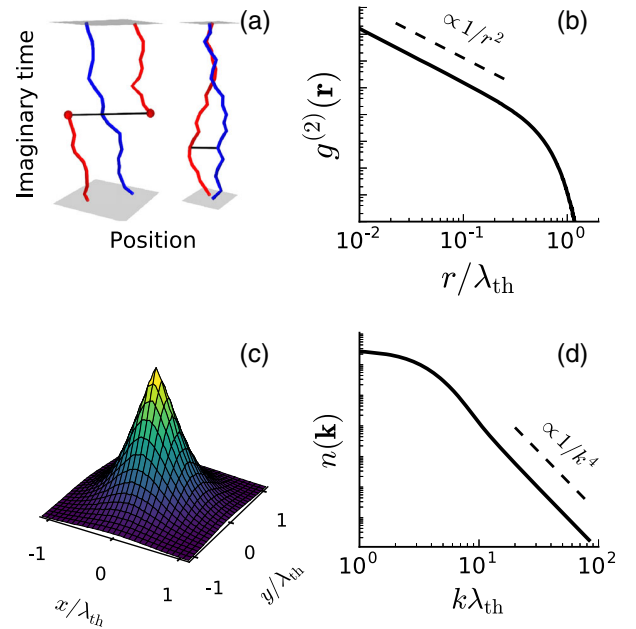


FIG. 1. Correlation functions for two unitary bosons. (a) Open (left) and closed (right) co-cyclic configurations in the path-integral representation. Closed configurations yield $g^{(2)}(\mathbf{r})$. Open configurations yield $n(\mathbf{k})$ and its inverse Fourier transform $g^{(1)}(\mathbf{r})$. (b) Pair-correlation function $g^{(2)}(\mathbf{r})$ (distance distribution in closed configurations), featuring a r^{-2} divergence at small r . (c) Cut of $g^{(1)}(\mathbf{r})$ (distribution of the distance between open ends), for $\mathbf{r} = (x, y, 0)$, illustrating the cusp at $\mathbf{r} = 0$. (d) Momentum distribution $n(\mathbf{k})$ with asymptotic decay, $\propto 1/k^4$, at large \mathbf{k} .

distribution and the momentum distribution for our model with the corresponding quantities for the universal Efimov trimer [4,25] [see Fig. 2(a) and Fig. 2(b)], providing also a parameter-free check of our computer program.

In the thermodynamic *NVT* ensemble, unitary bosons phase separate below a given temperature into a normal or Bose-Einstein-condensed gas dominated by entropy and a high-density Efimov liquid of low potential energy

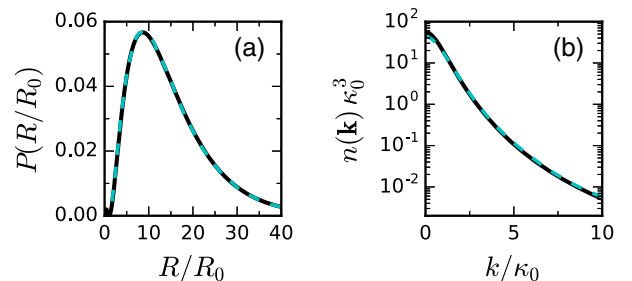


FIG. 2. Correlation functions for three unitary bosons. (a) Hyperradial probability distribution for three co-cyclical bosons with hyperradial cutoff at low temperature (cyan dashed line) and for the universal Efimov trimer (black solid line, from Ref. [4]). (b) Momentum distribution for three co-cyclical bosons (cyan dashed line), and for the universal trimer (black solid line, from Ref. [25]), in units of the trimer binding momentum κ_0 .

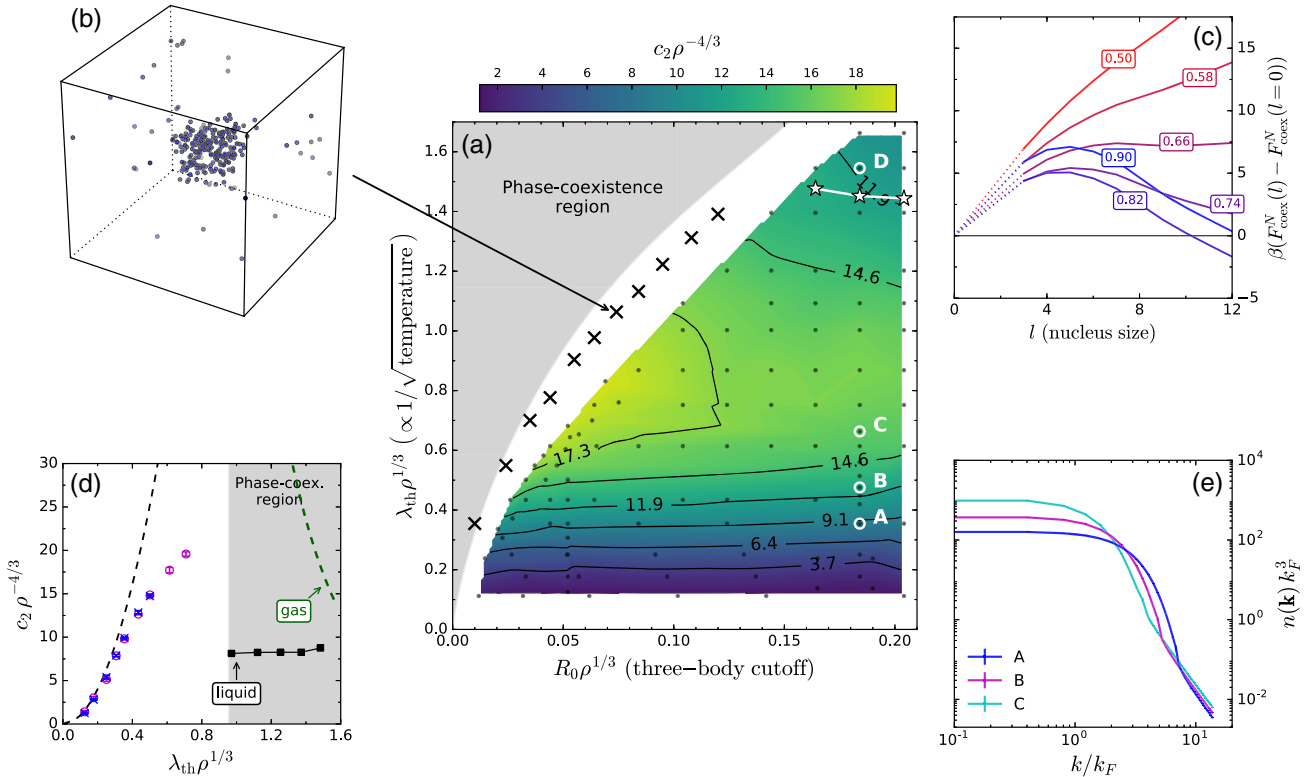


FIG. 3. Equilibrium phase diagram of unitary bosons. (a) Contact density $c_2 \rho^{-4/3}$, as a linear interpolation of numerical results [extracted from $g^{(2)}(\mathbf{r})$, for $N = 64$]. White stars: transition between normal gas and superfluid (Bose-Einstein condensed) phase. Black crosses: Phase-separated points. Gray area: Phase-coexistence region [23]. (b) Stable Efimov-liquid droplet coexisting with a normal gas ($N = 256$). (c) Excitation free energy for the Efimov-liquid nucleation, vs nucleus size l . $\lambda_{\text{th}} \rho^{1/3}$ varies between lines (see labels), between 0.5 (monotonically increasing, red line) and 0.9 (barrier, blue line). The hyperradial cutoff is fixed ($R_0 \rho^{1/3} = 0.03$), and the phase-separation region sets in at $\lambda_{\text{th}} \rho^{1/3} \approx 0.66$. (d) Contact density $c_2 \rho^{-4/3}$ vs $\lambda_{\text{th}} \rho^{1/3}$, for $R_0 \rho^{1/3} = 0.052$: Virial expansion (black dashed line) and numerical results, via the $n(\mathbf{k})$ and $g^{(2)}(\mathbf{r})$ estimators (crosses, circles). In the phase-coexistence region, the liquid and gas phases have different contact densities (for the gas, the virial expansion is used). (e) Momentum distribution [in units of the Fermi momentum $k_F = (6\pi^2 \rho)^{1/3}$] for parameters corresponding to points A, B, and C, in panel (a).

(see Fig. 3(a) and Ref. [23]). An equilibrium liquid bubble forms inside the gas [Fig. 3(b)], and the nucleation process is reversible across the coexistence line. For $R_0 \rightarrow 0$, the gas-to-liquid condensation energy $\propto 1/R_0^2$ overcomes the gas entropy loss at arbitrarily high temperatures, so that the coexistence line starts at $\lambda_{\text{th}} \rho^{1/3} = R_0 \rho^{1/3} = 0$. In the phase-coexistence region, the free energy $F_{\text{coex}}^N(l)$ is composed of two terms, corresponding to the Efimov-liquid nucleus of l particles and to the gas of the remaining $N - l$ particles. An analytical model, based on the virial expansion of the gas [9] and the known ground-state energies for small Efimov-liquid nuclei [26] (supposed incompressible), allows us to model the excitation free energy [see Supplemental Material (v) [22]]. In the homogeneous gas phase, $F_{\text{coex}}^N(l)$ monotonically increases with l [Fig. 3(c)]. At lower temperatures, the gas becomes metastable, with a free-energy barrier at a critical cluster size l^* . The nucleation rate per volume is proportional to $\exp(-\beta \Delta F)$, where $\Delta F = F_{\text{coex}}^N(l^*) - F_{\text{coex}}^N(0)$ is the free-energy barrier to overcome

the critical cluster size l^* . At low temperature, $\beta \Delta F$ and, therefore, the characteristic nucleation time for the Efimov liquid remain finite [see Fig. 3(c)]. The observed long experimental lifetime [13] is consistent with the idea that the phase-separation instability does not take place, in current experiments, as three-body losses effectively destabilize liquid droplets before the critical nucleus size $l^* \approx 5$ is reached. A study of the many-body quantum dynamics will be needed to confirm this hypothesis.

In the stable region of the phase diagram, the momentum distribution $n(\mathbf{k})$ is, in principle, obtained as the Fourier transform of $g^{(1)}(\mathbf{r})$, the distribution for distance vectors of open configurations [cf. Fig. 1(a)]. This estimator, however, poorly samples the short-distance cusp in $g^{(1)}(\mathbf{r})$ [equivalently, the large- k behavior of $n(\mathbf{k})$]. Our approach is rather based on an average of the analytical two-body expression, to determine $n(\mathbf{k})$ at arbitrarily large k [see Supplemental Material (i) [22]]. The asymptotic behavior of $n(\mathbf{k}) = C_2/k^4$ for $k \rightarrow \infty$ is also contained

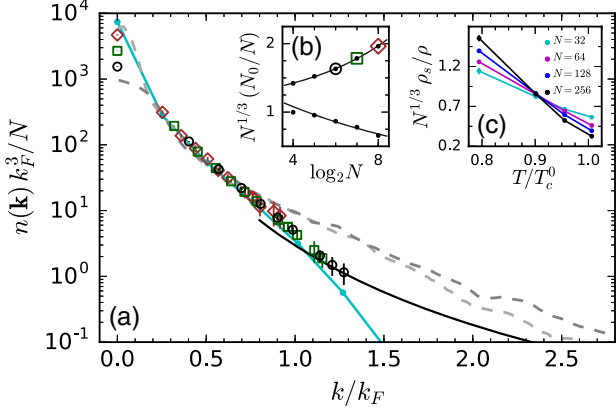


FIG. 4. Full momentum distribution $n(\mathbf{k})$ in the Bose-Einstein-condensed gas phase. (a) $n(\mathbf{k})$ at $\lambda_{\text{th}}\rho^{1/3} = 1.545$, $R_0\rho^{1/3} = 0.184$ [point D in Fig. 3(a)]. First-principles results for $N = 64$, 128, and 256 (black circles, green squares, brown diamonds, respectively), and $\propto C_2/k^4$ asymptotic behavior for $k \rightarrow \infty$ (for $N = 64$, black solid line). Dashed lines are experimental data of Ref. [13] for two different densities. The momentum distribution for $N = 256$ ideal bosons is also shown (cyan solid line). (b) Scaling of the condensed fraction N_0/N with the system size, in the normal and condensed phases. The upper curve (at $T < T_c$) corresponds to the parameters in panel (a), and the exact numerical data are fitted by $N^{1/3}(N_0/N) \approx 1.06 + 0.14N^{1/3}$ [same symbols for N as in panel (a)]. The lower curve is at $\lambda_{\text{th}}\rho^{1/3} \approx 1.373$ (corresponding to $T > T_c$), and is fitted by $N^{1/3}(N_0/N) \approx 1.71N^{-1/6}$. (c) Rescaled superfluid fraction vs temperature, at $R_0\rho^{1/3} = 0.184$. The crossing point at $T/T_c^0 \approx 0.9$ (corresponding to $\lambda_{\text{th}}\rho^{1/3} \approx 1.45$) shows that T_c is lowered by 10% with respect to the ideal Bose gas, in the limit $N \rightarrow \infty$.

in the contact density, obtained from closed-path configurations [see Fig. 3(d)]. In the normal phase, the small- k part of the momentum distribution $n(\mathbf{k})$ resembles the one of ideal bosons: The peak at $k = 0$ corresponds to the Maxwell-Boltzmann distribution $\exp(-\beta k^2/2)$ in the classical limit (at high temperature), and the narrowing at lower temperature is enhanced by bosonic statistics [see Fig. 3(e)]. At large k , $n(\mathbf{k})$ crosses over into the C_2/k^4 asymptotic behavior, with a crossover point which scales as $k/k_F \propto 1/(\lambda_{\text{th}}\rho^{1/3})$ for large temperature, where $k_F \equiv (6\pi^2\rho)^{1/3}$ is the Fermi momentum. In the phase-coexistence region, we obtain two different contact densities for the gas and for the Efimov liquid [see Fig. 3(d)].

Throughout the homogeneous region, the momentum distribution only depends weakly on $R_0\rho^{1/3}$, both in the full $n(\mathbf{k})$ and in its asymptotic tail, underlining the generality of the model under study. The slow decrease of c_2 for increasing $R_0\rho^{1/3}$ (absent at high temperature, $\lambda_{\text{th}}\rho^{1/3} \rightarrow 0$) corresponds to a small suppression of $g^{(2)}(\mathbf{r})$ at short distance, indirectly caused by the hyperradial cutoff. At high temperature, our first-principles results for the contact density rapidly fall below the predictions of the

virial expansion [27–29] [Fig. 3(d)], leveling off at intermediate temperature, and finally decreasing at lower temperature. This nonmonotonic behavior was already qualitatively predicted [29]. The low-temperature values of $c_2\rho^{-4/3}$ fall in the same range of previous zero-temperature approximate results [30–32] [cf. Supplemental Material (ii) [22]].

For large three-body cutoff ($R_0\rho^{1/3} \gtrsim 0.16$), the normal gas undergoes Bose-Einstein condensation before phase separation sets in. At finite k , $n(\mathbf{k})$ has very small finite-size effects, making the comparison with experiments feasible. Data for harmonically trapped Rb atoms [13] are available up to $k/k_F = 3$ and they are considered equilibrated for $k/k_F \gtrsim 0.5$. At small k , the harmonic-trap geometry has the strongest influence. Up to momenta $k \approx k_F$, the experimental curves overlap with the theoretical data [see Fig. 4(a)]. As the asymptotic k^{-4} behavior of $n(\mathbf{k})$ sets in for the numerical curve ($k \gtrsim 1.1k_F$, at the chosen temperature), the experimental curve remains higher. This deviation is difficult to reconcile with our model, as the k^{-4} prefactor is expected to decrease even further at lower temperature [see Supplemental Material (ii) [22]].

The condensate fraction is related to the $\mathbf{k} = \mathbf{0}$ component of $n(\mathbf{k})$, $N_0/N = n(\mathbf{k} = \mathbf{0})/(NV)$. Below the critical temperature T_c , it remains nonzero for $N \rightarrow \infty$, with finite-size corrections $\propto N^{-1/3}$. In the normal phase, in contrast, the large- N limit of N_0/N vanishes. These two behaviors are clearly distinguished in the data [see Fig. 4(b)]. The scaling of the superfluid fraction yields a precise estimate of the critical temperature [33] [see Fig. 4(c) and Supplemental Material (iii) [22]]. In the unitary Bose gas, T_c is reduced by 10%: The critical value of $\lambda_{\text{th}}\rho^{1/3}$ is between 1.44 and 1.48 [see Fig. 3(a)], while the ideal-bosons transition [34] is at $\lambda_{\text{th}}\rho^{1/3} \approx 1.377$. The deviation of T_c from T_c^0 (the ideal-bosons critical temperature) is larger for smaller values of $R_0\rho^{1/3}$. It is instructive to compare $n(\mathbf{k})$ with the ideal-gas curve. Unitary interactions cause a depletion of the condensate, i.e., a decrease of N_0/N . At temperature $T \lesssim T_c$, this follows from the negative shift of the critical temperature, $T_c < T_c^0$. While the $\mathbf{k} = \mathbf{0}$ component of $n(\mathbf{k})$ is smaller, on the other hand, the tail of the distribution is more important [cf. the power-law k^{-4} decay, vs the exponential suppression of $n(\mathbf{k})$ for ideal bosons]. At point D in Fig. 3(a), the depletion of the condensate is not entirely compensated by the large- k contribution [see Supplemental Material (iv) [22]]. This leads to the reweighting of the unitary gas momentum distribution with respect to the one of the ideal Bose gas, without introducing any new features.

Both for three-body and many-body states of unitary bosons, $n(\mathbf{k})$ has subleading oscillations around the C_2/k^4 asymptotic tail. These consist in a log-periodic function of k , modulated by C_3/k^5 [25,35]. The three-body contact parameter C_3 vanishes at the length scale of the short-range hyperradial repulsion between atoms, induced by the van

der Waals potential [14] or by the explicit hyperradial cutoff R_0 . Thus the subleading oscillations can, in our model, only be observed for $k \lesssim 1/R_0$. For our high-temperature results [cf. Fig. 3(e)], the asymptotic tail of $n(\mathbf{k})$ kicks in at $k > 1/R_0$, where C_3 is effectively zero, and we do not expect visible subleading corrections. At low temperature, however, the crossover into the asymptotic tail is at $k \approx 1/R_0$ [see Fig. 4(a)]. Thus, the subleading oscillations are possibly observable within the three-body-cutoff model, for a slightly smaller value of T or R_0 , despite being beyond the current resolution.

In conclusion, we have computed the equilibrium phase diagram and the momentum distribution of the unitary Bose gas from first principles, overcoming the technical challenges through a novel quantum Monte Carlo algorithm [15]. Our theoretical predictions will most easily be checked in the currently available homogeneous traps [36,37], which are less subject to three-body losses than the traditional harmonic traps. In the near future, we expect high-precision experimental measurements of the superfluid transition and of the momentum distribution $n(\mathbf{k})$ in the unitary Bose gas.

We thank Riccardo Rossi for insightful suggestions, and acknowledge extensive discussions with Kris van Houcke, Xavier Leyronas, and Félix Werner. We thank Yvan Castin and Eric Cornell for discussions, and for allowing us reuse of data in Ref. [25] and in Ref. [13]. This work was performed in part at the Aspen Center for Physics, which is supported by National Science Foundation Grant No. PHY-1066293. This work was granted access to the HPC resources of MesoPSL financed by the Region Ile de France and the project Equip@Meso (reference ANR-10-EQPX-29-01) of the programme Investissements d’Avenir supervised by the Agence Nationale pour la Recherche.

*tommaso.comparin@ens.fr
†werner.krauth@ens.fr

- [1] V. Efimov, *Phys. Lett. B* **33**, 563 (1970).
- [2] T. Kraemer, M. Mark, P. Waldburger, J. G. Danzl, C. Chin, B. Engeser, A. D. Lange, K. Pilch, A. Jaakkola, H.-C. Nägerl, and R. Grimm, *Nature (London)* **440**, 315 (2006).
- [3] C. Chin, R. Grimm, P. Julienne, and E. Tiesinga, *Rev. Mod. Phys.* **82**, 1225 (2010).
- [4] E. Braaten and H.-W. Hammer, *Phys. Rep.* **428**, 259 (2006).
- [5] G. Barontini, C. Weber, F. Rabatti, J. Catani, G. Thalhammer, M. Inguscio, and F. Minardi, *Phys. Rev. Lett.* **103**, 043201 (2009).
- [6] J. R. Williams, E. L. Hazlett, J. H. Huckans, R. W. Stites, Y. Zhang, and K. M. O’Hara, *Phys. Rev. Lett.* **103**, 130404 (2009).
- [7] R. Pires, J. Ulmanis, S. Häfner, M. Repp, A. Arias, E. D. Kuhnle, and M. Weidemüller, *Phys. Rev. Lett.* **112**, 250404 (2014).
- [8] T. D. Lee, K. Huang, and C. N. Yang, *Phys. Rev.* **106**, 1135 (1957).

- [9] Y. Castin and F. Werner, *Can. J. Phys.* **91**, 382 (2013) [English version arXiv:1212.5512].
- [10] B. S. Rem, A. T. Grier, I. Ferrier-Barbut, U. Eismann, T. Langen, N. Navon, L. Khaykovich, F. Werner, D. S. Petrov, F. Chevy, and C. Salomon, *Phys. Rev. Lett.* **110**, 163202 (2013).
- [11] R. J. Fletcher, A. L. Gaunt, N. Navon, R. P. Smith, and Z. Hadzibabic, *Phys. Rev. Lett.* **111**, 125303 (2013).
- [12] U. Eismann, L. Khaykovich, S. Laurent, I. Ferrier-Barbut, B. S. Rem, A. T. Grier, M. Delehaye, F. Chevy, C. Salomon, L.-C. Ha, and C. Chin, *Phys. Rev. X* **6**, 021025 (2016).
- [13] P. Makotyn, C. E. Klauss, D. L. Goldberger, E. A. Cornell, and D. S. Jin, *Nat. Phys.* **10**, 116 (2014).
- [14] J. Wang, J. P. D’Incao, B. D. Esry, and C. H. Greene, *Phys. Rev. Lett.* **108**, 263001 (2012).
- [15] T. Comparin and W. Krauth (to be published).
- [16] S. Tan, *Ann. Phys. (Amsterdam)* **323**, 2952 (2008).
- [17] F. Werner and Y. Castin, *Phys. Rev. A* **86**, 053633 (2012).
- [18] D. M. Ceperley, *Rev. Mod. Phys.* **67**, 279 (1995).
- [19] W. Krauth, *Phys. Rev. Lett.* **77**, 3695 (1996).
- [20] M. Boninsegni, N. V. Prokof’ev, and B. V. Svistunov, *Phys. Rev. E* **74**, 036701 (2006).
- [21] E. L. Pollock and D. M. Ceperley, *Phys. Rev. B* **36**, 8343 (1987).
- [22] See Supplemental Material at <http://link.aps.org/supplemental/10.1103/PhysRevLett.117.225301> for (i) the description of the $n(\mathbf{k})$ estimator, (ii) the study of c_2 at low temperature, (iii) more details on the superfluid transition, (iv) a comparison with the momentum distribution of noninteracting bosons, and (v) the analytical model for the gas-liquid coexistence.
- [23] S. Piatecki and W. Krauth, *Nat. Commun.* **5**, 3503 (2014).
- [24] Y. Yan and D. Blume, *Phys. Rev. A* **91**, 043607 (2015).
- [25] Y. Castin and F. Werner, *Phys. Rev. A* **83**, 063614 (2011).
- [26] J. von Stecher, *J. Phys. B* **43**, 101002 (2010).
- [27] D. H. Smith, E. Braaten, D. Kang, and L. Platter, *Phys. Rev. Lett.* **112**, 110402 (2014).
- [28] M. Barth and J. Hofmann, *Phys. Rev. A* **92**, 062716 (2015).
- [29] X.-J. Liu, B. Mulkerin, L. He, and H. Hu, *Phys. Rev. A* **91**, 043631 (2015).
- [30] J. M. Diederix, T. C. F. van Heijst, and H. T. C. Stoof, *Phys. Rev. A* **84**, 033618 (2011).
- [31] M. Rossi, L. Salasnich, F. Ancilotto, and F. Toigo, *Phys. Rev. A* **89**, 041602 (2014).
- [32] A. G. Sykes, J. P. Corson, J. P. D’Incao, A. P. Koller, C. H. Greene, A. M. Rey, K. R. A. Hazzard, and J. L. Bohn, *Phys. Rev. A* **89**, 021601 (2014).
- [33] E. L. Pollock and K. J. Runge, *Phys. Rev. B* **46**, 3535 (1992).
- [34] L. P. Pitaevskii and S. Stringari, *Bose-Einstein Condensation* (Oxford University Press, Oxford, 2003).
- [35] E. Braaten, D. Kang, and L. Platter, *Phys. Rev. Lett.* **106**, 153005 (2011).
- [36] A. L. Gaunt, T. F. Schmidutz, I. Gotlibovych, R. P. Smith, and Z. Hadzibabic, *Phys. Rev. Lett.* **110**, 200406 (2013).
- [37] N. Navon, A. L. Gaunt, R. P. Smith, and Z. Hadzibabic, *Science* **347**, 167 (2015).

Momentum distribution in the unitary Bose gas from first principles

Tommaso Comparin and Werner Krauth

*Laboratoire de Physique Statistique, École Normale Supérieure/PSL Research University,
UPMC, Université Paris Diderot, CNRS, 24 rue Lhomond, 75005 Paris, France*

(Dated: November 3, 2016)

Supplementary Item (i): Momentum-distribution estimator

In path-integral quantum Monte Carlo, the momentum distribution is usually computed from the exponential $e^{-i\mathbf{k}\cdot(\mathbf{x}-\mathbf{y})}$ (with open ends \mathbf{x} and \mathbf{y}), averaged over open-path configurations[1, 2]. At large momenta k – where $n(\mathbf{k})$ tends to zero – this estimator becomes unpractical, because of a vanishing signal-to-noise ratio. We construct a new estimator (used in Fig. 3(e)), based on the solution of the two-body problem represented in Fig. S1[3]. We analytically

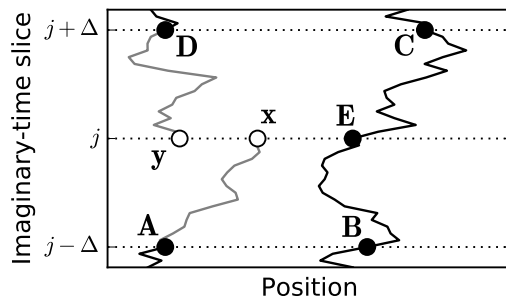


FIG. S1. Open $N = 2$ path configuration. An estimator for the momentum distribution is derived from the analytical expression for $n(\mathbf{k})$ for fixed positions $\mathbf{A}, \mathbf{B}, \mathbf{C}, \mathbf{D}, \mathbf{E}$.

determine $n(\mathbf{k}|\mathbf{A}, \dots, \mathbf{E})$, the average of $e^{-i\mathbf{k}\cdot(\mathbf{x}-\mathbf{y})}$ for given positions $\mathbf{A}, \mathbf{B}, \mathbf{C}, \mathbf{D}, \mathbf{E}$. For $N = 2$, $n(\mathbf{k})$ is obtained as an average of $n(\mathbf{k}|\mathbf{A}, \dots, \mathbf{E})$ over configurations $\mathbf{A}, \mathbf{B}, \mathbf{C}, \mathbf{D}, \mathbf{E}$ sampled during the simulation. For $N \geq 3$, this coarse-grained estimator holds for “local” configurations, where the two open ends are close to each other and to the nearest of the other bosons ($\mathbf{x} \sim \mathbf{y} \sim \mathbf{E}$). For non-local configurations we again resort to the direct estimator $\langle e^{-i\mathbf{k}\cdot(\mathbf{x}-\mathbf{y})} \rangle$, and finally obtain $n(\mathbf{k})$ as a weighted average of the two estimators (*cf.* Ref. [3]). This procedure relies on an appropriate cutoff between local and non-local configurations. At high enough temperature, where the procedure is used, we carefully check that the contact density c_2 extracted from the asymptotic behavior of $n(\mathbf{k})$ for $k \rightarrow \infty$ agrees with the $r \rightarrow 0$ limit of $g^{(2)}(\mathbf{r})$ (see Fig. 3(c)).

Supplementary Item (ii): Contact density at low temperature

In Fig. S2, the data of Fig. 3(a) are plotted as a function of T/T_c^0 , for a three-body cutoff $R_0\rho^{1/3} \simeq 0.184$. Our first-principles low-temperature values for $c_2\rho^{-4/3}$ are roughly compatible with the zero-temperature approximate results from Refs. [4–6]. These are obtained via a Jastrow ansatz and hypernetted-chain approximation[4], a quantum Monte Carlo calculations based on a Jastrow-Feenberg ansatz[5], and a time-dependent variational ansatz for the many-body state[6]. The value $c_2\rho^{-4/3} \simeq 22$, extracted from an analysis of the experimental data[7], appears significantly larger than our theoretical predictions.

Supplementary Item (iii): Superfluid transition

The critical temperature T_c is extracted from finite- N data using the scaling ansatz of Ref. [8]. This assumes that in the critical region the rescaled superfluid fraction $N^{1/3}\rho_s/\rho$ depends on the system size N only through the quantity $N^{1/(3\nu)}(T - T_c)/T_c$, where ν is the correlation-length critical exponent, and implies that $N^{1/3}\rho_s/\rho$ becomes

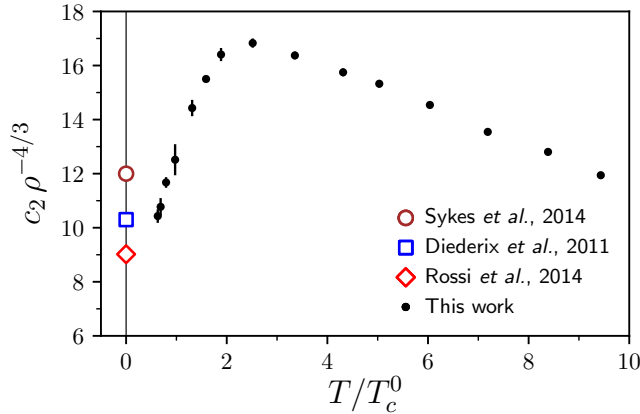


FIG. S2. Contact density at low temperature ($T/T_c^0 = 1$ corresponds to $\lambda_{\text{th}}\rho^{1/3} = 1.377$), for $R_0\rho^{1/3} = 0.184$ (black points), and zero-temperature approximate results for the models in Refs. [4–6] (open symbols).

size-independent at the critical temperature $T = T_c$ of the infinite system. The dependence of $N^{1/3}\rho_s/\rho$ on system size, for different values of the three-body cutoff $R_0\rho^{1/3}$, is shown in Fig. S3, and we observe that the crossing point is roughly at 90% of the critical temperature of ideal bosons[9]. The critical temperature T_c weakly depends on $R_0\rho^{1/3}$: In the range $0.164 \lesssim R_0\rho^{1/3} \lesssim 0.204$, it increases from $T_c/T_c^0 \approx 0.87$ to $T_c/T_c^0 \approx 0.91$.

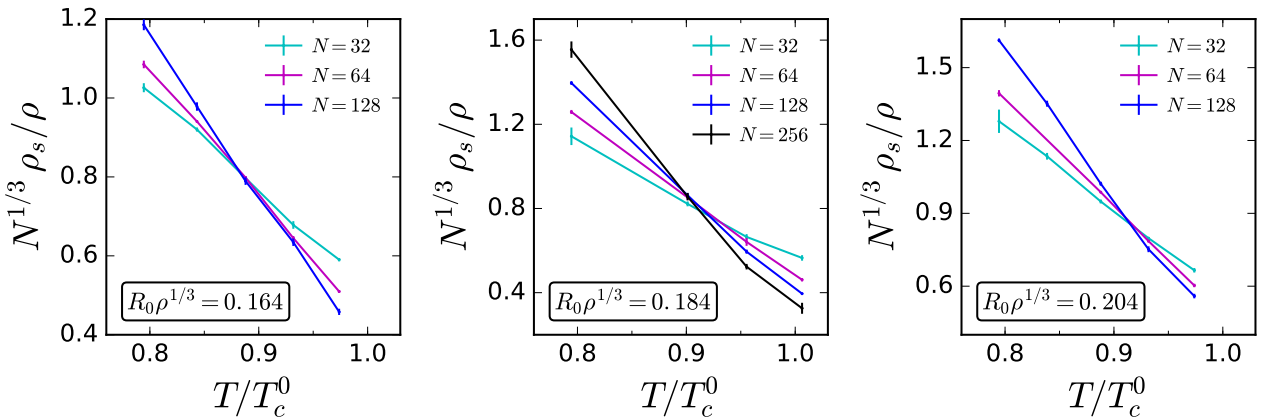


FIG. S3. Finite-size scaling of the superfluid fraction for different values of the three-body cutoff $R_0\rho^{1/3}$. The crossing point of $N^{1/3}\rho_s/\rho$ vs. T/T_c^0 establishes a 10% decrease of the superfluid transition temperature with respect to ideal bosons, in the limit $N \rightarrow \infty$ (cf. Fig. 4(c)).

Supplementary Item (iv): Effect of interaction on $n(\mathbf{k})$

In the Bose-condensed phase, the $\mathbf{k} = \mathbf{0}$ component of the momentum distribution is reduced by unitary interactions, and the presence of a slowly-decaying k^{-4} tail at large k does not fully compensate this decrease. Therefore, the unitary-gas momentum distribution has a stronger weight in the intermediate- k region, as clearly visible in Fig. S4. In both the interacting and non-interacting case, $n(\mathbf{k})$ does not show strong finite-size effects at $k > 0$.

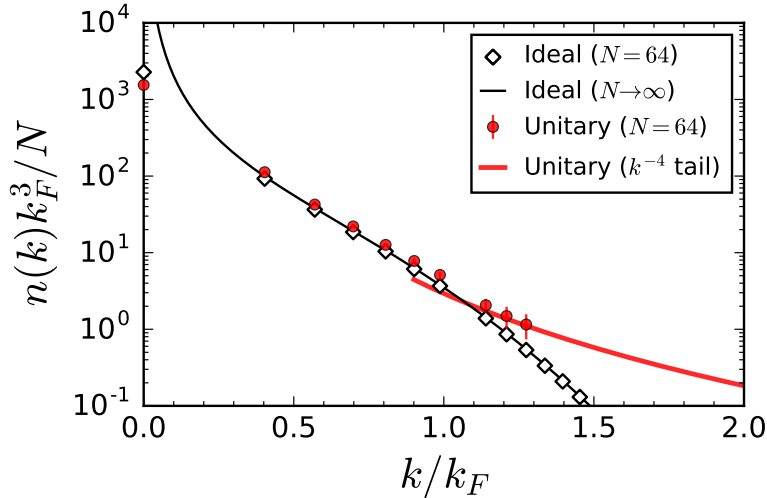


FIG. S4. Momentum distribution $n(\mathbf{k})$ in the Bose-condensed phase (point D in Fig. 3(a)) for the unitary Bose gas with $N = 64$ (same data as in Fig. 4(a)), compared to the curves for finite and infinite systems of ideal bosons at the same temperature.

Supplementary Item (v): Coexistence free energy

We consider N particles in a fixed volume V , in the presence of an l -particle nucleus of Efimov liquid. The coexistence free energy includes the liquid and gas contributions. For the liquid, we approximate $F_{\text{liq}}(l) \simeq E_{\text{liq}}(l)$, neglecting the entropic contribution, and we use the cluster energies from Ref. [10] for $l \leq 13$, in terms of the trimer energy $|E_T| \simeq 0.00214 \hbar^2/(mR_0^2)$ [11]. For the gas contribution, we consider $N - l$ particles in a volume $V - V_{\text{liq}}$ (where $V_{\text{liq}} \simeq l \times (3.65R_0)^3$), and compute $F_{\text{gas}}(N - l)$ up to the third virial coefficient[12]. At given values of N, V , and T , the coexistence free energy reads

$$F_{\text{coex}}^N(l) \simeq E_{\text{liq}}(l) + F_{\text{gas}}(N - l). \quad (\text{S1})$$

Computing $F_{\text{coex}}^N(l)$ as a function of l allows us to check for the existence of a free-energy barrier $\beta\Delta F$, which does not disappear in the low-temperature regime. The third-order virial and cluster expansions differ in their range of validity, the cluster expansion being more accurate at low temperature (*cf.* Fig. 3(c)). We find that the above model is not quantitatively reliable at large R_0 , for which the instability takes place at lower temperature. Its limit of validity is $R_0\rho^{1/3} \lesssim 0.04$, while for larger values of R_0 it does not correctly reproduce the coexistence line.

- [1] D. M. Ceperley, Rev. Mod. Phys. **67**, 279 (1995).
- [2] M. Boninsegni, N. V. Prokof'ev, and B. V. Svistunov, Phys. Rev. E **74**, 036701 (2006).
- [3] T. Comparin and W. Krauth, “,” In preparation.
- [4] J. M. Diederix, T. C. F. van Heijst, and H. T. C. Stoof, Phys. Rev. A **84**, 033618 (2011).
- [5] M. Rossi, L. Salasnich, F. Ancilotto, and F. Toigo, Phys. Rev. A **89**, 041602 (2014).
- [6] A. G. Sykes, J. P. Corson, J. P. D’Incao, A. P. Koller, C. H. Greene, A. M. Rey, K. R. A. Hazzard, and J. L. Bohn, Phys. Rev. A **89**, 021601 (2014).
- [7] D. H. Smith, E. Braaten, D. Kang, and L. Platter, Phys. Rev. Lett. **112**, 110402 (2014).
- [8] E. L. Pollock and K. J. Runge, Phys. Rev. B **46**, 3535 (1992).
- [9] L. P. Pitaevskii and S. Stringari, *Bose-Einstein Condensation* (Oxford University Press, Oxford, 2003).
- [10] J. von Stecher, J. Phys. B **43**, 101002 (2010).
- [11] E. Braaten and H.-W. Hammer, Phys. Rep. **428**, 259 (2006).
- [12] Y. Castin and F. Werner, Can. J. Phys. **91**, 382 (2013), English version: arXiv:1212.5512.

Ultracold atomic gases offer unprecedented possibilities to realize and manipulate quantum systems. The control on interparticle interactions allows to reach the strongly-interacting regime, with both fermionic and bosonic atomic species. In the unitary limit, where the interaction strength is at its maximum, universal properties emerge. For bosonic atoms, these include the Efimov effect, the surprising existence of an infinite sequence of three-body bound states.

In this thesis, we have studied a system of unitary bosons. Starting from the two- and three-body cases, we have shown that the chosen model correctly captures the universal features of the Efimov effect. For the corresponding many-body problem, we have developed a quantum Monte Carlo algorithm capable of realizing the different thermodynamic phases in which the system may exist: The high-temperature normal gas, the Bose-Einstein condensate, and the Efimov liquid.

A single ingredient of our model would remain relevant in the infinite-temperature limit, namely the three-body hard-core repulsion, which constitutes a generalization of the classical hard-sphere potential. For this model, we have proposed a solution to the two- and three-dimensional packing problem, based on an analytical ansatz and on the simulated-annealing technique. Extending these results to finite pressure showed that the system has a discontinuous melting transition, which we identified through the Monte Carlo method.

Keywords: Ultracold atoms, unitary Bose gas, Bose-Einstein condensation, Efimov effect, three-body hard-core model, Monte Carlo method.

Les gaz d'atomes ultrafroids offrent des possibilités sans précédent pour la réalisation et la manipulation des systèmes quantiques. Le contrôle exercé sur les interactions entre particules permet d'atteindre le régime de fortes interactions, pour des espèces d'atomes à la fois fermioniques et bosoniques. Dans la limite unitaire, où la force d'interaction est à son maximum, des propriétés universelles émergent. Pour les atomes bosoniques, celles-ci comprennent l'effet Efimov, l'existance surprenante d'une séquence infinie d'états liés à trois corps.

Dans cette thèse, nous avons étudiés un système de bosons unitaires. Partant des cas à deux et à trois corps, nous avons montré que le modèle choisi capturait correctement les caractéristiques universelles de l'effet Efimov. Pour le modèle à N-corps, nous avons développé un algorithme de Monte Carlo quantique capable de réaliser les différentes phases thermodynamiques du système : gaz normal à haute-température, condensat de Bose-Einstein, et liquide d'Efimov.

Un unique composant de notre modèle resterait pertinent à la limite de température infinie, à savoir la répulsion corps dur à trois corps, qui constitue une généralisation du potentiel classique entre sphères dures. Pour ce modèle, nous avons proposé une solution au problème d'empilement compact en deux et trois dimensions, fondée sur une Ansatz analytique et sur la technique de recuit simulé. En étendant ces résultats à une situation de pression finie, nous avons montré que le système présente une transition de fusion discontinue, que nous avons identifié à travers la méthode de Monte Carlo.

Mots-clefs: atomes ultrafroids, gaz de Bose unitaire, condensation de Bose-Einstein, effet d'Efimov, modèle de coeur dur à trois corps, méthode de Monte Carlo.